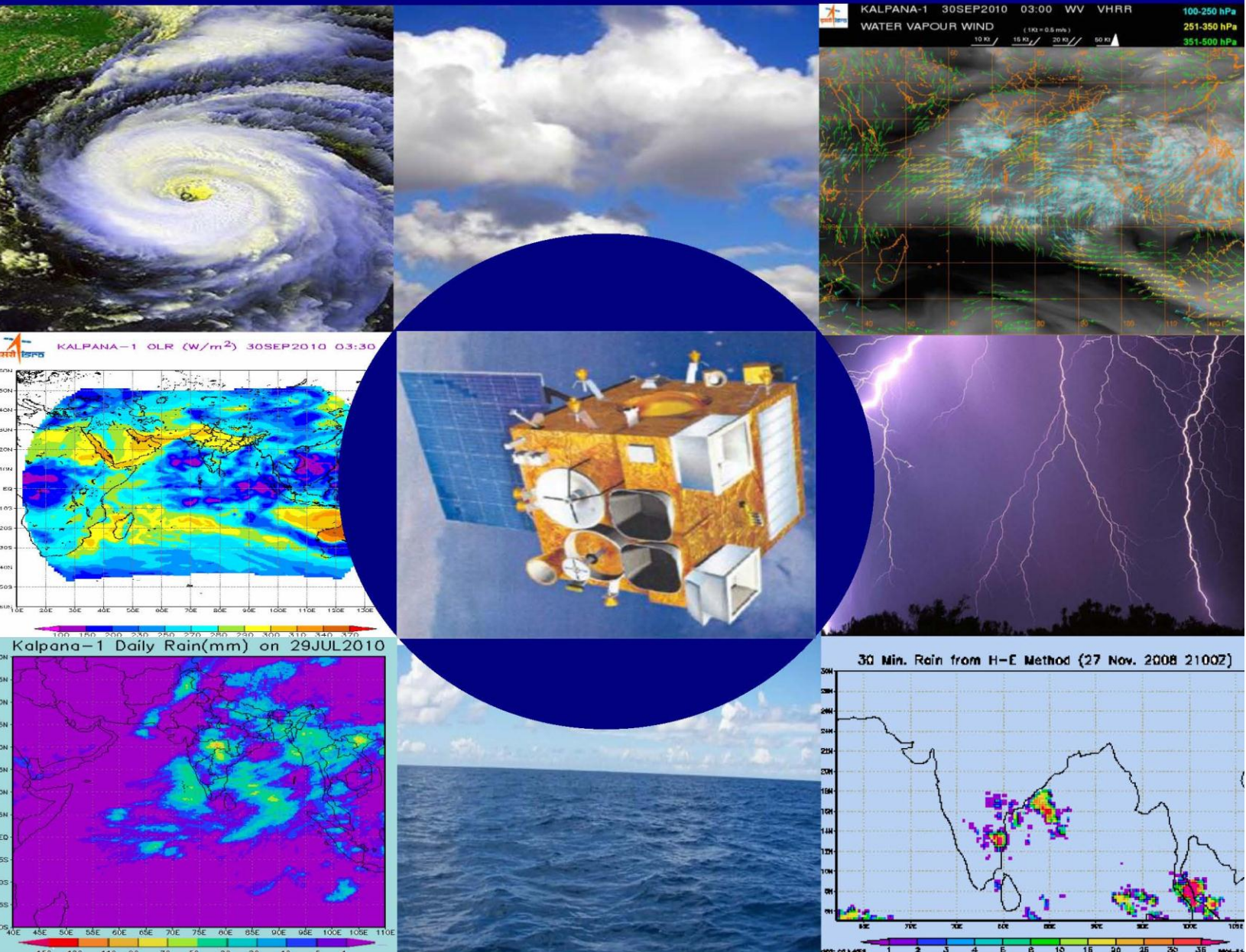


INSAT-3D

Algorithm Theoretical Basis Development Document



May -2015

Earth, Ocean, Atmosphere, Planetary Sciences & Applications Area
Space Applications Centre
Ahmedabad-380015

Contents

1. INTRODUCTION	9
1.1 INTRODUCTION	11
2. CLOUD MASK.....	14
2.1 ALGORITHM CONFIGURATION INFORMATION	16
2.2 INTRODUCTION	16
2.3 INPUTS	17
2.4 ALGORITHM FUNCTIONAL SPECIFICATIONS	18
2.5 OUTPUTS.....	25
2.6 VALIDATION	25
2.7 TECHNICAL ISSUES.....	25
2.8 FUTURE SCOPE.....	25
2.9 REFERENCES	26
3. OUTGOING LONGWAVE RADIATION.....	28
3.1 ALGORITHM CONFIGURATION INFORMATION	30
3.2 INTRODUCTION	30
3.3 INPUTS	32
3.4 ALGORITHM FUNCTIONAL SPECIFICATIONS	33
3.5 OUTPUTS.....	38
3.6 VALIDATION	39
3.7 TECHNICAL ISSUES.....	39
3.8 FUTURE SCOPE.....	39
3.9 REFERENCES	39
4. QUANTITATIVE PRECIPITATION ESTIMATE.....	42
(A) GPI AND IMSRA METHOD	44
4.1 ALGORITHM CONFIGURATION INFORMATION	44
4.2 INTRODUCTION.....	44
4.3 INPUTS	49
4.4 ALGORITHM FUNCTIONAL SPECIFICATIONS	50
4.5 OUTPUTS	60
4.6 VALIDATION	61
4.7 TECHNICAL ISSUES: (LIMITATION ETC.).....	63
4.8 FUTURE SCOPE.....	63
4.9 REFERENCES	64
(B) RAINFALL ESTIMATION – H-E METHOD.....	67
4.1 ALGORITHM CONFIGURATION INFORMATION	67
4.2 INTRODUCTION	67
4.3 INPUTS	68
4.4 ALGORITHM FUNCTIONAL SPECIFICATIONS	69
4.5 OUTPUTS.....	79
4.6 VALIDATION	79
4.7 FUTURE SCOPE.....	83
4.9 REFERENCES	83
5. SEA SURFACE TEMPERATURE.....	85
5.1 ALGORITHM CONFIGURATION INFORMATION	87
5.2 INTRODUCTION	87
5.3 INPUTS	88
5.4 ALGORITHM FUNCTIONAL SPECIFICATIONS	89
5.5 OUTPUTS.....	95
5.6 VALIDATION	95

5.7	FUTURE SCOPE.....	96
5.8	REFERENCES	96
6.	SNOW COVER.....	99
6.1	ALGORITHM CONFIGURATION INFORMATION	101
6.2	INTRODUCTION	101
6.3	INPUTS AND OUTPUT DATA.....	103
6.4	ALGORITHM FUNCTIONAL SPECIFICATIONS	104
6.5	OUTPUTS.....	108
6.6	VALIDATION AND ERROR ANALYSIS.....	109
6.7	FUTURE SCOPE.....	110
6.8	REFERENCES	110
7.	SNOW DEPTH	113
7.1	ALGORITHM CONFIGURATION INFORMATION	115
7.2	INTRODUCTION	115
7.3	INPUTS	118
7.4	ALGORITHM FUNCTIONAL SPECIFICATIONS	119
7.5	OUTPUTS.....	125
7.6	VALIDATION	126
7.7	TECHNICAL ISSUES:.....	126
7.8	FUTURE SCOPE.....	126
7.9	REFERENCES	126
8.	FIRE.....	129
8.1	ALGORITHM CONFIGURATION INFORMATION	131
8.2	INTRODUCTION	131
8.3	INPUTS	132
8.4	ALGORITHM FUNCTIONAL SPECIFICATIONS	133
8.5	OUTPUTS.....	137
8.6	VALIDATION	137
8.7	TECHNICAL ISSUES (LIMITATION ETC.).....	137
8.8	FUTURE SCOPE.....	138
8.9	REFERENCES	138
9.	SMOKE	139
9.1	ALGORITHM CONFIGURATION INFORMATION	141
9.2	INTRODUCTION	141
9.3	INPUTS	142
9.4	ALGORITHM FUNCTIONAL SPECIFICATIONS	144
9.5	OUTPUT.....	148
9.6	VALIDATION	148
9.7	TECHNICAL ISSUES.....	148
9.8	FUTURE WORK	148
9.9	REFERENCES	149
10.	AEROSOL.....	151
10.1	ALGORITHM CONFIGURATION INFORMATION.....	153
10.2	INTRODUCTION.....	153
10.3	INPUTS.....	154
10.4	ALGORITHM FUNCTIONAL SPECIFICATIONS	155
10.5	OUTPUTS	160
10.6	VALIDATION.....	160
10.7	TECHNICAL ISSUES (LIMITATION ETC.).....	161
10.8	FUTURE SCOPE.....	161
10.9	REFERENCES	161

11. ATMOSPHERIC MOTION VECTOR WINDS (TIR 1).....	163
11.1 ALGORITHM CONFIGURATION INFORMATION.....	165
11.2 INTRODUCTION.....	165
11.3 INPUTS.....	166
11.4 ALGORITHM FUNCTIONAL SPECIFICATIONS	167
11.5 OUTPUTS	175
11.6 VALIDATION.....	175
11.7 TECHNICAL ISSUES (LIMITATIONS ETC).....	177
11.8 REFERENCES	178
12. ATMOSPHERIC MOTION VECTOR WINDS (WV)	181
12.1 ALGORITHM CONFIGURATION INFORMATION.....	182
12.2 INTRODUCTION.....	182
12.3 INPUTS.....	183
12.4 ALGORITHM FUNCTIONAL SPECIFICATIONS	184
12.5 OUTPUTS	193
12.6 VALIDATION.....	193
12.8 REFERENCES	195
13. ATMOSPHERIC MOTION VECTOR WINDS (VIS)	199
13.1 ALGORITHM CONFIGURATION INFORMATION.....	201
13.2 INTRODUCTION	201
13.3 INPUTS.....	202
13.4 ALGORITHM FUNCTIONAL SPECIFICATIONS	202
13.5 OUTPUTS	208
13.6 VALIDATION.....	208
13.7 TECHNICAL ISSUES (LIMITATIONS ETC).....	210
13.8 REFERENCES	211
14. ATMOSPHERIC MOTION VECTOR WINDS (MIR).....	213
14.1 ALGORITHM CONFIGURATION INFORMATION.....	215
14.2 INTRODUCTION.....	215
14.3 INPUTS.....	216
14.4 ALGORITHM FUNCTIONAL SPECIFICATIONS	217
14.5 OUTPUTS	223
14.6 VALIDATION.....	223
14.7 TECHNICAL ISSUES (LIMITATIONS ETC).....	225
14.8 REFERENCES	226
15. UPPER TROPOSPHERIC HUMIDITY	229
15.1 ALGORITHM CONFIGURATION INFORMATION.....	231
15.2 INTRODUCTION.....	231
15.3 INPUTS.....	232
15.4 ALGORITHM FUNCTIONAL SPECIFICATIONS	232
15.5 OUTPUTS	239
15.6 VALIDATION.....	239
15.7 TECHNICAL ISSUES (LIMITATION ETC.)	240
15.8 FUTURE SCOPE.....	240
15.9 REFERENCES	240
16. TEMPERATURE, MOISTURE PROFILE AND TOTAL OZONE FROM SOUNDER.....	243
16.1 ALGORITHM CONFIGURATION INFORMATION	245
16.2 INTRODUCTION.....	245
16.3 INPUTS.....	247
16.4 ALGORITHM FUNCTIONAL SPECIFICATIONS	248

16.5	OUTPUT	261
16.6	VALIDATION.....	262
16.7	TECHNICAL ISSUES.....	264
16.8	FUTURE SCOPE.....	264
16.9	REFERENCES	264
17. FOG		271
17.1	ALGORITHM CONFIGURATION INFORMATION.....	273
17.2	INTRODUCTION.....	273
17.3	INPUTS.....	273
17.4	ALGORITHM FUNCTIONAL SPECIFICATIONS	275
17.5	OUTPUTS	277
17.6	VALIDATION.....	278
17.7	TECHNICAL ISSUES	278
17.8	FUTURE SCOPE	278
17.9	REFERENCES	279
18. LAND SURFACE TEMPERATURE		281
18.1	ALGORITHM CONFIGURATION INFORMATION.....	283
18.2	INTRODUCTION.....	283
18.3	THEORETICAL BACKGROUND	285
18.4	METHOD AND DATA USED IN THE STUDY	287
18.5	RESULTS.....	292
18.6	VALIDATION OF INSAT-3D IMAGER LST WITH K1/MODIS LST	298
18.7	CONCLUSIONS	302
18.8	REFERENCES	303
19. POTENTIAL EVAPOTRANSPIRATION		307
19.1	ALGORITHM CONFIGURATION INFORMATION.....	309
19.2	INTRODUCTION	309
19.3	INPUTS.....	313
19.4	ALGORITHM FUNCTIONAL SPECIFICATIONS	314
19.5	OUTPUTS	319
19.6	VALIDATION OF INSAT 3D GENERATED DAILY POTENTIAL EVAPO-TRANSPIRATION	319
19.7	STUDY OF POTENTIAL EVAPO-TRANSPIRATION WITH K1 VHRR DATA	319
19.8	SOURCES OF ERRORS / UNCERTAINTIES IN ET _O ESTIMATES AND VALIDATION ISSUES.....	331
19.9	FUTURE SCOPE OF IMPROVEMENT.....	332
19.10	REFERENCES	332
20. SURFACE INSOLATION OVER LAND		335
20.1	ALGORITHM CONFIGURATION INFORMATION.....	337
20.2	INTRODUCTION.....	337
20.3	INPUTS.....	341
20.4	ALGORITHM FUNCTIONAL SPECIFICATIONS	342
20.5	OUTPUTS	348
20.6	SENSITIVITY ANALYSIS FOR ERROR BUDGETING	350
20.7	VALIDATION.....	353
20.8	LIMITATIONS OF ALGORITHM AND ISSUES IN OPERATIONAL SCENARIO	358
20.9	FUTURE SCOPE OF IMPROVEMENT.....	359
20.10	REFERENCES	359
21. APPLICATION PARAMETERS FROM SOUNDER DERIVED PRODUCTS.....		363
21.1.	GEOPOTENTIAL HEIGHT	366
21.2.	LAYER AND TOTAL PRECIPITABLE WATER	369
21.3.	LIFTED INDEX FROM SOUNDER.....	372
21.4.	DRY MICROBURST INDEX.....	374

21.5.	MAXIMUM VERTICAL THETA-E DIFFERENTIAL.....	376
21.6.	WIND INDEX.....	378

1. Introduction

1.1 Introduction

This document is the Algorithm Theoretical Basis Definition (**ATBD**) for the geophysical parameter retrieval from INSAT-3D Imager and Sounder channels data.

This document contains 17 chapters which are structured as follows: Chapter 1 Describes the purpose and scope of the document, provides the sensor specifications of INSAT-3D.

Chapters 2 describes the preliminary cloud masking algorithm using only 3 IR channels of 4 km resolution which may be used by some parameter generation. Chapters 3 to 21 contain the theoretical basis for the individual algorithms of various geophysical parameters except HSCAS and tropical cyclone. Algorithms for tropical cyclone position and intensity estimation system and snow analysis system are to be written jointly with IMD because derivation of these parameters needs large number of auxillary inputs and operational meterological expertise. Discussion is going on with IMD for making these two algorithms.

The purpose of this document is to describe the scientific algorithms which will be used to extract the Meteorological Products from the pre-processed Level 1 image data acquired by the Very High Resolution Radiometer (VHRR) and 19 channel Sounder onboard INSAT-3D satellite. VHRR produces images in six spectral channels, in the Visible (VIS), Near Infra-red (NIR), Mid Wave Infra-Red (MWIR), and Infra-Red (IR) part of the spectrum covering the following channels: VIS 0.6 μ m, NIR 1.6 μ m, MWIR 3.9 μ m, WV 6.7 μ m, IR 10.8 μ m, IR 12.0 μ m. Each channel of the Imager has different resolution as mentioned in the following Table-1

Table – 1: INSAT-3D VHRR Specification

Channel No	Wavelength (μ m)	Resolution (Km)
1	0.55 - 0.75	1
2	1.55 - 1.70	1
3	3.8 - 4.0	4
4	6.5 - 7.1	8
5	10.2 - 11.3	4
6	11.5 - 12.5	4

INSAT-3D Sounder has 18 infrared channel and a visible channel to help cloud detection during daytime. Central wavelengths of these channels along with the typical noise sensitivity are summarized in the Table-2.

Table 2: INSAT-3D Sounder Channels Characteristics

Detector	Ch. No.	λ_c (μm)	v_c (cm^{-1})	$\Delta\lambda(\Delta v)$ μm (cm^{-1})	Principal absorbing gas	Purpose
Long wave	1	14.67	682	0.385 (18)	CO_2	Stratosphere temperature
	2	14.31	699	0.305 (15)	CO_2	Tropopause temperature
	3	14.03	713	0.321 (16)	CO_2	Upper-level temperature
	4	13.64	733	0.351 (19)	CO_2	Mid-level temperature
	5	13.33	750	0.352 (20)	CO_2	Low-level temperature
	6	12.59	794	0.541 (34)	water vapor	Total precipitable water
	7	11.98	834	0.768 (53)	water vapor	Surface temp., moisture
Mid wave	8	10.99	910	0.611 (51)	window	Surface temperature
	9	9.69	1032	0.262 (28)	ozone	Total ozone
	10	7.43	1346	0.299 (54)	water vapor	Low-level moisture
	11	7.04	1421	0.426 (86)	water vapor	Mid-level moisture
	12	6.52	1534	0.269 (63)	water vapor	Upper-level moisture
Short wave	13	4.61	2168	0.054 (25)	N_2O	Low-level temperature
	14	4.54	2202	0.053 (26)	N_2O	Mid-level temperature
	15	4.48	2232	0.057 (28)	CO_2	Upper-level temperature
	16	4.15	2408	0.078 (45)	CO_2	Boundary-level temp.
	17	4.01	2496	0.075 (46)	window	Surface temperature
	18	3.79	2642	0.143 (100)	window	Surface temp., moisture

The following Table 3 describes the VHRR specification in INSAT-3A / Kalpana

Table-3 INSAT-3A / Kalpana –1 VHRR

Channel No	Wavelength (μm)	Resolution (km)
1	0.55 - 0.75	2
2	5.7 - 7.1	8
3	10.5 - 12.5	8

The following Table – 4 gives the geophysical parameters which will be retrieved from INSAT-3D Imager and sounder channels

Table 4: Geophysical Parameters retrieved from INSAT-3D

No.	Parameters	Remarks	Product Name (acronyms)
1.	<i>Cloud Mask</i>	Revised	CMK
2.	<i>Outgoing Longwave Radiation (OLR)</i>	Revised	OLR
3.	<i>Quantitative Precipitation Estimation (QPE)</i>	Revised	GPI HEM
4.	<i>Sea Surface Temperature (SST)</i>	Revised	SST
5.	<i>Snow cover</i>	To be confirmed	
6.	<i>Snow depth</i>	To be confirmed	SNW
7.	<i>Fire</i>	No Change	FIR
8.	<i>Smoke</i>	Revised	SMK
9.	<i>Aerosol</i>	Revised	AOD
10.	<i>Cloud Motion Vector (AMV)</i>	Revised	AMV
11.	<i>Water Vapour wind (WVW)</i>	Revised	WVW
12.	<i>Visible wind vector</i>	New Algorithm	VWV
13.	<i>Upper Tropospheric Humidity (UTH)</i>	Revised	UTH
14.	<i>Temperature, Humidity profile and Total Ozone</i>	Revised	
15.	<i>Value added parameters from sounder products</i>	No Change	SND
16.	<i>Fog</i>	Revised	FOG
17.	<i>Potential evapotranspiration</i>	New Algorithm	PET
18.	<i>Land surface insolation</i>	New Algorithm	INSO_LAND
19.	<i>Land surface temperature</i>	New Algorithm	LST

The theoretical basis for the algorithm of each of these parameters is described in the following sections.

The details of the nomenclature of products can be found in the INSAT-3D product format guide which is available from the mosdac website (www.mosdac.gov.in).

2. Cloud Mask

S.No.	Product Name	Spatial Resolution	Temporal Resolution
1	3DIMG_L2B_CMK	4 km	30 minutes

2. Cloud Mask

2.1 Algorithm Configuration Information

2.1.1 Algorithm Name

Cloud Mask (CM)

(Ref: Additional to IMD RFP)

2.1.2 Algorithm Identifier

3DIMG_L2B_CMK

2.1.3 Algorithm Specification

Version	Date	Prepared by	Description
1.0	July 2014	P K Pal & Shivani Shah	Cloud Mask baseline document

2.2 Introduction

The discrimination of cloud from the clear sky is necessary for many geophysical parameter retrieval from INSAT data. Clouds are generally characterized by higher reflectance and lower temperature than the underlying earth surface. As such, simple visible and infrared window threshold approaches offer considerable skill in cloud detection. However, there are many surface conditions when this characterization of clouds is inappropriate, most notably over snow and ice. Additionally, some cloud types such as thin cirrus, low stratus at night, and small cumulus are difficult to detect because of insufficient contrast with the surface radiance. Cloud edges cause further difficulty since the instrument field of view will not always be completely cloudy or clear.

INSAT-3D VHRR will measure radiances in one visible and one SWIR band at 1 km spatial resolution, one MIR and two TIR bands at 4 km resolution, and one WV band at 8 km resolution. Radiances from 3 IR spectral bands TIR –1 , TIR –2 and MIR (Table 1) which are of same resolution of 4km are used in the INSAT cloud mask algorithm to estimate whether a given view of the earth surface is unobstructed by clouds.

This cloud mask parameter will be directly used for the retrieval of the following parameters: SST , UTH, Fire and Snow Cover. This will be partially used for retrieval of AOD where additional test may be required with the visible data.

2.2.1 Overview and background

The INSAT cloud mask algorithm benefits from several previous efforts to characterize global cloud cover using satellite observations. These algorithms have been used in global cloud climatology over long time periods and thus have overcome some of the difficulties facing the INSAT cloud mask algorithm. A wide variety of scientists have discussed the physical basis behind each of the spectral tests and applications to satellite or aircraft data are present in a variety of publications (*Ackerman et al. [1997]*). The INSAT cloud mask algorithm builds on these past works by combining the different tests into a single unified algorithm.

Operational GOES products by NESDIS also require cloud detection, an algorithm referred to as “cloud clearing.” In this application, an array of $n \times n$ contiguous pixels is categorized as *clear*, *cloudy* or *unusable*. The *clear* arrays are subcategorized as *truly clear* and *clear/cloudy*.

In an approach similar to the ITPP-5 method (Minnis et al 1995), clear conditions are determined based on brightness thresholds, difference thresholds, and comparison of observations with first guess profiles.

2.2.2 Objective

The objective of this algorithm is to discriminate the cloudy pixels from the clear pixel in the image data.

2.3 Inputs

2.3.1 Static Data

Parameter	Resolution	Accuracy	Source
Land sea mask	4 km	-	USGS file (Available)

2.3.2 Image and preprocessing data (Dynamic)

Note:

The BTmax (11μ) for each time, user defined no. of previous days (default 20 days) images of TIR -1 and TIR-2 for all times of the day will be needed. These Btmax images are generated for each time using previous 20 days data.

Parameter	Resolution	Quantization	Accuracy	Source
Radiometric and geometric corrected gray count values of MIR channel (3.9μ)	Pixel	10 bit	--	Derived from raw data by DP (data processing)
Radiometric and geometric corrected gray count values of TIR-1 channel (10.5μ)	Pixel	10 bit	-	Derived from raw data by DP
Radiometric and geometric corrected gray count values of TIR-2 channel (11.5μ)	Pixel	10 bit	-	Derived from raw data by DP
Gray value to brightness temperature conversion table for IR channels	-	-	0.3 K	Derived by DP
Geolocation file	Pixel	-	1 pixel	Derived by DP

2.4 Algorithm Functional Specifications

2.4.1 Overview

Here we have combined the GOES cloud detection technique and some of the MODIS cloud discrimination methods. The new concept included here is to determine the threshold on the basis of clear sky temperature determined by compositing the multi-date image data.

2.4.1.1 Theoretical Background

The theoretical basis of the algorithms and practical considerations are contained in this section. For nomenclature, we shall refer to the infrared radiance as brightness temperature (equivalent blackbody temperature determined using the Planck function) denoted as $B(T)$. Subscripts refer to the wavelength at which the measurement is made.

Clouds are generally characterized by higher reflectance and lower temperature than the underlying earth surface. Simple visible and infrared window threshold approaches offer considerable skill in cloud detection; however, many surface conditions reduce cloud surface contrast in certain spectral regions, (e.g. bright clouds over snow and ice).

2.4.1.2 Infrared Brightness Temperature Thresholds and Difference (BTD) Tests

The azimuthally averaged form of the infrared radiative transfer equation is given by

$$\mu \frac{dI(\delta, \mu)}{d\delta} = I(\delta, \mu) - (1 - \omega_0)B(T) - \frac{\omega_0}{2} \int_{-1}^1 P(\delta, \mu, \mu') I(\delta, \mu') d\mu'. \quad (1)$$

In addition to atmospheric structure, which determines $B(T)$, the parameters describing the transfer of radiation through the atmosphere are the single scattering albedo, $\omega_0 = \sigma_{\text{sca}}/\sigma_{\text{ext}}$, which ranges between 1 for a non-absorbing medium and 0 for a medium that absorbs and does not scatter energy, the optical depth, δ , and the Phase function, $P(\mu, \mu')$, which describes the direction of the scattered energy.

To gain insight on the issue of detecting clouds using IR observations from satellites, it is useful to first consider the two-stream solution . Using the discrete-ordinates approach (Liou 1973; Starnes and Swanson 1981), the solution for the upward radiance from the top of a uniform single cloud layer is:

$$\begin{aligned} I_{\text{obs}} &= M_L L \exp(-k\delta) + M_+ L_+ + B(T_c), \\ L_+ &= \frac{1}{2} \left[\frac{I_{\downarrow} + I_{\uparrow} - 2B(T_c)}{M_+ e^{-k\delta} + M_-} + \frac{I_{\downarrow} - I_{\uparrow}}{M_+ e^{-k\delta} + M_-} \right], \\ L_- &= \frac{1}{2} \left[\frac{I_{\downarrow} + I_{\uparrow} - 2B(T_c)}{M_+ e^{-k\delta} + M_-} + \frac{I_{\downarrow} - I_{\uparrow}}{M_+ e^{-k\delta} - M_-} \right], \\ M_{\pm} &= \frac{1}{1 \pm k} \left(\omega_0 \mp \omega_0 g (1 - \omega_0) \frac{1}{k} \right), \\ k &= \left[(1 - \omega_0)(1 - \omega_0 g) \right]^{\frac{1}{2}}. \end{aligned} \quad (2)$$

where

I_{\downarrow} is the downward radiance (assumed isotropic) incident on the top of the cloud layer, I_{\uparrow} the upward radiance at the base of the layer, and g the asymmetry parameter. T_c is a representative temperature of the cloud layer.

A challenge in cloud masking is detecting thin clouds. Assuming a thin cloud layer, the effective transmittance (ratio of the radiance exiting the layer to that incident on the base) is derived from equation (2) by expanding the exponential. The effective transmittance is a function of the ratio of $I_{\downarrow}/I_{\uparrow}$ and $B(T_c)/I_{\uparrow}$. Using atmospheric window regions for cloud detection minimizes the $I_{\downarrow}/I_{\uparrow}$ term and maximizes the $B(T_c)/I_{\uparrow}$ term. Figure 3 is a simulation of differences in brightness temperature between clear and cloudy sky conditions using the simplified set of equations . In these simulations, there is no atmosphere, the surface is emitting at a blackbody temperature of 290 K, the cloud particles are ice spheres with a gamma size distribution assuming an effective radius of 10 μm , and the cloud optical depth $\delta = 0.1$. Two cloud temperatures are simulated (210 K and 250 K). Brightness temperature differences between the clear and cloudy sky are caused by non-linearity of the Planck function and spectral variation in the single scattering properties of the cloud. This figure does not include the absorption and emission of atmospheric gases, which would also contribute to brightness temperature differences. Observations of brightness temperature differences at two or more wavelengths can help separate the atmospheric signal from the cloud effect.

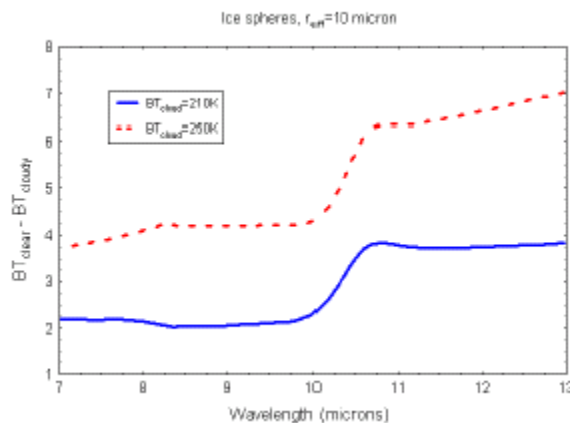


Figure 3: A simple simulation of the brightness temperature differences between a “clear” and cloudy sky as a function of wavelength. The underlying temperature is 290 K and the cloud optical depth is 0.1. All computations assume ice spheres with $r_e = 10 \mu\text{m}$.

2.4.1.3 Methodology

The basis of our methodology is, first to generate a clear composite of the maximum brightness temperature in thermal channels to get rough idea about the surface temperature in the clear sky condition at a particular time. Here assumption is that any pixel in the image will not be covered by cloud continuously at a particular time for several (user defined no.) days and the maximum brightness temperature will represent the clear sky background temperature of that location. This will be the reference background temperature on which the threshold for a particular location will be determined to discriminate cloud.

First step : Generation of BT_{\max}

$\text{BT}_{\max} = \max (\text{BT}_{11} \text{ of each time of previous several (user defined no.) days})$
Default number of days for clear composite image is 20.

SIMPLE BT THRESHOLD TEST

Several infrared window threshold and temperature difference techniques have been developed. These algorithms are most effective for cold clouds over water and must be used with caution in other situations. The first infrared test to apply is a simple threshold test. When the brightness temperature in the 11 μm (BT_{11}) channel is less by some threshold value than the maximum BT at that location, we assume the pixel to fail the clear-sky condition, because the change in BT will not be more than these due to change in other atmospheric condition. This was determined by some radiative transfer simulation for different atmospheric condition. This test gives a first set of cloudy pixels in the image.

Second step : First set of cloudy pixels

Over land :

If $(BT_{\max} - BT_{11}) > 12 \text{ K}$, then Cloudflag =1 (Cloudy pixels)

Over ocean :

If $(BT_{\max} - BT_{11}) > 6 \text{ K}$, then Cloudflag =1 (Cloudy pixels)

Third step : First set of clear pixels.

If $\text{abs}(BT_{\max} - BT_{11}) < 2 \text{ K}$, then Cloudflag = 0 (Clear sky pixel)

For rest of the points Cloudflag = 9 (For further test)

For points with Cloudflag = 9 ,

SOLAR ZENITH ANGLE CALCULATION

Solar zenith angle has to be calculated for determining the day / night condition of the pixel.

Solar zenith angle (θ_s) :

$$\theta_s (\text{in radian}) = \pi/2 - \text{ASIN}(\text{SIN}\delta \text{ SIN(latitude))} + \text{COS}\delta \text{ COS(latitude) COSH}) \quad (1)$$

$$\begin{aligned} \delta (\text{in radian}) = \text{solar declination angle} = 0.39785\text{SIN}(4.869 + 0.0172\text{cday} + \\ 0.03345\text{SIN}(6.224+0.0172\text{cday})) \end{aligned} \quad (2)$$

H = sun hour angle at time , 't' (in IST hrs.), in a calendar day (cday)

$$\begin{aligned} \text{IF } (t \text{ GT } 12) \text{ AND } (\text{longitude GT } 82.5) \text{ THEN} \\ H = t1 + L \end{aligned} \quad (3)$$

Otherwise,

$$\begin{aligned} \text{IF } ((t \text{ LT } 12) \text{ AND } (\text{longitude LT } 82.5)) \text{ THEN} \\ H = t1 + L \end{aligned} \quad (4)$$

Otherwise,

$$H = t1 - L \quad (5)$$

Where,

$$L = \text{ABS}(\text{longitude} - 82.5) \quad (6)$$

$$t1 = 15(\text{ABS}(12-t)) \quad (7)$$

If the solar zenith angle $> 86.5^\circ$

Then pixel is considered to be falling in the night time.

else

Pixel is in the day time.

BT₁₁ - BT_{3.9} TEST (For points with Cloudflag = 9)

Channel (3.9 μm) measures radiances in the window region near 3.8-4 μm so that the difference between BT_{11} and $BT_{3.9}$ can be used to detect the presence of clouds. At night the difference between the brightness temperatures measured in the shortwave (3.9 μm) and in the longwave (11 μm) window regions ($BT_{11} - BT_{3.9}$) can be used to detect partial cloud or thin cloud within the INSAT field of view. Small or negative differences are observed only for the case where an opaque scene (such as thick cloud or the surface) fills the field of view of the sensor. Negative differences occur at night over extended clouds due to the lower cloud emissivity at 3.9 μm .

During the daylight hours the difference between BT_{11} and $BT_{3.9}$ is large and negative because of reflection of solar energy at 3.9 μm . This technique is very successful at detecting low-level water clouds.

Moderate to large differences between BT_{11} and $BT_{3.9}$ result when a nonuniform scene (e.g., broken cloud) is observed. The different spectral response to a scene of non-uniform temperature is a result of Planck's law. The brightness temperature dependence on the warmer portion of the scene increasing with decreasing wavelength (the shortwave window Planck radiance is proportional to temperature to the thirteenth power, while the longwave dependence is to the fourth power). Differences in the brightness temperatures of the longwave and shortwave channels are small when viewing mostly clear or mostly cloudy scenes; however, for intermediate situations the differences become large (greater than 3°C). Table 2 lists examples of the thresholds as used in MODIS algorithm. We have used similar thresholds as used in MODIS algorithm.

The application of $BT_{11} - BT_{3.9}$ is difficult in deserts during daytime. Bright desert regions with highly variable emissivities tend to be incorrectly classified as cloudy with this test. The problem is mitigated somewhat in the cloud mask by making use of a double-sided test where brightness temperature differences greater than a "low" threshold but less than a "high" threshold are labeled clear while values outside this range are called cloudy. The thresholds are listed in Table 2. This threshold strategy along with the use of clear-sky restoral tests is effective for detecting low-level clouds over deserts. We are leaving these regions as undetermined if it is failing other tests.

Detecting clouds at high latitudes using infrared window is a challenging problem due to the cold surface temperatures. Yamanouchi et al. (1987) describe a nighttime polar (Antarctic) cloud/surface discrimination algorithm based upon brightness temperature differences between the AVHRR 3.7 and 11 μm channels and between the 11 and 12 μm channels. We are not attempting at those regions because data at such large angle of view is not very useful and not used for any parameter retrieval.

Table 2: Thresholds used for $BT_{11} - BT_{3.9}$ test for low clouds are same as in the MODIS cloud mask algorithm.

Scene Type	Threshold	High confidence clear	Low confidence clear
Day ocean	-8.0 K	-6.0 K	-1.0 K
Night ocean	0.0 K	-1.0 K	1.0 K
Day land	-12.0 K	-10.0 K	-14.0 K

BT3.7 - BT12 TEST

This window brightness temperature difference test is applied during the nighttime over some, but not all, surfaces. This difference is useful for separating thin cirrus and cloud free condition and is relatively insensitive to the amount of water vapor in the atmosphere (Hutchison and Hardy 1995). This test is executed over land at night. The three thresholds for MODIS algorithm are 15, 10, and 5 K, for low confidence, mid-point, and high confidence, respectively. Over snow-covered surfaces, the thresholds are 4.50, 4.00, and 3.50K. We shall be using only the high confidence thresholds.

NIGHT OCEAN SPATIAL VARIABILITY TEST

The standard deviation of 3x3 arrays of 11 μm brightness temperatures centered on the pixels of interest is calculated for ocean scenes at night. The clear-sky ocean surface is usually very uniform over regions of this size and, in general, the presence of clouds increases the variability. The thresholds for MODIS algorithm are 0.2K, 0.1K, and 0.05K for low, mid-point, and high confidences, respectively. The reader will note that these values are very restrictive, yet some very uniform low clouds are not detected by this test. For INSAT, we are using threshold of 0.05 K.

If the Standard deviation σ in 3 x 3 array of BT_{11} is less 0.05 then the pixel is a clear sky pixel.

If $\sigma < 0.05$ then cloudflag = 0 for the center pixel.

SPATIAL UNIFORMITY TEST

The previous test is applied only over the ocean. Spatial Uniformity test is applied to all pixels. The standard deviation σ , T_{mean} and T_{maxmean} of the 3 x 3 array for the 11 μm brightness temperatures centered on the pixel of interest is computed.

If the $|T_{\text{maxmean}} - T_{\text{mean}}| \leq 2.0$ and $\sigma < 1.5$ then for the center pixel, cloud flag = 0.

Over Land ,

If $(T_{\text{mean}} - T_{\text{maxmean}}) \leq -12.0$ K and $\sigma < 1.5$ then for the center pixel, cloud flag = 1.

Over Ocean,

If $(T_{\text{mean}} - T_{\text{maxmean}}) \leq -6.0$ K and $\sigma < 1.5$ then for the center pixel, cloud flag = 1.

ADJACENT PIXEL TEST

After all the above tests , for the remaining pixel, where cloudflag = 9, in the 3 x 3 array of the 11 μm brightness temperatures, find the number of cloudy (n1) and clear (n2) pixels.

If $n1 > 5$ then for the center pixel cloudflag = 1

If $n2 > 5$ then for the center pixel cloudflag = 0

TEMPORAL UNIFORMITY TEST

The remaining pixels with cloudflag 9 are compared with the pixels of previous hour image. If the difference in BT_{11} is less than 1K then it is assumed that the atmospheric condition over that pixel has not changed much from the previous hour and the cloudflag of that pixel from previous hour is carried over to the current data

If $|\text{BT}_{11}(\text{current image}) - \text{BT}_{11}(\text{previous hour image})| \leq 1$ K then

Cloudflag (current) = cloudflag (previous)

FINAL THRESHOLD TEST

For remaining uncertain points (cloudflag = 9) final threshold test is done to assign probably clear or cloudy flag to each pixel. In this test

Over land :

If $2 < |BT_{11} - BT_{max}| \leq 6$ then cloudflag = 2 (probably clear)

And if $6 < |BT_{11} - BT_{max}| \leq 12$ then cloudflag = 3 (probably cloudy)

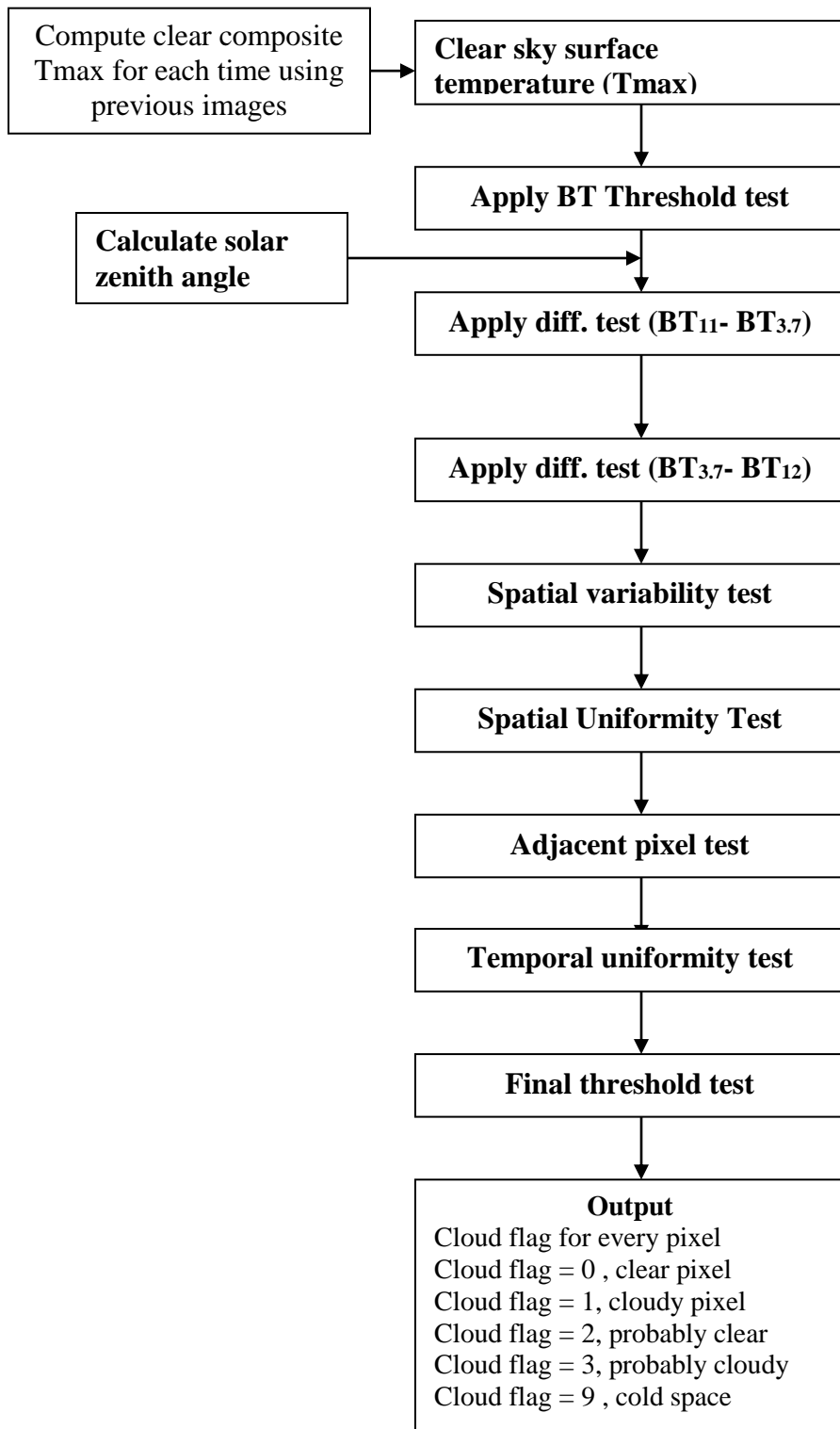
Over ocean :

If $2 < |BT_{11} - BT_{max}| \leq 3$ then cloudflag = 2 (probably clear)

And if $3 < |BT_{11} - BT_{max}| \leq 6$ then cloudflag = 3 (probably cloudy)

For further testing one can use the reflectance test in visible and some other test to determine whether it is clear or cloudy.

2.4.1.4 Flow Chart



2.4.2 Operational Implementation

2.4.2.1 Step 1 : Generation of BT_{max}

2.4.2.2 Step 2: BT threshold test

2.4.2.3 Step 3 : Solar zenith angle calculation

2.4.2.4 Step 4 : Difference Test (BT₁₁ – BT_{3.7})

2.4.2.5 Step 5 : Difference Test (BT_{3.7} – BT₁₂)

2.4.2.6 Step 6 : Spatial variability test

2.4.2.7 Step 7 : Spatial Uniformity test

2.4.2.8 Step 8 : Adjacent pixel test

2.4.2.9 Step 9: Temporal Uniformity test

2.4.2.10 Step 10: Final threshold test

2.5 Outputs

Parameter	Resolution
Cloud flag	Pixel

2.5.1 format of the output and the domain

Scan , pixel, cloud flag

If cloudflag = 0 , pixel is clear

If cloudflag = 1 , pixel is cloudy

If cloudflag = 2, probably clear

If cloudflag = 3, probably cloudy

If cloudflag = 9, Cold space

Domain :

Image Domain

2.6 Validation

2.6.1 Data required

MODIS cloud flag data

2.6.2 Methods of validation

Inter comparison of INSAT cloud product with MODIS cloud flag data.

2.7 Technical issues

This is a first cut cloud discrimination using only TIR-1, TIR-2 and MIR channels

2.8 Future Scope

- For pixels with probably clear or cloudy flag further test can be done with reflectance test in visible and near infrared channels using reflectance thresholds.

2.9 References

1. Ackerman, S.A., K.I. Strabala, W. P. Menzel, R. A. Frey, C. C. Moeller, L. E. Gumley, B. A. Baum, C. Schaaf, G. Riggs, 1997: Discriminating clear-sky from cloud with MODIS algorithm theoretical basis document (MOD35). EOS ATBD web site, 125 pp.
2. Kriebel, K. T., and R. W. Saunders, 1988: An improved method for detecting clear sky and cloudy radiances from AVHRR data. *Int. J. Remote Sens.*, **9**, 123-150.
3. P. Minnis, J. W. L. Smith, D. P. Garber, J. K. Ayers and D. R. Doelling, 1995 Cloud properties derived from GOES-7 for the Spring 1994 ARM Intensive Observing Period using version 1.0.0 of the ARM satellite data analysis programHampton, VA
4. Rizzi, C. Serio, G. Kelly, V. Tramutoli, A. McNally and V. Cuomo, 1994. Cloud clearing of infrared sounder radiances. *J. Appl. Meteor.*, **33**, 179-194.
5. Rossow, W. B. and L. C. Garder, 1993a. Cloud detection using satellite measurements of infrared and visible radiances for ISCCP. *J. Climate*, **6**, 2341-2369.
6. Saunders, R. W. and K. T. Kriebel, 1988. An improved method for detecting clear sky and cloudy radiances from AVHRR data. *Int. J. Remote Sens.*, **9**, 123-150.
7. Hayden, C. M., G. S. Wade, and T. J. Schmit, 1996: Derived product imagery from GOES-8. *J. Appl. Meteor.*, **35**, 153-162.

3. Outgoing Longwave Radiation

S.No.	Product Name	Spatial Resolution	Temporal Resolution
1	3DIMG_L2B_OLR	4 km	30 minutes
2	3DIMG_L3B_OLR_DLY	4 km	Daily (00 H to 23:30 H)

3. OUTGOING LONGWAVE RADIATION (OLR)

3.1 Algorithm Configuration Information

3.1.1 Algorithm Name

Outgoing Longwave Radiation (OLR)
(Ref: IMD RFP Section 11.1)

3.1.2 Algorithm Identifier

3DIMG_L2B_OLR

3.1.3 Algorithm Specification

Version	Date	Prepared by	Description
1.0	07.02.2013	R Singh P K Thapliyal C M Kishtawal P K Pal	OLR Baseline Document

3.2 Introduction

The total amount of the thermal radiation ($4 - 100 \mu\text{m}$ wavelength bands) that is emitted from the earth-atmosphere system to the outer space is called outgoing longwave radiation (OLR). Besides the broadband instruments that are dedicated for observing the OLR, for example, Cloud and Earth's Radiant Energy System (CERES), there are many algorithms that estimate OLR by converting the narrowband radiances into broadband flux (OLR; Ellingson et al. 1989, Ellingson et al. 1994, Singh et al., 2007, Sun et al., 2010). Algorithm to estimate the OLR from the Geostationary Indian National Satellite (INSAT-3D) imager observed WV ($6.5 - 7.1 \mu\text{m}$) and thermal infrared (TIR-1; $10.3 - 11.3 \mu\text{m}$ and TIR-2; $11.5 - 12.5 \mu\text{m}$) radiances has been developed in the frame of the IMDPS. The developed algorithm will be used operationally when data from the INSAT-3D satellite will be available. Algorithm to estimate the OLR is developed using two basic approaches:

- i. In the first approach, a large database of spectral radiance fields and broadband flux (OLR) built using Atmospheric Radiative Transfer Model (RTM) is used to develop the algorithm. The radiative transfer computations are performed at 19400 wavelengths covering the thermal region ($4-100 \mu\text{m}$) and for 4704 realistic conditions of the Earth-atmosphere system.
- ii. In the second approach, INSAT-3D imager radiances collocated (in space and time) with CERES OLR available from Terra and Aqua satellites, are used to develop the algorithm.

3.2.1 Overview and background

The earth and its atmosphere absorb the shortwave (*SW*) radiation coming from the sun and emit thermal longwave (*LW*) radiation to space. These two radiation streams can be represented approximately by blackbody radiation of 6000K for the solar *SW* and 290K for the terrestrial (*LW*). The balance between the incoming *SW* radiation and the *LW* determines the temperature in the atmosphere and on the earth's surface. Outgoing longwave radiation (*OLR*) is the emission to space of terrestrial radiation (*LW*) from the top of the earth's atmosphere. *OLR* is strongly controlled by three main meteorological variables, namely the temperature of the earth and the atmosphere above it, the presence of water vapor in the atmosphere (which strongly absorbs infra-red radiation attenuating the terrestrial signal) and the presence of clouds (which may completely block all outgoing infra-red radiation from the surface). Thus, *OLR* reveal information on the temperature, humidity and cloudiness of the atmosphere. Allan *et al.* (1999) state that changes in humidity in the mid-troposphere (400 to 700 hPa) are most important in explaining clear-sky *OLR* variations.

The estimates of outgoing longwave radiation, both operational and experimental have been particularly useful for variety of problems in climate sensitivity and diagnostics (e.g., Schmetz and Liu, 1988), numerical weather forecasting and climate models. The *OLR* has been used traditionally for radiation budget studies of the earth-atmosphere system. The top of the atmosphere radiative energy balance between net incoming solar radiation and *OLR* is crucial in determining the large-scale atmospheric circulation and, therefore, the synoptic evolution that is important for weather and climate prediction. *OLR* is a major component of the Earth's Radiation Budget, which drives the atmospheric circulation, particularly over the tropics. This is mainly due to the fact that in the tropics, the *OLR* is largely modulated by cloudiness. In particular, it varies with cloud top temperature and consequently, low radiation values indicate the major convective system. Generally, values less than 250 Wm^{-2} would give a good indication of the cloudiness over the tropics.

The observations of *OLR* by earth orbiting satellites have been made from the beginning of the environmental satellite program. Besides the broadband instruments that are dedicated for observing the *OLR*, for example, Earth Radiation Budget Experiment (ERBE), Scanner Radiometer for Radiation Budget (ScaRab), and Cloud and Earth's Radian Energy System (CERES), there are many algorithms that estimate *OLR* by converting the narrowband radiance observations into broadband flux (4–100 μm). The *OLR* was routinely obtained from the 10–12 μm window on operational National Oceanic and Atmospheric Administration (NOAA) polar-orbiting satellite beginning in 1974 (Gruber and Winston, 1978). Early operational estimation of *OLR* employed a simple parameterization using the window channel brightness temperature of the advanced very high resolution radiometer (AVHRR) on NOAA 6–7 (Ellingson and Ferraro, 1983; Gruber and Krueger, 1984). New algorithms were developed in subsequent years to improve the accuracy of the *OLR*. Ellingson *et al.* (1989) have shown that the linear combination of only four (6.6– 6.9 μm ; 7.9–8.5 μm ; 13.1–13.6 μm ; 14.3–14.7 μm) High Resolution Infrared Sounder (HIRS) channels could account for more than 99% of the *OLR* total variance. Comparison with the ERBE (Ellingson *et al.*, 1994) instrument flown in NOAA 9–11 satellites suggested that estimates made with HIRS data exhibited errors of the same order as the estimated accuracy of ERBE (5 Wm^{-2}), whereas use of AVHRR data exhibits monthly bias of -1 to +2 Wm^{-2} and rms differences of about 14 Wm^{-2} (Gruber *et al.*, 1994).

Geostationary satellite observations have also been used for OLR estimation. Schmetz and Liu (1988) and Cheruy et al. (1991) developed OLR retrieval technique using two channels (infrared window and water vapor) of Meteosat. Minnis et al. (1991) developed an algorithm to estimate OLR using Geostationary Operational Environmental Satellite (GOES) imager window channels with additional water vapor information from analysis. Ba and Ellingson (2001) estimated OLR using several channels of the GOES sounder and presented comparisons with the CERES measurements. Ba et al. (2003) adapted the HIRS technique to GOES sounder and validated the derived OLR with collocated OLR measured from CERES onboard Tropical Rainfall Measurement Mission (TRMM) and Terra satellites. Their results show instantaneous agreement within about 7 Wm^{-2} . Singh et al. (2007) estimated OLR using the infrared window and water vapor channels radiances from Kalpana.

Objective

To develop the algorithm for estimating OLR from narrow band radiances from WV ($6.5 - 7.1 \mu\text{m}$), TIR-1 ($10.3 - 11.3 \mu\text{m}$) and TIR-2 ($11.5 - 12.5 \mu\text{m}$) channels of INSAT-3D imager. Algorithm is developed using two basic approaches:

- i. First approach (ALG-1) uses RTM simulated INSAT-3D radiances and OLR
- ii. Second approach (ALG-2) uses simultaneously measured CERES OLR and INSAT-3D radiances

3.3 Inputs

3.3.1 Image and pre-processing data (Dynamic)

Parameter	Resolution	Quantization	Accuracy	Source
Gray count values of WV channel	Pixel	10 bit		DP (data processing)
Gray count values of TIR-1 channel	Pixel	10 bit	-	DP
Gray count values of TIR-2 channel	Pixel	10 bit	-	DP
Coefficients for conversion of Gray value to radiances	-	-	-	DP
Geolocation file	Pixel	-	1 pixel	DP

3.3.2 Other Auxiliary data and Model Input

To develop the empirical relationship between narrow band radiances and OLR using radiative transfer approach (ALG-1), a large database of the atmospheric profiles of temperature (T), pressure, water vapor (q), and ozone (O_3) concentrations are required. These profiles are extracted from the TIGR-3 database (Chevallier, Che'din, Che'ruey, & Morcrette, 2000), which is a representative set of 2311 profiles selected among a larger set of worldwide soundings. Additional 41 diverse profiles of temperature, water vapor and ozone from ECMWF are taken.

To develop the empirical relation between narrowband radiances and OLR using second approach (ALG-2), the Single Scanner Footprint (SSF) OLR product derived from the broadband observations by the CERES (on board Terra and Aqua) and FY-2D measured radiances (proxy for INSAT-3D) are used.

Approach	Parameter	Resolution	Accuracy	Source
ALG-1	Atmospheric profile (2311) of T, q, O ₃			TIGR-3 data base
	41 diverse profiles of T, q, O ₃			ECMWF
ALG-2	CERES OLR	20 Km	5 Wm ⁻²	http://eosweb.larc.nasa.gov
	FY-2D VISSR radiances	5 Km		http://www.nsmc.cma.gov.cn

3.4 Algorithm Functional Specifications

3.4.1 Overview

Generally, broadband Radiometer provides the accurate measurements of emitted longwave radiation at top of the atmosphere (TOA). Since narrow field-of-view (NFOV) radiometers on-board satellites, such as CERES, measure the upwelling radiance only in specific outgoing directions from a scene on Earth at any given time, OLR cannot be measured instantaneously. Given a radiance field, $L(\theta, \Phi)$, at the TOA, where θ is the satellite viewing zenith angle, and Φ the azimuth angle, the OLR leaving the earth-atmosphere system, is obtained by integrating the radiance field over the solid angle ω of the upper hemisphere:

$$\text{OLR} = \int_0^{\frac{\pi}{2}} \int_0^{2\pi} L(\theta, \phi) \cos \theta \sin \theta d\theta d\phi \quad (1)$$

$$L(\theta, \phi) = \int_{\lambda=4\mu\text{m}}^{\lambda=100\mu\text{m}} L_\lambda(\theta, \phi) d\lambda \quad (2)$$

For an isotropic radiance field, the radiance to OLR conversion is simple ($\text{OLR}=\pi L$). Unfortunately, the radiance field $L(\theta, \Phi)$ is not isotropic and an accurate portraying of the anisotropy is needed to estimate the OLR from the radiance measurement. The anisotropic emission factor (AEF) $R(\theta, \Phi)$ is defined as the ratio of the equivalent Lambertian OLR to the actual OLR (Loeb et al., 2003).

$$R(\theta, \phi) = \frac{\pi L(\theta, \phi)}{\text{OLR}} \quad (3)$$

Eq. (3) is widely used to infer the OLR from the radiance measurement $L(\theta, \Phi)$ available from the broadband (4 μm – 100 μm) radiometers (e.g CERES, ScaRab, ERBE, etc)

As mentioned above, the OLR is obtained by integrating the radiances over the long-wave spectral range and over hemispheric solid angles. However, if the observations at entire (e.g 4 μm – 100 μm) spectral range are not available, a mapping function of the following form should be determined to retrieve OLR from the available, narrow band radiances:

$$\text{OLR} = F(\theta, N_i(\theta)) \quad (4)$$

Where θ satellite zenith angle and N_i is the observed narrow band radiances in i^{th} channel. The radiance in a particular channel is related to the specific intensity I at wavelength λ and the instrument responsively η as

$$N_i(\theta) = \int_{\Delta\lambda_i} I(\lambda, \theta) \eta_i(\lambda) d\lambda \quad (5)$$

3.4.1.1 Radiative Transfer Model

Santa Barbara DISORT Atmospheric Radiative Transfer (SBDART) model developed by Ricchiazzi et al (1998) at University of California is used for INSAT-3D imager radiance simulations. SBDART is designed for the analysis of a wide variety of radiative transfer problems encountered in satellite remote sensing and atmospheric energy budget studies. SBDART is based on a collection of highly developed and reliable physical models developed by the atmospheric science community. A brief description to the key components of the model is discussed below:

Cloud Model: Clouds are a major modulator of the earth's climate by reflecting visible radiation and intercepting part of the infrared radiation emitted by the Earth and re-radiating it back to the surface. The computation of radiative transfer within a cloudy atmosphere requires knowledge of the scattering efficiency, the single scattering albedo, and the asymmetry factor, which indicates the strength of forward scattering. SBDART contains an internal database of these parameters for clouds computed with a Mie scattering code and covers a range of particle size effective radius in the range 2 to 128 μm . By default, the angular distribution of scattered photons is based on the simple Henyey-Greenstein parameterization, but more detailed scattering functions may be input as desired.

Gas Absorption Model: Standard SBDART uses low-resolution band models developed for the LOWTRAN 7 atmospheric transmission code (Pierluissi and Marogoudakis, 1986). These models provide the clear sky atmospheric transmission from 0 to 50000 cm^{-1} and include the effects of all radiatively active molecular species found in the earth's atmosphere. The models were derived from detailed line-by-line calculations, which were degraded to 20 cm^{-1} resolution for use in LOWTRAN. This translates to a wavelength resolution of about 0.005 μm in the visible and about 0.2 μm in the thermal infrared. A capability to read high-resolution k-distribution optical depths from a disk file is introduced in SBDART version 2.0 which is less convenient to use than the standard approach. However, it has the advantage of removing limitations in the ultimate spectral resolution available with SBDART.

Extraterrestrial Source Spectra: SBDART has options for three extraterrestrial solar spectrum models: LOWTRAN-7 solar spectrum (Shettle and Fenn, 1975), solar models used in 5s or MODTRAN-3 solar spectrum.

Standard Atmospheric Models: SBDART has six standard atmospheric profiles from the 5s atmospheric radiation code to model the following typical climatic conditions: tropical, mid-latitude summer, mid-latitude winter, subarctic summer, subarctic winter and US62. These model atmospheres (McClatchey et al, 1971) have been widely used in the atmospheric research community and provide standard vertical profiles of pressure, temperature, water vapor and ozone density. Optionally users can specify their own model

atmosphere, e.g., a radiosonde profile. The concentration of trace gases such as CO₂ or CH₄ are assumed to make up a fixed fraction (which may be specified by the user) of the total particle density.

Standard Aerosol Models: SBDART can compute the radiative effects of several common boundary layer and upper atmosphere aerosol types. In the boundary layer, the user can select from rural, urban, or maritime aerosols. The total vertical optical depth of boundary layer aerosols is derived from user specified horizontal meteorological visibility at 0.55 μm and an internal vertical distribution model. In the upper atmosphere up to 5 aerosol layers can be specified, with radiative characteristics that model fresh and aged volcanic, meteoric and the climatological tropospheric background aerosols. The aerosol models included in SBDART were derived from those provided in the 5s and LOWTRAN7.

Radiative Transfer Equation Solver: The radiative transfer equation is numerically integrated with DISORT (DIScrete Ordinate Radiative Transfer, Stamnes et al, 1988). The discrete ordinate method provides a numerically stable algorithm to solve the equations of plane-parallel radiative transfer in a vertically inhomogeneous atmosphere. The intensity of both scattered and thermally emitted radiation can be computed at different heights and directions. SBDART is configured to allow up to 65 atmospheric layers and 40 radiation streams (40 zenith angles and 40 azimuthal modes).

Surface Models: The ground surface cover is an important determinant of the overall radiation environment. In SBDART six basic surface types -- ocean water, lake water, vegetation, snow and sand are used to parameterize the spectral reflectivity of the surface. The spectral reflectivity of a large variety of surface conditions is well approximated by combinations of these basic types. For example, the fractions of vegetation, water and sand can be adjusted to generate a new spectral reflectivity representing new/old growth, or deciduous vs. evergreen forest. Combining a small fraction of the spectral reflectivity of water with that of sand yields an overall spectral dependence close to wet soil.

3.4.1.2 RTM simulated OLR and INSAT-3D radiances

To develop the empirical relationship between narrow band radiances and OLR a large database of spectral radiance fields was built using SBDART model. The radiative transfer computations were performed at 19400 wavelengths covering the thermal region 4–100 μm for 4704 realistic conditions of the Earth–atmosphere system. For each element in the database, the main inputs for the radiative transfer computations were: the atmospheric profiles of temperature, pressure, water vapor, and ozone concentrations. These profiles are extracted from the TIGR-3 database, which is a representative set of 2311 profiles selected among a larger set of worldwide soundings. Additional 41 diverse profiles of temperature, water vapor and ozone from ECMWF were also taken. The surface temperature is set close to the temperature at the level close to surface in the profile. The cloud cover is generated randomly. The cloud cover may contain up to three overlapping layers, each characterized by a random height, optical thickness, phase (water or ice), and drop size distribution. Half of the database (2352 elements) corresponds to cloud-free conditions and the other half corresponds to the same conditions but with the addition of cloud cover. For each element in the database, the OLR and the spectral radiance field L ($\theta=\{0^\circ, 5^\circ, \dots, 65^\circ\}$) are computed. Filter response function for the INSAT-3D imager WV and thermal channel (TIR-1 and TIR-2) were provided as input to the SBDART. Radiances were simulated for each set of profile

and zenith angle at the top of atmosphere (70 km) from SBDART for WV, TIR-1 and TIR-2 channels.

3.4.1.3 Conversion of Narrow Band Radiances to Broad Band Flux (OLR)

ALG-1 is developed using RTM simulated OLR and INSAT-3D radiances. While ALG-2 is developed using the INSAT-3D radiances and collocated (in space and time) CERES measured OLR. In practice, development of ALG-2 is possible only after the launch of INSAT-3D. However, to develop the preliminary version, we have used Visible Infrared Spin Scan Radiometer (VISSR) onboard FY-2D (positioned at 86.5° E) radiances to generate proxy radiances for INSAT-3D. This is due to the fact that INSAT-3D channels (TIR-1, TIR-2 and WV), which will be used for the development of OLR algorithm, are very similar to those of FY-2D channels. INSAT-3D radiances are generated using VISSR measured radiances by accounting the difference in the radiances due to the SRF differences of FY-2D and INSAT-3D channels. We have also developed the algorithm to estimate the OLR using FY-2D measured radiances.

The FY-2D radiance data from 1-15 July and 1-15 December, 2011 over the FY-2D full disk domain were collocated with CERES SSF data from all four instruments (FM1, FM2, FM3 and FM4) onboard Terra and Aqua satellites, respectively. The FY-2D radiance observations were averaged for 4x4 pixels (native resolution is 5 km at the sub-satellite point) to match the CERES resolution (about 20 km nadir). The criterion for the FY-2D and CERES collocations is taken as time coincidence within ± 5 minutes and a distance window of 5 km radius between the FY-2D and the CERES observations. These collocated narrowband radiances, satellite zenith angle and OLR are then used to find the empirical relationship between the OLR, satellite zenith angle and narrowband radiances (Channels; IR1, IR2 and IR3 of FY-2D). Using a radiative transfer simulation, we found empirical relationship between INSAT-3D and FY-2D radiances. The developed empirical relationship was then applied on FY-2D measured radiances to obtain the INSAT-3D radiances. These FY-2D measured radiances and the INSAT-3D simulated radiances using FY-2D measured radiances and collocated CERES OLR were used to develop the OLR algorithm (under second approach: ALG-2).

In both approaches (ALG-1 and ALG-2), genetic algorithm (GA) is used to determine the optimum relationship between broadband flux (OLR) and spectral radiances of WV and thermal infrared channels. A unique advantage of GA is that complex (often nonlinear) relationships between different variables can be obtained in the form of simple and usable equations. In the case of other nonlinear methods like ANN, the task of using the algorithm often requires a complete understanding of the neural network, which includes a complex array of input layers, hidden layers, the shape of the response function at each layer, and the weights connecting these layers. A major difference between other nonlinear techniques (like ANN) and GA is that the algorithm development under GA is almost completely objective and data adaptive.

The development of the OLR retrieval algorithm involves a number of steps. In the first step, the collocated data of narrowband radiances (both FY-2D and INSAT-3D), satellite zenith angle and OLR were divided into two unequal random samples. Sample I is used to train the GA and Sample II is used for evaluation of the algorithm. Genetic algorithm (GA) was then applied to find optimal relationship between narrow band radiances and OLR for

training data (Sample I). The GA training provides empirical equations (INSAT-3D as well as FY-2D) relating OLR to narrowband radiances and satellite zenith angle. The root mean square error (rmse) on the training data is about 7 Wm^{-2} . The developed algorithm was applied on the Sample-II data in order to compute the OLR. The computed OLR for Sample-II data was compared with observed OLR and the root mean square error (rmse) was computed. The root mean square error (rmse) is about 9 Wm^{-2} (about 3 %) for both FY-2D and INSAT-3D.

3.4.1.4 Genetic algorithm

Modeling natural phenomena has been a standard practice in atmospheric sciences. Traditionally, modeling a physical system requires one to derive the relevant equations from first principles taking into account the physical laws that determine the system under consideration. Alternatively, when such an approach is not feasible due to some reasons, e.g., the perfect physics of the system is not well understood, or the required computing resources are not available, empirical laws governing the physical processes can be obtained by model-fitting approaches based on the observed variability of the system and its relationship with other parameters. Let us assume that there exists a smooth mapping function $P(\cdot)$ that explains the relationship between a predicted variable x and a set of dependent variables $[a,b,c,d,e,\dots]$, so that

$$x = P [a,b,c,d,e, \dots] \quad (6)$$

In various areas of geophysics, it is a standard practice to employ linear or nonlinear regression techniques in order to obtain the form of $P(\cdot)$. However, the choice of a regression model is quite subjective, and it is difficult to ensure that a particular regression model provides the best possible explanation to the variance in a data set. This has inspired the researchers to look for more objective data fitting approaches like genetic algorithm (GA). A genetic algorithm is programmed to approximate the equation, in symbolic form, that best describes the relationship between independent and dependent parameters. The genetic algorithm considers an initial population of potential solutions, which is subjected to an evolutionary process, by selecting those equations (individuals) that best fit the data. The strongest strings (made up from a combination of variables, real numbers, and arithmetic operators) of choose a mate for reproduction whereas the weaker strings become extinct. The newly generated population is subjected to mutations that change fractions of information. The evolutionary steps are repeated with the new generation. The process ends after a number of generations *a priori* determined by the user. The procedural details of genetic algorithm can be found in Szpiro (1997), Alvarez *et al.*, (2000) and Singh et al (2006). A brief description of genetic algorithm is as follows.

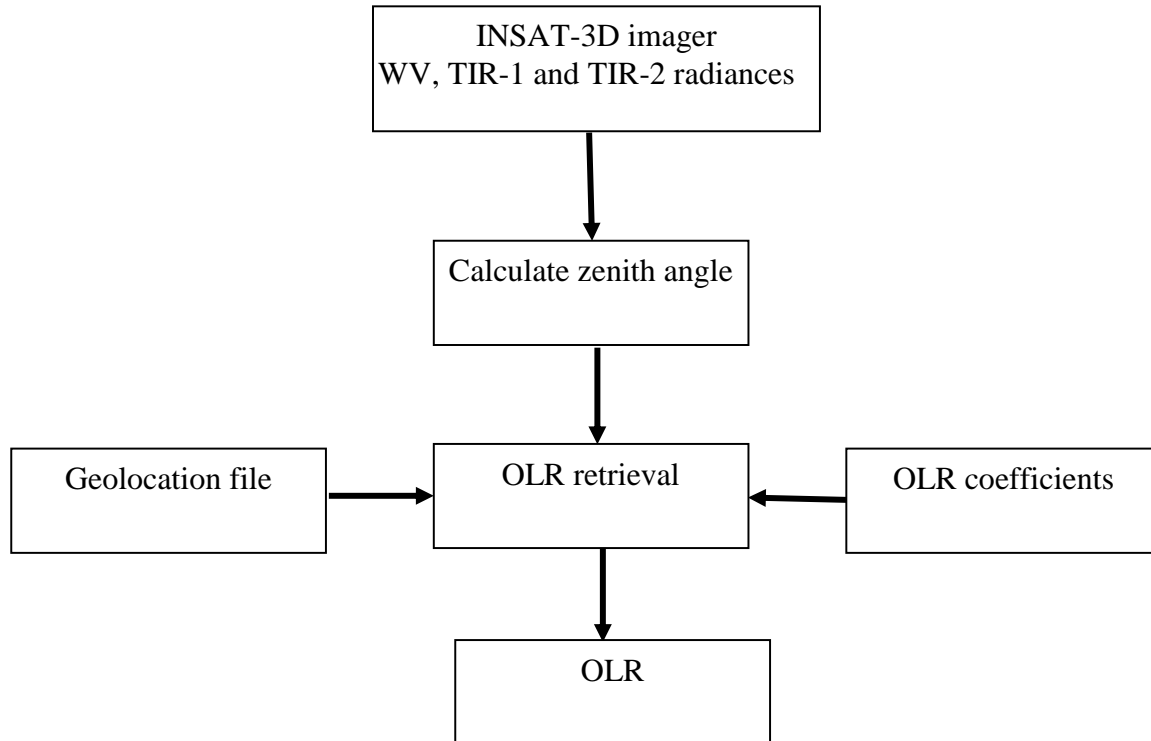
First, for a desired function x (e.g. in Eq.-6), a set of candidate equations for $P(\cdot)$ is randomly generated. An equation is stored in the computer as a set of characters that define the independent variables, a, b, c, d, e, \dots etc. in Eq. (6), and four elementary arithmetic operators ($+, -, \times, \text{and } /$). A criterion that measures how well the equation strings perform on a training set of the data is its fitness to the data, defined as sum of the squared differences between data and independent parameter derived from the equation string. The strongest individuals (equations with best fits) are then selected to exchange parts of the character strings between them (reproduction and crossover) while individuals less fitted to the data are discarded. Finally, a small percentage of the equation strings' most basic elements, single operators and

variables, are mutated at random. The process is repeated a large number of times to improve the fitness of the evolving population of equations. The fitness strength of the best scoring equation is defined as:

$$R^2 = 1 - [\Delta^2 / \sum (x_o - \langle x_o \rangle)^2] \quad (7)$$

where $\Delta^2 = \sum (x_c - x_o)^2$, x_c is parameter value estimated by the best scoring equation, x_o is the corresponding “true” value, $\langle x_o \rangle$ is the mean of the “true” values of x . Szpiro (1997) has shown the robustness of the genetic algorithm to forecast the behavior of one-dimensional chaotic dynamical system.

3.4.1.5 Flow Chart



3.4.2 Operational Implementation

3.4.2.1 Step 1 : Computation of the narrow band radiances from gray values

3.4.2.2 Step 2 : Computation of OLR from narrow band radiances

3.4.2.3 Step 3 : Merging of OLR with Geolocation files

3.5 Outputs

Parameter	Unit	Min	Max	Accuracy	Resolution
OLR	Wm⁻²	50	400	3 %	pixel

3.5.1 Format of the output and the domain

Lat, Lon, OLR,

Domain: 50 S to 50 N, 35 E to 135 E

3.6 Validation

3.6.1 Data required

The OLR computed by the developed algorithms will be compared with observed OLR. The following data can be used for validation:

- The OLR data from different satellites having broadband sensors (e.g CERES on Aqua, Teraa and NPP, ScaRaB on Megha-Tropiques)
- FY2D satellite derived OLR
- AIRS Derived OLR

Data	Resolution	Source
OLR, CERES	20 Km	NOAA
OLR, AIRS & IASI	45 Km	NASA
OLR, FY2D	5 Km	CMA
OLR, MT-ScaRaB	50 Km	ISRO

3.6.2 Method of validation

The root mean square Error (RMSE) and bias will be computed by comparing the retrieved OLR with that of observed OLR.

3.7 Technical Issues

- Limitations of narrowband to broadband conversion (ADM)
- Non-availability of in-situ measurements.

3.8 Future Scope

These coefficients may need fine-tuning based on the comparison between observed OLR and the OLR computed using the INSAT-3D measured radiances.

3.9 References

1. Alvarez A., Lopez C., Riera M., Hernandez-Garcia E., and Tintore J., 2000. Forecasting the SST space-time variability of the Alboran Sea with genetic algorithms, *Geophys. Res. Lett.* **27**, 2709–2712.
2. Ba, M. B., and R. G. Ellingson (2001), A study of diurnal cycle of OLR using GOES sounder data, in Current Problems in Atmospheric Radiation, pp. 505– 508, A. Deepak, St. Petersburg, Russia.
3. Ba, M. B., R. G. Ellingson, and A. Gruber (2003), A validation of a technique for estimating OLR with GOES sounder, *J. Atmos. Oceanic Technol.*, **20**, 79– 89.
4. Chevallier, F., Che'din, A., Che'ruy, F., & Morcrette, J. J. (2000). TIGR-like atmospheric profile databases for accurate radiative flux computation. *Quarterly Journal of the Royal Meteorological Society*, **126**, 777– 785.
5. Ellingson R, G., D, J, Yanuk, H-T, Lee, and A, Gruber, 1989: A technique for estimating outgoing longwave radiation from HIRS radiance observations. *J. Atmos. Oceans, Technol* **6**, 706-711

6. Ellingson, R. G., H.-T. Lee, D. Yanuk, and A. Gruber (1994), A validation of a technique for estimating outgoing longwave radiation from HIRS radiances observations, *J. Atmos. Oceanic Technol.*, 11, 357–365.
7. Gruber, A., and A. Krueger, 1984: The status of the NOAA outgoing longwave radiation dataset. *Bull. Amer. Meteor. Soc.*, **65**, 958–962.
8. Gruber, A., and J. S. Winston (1978), Earth-atmosphere radiative heating based on NOAA scanning radiometer measurements, *Bull. Am. Meteorol. Soc.*, 59, 1570–1573.
9. Loeb, N. G., Smith, N. M., Kato, S., Miller, W. F., Gupta, S. K., Minnis, P., and Wielicki, B. A. (2003). Angular distribution models for top-of-atmosphere radiative flux estimation from the Clouds and the Earth's Radiant Energy System instrument on the Tropical Rainfall Measuring Mission Satellite. Part I: Methodology. *J. Appl. Meteor.*, 42:240–265. 33, 34, 35, 39, 40, 41, 56, 57, 119
10. McClatchey, R. A., R. W. Fenn, J. E. A. Selby, F. E. Volz, and J. S. Garing, 1972: Optical properties of the atmosphere. 3rd ed. AFCRL Environ. Res. Papers No. 411, 108 pp.
11. Minnis, P., D. F. Young, and E. F. Harrison (1991), Examination of a relationship between outgoing infrared window and total longwave fluxes using satellite data, *J. Clim.*, 4, 1114– 1133.
12. Ohring, G., Gruber A and Ellingson R., 1984; Satellite determination of the relationship between total longwave radiation flux and infrared window radiance; *J. Clim., Appl. Met.*, 23, pp 416-425.
13. Pierluissi, J. H., and G.S. Peng, 1985: New molecular transmission band models for LOWTRAN. *Opt. Eng.*, **24** (3), 541– 547.
14. Raschke, E., T.H. Vonder Haar, W .R. Bandeen, and M. Pasternak, 1973: The annual radiation balance of the earth- atmosphere system during 1969-70 from nimbus 3 measurements. *J Atmos. Sci* 30, 341-364.
15. Ricchiazzi, P., and C. Gautier, 1998: Investigation of the effect of surface heterogeneity and topography on the radiation environment of Palmer Station, Antarctica, with a hybrid 3D radiative transfer model. *J. Geophys. Res.*, **103**, 6161– 6176.
16. Schmetz and Liu, 1988: Outgoing Longwave Radiation and its Diurnal Variation at Regional Scales Derived From Meteosat, *J. Geophys. Res.*, 93, 11,192-11, 204.
17. Shettle, E. P., and R. W. Fenn, 1975: Models of the atmospheric aerosols and their optical properties. *AGARD Conf. Proc., Optical Propagation in the Atmosphere*, Lyngby, Denmark, NATO Advisory Group for Aerospace Research, 2.1–2.16.
18. Singh R., Kishtawal. C.M., Pal. P. K., and Joshi. P. C., 2006 " Surface heat fluxes over global ocean exclusively from satellite observations. " *Monthly Weather Review*, 134, 965-980.
19. Singh, R., P. K. Thapliyal, C. M. Kishtawal, P. K. Pal, and P. C. Joshi (2007), A new technique for estimating outgoing longwave radiation using infrared window and

- water vapor radiances from Kalpana very high resolution radiometer, *Geophys. Res. Lett.*, 34, L23815, doi:10.1029/2007GL031715.
20. Sun, F., M. D. Goldberg, X. Liu, and J. J. Bates (2010), Estimation of outgoing longwave radiation from Atmospheric Infrared Sounder radiance measurements, *J. Geophys. Res.*, 115, *D09103*, doi:[10.1029/2009JD012799](https://doi.org/10.1029/2009JD012799).
21. Stamnes, K., S. Tsay, W. Wiscombe, and K. Jayaweera, 1988: Numerically stable algorithm for discrete-ordinate-method radiative transfer in multiple scattering and emitting layered media. *Appl. Opt.*, **27**, 2502–2509.
22. Szpiro G.G., 1997. Forecasting chaotic time series with genetic algorithms. *Phys. Rev. E* 55, 2557–2568.

4. Quantitative Precipitation Estimate

S.No.	Product Name	Spatial Resolution	Temporal Resolution
1	3DIMG_L2G_IMR	10 km	30 minutes
2	3DIMG_L3G_IMR_DLY	10 km	Daily (00 H to 23:30 H)
3	3DIMG_L2B_HEM	4 km	30 minutes
4	3DIMG_L2G_GPI	1.0X1.0 deg	30 minutes

4. RAINFALL ESTIMATION

(A) GPI and IMSRA method

4.1 Algorithm Configuration Information

4.1.1 Algorithm Name

Quantitative Precipitation Estimation (QPE) from GPI and IMSRA Techniques

4.1.2 Algorithm Identifier

3DIMG_L2G_IMR

3DIMG_L3G_IMR_DLY

4.1.3 Algorithm Specification

Version	Date	Prepared by	Description
1.0	15.08.2012	R M Gairola A.K. Varma	QPE Baseline Document

4.2 INTRODUCTION

Weather and climate affects many sectors of the human activity as well as many aspects of the world's natural ecosystems. The hydrological cycle is one of the important components of Weather and climate system. The hydrological cycle describes the exchange of water substance between sea, air, soil, rock, plants and animals. The precipitation and evaporation processes significantly affect the global hydrological cycle. The quantitative assessment of precipitation is needed to improve understanding of the behavior of global energy and circulation patterns as well as the nature of climate variability. The choice of measured parameter has been influenced by the cost of installation, operation, longevity and temporal as well as spatial coverage of the instruments. The land based techniques of rainfall estimation are not sufficient for global rainfall assessment as about 70% of the Earth is covered with water. The space borne measurement and monitoring of rainfall is, therefore, a topic of major interest since they provide global coverage both on land and ocean for an extended period of time. A longstanding promise of meteorological satellites is the improved identification and quantification of precipitation at time scales consistent with the nature and development of precipitation processes. Meteorological satellites expand the coverage and time span of conventional ground-based rainfall data for a number of applications. The primary scope of satellite rainfall monitoring is to provide information on rainfall occurrence, amount and distribution over the regional to continental scales. The uneven distribution of rain gauges and weather radars and the relative lack of rainfall measurements over the oceans have significantly limited the use of global as well local data. Precipitation is one of the most variable quantities in space and time. Precipitation also has a direct impact on human life that other atmospheric phenomena seldom have: an example is represented by heavy rain events and flash floods (Barrett and Michell, 1991). Geostationary weather satellite visible (VIS) and infrared (IR) imagers provide the rapid temporal update cycle needed to capture the growth and decay of precipitating clouds. Microwaves provide the interaction of radiation with hydrometeors but with coarser resolution and limited swath widths of satellites with in

tropical orbit such as the Tropical Rainfall Measuring Mission (TRMM) (Kummerow et al., 1998) and of sensors in polar orbits like the Special Sensor Microwave Imager (SSM/I) series.

4.2.1 Overview

Operational applications, require quantitative rainfall determination from a variety of precipitating systems, which differ both dynamically and microphysically. This fact prompts for non-unique solutions based on the physics of precipitation formation processes. Barrett and Martin (1981) and Kidder and Vonder Haar (1995) give excellent reviews of the available methods. Petty (1995) has examined the status of satellite rainfall estimation over land. Recent reviews Levizzani et al. (2001) has covered results and future perspectives from the geostationary orbit. The perspective varies widely from the relatively simple methods used for climatic-scale analyses (e.g. Arkin and Ardanuy, 1989; Arkin and Janowiak, 1991) to the more elaborate instantaneous rainrate estimations for research and nowcasting (Ba and Gruber, 2001; Turk et al., 2000; Vicente et al., 1998).

Recent technological developments of MW instruments on board polar orbiters have been dramatic but the use of VIS, IR and water vapor (WV) channels of geostationary satellites is still indispensable. In particular, the launch of the newest generation of geostationary satellites, the Geostationary Operational Environmental Satellite GOES-I-M series (Menzel and Purdom, 1994) and the upcoming METEOSAT Second Generation (MSG) (Schmetz et al., 2002) with its Spinning Enhanced Visible and Infrared Imager (SEVIRI), adds new channels to the traditional VIS/IR/WV triplet. Some of the new channels have been tested for decades as part of the Advanced Very High Resolution Radiometer (AVHRR) series on board the National Oceanic and Atmospheric Administration (NOAA) polar orbiters or have other heritages.

Multispectral data have long since been available both from polar orbiting and geostationary satellite sensors and used for retrieving cloud properties. The relevant channels for cloud characterization were part of the payload of the polar satellites, while the sensors at geosynchronous altitude were almost exclusively devoted to VIS-IR operational monitoring of precipitation system displacements. This has considerably changed in the past few years since more and more sophisticated sensors have been conceived for the GEO orbits that will allow for global real-time cloud characterization.

Cloud radiative properties at VIS, near IR (NIR) and IR wavelengths have long since been studied and documented (among others Arking and Childs, 1985; Cheng et al., 1993, Saunders and Kriebel, 1988; Slingo and Schrecker, 1982). In the thermal IR the radiative properties are sensitive to the size distribution of the hydrometeors. In particular, an increase in the particle size increases the transmissivity, decreasing the reflectivity and increasing the emissivity of the cloud layer. This latter dominates at these wavelengths. In the NIR (e.g. the 3.9 mm MSG channel) the emissivity of a cloud layer is lower than in the thermal IR window: there is a large contribution of reflected radiation at the cloud top. Clouds with small hydrometeors scatter and reflect much of the 3.9 mm radiance. An increase in cloud particle size or the presence of large drops or ice crystals near the cloud top reduces the 3.9 mm reflectance from the cloud. containing more ice reflect less solar radiation in the 3.7 - 3.9 mm range as ice strongly absorbs at these wavelengths and ice crystals are generally larger than cloud droplets at cloud top. NIR reflectance mostly refers to cloud particles effective radius (re).VIS reflectance is primarily due to cloud optical depth.

Several methods have been proposed for the retrieval of cloud parameters from various cloud types. Pioneering studies were conducted by Arking and Childs (1985) and Nakajima and King (1990). Water Vapor images show the presence of water in the gas form between 22,000 and 35,000 feet above the earth's surface. The brighter white color indicates areas of moisture. Black depicts neutral. Lensky and Rosenfeld (1997) have conceived a multispectral rainfall estimation technique based on the method of Rosenfeld and Gutman (1994). They concentrated on areas of around 2000 km² that Rosenfeld and Gagin (1989) showed to be the critical limit beyond which a further increase in cloud cluster area does not result in higher rain rates.

IR and NIR channels other than the thermal IR window show some potential for application to rainfall estimations. Techniques for the instantaneous delineation of convective rainfall areas using split window data were initially conceived for the NOAA AVHRR (Inoue, 1987a,b, 1997) and are instrumental for the detection of semi-transparent cirrus clouds (Inoue, 1985). These techniques rely upon the detection of non-precipitating cirrus and low-level cumulus clouds using the two window channels at 10.5 - 11.5 and 11.5 - 12.5 μm (the so-called *split window*). The information content of the split window channels partially corrects erroneous rainfall area delineation (and consequent frequent rainfall overestimate) of simple IR techniques producing better false alarm ratios (FAR). The NIR 3.9 μm channel of GOES-8/9 satellites includes spectral features suitable for applications to rainfall detection and estimation. This channel was included for a long time in NOAA/AVHRR instruments (centered at 3.7 μm) for a variety of purposes including ice discrimination and sun-glint detection. Vicente (1996) developed a simple and fast algorithm for rainfall retrieval using the 11 and 3.9 μm channels with the obvious advantage of nighttime use and sensitivity to the presence of ice and water vapor.

In the present ATBD document the description of the scientific algorithms which will be developed and used to estimate rainfall from two of the standard operational algorithms of NOAA from the data acquired by the Very High Resolution Radiometer (VHRR) onboard INSAT-3D satellite. VHRR produces images in six spectral channels, in the Visible (VIS), Near Infra-red (NIR), Mid Wave Infra-Red (MWIR), and Infra-Red (IR) part of the spectrum covering the following channels: VIS 0.6 μm , NIR 1.6 μm , MWIR 3.9 μm , WV 6.7 μm , IR 10.8 μm , IR 12.0 μm . Each channel of the Imager has different resolution as mentioned in the Table-1 in sections ahead.

4.2.2 Objectives

There are two main objectives under the rainfall retrieval algorithms from INSAT-3D.. These techniques are popularly known as GOES Precipitation Index (GPI) and GOES Multispectral Rainfall Algorithm Technique (GMSRA). Both the algorithms are state of art and aimed at estimation of rainfall with different applications at different spatial and temporal requirements respectively. First GPI related objectives are the implementation of the algorithm following Arkin (1979), while the second one is related to the development of the algorithm named GMSRA following Ba and Gruber (2001). Originally the GPI technique has been in operation for a large scale rainfall estimation by Global community for more than two decades. The GMSRA on the other hand is a new one and is developed and used only by USA based on integrated efforts from many group of researchers along with the supporting

infrastructure (like ground truths with high spatial and temporal coverage's etc.). from a hundred of radars on the ground.

The inherent limitations of optical channels remains persistent for rainfall retrieval as the rainfall in the ground is inferred by cloud top signatures only. There is no direct physical connection between the rain/cloud and ice hydrometeors within the clouds with radiance emanating from cloud tops to the sensor. The accuracy of rainfall estimate is improves only marginally even with significant new efforts. However, the high spatial and temporal coverage of Geostationary optical measurements is the very strong point along with the resolution capabilities of the sensors. At the same time microwaves have a direct physical connections with vertical structure of rainfall and thus with the cloud, rain and ice hydrometeors. But the non-portability of microwave sensors to the geostationary platforms till date due to technological constraints is a limitation and thus only low earth orbiting satellites can provide the rainfall information of land, ocean and atmosphere as on now. With the advent of active and passive radar and radiometric sensors onboard a single satellite (e.g. Tropical Rainfall Measuring Mission-TRMM) we envisage that a technique like GMSRA can be further improved for Indian tropical regions and more reliable rainfall information can be retrieved. We henceforth call this technique as INSAT Multispectral Rainfall Algorithm (IMSRA), as a specific technique for Indian Tropical regions. Our objectives for both the techniques (GPI and IMSRA) here are based on these premises and are outlined below (mainly in cases of IMSRA).

A1. INSAT-3D Rainfall using GPI Method:

1. To generate a total day rainfall maps using 3 hourly brightness temperatures of IR (11 um) images for 1.0×1.0 deg latitude /longitude boxes in an area -50° to $+50^{\circ}$ lat and 30° E to 130° E using Arkin's GPI method.
2. To generate mean spatial variance and histogram of 24 classes of temperatures at 1.0×1.0 deg latitude/longitude.
3. To derive QPE based on daily basis following the 3 hourly data of IR observations (8 images a day).
4. Validation of rainfall products using rain gauges and Doppler Weather Radar data.
- 5 . Inter-satellite comparison using other contemporary satellites like Meteosat, NOAA etc.
6. Estimation of rainfall on pentad, monthly mean, seasonal mean and annual mean scales after due calibration/validation from radar and inter-satellite comparisons as above, rainfall.

A2. To Develop Precipitation Estimates Using the Multispectral Rainfall Algorithm (IMSRA) Technique:

The relation between precipitation amount and cloud fraction as seen from satellite passive radiometers in case of GPI technique above, though simple and straightforward it might seem, has not yet reached completely satisfactory accuracy, effectiveness, and time/space coverage. There are numerous applications in meteorology and hydrology where accurate information at scales smaller than the existing 1.0° products (e.g. daily or sub daily estimates at resolutions of 1° and down to the 0.25°) would be invaluable. There is also increasing demand from the meteorology and climate community for such products over extended periods. High-resolution rainfall information is available for limited areas using

combinations of ground-based radar and dense networks of rain gauges. In India in particular, where the need of high spatial and temporal rainfall is essential, for large and varied areas of India (Western Ghats, plateaus, Himalayan Regions, North-Eastern Regions, Arid and Semi-Arid Zones) however, the *in-situ* infrastructure necessary for this form of precipitation monitoring network is not in place. Recent developments mostly refer to microwave (MW) sensors on board polar orbiters, but the use of visible (VIS) and infrared (IR) sensors of geostationary satellites for a variety of applications is by no means over. Thus a suit of both supplementing each others would be the ideal situation, particularly when the highly advanced microwave sensors data from various international satellites are available on near real time basis.

The main objectives here in IMSRA algorithm are to estimate rainfall by developing a Multispectral Rainfall Algorithm which is an optimal combination of GMSRA and some of the innovative proposed approaches that utilizes microwave remote sensing measurements from polar orbiting satellites. Here, the rainfall algorithm is with more advantageous that combines satellite passive microwave and infrared (IR) data to account for limitations in both data types. Rainfall estimates are produced at the high spatial resolution and temporal frequency of the IR data using rainfall information from the PMW data. Over the last few years, a number of groups world wide have embarked on development of such techniques wherein the advantages of geosynchronous viz. vast coverage and near sufficient space-time sampling, and polar passive microwave radiometers viz. more physically based retrievals, are synergistically used to generate tropical rainfall on various scales (e.g. Adler et al. 1994, Todd et al. 2001, Gairola and Krishnamurti 1992). With above background the objectives for Multi Spectral Rainfall Algorithm (IMSRA) are as follows.

The technique has the following components:

1. Identify areas for very deep convective cores from IR and WV channels ($11\mu\text{m}$ - $6.7\mu\text{m}$), which corresponds well with rainfall.
2. To screen mid-to upper level clouds with or without thin cirrus above the rain and non-rain bearing clouds.
3. Cloud growth classification based on temporal gradients of TIR – TB's.
4. Filtering of low and non raining clouds along with the warm and semi-transparent clouds based on IR and WV when rainfall is estimated for clouds having brightness temperatures colder than 240K.
5. Spatial and temporal co-location of INSAT-TIR brightness temperature, and TRMM / SSM/I rainfall for creation of matched database.
6. To compute instantaneous rain rate using pre-calibrated rain rate for cloud top brightness temperature ($11\mu\text{m}$) for each pixel classified as containing raining clouds along with Satellite Microwave Radiometric measurements (e.g TRMM Microwave Imager-TMI).

7. To adjust the rainfall estimates in association with the product of Integrated Precipitable water and Relative Humidity from 500 mb – Surface (from Eta/IMD model).
8. Validation of rainfall with Doppler Weather Radar data and fine tuning of algorithm.
9. Finally to estimate rainfall would be estimated in different spatial and temporal grid scales based on all the above components of the IMSRA algorithm.

4.3 Inputs

4.3.1 Image and preprocessing data (Dynamic)

The details for the required satellite data for both GPI and IMSRA are provided in following table:

Parameter	Resolution	Quantization	Accuracy	Source
Radiometric and geometric corrected gray count values of TIR-1 channel (10.5)	pixel	10 bit	--	Derived from raw data by DP (data processing)
Radiometric and geometric corrected gray count values of TIR-2 channel (11.5)	pixel	10 bit	-	Derived from raw data by DP
Radiometric and geometric corrected gray count values of VIS channel	pixel	10 bit	-	Derived from raw data by DP
Radiometric and geometric corrected gray count values of , WV channel (6.7)	pixel	10 bit	-	Derived from raw data by DP
Radiometric and geometric corrected gray count values of 3.9 mm	pixel	10 bit	-	Derived from raw data by DP
Gray value to brightness temperature conversion table	-	-	0.3 K	Derived by DP
Geolocation file	Pixel	-	1 pixel	Derived by DP using Calibration Table

4.3.2 Other Auxiliary data and Model Inputs

In addition to satellite data from INSAT-3D, radar and rain gauge data, and atmospheric moisture products (integrated precipitable water and relative humidity from 500-mb surface) obtained from the IMD/Eta Model analysis are essential on required grid spacing in different temporal scales. The gridded rainfall data from Doppler Weather Radars are needed from

IMD at every one hourly time interval on 1x1 and 0.25x0.25 deg grid resolution for GPI and IMSRA techniques. The rainfall from DWRs should be well calibrated and the products should be well converted to rain rate using an appropriate Z-R relation well tested and validated over Indian regional sites of the respective radar locations. In some cases one hourly rainfall from fast response rain gauges would be highly desirable particularly the areas where the DWR coverage is not at all there. Thus 1 to 3 hourly gauge-adjusted DWR rain rates, and hourly and daily gauge rainfall obtained from the IMD stations are important. The Eta / IMD model forecast/analysed fields of total precipitable water (TPW) and relative humidity fields should be available from IMD at every 3 hourly within 0.5x0.5 respectively.

Parameter	Resolution	Accuracy	Source
Total Water Vapour	0.5 X 0.5 deg	-	Eta Model Analysis (IMD) (500 mb to surface)
Relative Humidity	0.5 X 0.5 deg	-	Eta Model Analysis (IMD) (500 mb to surface)
Doppler Weather Radar - Surface Rain	0.25 X 0.25 deg		DWR observations at IMD Sites (Every 1-3 Hour, in 0.25°x0.25° grids)
Surface Rain Gauge on hourly basis (from Fast Response Rain Gauges, AWS) and Total Day basis			----- Do -----
TRMM / SSM/I Rainfall	1. Scan-mode Orbital data 2. Grid mode 0.25° X 0.25° data	-	From Internet Site

4.4 Algorithm Functional Specifications

4.4.1 Overview:

NOAA/NESDIS emphasizes use of meteorological satellites for the study of flash floods. Heavy precipitation and flash floods are often a multi scale and concatenating event from the global scale to the synoptic scale, to the mesoscale and finally to the storm scale. Satellite-derived algorithms, conceptual models, and interpretation techniques are used to provide information on these various scales to monitor, assess, and predict heavy precipitation and flash floods. In the satellite data, global scale connections between the tropics and middle latitudes are observed. These connections are movements, surges, or plumes of water vapor that are often associated with unstable air and prepare the environment for heavy precipitation and flash floods. On the synoptic scale, the 6.7 μm water vapor is especially

useful for detecting jet streaks, vorticity centers and other features that are associated with upward vertical motion and lift the moist, unstable air resulting in the production of clouds and precipitation. Whether or not heavy precipitation and flash floods will occur are generally determined on the mesoscale to storm scale. On the mesoscale, infrared (10.7 μm and 3.9 μm), visible, and water vapor (6.7 μm) are used to locate boundaries (both frontal and thunderstorm-produced) and short waves that may initiate, focus, and maintain the heavy precipitation. Terrain features such as orographic uplift have the same effect of anchoring, intensifying, and prolonging the precipitation. On the storm scale, the intensity, movement, and propagation of the precipitation system (e.g., thunderstorms) is used to determine how much, when, and where the heavy precipitation is going to move during the next zero to three hours (called Nowcasting). High resolution infrared (10.7 μm) and visible are the principal data sets used in this diagnosis.

Large scale precipitation values are of importance in many fields and anomalies in large scale precipitation are also known to have a close relationship with global circulation anomalies. Satellite based rain estimation techniques can be classified into two broad categories, viz, (1) estimation of precipitation on near real time, e.g. Scofield and Oliver (1977), etc. and (2) estimation of average precipitation over a large area for a period of time ranging from a day to a month e.g., Richards and Arkin (1981) etc. In any of these two the estimation criteria is based on some statistical relationship.

In case of GOES, data from five channels are used: the visible channel (0.65 mm), used when available to select optically thick clouds; channel 2 (3.9 mm), used to retrieve reff of hydrometeors during daytime; the water vapor channel (6.7 mm); and thermal channels 4 (11 mm) and 5 (12 mm). The 11 mm channel is used to determine cloud-top brightness temperature, and the 12-mm channel is used in conjunction with the 11-mm channel to estimate cloud-top temperature. The estimated cloudtop temperature is utilized to compute the thermal emission at 3.9 mm , which is then subtracted from measurements of that channel to yield the reflected solar radiation in the 3.9-mm spectral band.

In the statistical relationship between IR cloud pixel brightness temperature from satellite sensor and surface rainfall measurements the mean rainfall rate R varies as a function of brightness temperature (BT). But the uncertainty in rainfall rate is quite large and also varies with BT. The GPI method uses a simple two-piece threshold function approximation of this relationship. Although crude, the GPI method works quite well for the estimation of monthly rainfall over large areas, partly because the over- and underestimation of spatial and temporal errors cancel each other in the aggregation procedure.

Complete software package for derivation of QPE using Kalpana-1, INSAT-3A, INSAT-3D VHRR data from two important algorithms like GPI, and IMSRA has been asked for. Both of them are the operational at NOAA/NESDIS and has been developed after years of research and development efforts by various investigators. The theoretical background for GPI and GMSRA respectively are given below:

4.4.1.1. Theoretical Background for GPI Algorithm:

4.4.1.1.1 Physical explanation of rainfall with infrared (IR) images

The satellite IR images are composed of measured radiant energy originating in the atmosphere or from the land and water surface below. The intensity of this energy integrated over all wavelength, by Stefan-Boltzmann law, is proportional to fourth power of

temperature. The Stefan-Boltzmann law is valid for a perfect black body. If the medium emits spectral radiant energy according to some temperature less than its thermal temperature, than a second factor called emissivity is introduced. The emissivity of a body determine its emission efficiency. Thus, we can define brightness temperature of a body T_b , which is related to its physical temperature T by following equation:

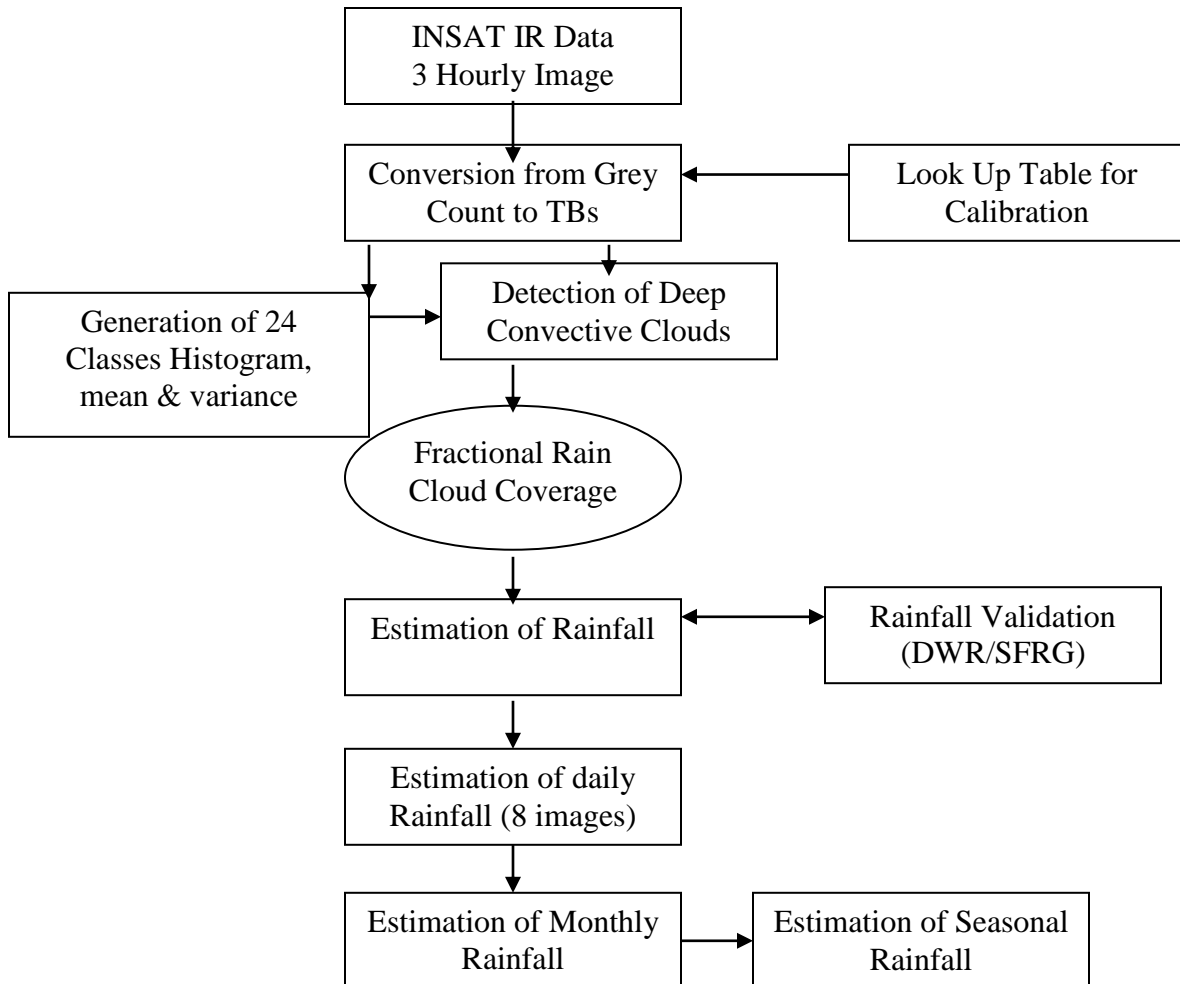
$$T_b = \varepsilon T$$

where, ε is emissivity of the object. If. $\varepsilon = 1$, $T_b = T$, its a black body; if $\varepsilon = 0$, $T_b = 0$, its a white body; if $0 < \varepsilon < 1$, $T_b < T$, and its a gray body.

The IR, for rainfall estimation, refers to thermal IR band that is 10.0 - 12.5 μm . This is a atmospheric window, and all earthly objects radiate maximum spectral power in this band. In this band the absorption is strong for clouds and land/water surfaces and slight for gaseous constituents of the atmosphere. For surfaces, which are opaque and do not transmit radiation, measured intensity is closely approximated by the fourth power of the temperature. For those surfaces, which are not opaque - such as some clouds - measured intensity is approximated by effective emissivity times fourth power of the temperature. This effective emissivity will be referred more often as cloud emissivity here after. The cloud emissivity cannot be measured from observations at a single wavelength interval. Often it is simply assumed to be unity. Then the temperature calculated from observed intensity of radiation is called 'brightness temperature'. Only when $\varepsilon = 1$, brightness temperature equals to black body temperature.

The value of IR measurements to rainfall estimate lies in the nearly universal condition of lapse of temperature with height through the troposphere. If the temperature is known with height, either from actual sounding or from climatology, the height of the cloud can be infrared from the satellite IR observations. Ordinarily, gray clouds are not useful in this context, because $\varepsilon < 1$ implies clouds which are thin (and therefore without precipitation). The more serious problem is distinguishing between cold clouds that are radiometerelly thick but are confined to the upper and middle troposphere, and cold clouds which extend into lower troposphere.

4.4.1.1.2 Flow Chart for QPE from GPI:



4.4.1.1.3 Operational Implementation

Step 1 : Conversion from gray count to BT

The INSAT-3D infrared thermal images of 0000, 03000, 0600, ..., 2100 UTC, i.e., every three hours, are to be used. Infrared pixel has dimensions of 8 x 8 km in case of KALPANA and INSAT-3A and 4x4 km in case of INSAT-3D, so that several pixels fall within $1.0^{\circ}\text{x}1.0^{\circ}$ box. The grey shade value (0-1023) of each pixel in a given image is read and the corresponding brightness temperature is to be calculated from a look-up table. Pixel lying outside the chosen area of analysis are to be ignored while within it are assigned to appropriate box.

Step 2: Histogram Generation:

After the temperatures of all the pixels in a box are known they are to be distributed to generate 3 hourly 24 class histogram of brightness temperatures of IR (11 um)

images for 1.0 x 1.0 deg latitude /longitude boxes in an area -50 to + 50 deg. lat and 30 to 130 deg longitude from the sub-satellite point.

Step 3: Grid-wise Statistics

Generate 3 hourly mean and spatial variance of temperatures at 1.0 x 1.0 deg latitude/longitude within the area 40 deg lat/long from the sub-satellite point.

Step 4: Grid-wise Rain Clod Detection:

The fractional cloud coverage within a grid box is the ratio of the pixels of cooler than specified threshold temperature to the total number of pixels. This gives the measure of the fractional area of the box covered by clouds with tops colder than threshold. Finally the estimates of precipitation using the GPI technique in the grid spacing of 1.0° x 1.0° lat/lon will be carried out. This work indicated a high correlation between the fractional coverage of "cold" clouds and observed rainfall. It was determined that the highest correlation between the parameters was produced using a 1.0 degree latitude/longitude spatial scale. An estimation method using linear regression was developed. The regression procedure yielded the simple estimation equation:

$$R = [3 \text{ mm h-1}] \times [\text{frac}] \times [\text{hours}]$$

where R is the rainfall estimate in millimeters; frac is the fractional coverage of cloud-top temperature < 235K for the desired 1.0 degree latitude/longitude region; and hours indicate the number of hours in the observation period.

Step: 5 Sub-Grid Scale Rainfall:

In order to produce precipitation estimates at finer temporal and spatial resolutions, it is necessary to develop an improved method. Sub –grid scale is possible with help of recent developments at NOAA/NESDIS. However, the GPI algorithm will also be attempted to provide at 0.5 degree latitude/longitude grids by some alternative approach. Based on this algorithm QPE on daily, pentad, moving average, monthly mean, seasonal mean and annual mean will be produced.

Step: 6 Validations:

Regarding the validation of the derived QPE the DWR (at present four at Chennai, SHAR, Kolkatta, Machliputtnam and some more are planned by IMD) and Surface Rain Gauges (SFRG) Data at different spatial and temporal scales will be highly desirable in and around the maximum validation sites in temporal window of every hour.

Remarks:

During the days when all the 8 images per day are not available, rain rate will be provided with a flag. Provisions of average rainfall estimation will be made for all the cases when more than 50% of data is available. Similar approach will be followed with the Pentad or Monthly scale average rainfall estimates.

4.4.1.2 IMSRA technique:

4.4.1.2.1 Theoretical Background:

The developmental work related to the INSAT Multi-Spectral Rainfall Algorithm (IMSRA) proposed here as an inhouse R & D effort, originally follows the GMSRA approach along with innovative alternative features (i.e. the satellite microwave radiometric measurements) for the estimation of precipitation. The theoretical basis is that

1. Bright clouds in the VIS and clouds with cold tops in the IR imagery that are expanding (in early and mature stages of development) produce more rainfall.
2. Clouds with cold tops that are becoming warmer produce little or no rainfall.
3. Merging of cumulonimbus (Cb) clouds increases the rainfall rate of the merging clouds.
4. Most of the significant rainfall occurs in the upwind (at anvil level) portion of a convective system.
5. Cloud micro-physics plays an important role in understanding the precipitation and thus effective radius of cloud top temperatures are to be known (say 3.9 mm during day time).
6. The humidity and total precipitable water as a background field characterizes the rainfall process identification.
7. For each pixel classified as containing raining clouds based on above criterions, the associated instantaneous rain rate can be computed using pre-calibrated mean rain rate for cloud top brightness temperature using Satellite Passive Microwave Radiometer (e.g. TRMM-TMI) and/or Active Microwave Radar (TRMM-PR).
8. Finally the retrieved rainfall from earlier step and Doppler Weather Radar data on available locations in India would be used both for calibration and validation of the algorithm.
9. Production of rainfall maps on every 3 hourly and daily basis on $0.5^{\circ} \times 0.5^{\circ}$ and above grid spacing.

Several such features are integrated in finalizing the estimation of rainfall using measurements from mult-spectral channels (Vis, IR, WV and microwave etc.). Physical explanation of rainfall with infrared (IR) images have been discussed previously which is common for GPI algorithm. In addition the Physical explanation of rainfall with visible (vis) images is being presented here in brief. Various researches so far have pointed that that with thicker clouds the probability of rainfall and rain intensity is increased. This relationship is strongest for clouds warmer than -15° C. It is also noted that marine clouds produce heavier rainfall. The possible explanation for this lies in the process of cloud growth and droplet growth rates. In clouds warmer than -15° C, precipitation results from coalescence. The large cloud thickness allows more time for growth before droplets fall out of the cloud. However, the other factors like droplet concentration, evaporation and cloud temperature are also important. Difference in precipitation probability between marine and continental clouds

were attributed to difference in concentration of condensation nuclei and of droplets, and difference in evaporation below the cloud base.

Satellite passive microwave and more recently, active microwave rain radar are able to provide accurate estimation of rain rates. However they are known to have but poor temporal sampling. Again the estimates from polar orbiting satellites are subject to the bias in regions where diurnal cycle of rainfall is pronounced. Still the instantaneous measurements of rainfall from microwave sensors are more accurate and thus are useful in calibrating other sensors like visible and IR. At present, the algorithms for the quantitative estimation of rainfall from microwave observations are quite successful but suffer from a scarcity of sufficient verification data over the oceans. Theoretical and empirical studies addressing the problem of rain retrieval and their critical assessment continues to appear. A definitive algorithm is continuously in developing stage because of the complex and variable microphysical and mesoscale structure of precipitation vis-à-vis coarser resolution of microwave sensors. As a source of microwave measurements, we use the rainfall data from the SSM/I Defense Meteorological Satellite Program (DMSP). Several algorithms have been developed for various SSM/I sensors of the DMSP series. The SSM/I rainfall used here is based on Ferraro and Marks (1995). The SSM/I had a conical scan with a swath width of about 1400 km and TRMM has swath width of about 800 km and the rainfall is retrieved by NASA-GPROF (Goddard Profiling) algorithm. Use of microwave data with those of VI/IR is most plausible choice to mitigate the problem of resolution in microwaves and augmentation of rain estimates from IR measurements.

Following the main features of Ba and Gruber (2001), from GMSRA, that combines multispectral measurements of the satellites to estimate rainfall along with the present algorithm, IMSRA is thus proposed in combination with additional satellite microwave measurements. Thus the principal innovations of IMSRA relative to previous infrared/visible algorithms alone is that it combines several cloud properties used in a variety of techniques in a single and comprehensive rainfall algorithm. For example, the technique uses cloud-top temperatures as a basis of rain estimation (e.g., Arkin and Meisner 1987; Ba et al. 1995; Vicente et al. 1998), and it utilizes the effective radii of cloud particles (e.g., Rosenfeld and Gutman 1994) and spatial and temporal temperature gradients (e.g., Adler and Negri 1988; Vicente et al. 1998) to screen out nonraining clouds. The algorithm have the following steps which are heavily drawn from (Ba, M., and A. Gruber, 2001).

Step 1. Screening Method:

One of the most important aspects in estimating rainfall using IR measurements is to distinguish nonprecipitating cirrus from active cold convective clouds. To remove cirrus clouds, an empirical procedure developed by Adler and Negri (1988) was adapted in NOAA/NESDIS for areas smaller than originally applied. A slope (S) and a temperature gradient (G) are computed for each local temperature minimum in a window of 25 GOES pixels [note that Adler and Negri (1988) searched an entire cloud area for points colder than their neighbors]. The terms G , and S are given by Eq. (1) and Eq. (2), respectively:

$$G_t = T_{avg} - T_{min} \quad \text{and} \quad (1)$$

$$S = 0.568 (T_{min} - 217) \quad (2)$$

where T_{min} is the local minimum in the window of 25 X 25 pixels, and as in Adler and Negri (1988), T_{avg} is the mean temperature of the 6 pixels surrounding the current pixel (4 pixels along the scan and 2 pixels across the scan because the pixel offset along the scan is

approximately one-half as large as across the scan). Based on G and S the decision is made about the cirrus delineation.

There are many channels needed for this screening procedure and has been originally developed only for mid latitudes, we are aware of a more recent cloud classification approach by CNES as an alternative (Roca et al. 2002). This method is based on classification of clear sky, low clouds, warm semitransparent clouds, mid-to-upper level clouds or without thin cirrus above, mid-to-upper level clouds, and finally deep convection with or without thin cirrus above.

Step 2: Micro-physical properties of clouds:

During the day time when the visible channel is available and the radiance at 3.9 mm is dominated by the solar reflected part, the effective radius of cloud particles at the cloud tops can be computed for overcast pixels. As stated by Ba and Gruber (2001), the first step in deriving the effective particle radius consists of selecting only pixels filled with optically thick clouds because measurements obtained from thin clouds include radiances both emitted and reflected by clouds. For optically thick clouds defined as having a visible reflectance greater than 0.40, the transmissivity at 3.9mm wavelength can be neglected. So with the assumption that the cloud is a Lambertian surface, the emissivity can be expressed by $1 - A$, where A is the spectral albedo at 3.9 mm. Thus, the observed radiance L at 3.9 mm is then given by

$$L = AS_0/\pi + (1-A) P_{EBB} \quad (3)$$

where S_0 is the solar irradiance in the GOES 3.9-J.101 band and P_{EBB} is the equivalent blackbody emitted thermal radiation at 3.9 mm for cloud-top temperature T_c . Thus, the albedo A is obtained from Eq. (4):

$$A = L - P_{EBB} / (S_0/\pi - P_{EBB}) \quad (4)$$

The effective radius of cloud particles is defined as

$$r_{\text{eff}} = \sqrt{\frac{\int r^3 N(r) dr}{\int r^2 N(r) dr}} \quad (5)$$

where $N(r)$ is the number concentration of particles having radius r . The effective radius, which is dependent on the spectral albedo A at 3.9 μm , is retrieved using the results obtained by Rosenfeld and Gutman (1994), which were tabulated in a lookup table of A versus r_{eff} using an inversion of a radiative transfer model (Nakajima and King 1990). This is however, a grey area of research and the studies for microphysical properties of clouds is replaced with more innovative research element of using more physically based microwave observations of hydrometeors in synergism with the Geostationary infrared observations.

Step 3. Pre-calibration of Rain Rate Using Satellite Microwave Data

After the clouds are classified for their rain–no-rain barring properties, the IR radiances are to be calibrated against the near instantaneously collocated microwave rainfall measurements. The calibration with the contemporary satellites like TRMM and SSM/I (whichever is available during IR acquisitions) would be highly desirable. TRMM is a low inclination tropical orbiting, while SSM/I (at present two functional) are the polar orbiting satellites. The

rainfall estimation from these satellite sensors are based on NASA's GPROF (Goddard Profiling) Algorithm. These are most reliable microwave satellite rainfall estimates for calibrating the thermal IR radiances to estimate rainfall. A large data base of collocated INSAT-3D – IR Radiances along with TRMM/SSMI rainfall rates will be generated over land and oceanic regions. The retrieval of rainfall thus, would be carried out using this data base using multiple regression approach. The coefficients for land and oceanic regions will be derived separately. Over land regions the further classification would be possible only after extensive validations. The calibration with microwave derived rain will be dynamically updated in case there are changes in the rainfall products itself.

Step 4. Moisture Availability and Sub-cloud Adjustments:

A moisture correction factor is to be used to adjust for the tendency of the overestimation of precipitation in wet regions and underestimate in dry regions (Vicente et al. 1998). This correction factor, as first proposed by Scofield (1987) consisted of the precipitable water (PW, in inches) and relative humidity (RH, expressed as a decimal fraction) from the 500 hPa to surface layer of the IMD model. The functional form of rainfall and IR brightness temperature relationship would be further developed under different moisture conditions. The relationship is adjusted by moisture factor, which is designed to modulate the evaporation effects on rain below cloud base for different moisture environments. The amount of moisture factor will also determine the growth factor along with the successive image data. Thus the final rainfall equations will be different for different RH and PW amounts so that the real time PW and RH data can be ingested properly with a priori knowledge well established for the region of study/operation.

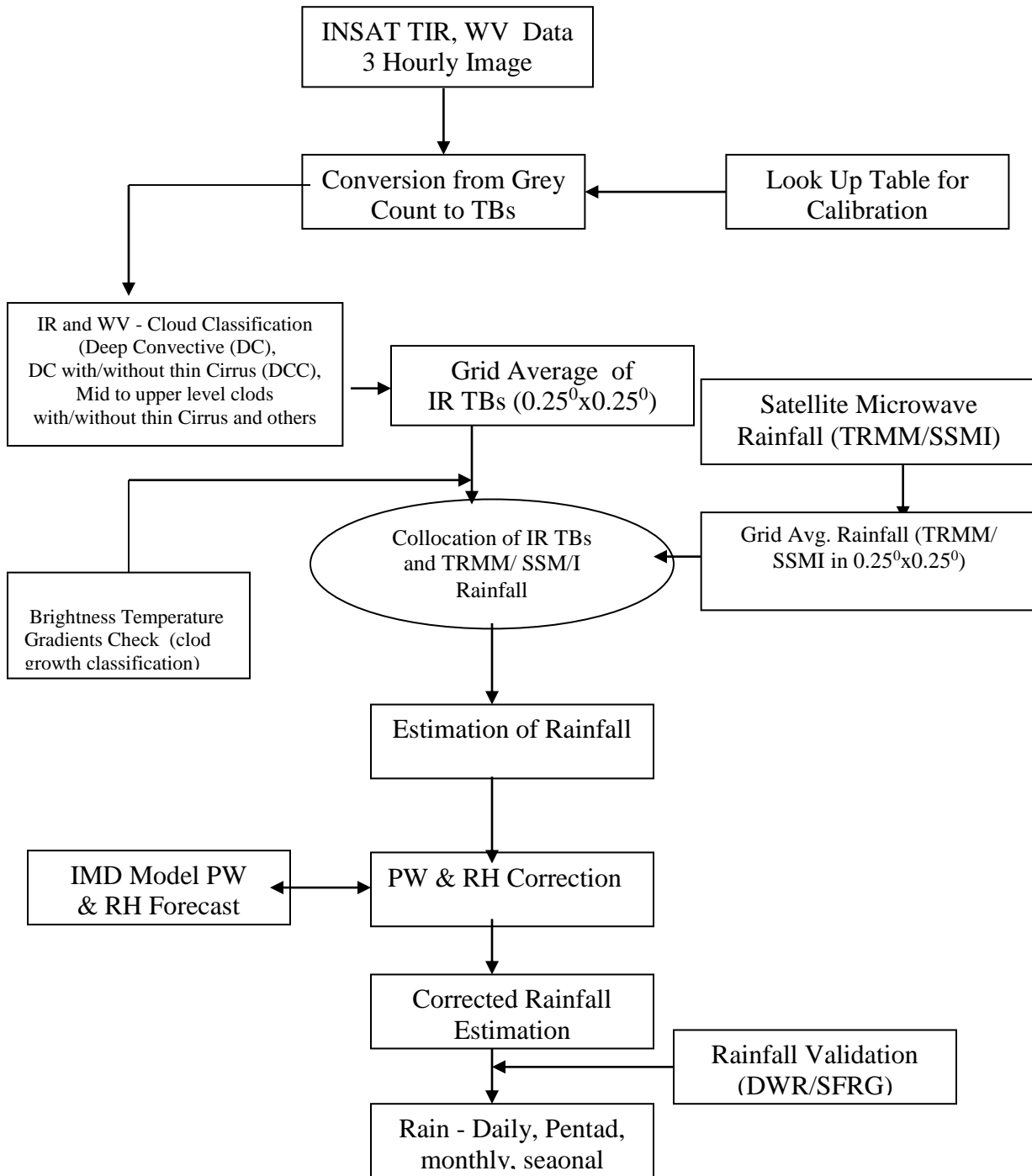
Step 5: Calibration and validation and Fine Tuning of algorithm:

Finally the retrieved rainfall from earlier steps and Doppler Weather Radar data on available locations in India would be used both for calibration and validation of the algorithm. The error analysis will be carried out and accordingly the algorithm will be fine tuned. A complete error statistics (regression, correlation, RMSE, BIAS, Mean, Standard Deviation etc.) will be performed for the desired period (validation period of about 3-4 months).

Step 6: Generation of Rainfall maps:

Rainfall maps on every 3 hourly and daily basis on $0.5^{\circ} \times 0.5^{\circ}$ and bigger grid spacing will be produced with all provisions to have maximum possible information (like contours, color shades, statistical information etc.). Based on this algorithm QPE on daily, pentad, monthly mean, seasonal mean and annual mean will be produced. The capability of to derive QPE from IMSRA over meteorological subdivisions will be attempted along with Image Analysis System Group. Accordingly the algorithm will be made operational after due testing and validation.

4.4.1.2.2 Flow Chart for IMSRA Algorithm



4.4.1.3 Operational Implementation Steps for QPE from IMSRA

Step 1 : Conversion from gray count to BT: With the calibration and geolocation information the raw counts are to be converted into the brightness temperatures at different pixel locations respectively.

Step 2: Cloud Classification (Deep Convective (DC), DC with/without thin Cirrus (DCC), Mid to upper level clods with/without thin Cirrus using an IR and WV channels.

Step 3: Grid Average of IR TBs ($0.25^0 \times 0.25^0$) to match with microwave rainfall from TRMM (i.e. collocation of INSAT-3D-IR-TBs and TRMM rainfall).

Step 4: Calibration of IR brightness temperatures with the contemporary microwave radiometric measurements of rainfall (e.g. TRMM Rainfall from NASA's GPROF algorithm).

Step 5. The IMD model based forecast of precipitable water and relative humidity for correction of rainfall equation based on above calibration procedure to be made available from IMD on every 6 hourly interval.

Step 6: Validation and fine tuning of the algorithm based on IMD's DWR and AWS and fast response rain gauges on hourly basis.

Step 7. Processing of the data for the different temporal scales (3, 6, 12 hours and etc.) based on the above steps of the development and validation of the algorithm.

Remarks:

Some of the steps like the cloud microphysics (cloud microphysics and their optical properties, etc.) are a grey area of research and needs experience and thus can be taken up only as R&D efforts. The hourly rainfall from rain gauges and DWRs and the IMD model forecasts from IMD in proper grid sizes (3-6 hourly, 0.5×0.5 deg. grid) are essential. In addition, the advanced approach suggested here to use satellite microwave information to augment thermal IR rainfall measurements along with VIS and WV would also require a large R & D effort (in terms of man hours).

4.5 Outputs

Parameter	Unit	Min	Max	Accuracy	Resolution
QPE (GPI)	mm	0	72 mm/ day	TBD	1.0×1.0 and 0.5×0.5 deg
Histogram of BT's	K	< 180 K	> 280 K	24 Class	1.0×1.0
Daily, Pentad, Monthly & seasonal rainfall	mm	0	72 mm/day	TBD	1.0×1.0
QPE (IMSRA)	mm	0	TBD	TBD	1.0×1.0 and 0.5×0.5 deg
Histogram of BT's	K	< 170 K	> 300 K	24 Class	-- do --
Daily, Pentad, Monthly & Seasonal rainfall	mm	0	TBD	TBD	-- do --

4.5.1 Format of the output and the domain

Basic format would be to obtain QPE on a give domain with geolocation, and rainfall values. However, the QPE would be represented in various shades, contours and with desired color coding thereof. The 24 class histogram also will be generated.

Domain : For both GPI and IMSRA the domain for rainfall estimation mainly would be 50° S to 50° N, 30° E to 130° E.

4.6 Validation

Rainfall products from the operational algorithms are to be obtained from two different methods mentioned above. These are required to be used for many diverse meteorological, climate, hydrological, agricultural, and other applications. It is therefore important to have an idea of their accuracy and expected error characteristics. This is done by validating the satellite precipitation estimates against "ground truth" from rain gauge and radar observations. A thorough verification of satellite-based precipitation products should quantify their accuracy in a wide range of weather and climate regimes, give users information on the expected errors in the estimates, help algorithm developers understand the strengths and weaknesses of the satellite rainfall algorithms. To get good estimates of absolute accuracy satellite products are verified against very high quality radar and gauge data. However, these sites are only few in number. To get estimates of regional and spatial accuracy it is necessary to use a much larger quantity of data, for example, from national rain gauge networks. While these verification data are less reliable than those from high-quality sites, their errors are usually much smaller than those associated with the satellite estimates, at least on short time scales. For validation of QPE with the ground truth on different temporal and spatial scale are required mainly with the data of DWR and Rain Gauges.

4.6.1 Data Required:

The following data for validation will be needed

Parameter	Resolution	Quantization	Accuracy	Source
Doppler Weather Radar	0.25°x0.25°	--	--	IMD - At all DWR locations (Every 1 Hourly basis 0.25°x0.25° grids)
Fast Response Rain Gauges (for hourly rainfall) & Other Rain gauge Data Rain/day	Ground Truth (over land and oceans) point observation	--	--	IMD - At all Daily observation sites and to plan for oceanic locations
Total Water Vapour Relative	0.5 X 0.5 deg 0.5 X 0.5 deg			3-6 hourly Eta /IMD Model Analysis from IMD, (500 mb)

Humidity				to surface)
TRMM Analysed Data	Orbital and 3 hourly - $0.25^0 \times 0.25^0$ and $1^0 \times 1^0$			Data available through internet

4.6.2 Method of Validation:

Currently pulsed Doppler technique are applied in weather radars to map severe storm reflectivity and velocity structure with great success in showing in real time the development of cyclones providing quantitative measure of intensity, track and information on winds within and around the storm. By studying the characteristics of radar returns and analyzing the variations in their amplitude (or power received), phase or frequency shift or change in polarization state, DWR quantifies the different characteristics of the precipitating medium within the pulse volume. The amount of received power from the distributed target depends on the number of particles within the pulse volume of the beam, their size, composition, shape, orientation etc.

The DWR's are located at Kolkatat, Chennai, Muchlipattanm and Shri-Harikota (SHAR). The SHAR radar is S-band and Doppler. It is situated as an Island north of Chennai. All are working operationally. DWR's estimates 3 base products namely Reflectivity (Z), Velocity (V) and Spectrum Width (W) as a function of range. From these base products, advanced data products are required to be generated to meet the validation needs.

Ground-based radar and gauge rainfall observations (from IMD, ISRO's AWS etc), at high resolution (hourly), are thus required to be used for validating rain product. High resolution IMD DWR products (hourly 4 Km x 4 Km) is required for evaluation over several small size study sites with hourly (daily when hourly is not available) rain-gauge density, for instance in $1^{\circ} \times 1^{\circ}$ degrees. The size of every validation study site varies from $0.5^{\circ} \times 0.5^{\circ}$ to $2^{\circ} \times 2^{\circ}$ degrees, depending on the density and distribution of available hourly rain-gauge stations over the study site and horizontal rain extents. In case of proper validation of GPI rainfall in particular, which is for a grid size of $1.0^{\circ} \times 1.0^{\circ}$, there should be minimum 3 rain gauges (IMD or AWS) to average out for comparison within a GPI grid size. For IMSRA, an hourly, and daily DWR and rain gauge information would be required on routine basis, preferably in $0.25^{\circ} \times 0.25^{\circ}$ or atleast in $0.5^{\circ} \times 0.5^{\circ}$ grids.

Pre-launch Field Experiments

Pre-launch validation campaign will be launched for existing Kalpana, INSAT-3A based rainfall algorithms as a prelude to INSAT-3D. A three months period will be selected (mainly rainy season) for collecting data from DWRs, all possible and quality assured rain gauges and the algorithm will be tested.

Post-Launch Special Field Experiments

Many of the present ground-truth observations data networks are being augmented for the measurements of precipitation on ground. This includes the plans of IMD to put more DWR in various Indian regions. However, the existing ground based data sources will be utilized for the INSAT-3D Imager derived rainfall estimates. Some more details of the

validation campaigns (timing, location, instrumentation, etc.) will be decided later in mutual consultation with IMD.

4.7 Technical Issues: (Limitation etc.)

The approaches for the retrieval of rainfall from these two techniques are distinctly different with different application areas in mind by NOAA. Thus the validity of these methods in Indian Tropical Regions is an important and still an open issue. For large scale rainfall GPI technique has been found suitable over tropical regions and can be implemented.

However, the inherent limitations of IR / VIS based methods due to their indirect measurements poses challenges for the accuracy of the rainfall products. More importantly GMSRA is the algorithms, which is a large effort from various scientific institutions put together for many years and then integrated at NOAA. To follow them for the algorithm development directly over tropical regions of India needs a lot of R & D, experience and innovations pertaining to the region. It is because, some of the steps like the cloud microphysics (estimation of effective radius of cloud particles, their optical properties etc.) and associated parameters estimation are the important but grey areas of research and can be accomplished fully only with the R&D efforts and experience in the field.

In addition the GMSRA, however, is a highly specific to US regions particularly with very large spatial and temporal coverage's of the background data of Doppler Weather Radars (as a dominant characteristics of the algorithm) along with the satellite data. In case of GMSRA, some of the efforts are highly innovative (optical and cloud microphysics) and as mentioned earlier we have proposed to alternatively apply some advanced elements in our proposed IMSRA algorithm, so that the method is more prone to Indian tropical regions. However, the advanced approach suggested here to use microwave information from most recent satellites like low/polar orbiting TRMM/SSM/I to augment thermal IR rainfall measurements along with VIS and WV channels from Geostationary satellite would also require large R & D efforts.

4.8 Future Scope

Due to the heterogeneity of precipitation over the Earth's surface it is important that corrections be applied time to time to the algorithms depending on region specific processes. Conventional means are restricted primarily to certain land regions, and although satellite measurements are now commonly available, these have limitations too. Frequent observations from visible (VIS) and infrared (IR) sensors are hindered by the fact that estimates of precipitation are indirect and therefore prone to errors caused by cloud-top to surface rainfall variations. More direct measurements of precipitation through the use of passive microwave (PMW) instruments are somewhat restricted due their relative infrequent sampling of precipitation. Thus the algorithms for merging of microwave data with IR images to generate rainfall rates at the spatial and temporal resolutions of the IR sensor is highly desirable. The combined approaches can improve rainfall estimates using the temporal sampling of the VIS/IR data and the more direct nature of the microwave estimates, avoiding the mentioned weaknesses and re-inforce the mutual strengths. At present we have proposed to use Geostationary optical channels and low earth orbiting microwaves for the rainfall estimation by their inter-calibration process and finally validations with the ground truth. In future this approach can be further advanced by optimally integrating optical and microwave

measurements by proper data assimilation schemes which will provide better rainfall than any of the sensors (optical, microwave and ground truth) alone.

4.9 References

1. Adler, R. F., and A. J. Negri, 1988: A satellite infrared technique to estimate tropical convective and stratiform rainfall. *J. Appl. Meteorol.*, **27**, 30-51.
2. Adler, R. F., G. J. Huffman, and P. R. Keehn, 1994: Global tropical rain estimates from microwave-adjusted geosynchronous IR data. *Remote Sens. Rev.*, **11**, 125-152.
3. Arkin, P. A., 1979: The relationship between fractional coverage of high cloud and rainfall accumulations during GATE over the B-scale array. *Mon. Wea. Rev.*, **106**, 1153-1171.
4. Arkin, P. A., and P. Xie, 1994: The Global Precipitation Climatology Project: First algorithm intercomparison project. *Bull. Amer. Meteor. Soc.*, **75**, 401-419.
5. Arking, A., and J. D. Childs, 1985: Retrieval of cloud cover parameters from multispectral satellite images. *J. Climate Appl. Meteorol.*, **24**, 322-333.
6. Ba, M. B., and A. Gruber, 2001: GOES Multispectral Rainfall Algorithm (GMSRA). *J. Appl. Meteorol.*, **40**, 1500-1514.
7. Ba, M. B., D. Rosenfeld, and A. Gruber: 1998: AVHRR multispectral derived cloud parameters: relationship to microwave scattering signature and to cloud-to-ground lightning. *Prepr. 9th Conf. Satellite Meteorology and Oceanography*, AMS, 408-411.
8. Barrett, E. C., and D. W. Martin, 1981: *The Use of Satellite Data in Rainfall Monitoring*. Academic Press, 340 pp.
9. Cheng, M., R. Brown, and C. G. Collier, 1993: Delineation of precipitation areas using METEOSAT infrared and visible data in the region of the United Kingdom. *J. Appl. Meteorol.*, **32**, 884-898.
10. Gilberto A. Vicente, Roderic A. Scofield and W. Paul Menzee, 1998. Bulletin of American Meteorological Society.
11. Espinoza, R. C., Jr., and Harshvardhan, 1996: Parameterization of solar near-infrared radiative properties of cloudy layers. *J. Atmos. Sci.*, **53**, 1559-1568.
12. Ferraro, R. R., and G. F. Marks, 1995: The development of SSM/I rain-rate retrieval algorithms using ground-based radar measurements. *J. Atmos. Oceanic Technol.*, **12**, 755-770.
13. Gairola R.M. and T.N. Krishnamurti, Rain rates based on OLR, SSM/I and rain gauge data sets. *Meteorology and Atmospheric Physics*. **50**, 165-174 (1992).
14. Gruber, A., X. Su, M. Kanamitsu, and J. Schemm, 2000: The comparison of two merged rain gauge-satellite precipitation datasets. *Bull. Am. Meteorol. Soc.*, **81**, 2631-2644.
15. Huffman, G. J., R. F. Adler, M. M. Morrissey, D. T. Bolvin, S. Curtis, R. Joyce, B. McGavock, and J. Susskind, 2001: Global precipitation at one-degree daily resolution from multisatellite observations. *J. Hydrometeorol.*, **2**, 36-50.
16. Inoue, T., and K. Aonashi, 2000: A comparison of cloud and rainfall information from instantaneous Visible and InfraRed Scanner and Precipitation Radar observations over a frontal zone in East Asia during June 1998. *J. Appl. Meteorol.*, **39**, 2292-2301.

17. Inoue, T., 1987a: A cloud type classification with NOAA 7 split-window measurements. *J.Geophys. Res.*, **92 D**, 3991-4000.
18. Inoue, T., 1987b: An instantaneous delineation of convective rainfall area using split window data of NOAA-7 AVHRR. *J. Meteorol. Soc. Japan*, **65**, 469-481.
19. Janowiak, J. E., R. J. Joyce, and Y. Yarosh, 2001: A real-time global half-hourly pixel-resolution infrared dataset and its applications. *Bull. Am. Meteor. Soc.*, **82**, 205-217.
20. Jobard, I., and M. Desbois, 1994: Satellite estimation of the tropical precipitation using the Meteosat and SSM/I data. *Atmos. Res.*, **34**, 285-298.
21. Kidd, C., D. Kniveton, and E. C. Barrett, 1998: The advantages and disadvantages of statistically derived-empirically calibrated passive microwave algorithms for rainfall estimation. *J. Atmos. Sci.*, **55**, 1576-1582.
22. Kidder, S. Q., and T. H. Vonder Haar, 1995: *Satellite Meteorology: An Introduction*. Academic Press, 466 pp.
23. King, M. D., S.-C. Tsay, S. E. Platnick, M. Wang, and K.-N. Liou, 1997: Cloud retrieval algorithms for MODIS: optical thickness, effective particle radius, and thermodynamic phase. *MODIS Algorithm Theoretical Basis Doc.*, ATBD-MOD-05 and MOD-06.
24. Kummerow, C. D., W. Barnes, T. Kozu, J. Shiue, and J. Simpson, 1998: The Tropical Rainfall Measuring Mission (TRMM) sensor package. *J. Atmos. Oceanic Technol.*, **15**, 809-817.
25. Kummerow, C. D., Y. Hong, W. S. Olson, S. Yang, R. F. Adler, J. McCollum, R. Ferraro, G. Petty, D.-B. Shin, and T. T. Wilheit, 2001: The evolution of the Goddard Profiling Algorithm (GPROF) for rainfall estimation from passive microwave sensors. *J. Appl. Meteorol.*, **40**, 1801-1820.
26. Kuligoski R.J., Davenport J.C. and Scofield R.A., The hydro-estimator technique for high resolution geostationary satellite rainfall estimates, Pre-print, 2006.
27. Kuligoski R.J., Scofield R.A., and Gruber A., The NESDIS satellite verification program. Preprint, 11th Conf. on Satellite Meteorology and Oceanography, Madison, WI, Amer. Meteor. Soc., 383-384.
28. Lensky, I. M., and D. Rosenfeld, 1997: Estimation of precipitation area and rain intensity based on the microphysical properties retrieved from NOAA AVHRR data. *J. Appl. Meteorol.*, **36**, 234-242.
29. Levizzani, V., J. Schmetz, H. J. Lutz, J. Kerkmann, P. P. Alberoni, and M. Cervino, 2001: Precipitation estimations from geostationary orbit and prospects for METEOSAT Second Generation. *Meteorol. Appl.*, **8**, 23-41.
30. Nakajima, T., and M. D. King, 1990: Determination of the optical thickness and effective particle radius of clouds from reflected solar radiation measurements. Part I: theory. *J. Atmos. Sci.*, **47**, 1878-1893.
31. Menzel, W. P., and J. F. W. Purdom, 1994: Introducing GOES-I: the first of new generation of Geostationary Operational Environmental Satellites. *Bull. Am. Meteor. Soc.*, **75**, 757-781.
32. Miller, S. W., P. A. Arkin, and R. J. Joyce, 2000: A combined microwave/infrared rain rate algorithm. *Int. J. Remote Sens.*, **22**, 3285-3307.

33. Roca Remi, Voiler, M. Desbois, 2002, A multi satellite analysis of deep convectionand its moist environment over Indian ocean during winter monsoon, *Jour Geophys. Res.*
34. Rosenfeld, D., and G. Gutman, 1994: Retrieving microphysical properties near the tops of potential rain clouds by multispectral analysis of AVHRR data. *Atmos. Res.*, **34**, 259-283.
35. Rosenfeld, D., and I. M. Lensky, 1998: Satellite-based insights into precipitation formation processes in continental and maritime convective clouds. *Bull. Am. Meteor. Soc.*, **79**, 2457-2476.
36. Rosenfeld, D., and A. Gagin, 1989: Factors governing the total rainfall yield of ontinental convective clouds. *J Appl. Meteorol.*, **28**, 1015-1030.
37. Rosenfeld, D., and A. Gagin, 1989: Factors governing the total rainfall yield of continental convective clouds. *J Appl. Meteorol.*, **28**, 1015-1030.
38. Schmetz, J., P. Pili, S. A. Tjemkes, D. Just, J. Kerkmann, S. Rota, and A. Ratier, 2002: An introduction to Meteosat Second Generation (MSG). *Bull. Amer. Meteor. Soc.*, in press.
39. Slingo, A., and H. M. Schrecker, 1982: On the shortwave radiative properties of stratiform water clouds. *Q. J. R. Meteorol. Soc.*, **108**, 407-426.
40. Sheu, R.-S., J. A. Curry, and G. Liu, 1995: Satellite retrieval of tropical precipitation using combined International Satellite Cloud Climatology Project DX and SSM/I data. *J. Geophys. Res.*, **101**, 21 291–21 301.
41. Saunders, R. W., and K. T. Kriebel, 1988: An improved method for detecting clear sky and cloudy radiances from AVHRR data. *Int. J. Remote Sensing*, **9**, 123-150.
42. Tjemkes, S. A., L. van de Berg, and J. Schmetz, J., 1997: Warm water vapour pixels over high clouds as observed by METEOSAT. *Contr. Atmos. Phys.*, **70**, 15-21.
43. Todd MC, C. Kidd, D Kniveton, TJ Bellerby, A combined satellite infrared and passive microwave technique for estimation of small scale rainfall.
44. Turk, F. J., J. Hawkins, E. A. Smith, F. S. Marzano, A. Mugnai, and V. Levizzani, 2000a: Combining SSM/I, TRMM and infrared geostationary satellite data in a near-realtime fashion for rapid precipitation updates: advantages and limitations. *Proc. The 2000 EUMETSAT Meteorological Satellite Data Users' Conference*, 452-459.
45. Vicente, G. A., 1996: Algorithm for rainfall rate estimation using a combination of GOES-8 11.0 and 3.9 micron measurements. *Prepr. 8th Conf. Satellite Meteorology and Oceanography*, AMS, 274-278.
46. Vicente, G. A., R. A. Scofield, and W. P. Menzel, 1998: The operational GOES infrared rainfall estimation technique. *Bull. Am. Meteor. Soc.*, **79**, 1883-1898.

(B) RAINFALL ESTIMATION – H-E Method

4.1 Algorithm Configuration Information

4.1.1 Algorithm Name

Quantitative Precipitation Estimation (QPE) from Hydro-Estimator Method

(Ref: IMD RFP Sec. 11.5)

4.1.2 Algorithm Identifier

3DIMG_L2B_HEM

4.1.3 Algorithm Specification

Version	Date	Prepared by	Description
1.0	14.02.2007	Atul K. Varma R M Gairola	QPE from HE Baseline Document

4.2 Introduction

Rainfall affects the lives and economies of a majority of the Earth's population. Rain systems, such as hurricanes, typhoons, monsoons, and fronts are crucial to sustaining the livelihood of many countries. Excess rainfall can cause flood, property and crop damages. A deficiency causes drought and crop failure. Flood is a disaster that often resulted from intense precipitation in short time. Floods are among the most devastating national hazards in the world, claiming more lives and causing more property damage than any other natural phenomena. Within the USA an average of more than 225 people are killed and more than \$3.5 billion in property is damaged by heavy rain and flooding each year (1993, 1999). These figures are more devastating for India with population over 1 billion. As of today, the floods is one the greatest challenges in weather prediction.

Conventionally rainfall over the ground is measured using rain gauges and radar. Rain gauges offer point measurements and thus they do not represent spatial variability of the precipitation that varies from few meters to several kilometers. The distribution of the rain gauges is far from adequate to present the meaningful variability for the study of various rain-induced events/processes, like flash flood, dam failure, river catchment, etc. On the other hand, radars are better representative of the areal rain, but their coverage is limited due to their high cost. The radar measurements often suffer due to poor calibration of radar reflectivity and also of Z_e-R relationship. Apart from that, ground clutter and anomalous propagation also mars its usability. At the time of severe weather conditions, ground based observation network often failed to work. In view of the limitations of the ground measurements, the most convenient means to measure the precipitation over large area is by using the satellite-based methods. The satellites offer frequent uniform coverage over large area. However, the satellite measurements also suffer from large errors. While Vis./IR methods suffer from their inability to sense hydrometeors (Bhandari and Varma, 1995), microwave measurements suffer due to so called beam filling problem, and uncertainty in the drop-size distribution, drop temperature, fall velocity and shape and orientation of the drops (Varma et al, 2003, 2004 and Varma and Liu, 2006).

In this document, a new most advanced method is described for precipitation measurement. This method called Hydro-Estimator (H-E) method is developed by Robert Kuligowski utilizes the infrared (IR) measurements from a geostationary satellite and is operationally used at NOAA/NESDIS.

4.2.1 Overview and Background

Scofield (1987) described a method for measuring the intense precipitation over a storm. His method called Interactive Flash Flood Analyzer (IFFA) that used half-hourly satellite images to measure the precipitation over the active area of a storm. His method utilized the skill of a trained meteorologist to find out active portion of a storm. His method also utilized the precipitable water (PW) and water vapour (WV) correction to make modifications for dry/wet environment and saturation level adjustments for rain that comes from the warm clouds. This method was very successful for precipitation measurement but was highly subjective and needed continuous interaction of a trained meteorologist to decide the precipitation amount. Due to this reason, it was not very easy to implement it with ease. Successively, an alternate method called Auto-Estimator was developed. The aim of the Auto-Estimator was to provide an automated method without human intervention and that could take care of the subjective nature of the IFFA, but this method failed on many occasions because many features of IFFA were not properly implemented in it. Hydro-Estimator is most recent of the attempts by NESDIS to improve and make IFFA automated. The H-E incorporated many new features that were either not present in IFFA or were defined differently.

Till date there is no published literature on H-E method is available (or known to us). The method/procedure described in this document is based on pre-prints of a paper and personal communication with Dr. Robert Kuligowski who pioneered in developing H-E method at NOAA/NESDIS.

4.2.2 Objectives:

- To develop Hydro-Estimator method for precipitation measurement over Indian region encompassing area between longitudes 30° E -to130° E and latitudes 50° N - 50° S.

4.3 Inputs

4.3.1 Static Data:

Topography data – Etopo – topography/elevation data from NGDC (USA).

4.3.2 Image and preprocessing data (Dynamic)

Parameter	Resolution	Quantization	Accuracy	Source
Radiometric and geometric corrected gray count values of TIR-1 channel (10.7 μm)	Spatial:pixel Temporal: 30 min	10 bit	-	Derived from raw data by DP
Gray value to brightness temperature conversion table	-	-	0.3 K	Derived by DP
Geolocation file	Spatial:pixel Temporal: 30 min	-	1 pixel	Derived by DP

4.3.3 Other Auxillary data and Model Inputs

Parameter	Resolution	Quantization	Accuracy	Source
Eta Model - Equilibrium level in K	Spatial: pixel size Temporal: 3/6 hourly			Provided by IMD
Eta model- observations of wind at 850 hPa and relative humidity (%), and PW (inch)	Spatial: pixel size Temporal: 3/6 hourly			Provided by IMD
Eta model - Profiles of temperature and dew point.	Spatial: pixel size Temporal: 3/6 hourly			Provided by IMD

In RFP, IMD has proposed its own model instead of Eta model. It is assumed that IMD model works as good (or even better) as Eta model in terms of spatial resolution and accuracies.

4.4 Algorithm Functional Specifications

4.4.1 Overview:

4.4.1.1 Theoretical Background

Physical explanation of rainfall estimation from Visible and IR images

The most satellite rainfall monitoring methods seek to:

1. Identify areas of probable precipitation, through recognition of most rain/no-rain boundaries

2. Evaluate associated rainrate
3. Combine (1) and (2) through time where estimates of total accumulated rainfall are required

The objective of present day satellite research is blending of different types of data, from both satellite and non-satellite sources, into the 'best possible' rainfall product.

Rainfall estimation using Visible and IR satellite rainfall algorithm - physical premise

1. In the visible region of the spectrum the basic physical assumption is that cloud brightness is an indicator of cloud thickness, and this in turn is an indicator of rainfall. *Unfortunately these relationships are neither simple nor constant; for example, because by no means all bright clouds precipitate.*
2. In the thermal IR, the basic physical premise is that cloud top temperature is a function of cloud top height, and that higher and colder cloud tops evidence thicker clouds which are more likely to rain. *While this set of relationship is more often true than (1) above, unfortunately not all cold clouds precipitate, nor does rain always come from cold clouds.*

Physical explanation of rainfall with infrared (IR) images

The satellite IR images are composed of measured radiant energy originating in the atmosphere or from the land and water surface below. The intensity of this energy integrated over all wavelength, by Stefan-Boltzmann law, is proportional to fourth power of temperature. The Stefan-Boltzmann law is valid for a perfect black body. If the medium emits spectral radiant energy according to some temperature less than its thermal temperature, than a second factor called emissivity is introduced. The emissivity of a body determines its emission efficiency. Thus, we can define brightness temperature of a body T_b , which is related to its physical temperature is T by following equation:

$$T_b = \varepsilon T$$

where, ε is emissivity of the object. If. $\varepsilon = 1$, $T_b = T$, its a black body; if $\varepsilon = 0$, $T_b = 0$, its a white body; if $0 < \varepsilon < 1$, $T_b < T$, and its a gray body.

The IR, for rainfall estimation, refers to thermal IR band that is 10.0 - 12.5 μm . This is a atmospheric window, and all earthly objects radiate maximum spectral power in this band. In this band the absorption is strong for clouds and land/water surfaces and slight for gaseous constituents of the atmosphere. For surfaces, which are opaque and do not transmit radiation, measured intensity is closely approximated by the fourth power of the temperature. For those surfaces, which are not opaque - such as some clouds - measured intensity is approximated by effective emissivity times fourth power of the temperature. This effective emissivity will be referred more often as cloud emissivity here after. The cloud emissivity cannot be measured from observations at a single wavelength interval. Often it is simply assumed to be unity. Then the temperature calculated from observed intensity of radiation is called 'brightness temperature'. Only when $\varepsilon = 1$, brightness temperature equals to black body temperature.

The value of IR measurements to rainfall estimate lies in the nearly universal condition of lapse of temperature with height through the troposphere. If the temperature is known with height, either from actual sounding or from climatology, the height of the cloud can be inferred from the satellite IR observations. Ordinarily, gray clouds are not useful in this

context, because $\varepsilon < 1$ implies clouds which are thin (and therefore without precipitation). The more serious problem is distinguishing between cold clouds that are radiometrely thick but are confined to the upper and middle troposphere, and cold clouds that extend into lower troposphere.

Physical explanation of rainfall with visible (vis) images

In middle and late fifties and earlier sixties, various researches concluded that with thicker clouds the probability of rainfall and rain intensity is increased. This relationship is strongest for clouds warmer than -15° C . It is also noted that marine clouds produce heavier rainfall. The possible explanation for this lies in the process of cloud growth and droplet growth rates. In clouds warmer than -15° C , precipitation results from coalescence. The large cloud thickness allows more time for growth before droplets fall out of the cloud. However, the other factors like droplet concentration, evaporation and cloud temperature are also important. Difference in precipitation probability between marine and continental clouds were attributed to difference in concentration of condensation nuclei and of droplets, and difference in evaporation below the cloud base. Very high droplet concentrations ($> 400 \text{ cm}^{-3}$) inhibit coalescence and formation of rain. The evaporation of raindrops is proportional to saturation vapor deficit and fall period. Both droplet concentration and subcloud moisture and thickness are more variable over land than over water. Temperature governs various processes. At temperature $\leq -10^{\circ}\text{ C}$ growth of hydrometeors is dominated by sublimation and collisions involving ice particles; that is, by Wegener-Bergeron rather than coalescence processes. Less important factors influencing precipitation are condensation nuclei, updraft speed, and electrification. Thus cloud thickness, though important, is one of the several factors determining production of rain in the clouds.

Various researchers have tried to relate cloud thickness with satellite observed brightness. The contradictory claims are made. Some of them have found high correlation between two, while others could not notice so encouraging results with their studies. It is concluded that cloud brightness alone cannot always imply cloud thickness. In more than one instance, Erickson and Hubert (1961) found in their study that large thunderstorms having vertical depths of the order of 30000 feet appeared no brighter, than a rather dense overcast of much smaller vertical extent.

The understanding of the factors governing cloud brightness is complicated as it is a problem of optics that again requires an excursion into the theory of electromagnetic radiation.

The light scattering from water clouds can be described as a problem of effect of light scattering by particles of size comparable or slightly more than the wavelength of the incident light. For water clouds, the particles (or droplets) may vary in size (the number of particles as a function of their size), and the cloud geometry is variable (the arrangement of particles in relation to the incident beam of solar radiation). This problem is generally treated in two parts: single scattering and multiple scattering.

The single scattering theory describes the fate of incident light in a very small part of a natural cloud. The aggregate effect on the incident beam of all parts of a cloud is treated through the theory of multiple scattering. Here, the dimensions of the cloud and its orientation with respect to a given incident beam become important.

Twomey et al. (1967) calculated reflectance as a function of geometric thickness for a cloud drop distribution of 6 μm average radius and 1 μm standard deviation. Liquid water content was 0.2 and 0.4 gm^{-3} , and two solar zenith angles were considered. They found that reflectance increases rapidly in hyperbolic fashion for both values of liquid water content, implying little additional increase above the thickness of 0.7 km. The effect of absorption was to increase the rate of hyperbolic convergence. Changing solar zenith angle had little effect (though at large zenith angles reflectance would approach unity), and the effects on reflectance of changing drop size distribution radius and variance were small for optical thickness, $\tau > 100$.

The radiance (brightness) from the striated cloud is larger than plan parallel radiance in antisolar direction with inclined illumination (Wending, 1977). Wending tested two drop size distributions, one peaking at $r \sim 5 \mu\text{m}$ and other at $5 \sim 2 \mu\text{m}$, both appropriate to stratus clouds. The difference in albedo and radiance at small zenith angles were comparable to differences resulting from geometry of the cloud top; however, these also decreased with increasing optical thickness. Therefore, at optical thickness typical of precipitating clouds, texture and drop size distribution may be of secondary importance in explaining cloud brightness. McKee and Klehr (1978) with their RT (radiative transfer) model found that cloud geometry is far more important factor than drop size distribution.

A composite picture emerging out of various studies in the past has proved the main factors governing cloud brightness are:

- thickness
- the area to volume ratio
- orientation of solar beam

These factors collectively called geometry, determine optical path within the cloud. Drop size distribution and liquid water content are secondary in importance. Background albedo may be significant over land areas. Interactions apparently are important when clouds are close together. The phase is not appears to be an important variable.

The proposed method is the H-E method as developed at NOAA/NESDIS. The details of this method are described in the next section.

Retrieval Algorithm Method

The H-E method described in this section is based on pre-prints of a paper by Kuligowski et al. (2003). This paper is received from the author through personal communication.

The H-E method offers improvement over A-E method for precipitation estimation. In A-E method, the relationship between 10.7 μm brightness temperature ($\text{Tb}_{10.7}$) and rain rate (mm h^{-1}) (R) is defined as:

$$R = a \exp(-b \text{Tb}_{10.7}^{12}), \quad \dots(1)$$

where, a and b are regression coefficients having values $a = 1.1183 \times 10^{11}$; $b = 0.036382$ (Vicente et al. 1995). The A-E method provides same relationship for convective and non-convective precipitation. The above equation provides first guess of the precipitation value.

In H-E method, convective and non-convective cores are identified and different R-Tb relationships are provided for them. This allows higher precipitation rates for the convective cores. For convective core, an equation similar to (1) is used, however the coefficients a and b are varied as per precipitable water (PW) provided by Eta model. This allows higher precipitation value for wetter atmosphere. The above (1) is constrained such a way that it yields a value of 0.5 mm h^{-1} of rain rate at 240 K, and a precipitable water (from Eta model) dependent value at 210 K of $\text{Tb}_{10.7}$. In H-E method, the maximum possible rain value at any pixel is limited depending upon availability of PW. This allows the maximum precipitation to become a function of available moisture. The maximum possible rain value in mm h^{-1} is given as 40 times the precipitable water in inches.

If a pixel is assigned maximum rain but there exist a colder pixel in its vicinity. In principle, the rain rate at the colder nearby pixel would be higher. Thus the rain rate curves are recomputed based on rain rate of 0.5 mm/h at 240 K and of the theoretical maximum value at the lowest temperature in the vicinity.

For a non-convective core, the relationship between $\text{Tb}_{10.7}$ and R_s is given as:

$$R_s = (250 - \text{Tb}_{10.7}) * (R_{\max}/5) \quad \dots \dots \dots (2)$$

R_{\max} is again a function of PW. The relationship between R_{\max} and PW is not known in this case and needs to be determined. R_s is not allowed to exceed - corresponding convective rain rate (R_c) or 12 mm h^{-1} , whichever is lower.

The relationship between Eta model derived PW and R (in mm h^{-1}) at 210 K is shown in figure 1(a). The figures 1 (b) and 1(c) shows the relationship between R and $\text{Tb}_{10.7}$ at different PW values for convective and non-convective cores, respectively. These figures are taken from the pre-prints of Kuligowski et al. (2003).

In H-E method, the precipitation at a pixel is allowed to be combination of both convective and non-convective core. This is worked out by considering a pixel box of 101X101 pixels surrounding the pixel of interest. The minimum, mean and standard deviation of $\text{Tb}_{10.7}$ (T_{\min}), in this pixel box is determined. This T_{\min} is used to find the radius of actual region of interest. Within this radius of interest, the mean (T_{mean}) and standard deviation (σ) of $\text{Tb}_{m10.7}$ is determined. The active/inactive and also core/non-core fraction of the pixel is determined through the parameter Z, which is defined as:

$$Z = (T_{\text{mean}} - \text{Tb}_{10.7}) / \sigma \quad \dots \dots \dots (3)$$

The maximum allowable value of Z is 1.5.

If $Z < 0$; $R = 0$, i.e., pixel either cirrus or inactive convective

$$\text{Otherwise, } RR = [R_c * Z^2 + R_n * (1.5 - Z)^2] / [Z^2 + (1.5 - Z)^2] \quad \dots \dots \dots (3)$$

R_c is the rain from the convective core given by (1) with coefficients determined by PW from Eta model. R_n is rain from non-convective core given by (2). If $Z=1.5$, the pixel rain rate RR reduces to convective type only (given by (1)). On the other hand, if $Z=0$, the pixel rain rate RR is determined by purely non-convective rain (given by (2)).

In fact, the convective systems generally have multiple brightness temperature minima, and hence a single radius is inappropriate for differentiating local from global minima. Thus, this same computation of rain rate is performed for a smaller (15-pixel) radius, and the final rain rate is the square root of the product of the two rates. The exception to this is if the rain rate computed from the smaller radius is zero, in which case it is not considered in the final rain rate calculation.

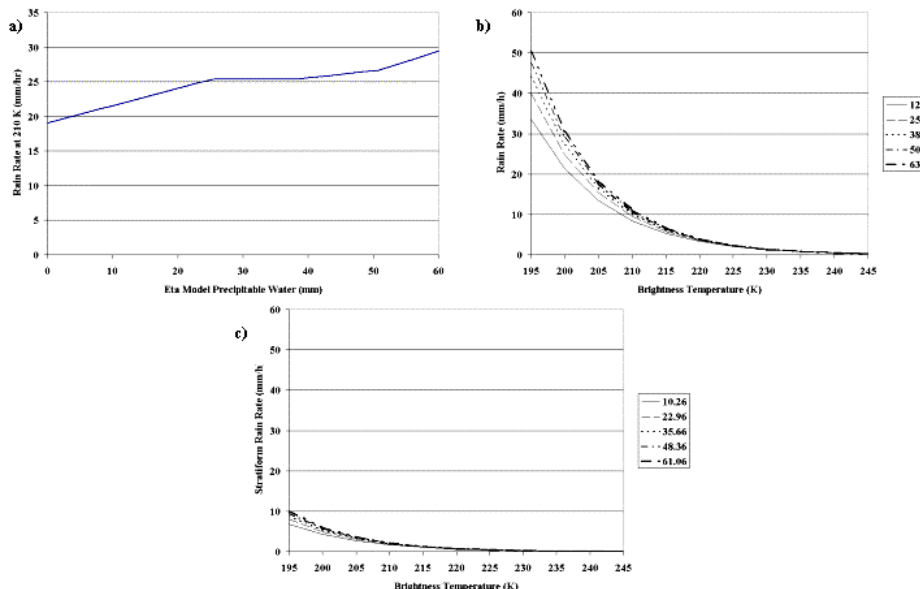


Figure 1. Adjustment functions used in the Hydro-Estimator: (a) rainfall rate at 210 K (mm/h) as a function of Eta model precipitable water (mm) that is used to produce the brightness temperature-rainfall rate relationship; (b) the brightness temperature-rainfall rate relationship for various values of precipitable water (mm) for "convective core" precipitation; and (c) the corresponding relationship for "non-core" precipitation. The legend in (b) and (c) indicates the value of precipitable water corresponding to each curve.

(This figure is taken from the pre-prints of Kuligowski et al. (2003))

The (3) above provides the first guess precipitation amounts. The precipitation thus estimated is further modified to account for the wetness/dryness of the atmosphere and also for the precipitation that comes from the warm clouds. The several steps involved for such modifications are as follows:

(a) Correction for Wet/dry Environment

A small correction in the brightness temperature ($T_{b10.7}$) values is carried out to account for wetness of the environment. This adjustment is needed to account for evaporation of the precipitation in the dryer environment below the cloud. A higher or lower value of the brightness temperature at $10.7\mu\text{m}$ is set for dry or wetter environment. This is carried out in two steps. In the first step, brightness temperature is adjusted based on the PW value to compute rain rate from (3). This is shown in Fig. 2 (a), where brightness temperature correction is additive or subtractive depends upon value of PW. In the second step, first, the

RH itself from the Eta model is adjusted to account for the falling rain, and then depending upon RH value, a subtraction from the rain amount given by (3) is made. Fig. 2(b) shows the correction of RH as a function of rain. Fig. 2(c) shows the correction rain amount as a function of corrected RH.

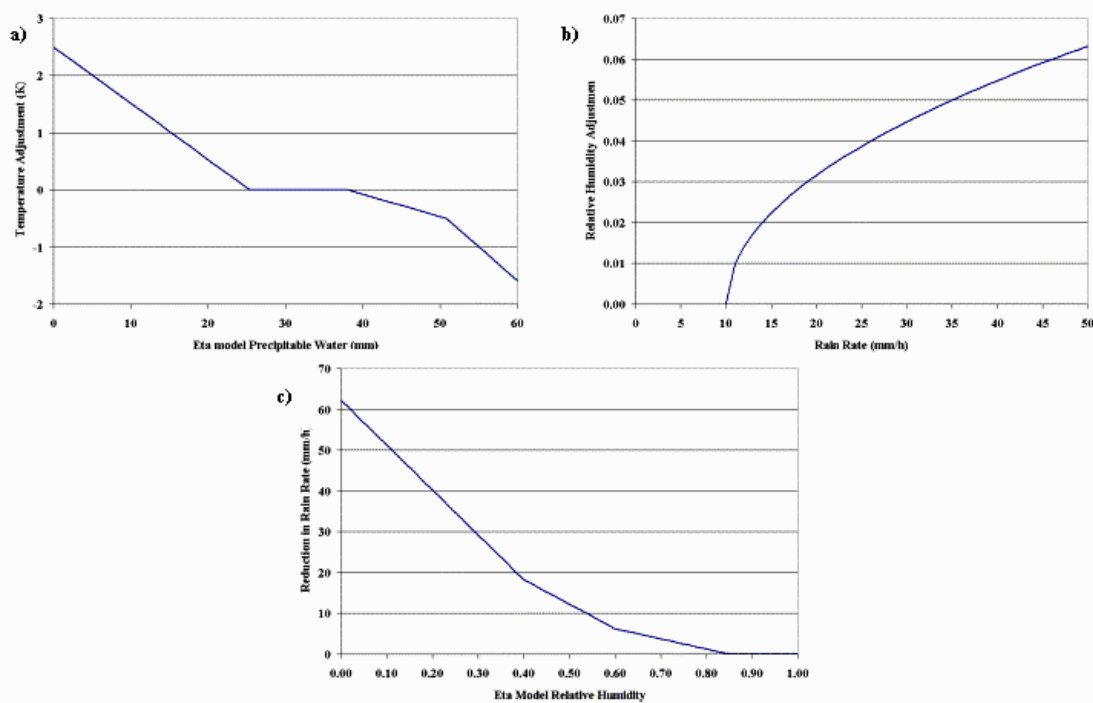


Figure 2. Additional HE adjustment functions: (a) brightness temperature adjustment (K) as a function of Eta model precipitable water (mm); (b) augmentation of Eta relative humidity as a function of HE rainfall rate (mm/h); and (c) reduction in HE rainfall rate (mm/h) as a function of adjusted Eta model relative humidity.

(This figure is taken from the pre-prints of Kuligowski et al. (2003))

(b) Warm-top modification

The equilibrium level is computed by following a parcel along a saturation adiabat upward (from lifting condensation level) to where the parcel temperature becomes equal to the environmental temperature. Strength of the convection is determined by comparing the temperatures of the convective tops with that of equilibrium level. This level comes before tropopause for the warm rain.

In H-E method, Eta model temperature and dewpoint profiles are used to determine equilibrium temperature of a particulate pixel. This correction is applied to pixels that are warmer than the equilibrium level temperature.

- If the $(T_{eq} - T_{min}) < 10$ K, then T_{min} in the pixel-area is used instead of $Tb_{10.7}$ of the pixel for warm top correction. The modification is as follows:

- $T_{b10.7} - [(213-T_{eq}) * 0.9]$ or 25 K (whichever less)
- If the $(T_{eq} - T_{min}) > 10$ K, the modification is as follows
 $T_{b10.7} - [(213-T_{eq}) * 0.6]$ or 15 K (whichever less)

(c) Orography and Parallax correction

Orography adjustment is carried out using 850 –hPa Winds and topography from a digital elevation model at 4 km resolution to derive vertical component of wind (Vicente et al., 2002). This vertical wind component is then scaled into a multiplicative adjustment to the rain rate.

The parallax correction described in the same paper, adjusts the horizontal location of the satellite pixel prior to rain rate computation, based on cloud height (using T_b and standard atmosphere) and satellite zenith angle.

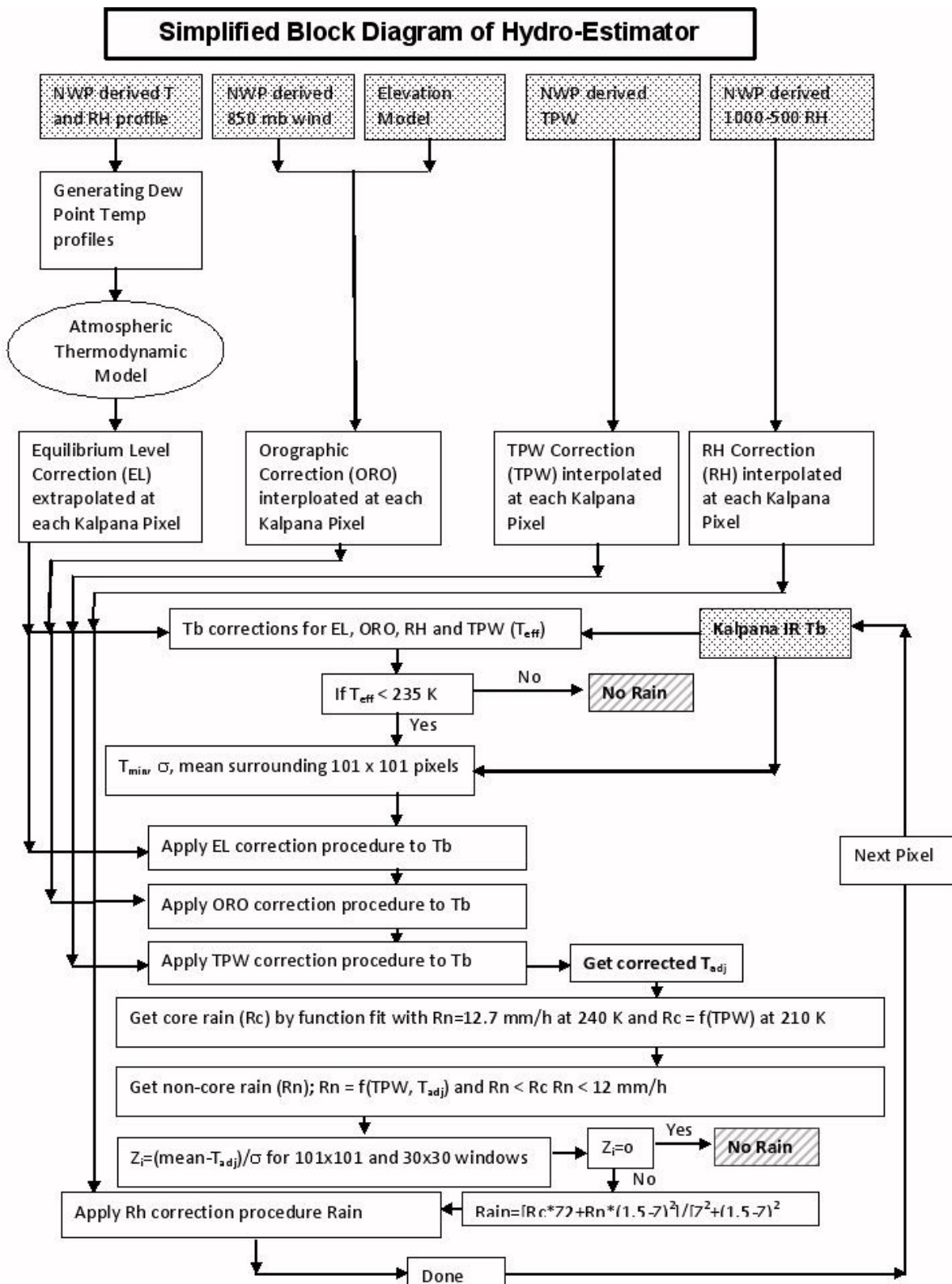
Satellite Zenith angle correction is carried out to take into accounts the increased path length at higher angles. A technique developed by Joyce et al. (2001) is used.

Derived Products

Precipitation rain rate at 30 minute duration.

Integrated daily, weekly and monthly precipitation amounts.

4.4.1.2 Flow Chart



4.5 Outputs

Parameter	Unit	Min.	Max.	Accuracy	Resolution
Precipitation amount	mm/h	>0	>100	Section 4.6 on validation	Horizontal: pixel scale Temporal: half-hourly.

4.5.1 format of the output and the domain:

lat , lon, precipitation
 Domain :50 S to 50 N, 30 E to 130 E

4.6 Validation

4.6.1 Validation of weekly Met-subdivision rain:

We have computed the H-E rain from modified algorithm for 10 week period from 3 July to 10 September 2014. The rain values are averaged in met-subdivisions on weekly basis and compared with rain values provided by IMD in Weakly Weather Report (WWR). A scatter plot of comparison is shown in Fig. 3 below.

The Fig. 3 provides statistics of comparison for all the 10 weeks of comparison, the week-by-week comparison statistics is provided in Table 1.6.1 below.

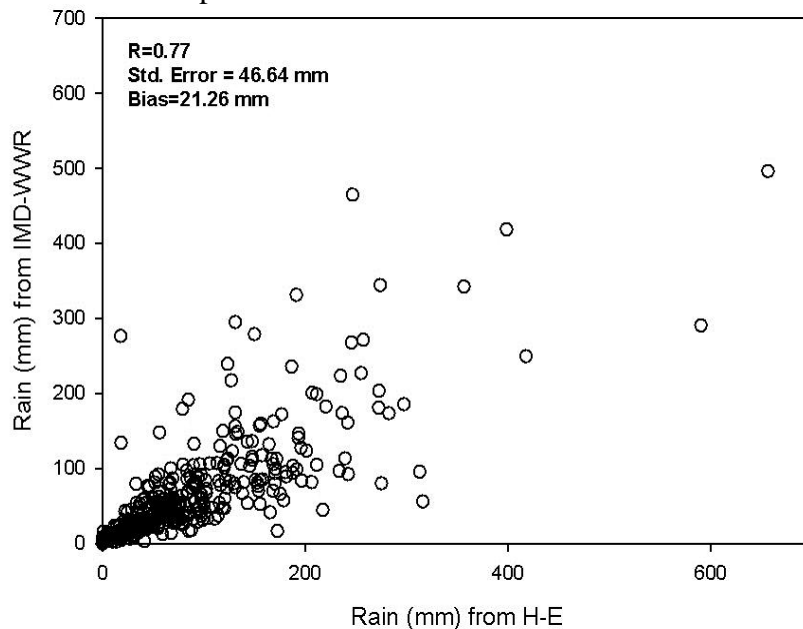


Fig. 3: Comparison of weekly meteorological subdivision averaged rain from H-E and IMD WWR for 10 weeks from 3 July to 10 September 2014.

Table 1.6.1: Week-by-Week comparison statistics of weekly meteorological subdivision averaged H-E rain with IMD WWR.

Week ending on	HE Vs IMD WWR		
	R	Err	Bias
9 July 2014	0.80	40.93	20.29
16 July 2014	0.74	86.62	47.98
23 July 2014	0.64	92.46	43.11
30 July 2014	0.87	36.44	15.29
06 Augt 2014	0.89	60.09	27.02
13 Augt 2014	0.74	37.03	-2.88
20 Augt 2014	0.81	49.74	18.37
27 Augt 2014	0.81	47.38	24.96
03 Sept 2014	0.72	58.64	19.92
10 sep 2014	0.90	25.70	-1.44
All 10 weeks	0.78	46.64	21.26

The statistics provided in Table 1.6.1 should be seen in the light of simliar comparisons carried out between 3B42 V7 and WWR and 3B42 V7 and H-E and statistics provided in Table 1.6.2.

Table 1.6.2: Week-by-Week comparison statistics of weekly meteorological subdivision averaged 3B42 V7 rain with IMD WWR and H-E rain.

Week ending on	3B42 vs WWR			3B42 Vs HE		
	R	Err	Bias	R	Err	Bias
9 July 2014	0.53	57.24	0.32	0.49	70.94	-19.59
16 July 2014	0.91	58.67	-18.63	0.91	81.48	-45.65
23 July 2014	0.82	23.98	1.94	0.86	40.23	-18.35
30 July 2014	0.61	45.63	-4.66	0.48	44.90	-3.22
06 Augt 2014	0.52	50.53	-17.23	0.63	38.00	-14.34
13 Augt 2014	0.92	49.09	1.66	0.86	68.90	-46.32
20 Augt 2014	0.82	30.17	-7.46	0.87	53.34	-25.83
27 Augt 2014	0.82	43.01	-5.20	0.61	97.40	-48.31
03 Sept 2014	0.77	51.67	22.68	0.92	29.32	-2.28
10 sep 2014	0.93	24.83	-8.11	0.88	39.21	-23.40
All 10 weeks	0.78	45.15	-3.47	0.76	60.19	-24.73

If we compare Table 1.6.1 and 1.6.2, we may conclude that overall (with all 10 weeks of dataset) correlation of WWR with H-E is same as that with TRMM 3B42 V7. The rms difference of WWR with H-E is also very close to that with TRMM 3B42 V7. Despite of these similarities, there is remarkable difference between these 2 comparisons, that is, the correlation between H-E and WWR varies from moderate a range of 0.64 to 0.90, whereas that between TRMM 3B42 V7 and WWR varies from low value of 0.52 to high value of 0.93. Thus statistics between H-E and WWR is more stable compared to that between TRMM

3B42 V7 and WWR. The comparison between TRMM 3B42 V7 and H-E is also attempted and is shown in the Table 1.6.2.

4.6.2 Validation of daily 0.25°x0.25° gridded rain

The comparisons in section 4.6.1 are carried out in weekly meteorological sub-division scales. The rain is known to have variability from few meters to continental scales and from few seconds to any time scale. In shorter measuring scales, it behaves as quasi-random stochastic process. Therefore, rain comparisons in shorter time scales and from observations in different spatial scales lead to large errors (Piyush et al., 2012). Nevertheless, we have compared daily 0.25°x0.25° averaged rain from modified H-E method with gridded dataset from IMD. The comparisons of H-E and 3B42 V7 are carried out with IMD gridded dataset for each of the met subdivisions as provided in Table 1.6.3 to table 1.6.4.

Table 1.6.3: Comparison statistics of 0.25°x0.25° daily gridded rain from H-E and IMD in each met subdivisions.

Met Sub Division	R	rmse	bias	Met Sub Division	R	rmse	bias
Arunachal Pradesh	0.26	43.63	-5.87	East MP	0.45	30.11	-7.24
Assam & Megha.	0.52	46.41	-3.34	Guj, DNH & Dam.	0.42	19.02	1.66
NMMT	0.17	28.77	-6.89	Saur., Katch & Diu	0.39	13.54	0.43
SHWB	0.22	38.85	0.84	Konkan & Goa	0.44	43.31	8.26
Gangetic WB	0.41	23.45	-4.51	Madhya Maha	0.39	34.42	-7.83
Orissa	0.51	31.85	-5.05	Marathwada	0.46	27.38	-6.36
Jharkhand	0.57	26.48	-8.14	Vidarbh	0.57	23.43	-3.93
Bihar	0.63	18.70	-2.30	Chattisgarh	0.61	26.18	-5.55
East UP	0.56	20.82	-4.61	Coastal AP	0.32	25.28	-4.64
West UP	0.45	16.03	-2.86	Telengana	0.40	18.04	-2.77
Utrakhand	0.36	34.28	-3.33	Rayalaseema	0.51	9.15	-1.17
HR., Chd. & Delhi	0.39	10.43	-1.25	TN & Pondicherry	0.34	12.65	-2.46
Punjab	0.45	9.16	0.21	Coastal Karnataka	0.51	47.31	-3.04
HP	0.30	31.83	-2.97	N.I. Karnataka	0.42	16.94	-2.38
J & K	0.34	15.06	-1.28	S.I. Karanataka	0.54	21.76	-5.62
West Raj	0.54	11.78	-1.98	Kerala	0.47	28.09	-1.00
East Raj	0.54	19.79	-2.93	All regions	0.47	25.40	-3.24
West MP	0.42	25.20	-3.71				

Table 1.6.4: Comparison statistics of 0.25°x0.25° daily gridded rain from TRMM-3B42 V7 and IMD in each met subdivisions.

:

Met Sub Division	R	rmse	bias	Met Sub Division	R	rmse	bias
Arunachal Pradesh	0.42	24.04	3.37	East MP	0.60	14.67	0.33
Assam & Megha.	0.56	28.02	0.31	Guj, DNH & Dam.	0.61	20.14	-0.77
NMMT	0.26	15.75	-2.33	Saur., Katch & Diu	0.57	16.03	-1.09
SHWB	0.39	24.06	3.57	Konkan & Goa	0.55	38.99	9.71

Gangetic WB	0.43	14.67	-0.41	Madhya Maha	0.51	21.11	-2.51
Orissa	0.62	22.52	-0.15	Marathwada	0.58	14.10	-3.22
Jharkhand	0.51	15.63	-0.13	Vidarbh	0.74	14.98	-1.45
Bihar	0.60	15.53	0.54	Chattisgarh	0.62	18.73	0.96
East UP	0.51	17.44	-2.31	Coastal AP	0.50	11.79	-1.14
West UP	0.57	12.07	-1.90	Telengana	0.55	11.42	-0.51
Utrakhand	0.57	16.72	1.67	Rayalaseema	0.62	7.50	-0.87
HR., Chd. & Delhi	0.53	7.88	-0.75	TN & Pondicherry	0.53	8.97	-1.33
Punjab	0.38	10.26	-0.45	Coastal Karnataka	0.60	36.46	10.83
HP	0.50	12.93	1.47	N.I. Karnataka	0.51	13.19	-0.91
J & K	0.43	6.06	0.04	S.I. Karnataka	0.58	14.61	-0.35
West Raj	0.58	7.67	-0.05	Kerala	0.55	23.91	4.18
East Raj	0.64	14.66	-0.16	All regions	0.53	19.30	1.65
West MP	0.60	16.34	-0.07				

A comparison of rain from modified H-E and TRMM-3B42 V7 in $0.25^{\circ}\text{x}0.25^{\circ}$ degree in each met subdivision is shown in Table 1.6.5, which shows significantly higher correlations and smaller rmse for most of the regions. This is mainly due to spatially averaged measurement of rain from H-E and TRMM TRMM-3B42 V7. The Table 1.6.5 also shows the performance of modified H-E with respect to TRMM 3B42 V7 over oceans. It may be noted here that neither IMD WWR nor gridded dataset provides measurements over oceans. So the comparison with TRMM 3B42 V7 is the only source for accessing the quality of H-E rain over oceans. It may be noted from Table 12 that daily $0.25^{\circ}\text{x}0.25^{\circ}$ gridded rain from H-E and 3B42 V7 has a good agreement over oceans with correlation of 0.65 and rmse of 15.88 mm/day. If all area including land and oceans including and surrounding India are taken into consideration, the correlation and rmse between H-E and TRMM-3B42 V7 is 0.59 and rmsd of 22.44 mm/day.

Table 1.6.5: Comparison statistics of $0.25^{\circ}\text{x}0.25^{\circ}$ daily gridded rain from H-E and TRMM 3B42 V7 in each met subdivisions.

Met Sub Division	R	rmse	bias	Met Sub Division	R	rmse	bias
Arunachal Pradesh	0.51	37.82	9.11	Guj, DNH & Dam.	0.58	20.43	-2.42
Assam & Megha.	0.61	40.53	3.55	Saur., Katch & Diu	0.66	14.67	-2.04
NMMT	0.39	25.09	4.31	Konkan & Goa	0.67	34.83	0.68
SHWB	0.37	34.26	2.61	Madhya Maha	0.71	26.84	5.59
Gangetic WB	0.57	20.69	3.89	Marathwada	0.71	21.00	3.29
Orissa	0.57	30.05	4.69	Vidarbh	0.73	19.33	3.05
Jharkhand	0.62	25.59	7.93	Chattisgarh	0.66	24.44	6.25
Bihar	0.68	16.77	2.75	Coastal AP	0.53	22.76	3.33
East UP	0.73	16.74	2.22	Telengana	0.55	15.78	2.24
West UP	0.59	14.08	0.91	Rayalaseema	0.60	8.27	0.32
Utrakhand	0.50	31.89	4.83	TN & Pondicherry	0.48	11.47	1.15

HR., Chd. & Delhi	0.45	10.53	0.17	Coastal Karnataka	0.49	49.59	13.70
Punjab	0.47	8.46	-0.63	N.I. Karnataka	0.51	16.72	1.75
HP	0.50	26.72	4.22	S.I. Karanataka	0.46	24.12	5.35
J & K	0.34	14.14	1.28	Kerala	0.51	27.64	4.40
West Raj	0.65	10.51	1.97	Oceans	0.65	15.88	-1.09
East Raj	0.67	16.71	2.87	Land outside India	0.33	46.52	10.53
West MP	0.60	21.62	4.18	All regions	0.59	22.44	3.28
East MP	0.62	28.30	8.01				

The validation results provided here indicate reasonably good agreement of INSAT-3D H-E rain with surface observations. The changes that are carried out in the modified algorithm are able to successfully represent the orographic rain which otherwise was not found to suffer from huge errors. The rain is highly variable parameter over space and time and its validation in smaller scales always resulting large huge errors (Piyush et al., 2012). The results presented above should be viewed with respect to validation comparison results of the global standard rain products by other researchers. For example, in a recent study by Tan et al. (2015) in which they evaluated six high resolution precipitation products including TRMM-3B42 V7 over the Malaysia. They reported that among 5 satellite based rain products, the 3B42 V7 and is the best performing with respect to surface observations, which on daily scale provides a correlation of 0.39 and rmse of 18.35 mm/day. While the India has much more diverse surface and climatic conditions with different cloud types and wide range of precipitation rates during S-W months, we achieve much higher correlation between modified H-E rain with surface observations. A more important aspect of the rain from H-E vis-à-vis TRMM 3B42 V7 is timely availability of H-E product from IMD and MOSDAC sites. The TRMM 3B42 V7 is available after latency of about 4 months, whereas INSAT-3D H-E is available within 15 minutes of data acquisition, which makes H-E very important for operational users, especially those working with rain related natural disasters, nowcasting and numerical weather predictions.

4.7 Future Scope

The scheme has to be regularly calibrated with more varied calibration data. Further merging of H-E with microwave observations is desired for more accurate rain measurement.

4.9 References

1. Barrett, E. c., and D. W. Martin, 1981: The use of satellite data in rainfall monitoring. Academic Press, New York, 340 pp.
2. Bhandari, S.M and A.K. Varma, On Estimation of Large Scale Monthly Rainfall Estimation Over the Indian Region Using Minimal INSAT-VHRR Data, *International Journal of Remote Sensing*, **16**, 2023-2030, 1995.
3. Erickson, C.O., and Hubert, L.F., 1961, Identification of cloud forms from TIROS-1 pictures, Meteorological Sat. Lab. Rep. No. 7, US Weather Bureau, p 68.

4. Joyce, R., J. Janowiak, and G. Huffman, 2001: Latitudinally and seasonally dependent zenith-angle corrections for geostationary satellite IR brightness temperatures. *J. Appl. Meteor.*, **40**, 689-703.
5. Kuligowski, R.J., Davenport, J.C., and Scofield, R.A., 2003, The Hydro-Estimator Technique for High-Resolution Geostationary Satellite Rainfall Estimates, pre-prints. Received through personal communication.
6. McKee, T.B., and Klehr, J.S., 1978, Effect of cloud shape on scattered solar radiation, *Mon. Wea. Rev.*, **106**, 399-404.
7. Piyush, D N, A K Varma, P K Pal and G Liu, 2012, An Analysis of Rainfall Measurements over Different Spatio-Temporal Scales and Potential Implications for Uncertainty in Satellite Data Validation, *Journal of Meteorological Society of Japan*, 90 (4), DOI: 10.2151/JMSJ.2012-408.
8. Scofield, R.A., 1987: The NESDIS operational convective precipitation estimation technique, *Monthly Weather Review*, **115** (8), 1773 - 1792.
9. Tan, M.L., A. L. Ibrahim, Z. Duan, A. P. Cracknell, V. Chaplot, 2015, Evaluation of Six-High Resolution Satellite and Ground Based Precipitation Products over Malaysia, *Remote Sensing*, **7**, 1504-1528.
10. Twomey, S., Jacobowitz, H., and Howell, H.B., 1967, Light scattering by cloud layers, *J. Atmos. Sci.*, **24**, 70-79.
11. Varma, A. K., and Liu, G, 2006, Small-Scale Horizontal Rainrate Variability by Satellite, *Monthly Weather Review*, **134** (10), 2722-2733.
12. Varma, A. K., Liu, G, and Noh, Y.J., 2004, Sub-Pixel Scale Variability of Rainfall and Its Application to Mitigate the Beam-Filling Problem, *Journal of Geophysical Research*, **109**, D18210, doi:10.1029/2004JD004968.
13. Varma, A.K., Pokhrel, S., Gairola, R.M., and Agarwal, V.K., 2003, An Empirical Algorithm for Cloud Liquid Water From MSMR and Its Utilization in Rain Identification, *IEEE Transactions on Geosciences and Remote Sensing*, **41** (8), 1853-1858.
14. Vicente, G. A., J. C. Davenport, and R. A. Scofield, 2002: The role of orographic and parallaxcorrections on real time high resolution satellite rainfall estimation. *Int. J. Remote Sens.*, **23**, 221-230.
15. Wending, P., 1977, Albedo and reflected radiance of horizontally inhomogenous clouds, *J. of Atmos. Sci.*, **34**, 642-650.

5. Sea Surface Temperature

S.No.	Product Name	Spatial Resolution	Temporal Resolution
1	3DIMG_L2B_SST	4 km	30 minutes
2	3DIMG_L2B_SST_DLY	4 km	Daily (00 H to 23:30 H)

5. Sea Surface Temperature

5.1 Algorithm Configuration Information

5.1.1 Algorithm Name

Sea surface temperature (SST)
 (Ref: IMD RFP Sec. 11.7)

5.1.2 Algorithm Identifier

3DIMG_L2B_SST
 3DIMG_L2B_SST_DLY

5.1.3 Algorithm Specification

Version	Date	Modified by	Description
1.0	14.02.2007	A K Mathur, N. Agarwal	SST Baseline Document
1.1	09.07.2014	A K Mathur, Rishi Gangwar	Modified after ATBD review

5.2 Introduction

ISRO is launching INSAT-3D geostationary satellite in 2007/8. The inheritance of this satellite has come from GOES series of NOAA. Meteorological payloads onboard would be a 6 channel imager and a 19 channel sounder mainly for cyclone and monsoon monitoring, cloud motion vectors winds, rainfall estimation, floods/intense precipitation monitoring, snow cover detection, mesoscale studies etc. 19 channel Sounder, split thermal window channels, a mid IR thermal window channel and shortwave IR channel are the additions to earlier INSAT-3A/Kalpana satellites. Details of Imager channels are given in Table-1.

Sea surface temperature would be derived from split thermal window channels (10.2–11.3 μm , 11.5–12.5 μm) during daytime and using additional mid IR window channel (3.7–4.1 μm) during nighttime over cloud free oceanic regions. The most important part of the SST retrieval from IR observations is the atmospheric correction. Specially over tropics, this atmospheric correction is dominated by the high variability in vertical distribution of the intervening atmospheric water vapor. This correction will be determined through suitable characterization of tropical atmospheres in radiative transfer model to simulate the brightness temperatures of INSAT-3D channels and then generating the regression coefficients for SST retrieval. Details of the algorithm have been given in section 1.4.1.1.

5.2.1 Overview and background

This algorithm basis theoretical document (ATBD) describes our current working models of the algorithms for the retrieval of sea surface temperature from INSAT-3D imager channels data. While effort has been made to make this document as complete as

possible, it should be recognized that algorithm development is an evolving process. This document (V1.0) is a description of the prototype algorithm for INSAT-3D sea surface temperature estimation as it currently exists, and is being delivered for inclusion in the INSAT-3D processing scheme.

Current research on the physics of the atmospheric transmission in the infrared, the processes at the ocean surface, and new information about the performance of the satellite will lead to periodic revisions of the algorithms. Also, the document may appear incomplete in places as research continues to improve our understanding of the processes at work. Subsequent revisions of the document will reflect new knowledge and, it is hoped, fill the gaps in what is reported here.

5.2.2 Objective

Development of complete application software package for derivation of SST using multi channel Imager data from INSAT-3D.

5.3 Inputs

5.3.1 Static Data

Parameter	Resolution	Accuracy	Source
Land /Sea Mask	Pixel (~4 km)	1 pixel	USGS(available)

5.3.2 Image and preprocessing data (Dynamic)

Parameter	Resolution	Quantization	Accuracy	Source
Radiometric and geometric corrected gray count values of Channel-5 (10.2-11.3 μm)	pixel	10 bit	-	Derived from raw data by DP
Radiometric and geometric corrected gray count values of Channel-6 (11.5-12.5 μm)	pixel	10 bit	-	Derived from raw data by DP
Radiometric and geometric corrected gray count values of Channel-3 (3.8 – 4.0 μm)	pixel	10 bit	-	Derived from raw data by DP
Gray value to brightness temperature	-	-	0.3 K	Derived by DP

conversion lookup table				
Geolocation file	Pixel	-	1 pixel	Derived by DP
Satellite Zenith angle	pixel			Derived by DP
Solar Zenith angle	pixel			Derived by DP
Cloud Flag	Pixel	-	-	Cloud Routine

5.3.3 Other Auxiliary data and Model Inputs

Parameter	Resolution	Accuracy	Source
Climatological SSTdata	1 X 1 deg	0.5 K	Reynolds
Climatological WV data	1 X 1 deg	5 mm	NVAP
Total water vapour (In case of failure of any one of the split thermal channel)	0.5 X 0.5 deg	5 mm	Model output, IMD

5.4 Algorithm Functional Specifications

5.4.1 Overview

5.4.1.1 Theoretical Background

Radiance from Earth's terrestrial emission peaks at around 9.6 μm and it has minimum absorption by atmospheric gases, hence in order to measure earth's temperature, spaceborne sensors are designed around this band (8-12 μm). Still this band is not completely transparent. Atmospheric water vapour and CO₂ are the major components that attenuate the IR signal reaching at the top of the atmosphere. Since CO₂ is a uniformly mixed gas, its effect can be taken care, but water vapour being highly variable its effect can only be removed by its measurement(directly or indirectly). Retrieval of sea surface temperature (SST) from thermal infrared window channels (10-12 μm) requires atmospheric corrections arising due to attenuation of signal by intervening moisture. This correction is more in tropics during summers due to higher amount of atmospheric moisture (Barton 1983, Anding and Kauth 1970, Gohil et al 1994, Mathur & Agarwal 1991, 2002, Shenoy 1999). Our radiative transfer simulations studies have shown that with proper characterization of tropical marine conditions in the atmosphere, a suitable algorithm can be developed for accurate SST retrieval (<0.7K) using split thermal window and mid IR thermal channels provided the sensor noise is of the order of 0.1K.

The regression equation to correct for atmospheric absorption and emission has the form

$$\text{SST} = A_0 + A_1 T_{11} + A_2 dT + A_3 dT^2 \quad (1)$$

Where A_0 , A_1 , A_2 and A_3 are coefficients determined by simulation and may have satellite zenith angle dependence

$$dT = T_{11} - T_{12}$$

T_{11} and T_{12} are brightness temperatures for the split-window channels.

To determine the regression coefficients in the above equation, radiative transfer simulations to generate INSAT-3D channels' brightness temperatures for Indian marine tropical environmental conditions would be carried out. The important step in regression is to ensure that the sample dataset is fully and solely representative of the population for which the SST is to be derived. Instrument noise in simulated data for INSAT-3D channels would be introduced as per the availability from sensor team.

A case study for SST retrieval using GOES-9 data (19th August 2005) yielded 0.68 K RMS deviation.

5.4.1.1 Radiative Transfer Model

To simulate the brightness temperatures, MODTRAN is being used. MODTRAN is a computer code developed by Spectral Sciences Inc. and is designed to determine atmospheric transmittance and radiance at moderate resolution (1 cm^{-1}). It is based on AFGL's LOWTRAN-7 code. Thermodynamic Initial Guess Retrieval (TIGR) dataset has been used to construct the tropical marine subset. These profiles have been extracted from $50^{\circ} \text{ S} - 50^{\circ} \text{ N}$ and $30^{\circ} \text{E} - 120^{\circ} \text{E}$. The simulations have been performed on each radio sounding of the TIGR "tropical maritime" subset under the following conditions:

- TIGR profiles are available on 48 levels. They have been converted to the 34 level MODTRAN inputs by using directly the TIGR levels from the surface to 300 hPa (15 levels), sampling every 4 levels above 300 hPa (5 levels are excluded this way) and removing the upper 9 levels.

- In addition to the profiles of temperature and water vapor of TIGR, mixed gases profiles from MODTRAN standard atmospheres have been added according to the time and location of each radiosounding.

- No aerosols have been considered.

- Satellite zenith angles: 4 values of the secant have been retained: 1., 1.5, 1.75, 2. This sampling aims to detect possible non linearities in the dependance of any given quantity in function of $\sec(\theta)$.

- Surface temperatures: For each radio sounding 3 surface temperatures have been assigned: Ta1000 (1000 mb air temperature), Ta1000+1C, Ta1000-1C.

- Radiiances have been simulated for INSAT-3A and INSAT-3D thermal channels (i.e. $10.5-12.5 \mu\text{m}$, $10.3-11.3 \mu\text{m}$, $11.5-12.5 \mu\text{m}$, $3.7-4.1 \mu\text{m}$) with emissivity values calculated from the tables of Masuda 1988 with a moderate wind speed of 5 ms^{-1} (see table 1 below). They have been calculated for each channel as means of tabulated values at the central and neighbouring wavelengths to account for the width of the filter function. For instance, emissivities for channels centred on $11 \mu\text{m}$ were calculated as the mean

values of emissivities at 10.5 and 11 μm , etc. They were then interpolated in function of $\sec(\theta)$ and used with a step of 0.0025 induced.

$\lambda \sec(\theta)$	1.	1.5	1.75	2.
3.7	0.9775	0.9625	0.9450	0.9300
11.	0.9925	0.9825	0.9725	0.9625
12.	0.9875	0.9750	0.9575	0.9450

Table 1. Surface emissivities in function of wavelength λ and secant of the satellite zenith angle $\sec(\theta)$

Radiances will be integrated for each channel with the filter functions provided by Sensor Group and converted into radiative temperatures.

The simulations applied on the "tropical maritime" subset of TIGR produced 5820 cases. Before being used to derive algorithms, the simulated radiative temperatures were filtered. To keep the simulated temperatures within realistic limits, the following thresholds were finally applied on the simulation file:

$$\begin{aligned} Ts - T11 &> 0.5C \\ -2C < Ts &< 35C \\ W &> 0.5 \text{ g/cm}^2 \end{aligned}$$

5.4.1.1.2 Inversion Methods

To generate regression coefficients from the simulated brightness temperatures as per the form prescribed in equation (1), multiple regression using least square method will be adopted.

5.4.1.1.3 Single Channel SST retrieval

In case of failure in any one of the thermal split channels, provisions are provided to retrieve SST using single functional channel (water vapour correction in that case will be carried out by ingesting total water vapour content externally from model output, and applying water vapour dependent SST coefficients similar to SST retrieval from INSAT-3A/Kalpana data). If external total WV content is not available, climatological water vapor will be used.

Single channel SST is computed as

$$SST = a + b * Tb + c * WV$$

Where

Tb is brightness temperature of the IR imager channel, WV is total water vapour content, a, b and c are regression coefficients generated through radiative transfer simulations and may have satellite zenith angle dependence.

5.4.1.1.4 Cloud Detection

In the present algorithm, cloudy pixels are detected through thresholding and spatial coherence techniques in thermal band and the pixels are rejected based on the above criterion. Thresholding technique assumes that over oceans in Indian domain brightness temperature in thermal band is greatly affected by the presence of clouds, resulting in decreased brightness temperature from cold cloud tops. Spatial coherence method is

based on the assumption that SST is homogeneous and warmer than clouds; thus clouds can be identified where the scene brightness temperature has lower mean value or larger standard deviation. Further, the cloud flags generated by cloud mask routine will be used to detect the clouds. SST is computed only over clear oceanic regions.

5.4.1.1.5 Error analysis

The uncertainty in the INSAT-3D SST retrieval is straightforward to calculate. Taking equation (1) and performing an error analysis, one sees that the error in SST can be represented

as:

$$e_t = \sqrt{\sum_{i=1}^n a_i e_i^2}$$

where e_t is the total error, a_i are the estimation coefficients, and e_i is the error apparent for each band i used in the algorithm. e_i is given by

$$e_i = \sqrt{(e_i^a)^2 + (NE\Delta T_i)^2}$$

with e_i^a being the error due to atmospheric correction and $NE\Delta T_i$ deriving from instrumental design and performance considerations. Since the constants a_i are order 1, and one assumes that the nadir and/or atmospheric errors are comparable and the various bands have similar characteristics, one can see the error scales as

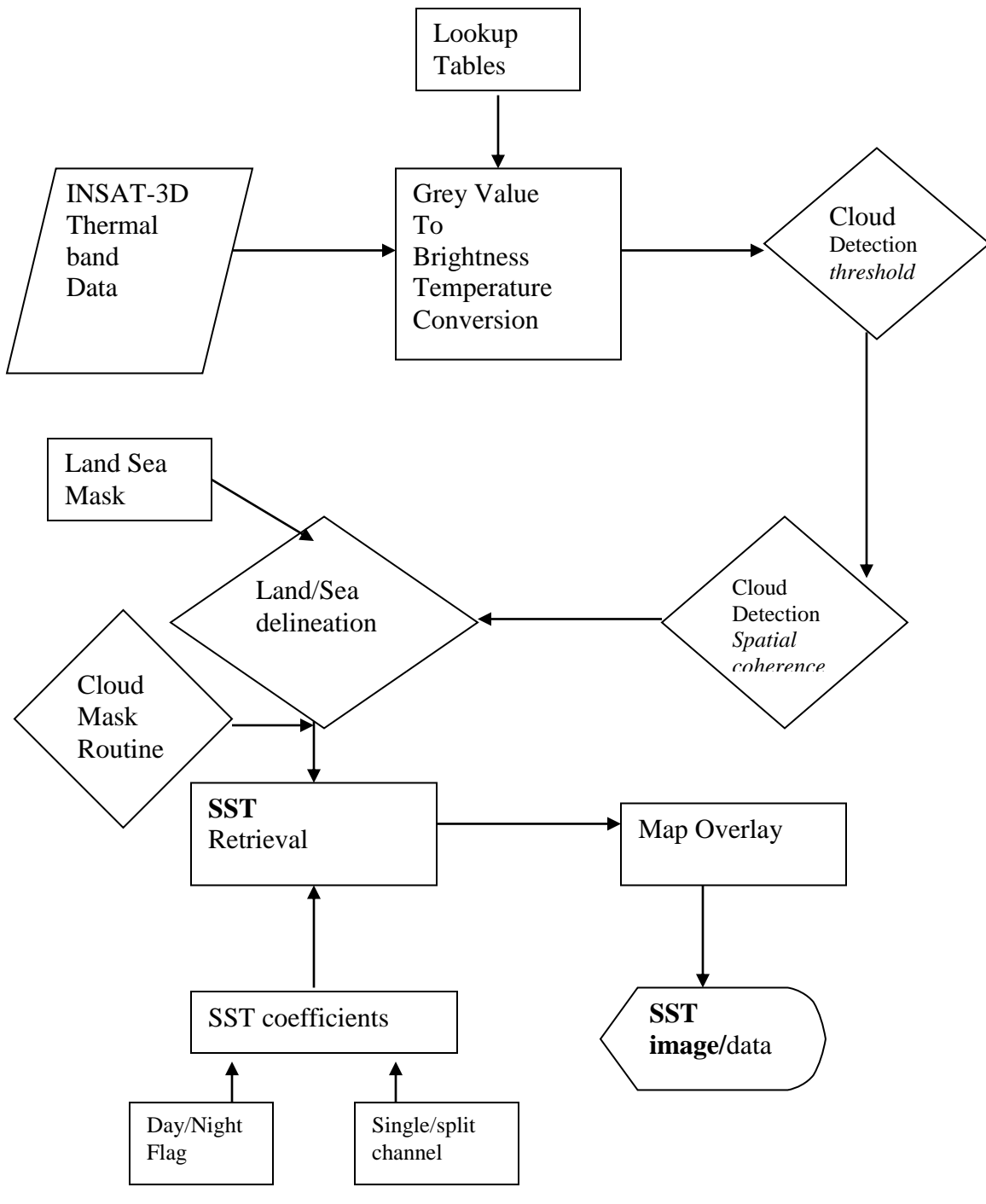
$$e_t = \sqrt{n} e_i$$

where n is the number of bands used.

This analysis makes clear the fact that calibration and/or atmosphere correction errors are important components of the error budget, *i.e.*, 0.1K of error in calibration for a band is effectively an rms error in a dual band algorithm of 0.14K, assuming perfect atmospheric correction. Therefore, we have requested that the calibration be demonstrably accurate at the choice of 0.05K level to minimize the effect of calibration errors. The best atmospheric correction currently available for ATSR suggests that errors due to atmospheric correction in optimal cases for a nadir viewing instrument are approximately 0.3K [Mutlow, *et al.*, 1994; Minnett, 1990; Barton, *et al.*, 1993; Minnett, 1995b].

If one assumes that the calibration errors and the atmospheric errors are random and thus can be RSS'd, as in the preceding analysis, one sees that expected errors of 0.35K-0.4K in the result are the best that can be expected for two-band configurations. This equation also points out that there is a cost associated with adding more bands to improve atmospheric correction. In addition to providing information potentially useful for correcting the effects of the intervening atmosphere, each additional band also introduces noise into the SST retrieval.

5.4.2 Flow-Chart:



Flowchart of SST processing software for INSAT-3D

5.4.3 Operational Implementation

Step-1. Determine radiances using the processed Imager data and convert radiances to temperature using lookup table.

Step-2. Processing for discrimination between radiances from cloud free sea surface and those from the cloud tops as discussed in section 1.4.1.1.4

Step-3. Correction for atmospheric attenuation is taken care in SST computation for multichannel SST retrieval, but in case of availability of only one thermal channel, total water vapour field will be required externally from model output.

Step-4. Computation of SST

During daytime, for cloud free pixels, SST is computed as

$$\text{SST} = A_0 + A_1 T_{11} + A_2 dT + A_3 dT^2$$

Where A_0 , A_1 , A_2 , and A_3 are coefficients determined by regression and may have satellite zenith angle dependence.

$$dT = T_{11} - T_{12}$$

T_{11} and T_{12} are brightness temperatures for the split-window channels

During Nighttime, for cloud free pixels, SST is computed as

$$\text{SST} = A_0 + A_1 T_3 + A_2 dT + A_3 dT^2$$

Where A_0 , A_1 , A_2 , and A_3 are coefficients determined by regression and may have satellite zenith angle dependence.

$$dT = T_{11} - T_{12}$$

T_{11} and T_{12} are brightness temperatures for the split-window channels and T_3 is the brightness temperature for channel 3 of IMAGER.

Single channel SST is computed as

$$\text{SST} = a + b * \text{Tb} + c * \text{WV}$$

Where

Tb is brightness temperature of the IR imager channel, WV is total water vapour content, a , b and c are regression coefficients generated through radiative transfer simulations and may have satellite zenith angle dependence.

Step-5. Quality control/Editing of derived SSTs.

Satellite data are flagged 3(highest quality SST) if the absolute difference between the satellite SST and the climatology is strictly below 3° C and the channel 5 standard deviation is lower or equal to 1° C. If both the criterion are not true, flag value is put as 2. In case of cloudy pixel, flag value is 1. Pixels over land are flagged as 4.

5.5 Outputs

SST maps and data (HDF5) will be available every half hourly, daily, weekly, monthly and seasonally

Parameter	Unit	Min	Max	Theoretical Accuracy	Resolution
SST(day)	Kelvin	285	310	~ 0.8 K (with 0.12 K noise)	Pixel (~4 km)
SST(night)	Kelvin	285	310	~ 0.5 K (with 0.12 K noise)	Pixel(~4 km)

5.5.1 format of the output and the domain

HDF5 datasets: latitude , longitude , sst, flag

Domain :

40 to 40 N, 30 E to 120 E

5.6 Validation

Validation of the derived SST will be done using all the available data from buoys, special cruise by ORV SagarKanya and available similar products from various satellite missions. Validation will be jointly done with IMD.

5.6.1 Data required

Buoy or ship data for SST validation should consists of following parameter

- SHIP/Buoy ID
- Location of the measurement
- Time of the measurement
- SurfaceWind speed and direction
- Surface Relative humidity
- SST
- Depth at which measurement is taken
- Instrument accuracy of SST.

5.6.2 Methods of validation

The *in situ* records are first temporally matched-up against the INSAT extractions. To limit variability introduced by the time separation between the two data sources, the

absolute difference between the time of the *in situ* SST measurement and the time at which that location is viewed by the INSAT (*i.e.*, the matchup time window) is restricted to a maximum of ± 30 minutes or ± 15 minutes. *In situ* records that do not fall within the stipulated time window will be rejected. The *in situ* records that pass the temporal matchup subsequently have to pass a spatial test. A maximum distance of 0.1° will be accepted between an *in situ* SST location and the location of the central pixel in the INSAT extraction box.

Measurement quality control: The climatological SST is then calculated for this box by spatial averaging and time interpolation. If the absolute value of the difference between the *in situ* measurement and the climatology is strictly below 2°C the box is included into the database.

5.6.3 Technical issues (limitation etc.)

Accuracy of the product depends on the accuracy of the radiative transfer model to simulate the satellite radiances, instrument noise and atmospheric correction. Biases in radiative transfer model simulations can be accounted for by validating the derived SST with reliable and concurrent insitu data. In the absence of split thermal window channel observations and a channel sensitive to intervening atmospheric total water vapour content, the atmospheric correction applied is an indirect. The accuracy of this correction will heavily depend upon the accuracy of the model reanalysis for total water vapour. Major constraints on data quality outside the scope of this effort focus in the following areas: accurate pre-launch instrument characterization, instrument NE σ T for each band, calibration model performance, availability of quality controlled surface calibration-validation observations, availability and access to the various quality assessment data sets, and timely access to continuing performance assessment data sets. The on-orbit instrument NE σ T performance is a primary input to the algorithm error budget.

5.7 Future Scope

Initially, prelaunch algorithm would be used to derive SST. Over a period of approximately one year, after complete calibration and validation of the product, bias correction and other fine tuning of the coefficients would be carried out. This should improve the accuracy of the product to the desired level. Of course, instrument noise also plays a crucial role in determining the overall accuracy of the product. Generation of regression coefficients for SST retrieval from simultaneous satellite and buoy observations data base require nearly 250 buoys distributed over Arabian Sea, Bay of Bengal and Indian Ocean continuously for minimum 2/3 years.

5.8 References

- 1 Anding D and R Kauth (1970) "Estimation of sea surface temperature from space", *Remote Sensing of Environment*, 1, 217-220.
- 2 Barton I J (1983) Dual channel satellite measurements of sea surface temperature. *Quarterly journal of Royal Meteorological Society*, 109, 365-378.

- 3 Coakley J A and F P Bretherton (1982) Cloud cover from high resolution scanner data: detecting and allowing for partially clouded fields of view. *Journal of Geophysical Research*, 87,4917-4932.
- 4 Gohil B S, A K Mathur and P C Pandey(1994), An algorithm for sea surface temperature estimation from ERS-1 ATSR using moisture dependent coefficients: a simulation study; *International Journal of Remote Sensing*, Vol. 15, No.5, 1161-1167.
- 5 Kneizys F., E.P. Shettle, G.P. Anderson, L.W. Abreu, J.H.Chetwind, J.E.A. Selby, S.A. Clough and W.O. Gallery (1989): Atmospheric Transmittance/Radiance computer code-LOWTRAN-7. Airforce Geophysical Laboratory, Massachusetts, U.S.A, 01731.
- 6 Mathur A.K., and V.K. Agarwal, 1991: A quantitative study on the effect of water vapour on estimation of sea surface temperature using satellite IR observations. *Oceanography of the Indian Ocean*, B.N.Desai, Ed., Oxford & IBH publishing Co. Pvt.Ltd., 673-680.
- 7 Mathur A K, V K Agarwal and T C Panda (2002),' Validation of ERS-1/ATSR derived SST in Indian waters", *International Journal of Remote Sensing*, Vol. 23, No. 24, 5155-5163 pp.
- 8 Prabhakar C, G Dalu and V G Kunde (1974) 'Estimation of Sea surface temperature from remote sensing in 11-13 μm window region'. *Journal of Geophysical research*,79, 5039-5044.
- 9 Stephens G L, (1990) ' On the relationship between water vapour over the oceans and sea surface temperature', *Journal of Climate*, vol. 3, No.6, 634-645.
- 10 Shenoy S C (1999), On the suitability of global algorithms for the retrieval of SST from the north Indian Ocean using NOAA/AVHRR data, *International Journal of Remote Sensing*, 20, 1, 11-29.
- 11 Smith, W.L., P.K. Rao, R. Koffler, and W.R. Curtis, 1970 : The determination of sea-surface temperature from satellite high resolution infrared window radiation measurements. *Mon. Wea. Rev.* , 98, 604-611.
- 12 Wentz F J, C Gentemann, D Smith and D Chelton (2000) 'Satellite measurements of sea surface temperature through clouds', *Science*, 288, 847-850.
- 13 Wu, X., W.P. Menzel and G.S. Wade, 1999 : Estimation of sea surface temperatures using GOES-8/9 radiance measurements. *Bull. Amer. Met. Soc.*

6. Snow Cover

S.No.	Product Name	Spatial Resolution	Temporal Resolution
1	3DIMG_L2C_SNW	4 km	Once per day

6 Snow-Cover Mapping Algorithm

6.1 Algorithm Configuration Information

6.1.1 Algorithm Name

Snow Cover Mapping (SCM).

(Ref: IMD RFP Sec. 11.9)

6.1.2 Algorithm Identifier

3DIMG_L2C_SNW

6.1.3 Algorithm Specification

Version	Date	Prepared by	Description
1.0	30.05.2013	S. K. Singh	Snow Cover Mapping

EXECUTIVE SUMMARY

Algorithms will be developed to map snow cover using INSAT 3D Meteorological payload. The snow mapping algorithm will use a grouped-criteria technique using the Normalized Difference Snow Index (NDSI) and other spectral threshold tests to identify snow on a pixel-by-pixel basis, and to map snow cover in dense forests. The NDSI is useful for snow mapping, as it reflects strongly in the visible region than in the short-wave IR (SWIR) part of the spectrum. In addition, the reflectance of clouds remains high in the short-wave IR, while the reflectance of snow is considerably low.

Validation of the INSAT snow maps will be carried out using snow products of AWIFS data of Resourcesat1/2 and a limited amount of field measurements. In addition, validation will also be carried out using visual interpretation and the MODIS snow maps. The accuracy of the snow maps will vary with land-cover type. Hence, the Snowmap algorithm has been and will continue to be tested for a variety of land covers. Error estimates have been determined from field measurements for different land covers, and these errors are used to estimate the expected maximum monthly and annual errors in Himalayan snow mapping using the algorithm.

6.2 Introduction

6.2.1 Overview and background

The purpose of the snow-mapping algorithm is to generate Himalayan snow cover product from INSAT 3D data. This algorithm is based on the ratio techniques, which was used successfully to monitor snow using AWIFS data of Resourcesat-1. Daily snow and 10 days snow covered digital map products will be generated.

Snow covers almost 40 per cent of the Earth's land surface during Northern Hemisphere winter. This makes snow albedo and area an important component of the Earth's radiation balance (Foster and Chang, 1993). Large areas in the Himalayas are also covered by snow during wintertime. Area of snow can change significantly during winter and spring. This can affect stream flow during spring and summer of the rivers originating in the Higher Himalayas. In addition, snow pack ablation is highly sensitive to climatic variation. Increase in atmospheric temperature can influence snowmelt and stream runoff pattern (Kulkarni, et

al. 2002a). Therefore, mapping of areal extent and reflectance of snow is an important parameter for various climatological and hydrological applications. In addition, extent of snow cover can also be used as an input for avalanche investigation.

Snow was first observed in April 1960 by TIROS-1 satellite in eastern Canada. Since then, the potential for operational satellite-based mapping has been enhanced by the development of higher temporal-frequency and satellite sensors with higher spatial resolution. In addition, satellite sensors with better radiometric resolutions, such as MODIS and AWIFS have been used successfully for snow mapping (Hall et al. 2002; Kulkarni et. al. 2006). This is possibly due to distinct spectral reflectance characteristics of snow in visible and short wave infrared region. Information generated from satellite observations has been extensively used for snowmelt runoff modeling (Kulkarni et al. 2002b). Remote sensing technique has been extensively used for snow cover monitoring in the Himalayan region with the help of numerous satellite sensors (Kulkarni and Rathore. 2003). Various analysis techniques as visual, hybrid (Visual and supervised classification) have been used to estimate areal extent of snow cover (Kulkarni and Rathore, 2003). However, major difficulty in snow cover monitoring using automated technique in the Himalayan region is mountain shadow and confusing signature of snow and cloud in the visible and near infrared region. Because of above-mentioned reasons, combination of digital and visual interpretation technique is needed to monitor snow cover. This makes snow cover mapping cumbersome and time consuming. To over come this problem normalized difference snow index method is developed and discussed in this paper. In optical region snow reflectance is higher as compared to other land features as grass, rock and water. However, in SWIR region snow reflectance is lower than rock and vegetation (Kulkarni et. al. 2002c). Therefore, snow on satellite images appears white in visible and black in SWIR region. This characteristic has been effectively used to develop Normalized Difference Snow Index (NDSI) for snow cover mapping (Hall et al. 1995).

6.2.1.1 Remote Sensing of Snow Cover

One of the earliest method was used for snow cover monitoring was visual interpretation. During this investigation Large Format Optical Enlarger was used and investigation was carried out using band 2 of Landsat MSS and IRS LISS-I sensor. The investigation was extensively used for snow cover monitoring in Malan, Tosh and many small basins in the Himalayas (Kulkarni, et. al. 2004).

This technique was further modified with advancement of Digital Analysis Technique and availability of higher frequency satellite data such as WiFS of IRS and VHRR of NOAA satellite. In this technique, a combination of visual and digital analysis was used. This was necessary because mountain shadows in the months from November to February normally make it difficult to use only digital technique for snow cover delineation. From the month of March mountain shadows are negligible and snow extent can be estimated from supervised classification technique. This technique has been extensively used to map snow cover in Western Himalaya, Baspa and Satluj basins (Kulkarni and Rathore, 2003).

Another major difficulty in snow cover monitoring is cloud cover. It is further compounded due to similar reflectance characteristics of snow and cloud. The discrimination between snow and cloud can be done by using various techniques such as textural analysis, association with shadow and by using multi temporal analysis. In Himalayas and in present

investigation, snow/cloud discrimination was done by using texture, where snow shows characteristic mountainous pattern, which can not be seen when area is cloud covered. In visible and near infrared region reflectance of snow and cloud is very high. Therefore discrimination between snow and cloud is not possible. This is because of similar reflectance characteristics in this region. In spectral range between 1.55-1.75 μm , 2.1-2.35 μm and 3.55-3.93 μm have shown potential for snow/cloud discrimination. In these bands snow shows lower reflectance than cloud. Spectral region between 1.55-1.75 μm has been successfully used to separate certain types of clouds from snow (Kulkarni et. al., 2006).

Reflectance of fresh snow is very high in the visible part of the electromagnetic spectrum, but decreases in the near-IR especially as grain size increases (O'Brien and Munis, 1975; Warren and Wiscombe, 1980; Srinivasulu et. al. 2002). In addition, soot from industrial pollution becomes incorporated into the snowpack and this may decrease albedo and enhance snowmelt (Clarke and Noone, 1985; Negi, et. al. 2006). Both because of natural aging and other factors (e.g. soot or volcanic ash deposition), the reflectance of snow decreases over time. Fresh snow can have a reflectance (integrated over the reflective part of the spectrum) up to about 80 percent but its reflectance may decrease to below 40 percent after snow crystals metamorphose.

Snow, like all natural surfaces, is an anisotropic reflector (Nolin and Liang, 2000). The reflectance from snow is high in the forward direction and is largely specular. While freshly fallen snow can be nearly a Lambertian reflecting surface, as snow metamorphoses the specular component characteristic of forward scattering increases.

6.2.2 Objective

The purpose of the snow-mapping algorithm is to generate Himalayan snow cover product from INSAT 3D data. This algorithm is based on Normalised Difference Snow Index method, which was used successfully to monitor snow using AWIFS data of Resourcesat. Daily snow and maximum 10-day snow covered area digital-map products will be generated.

This algorithm will be further modified, in conjunction with NDVI and infrared brightness temperature to identify snow in forest covers and identify cloud pixels, respectively (Romanov et al, 2003).

6.3 Inputs and output data

6.3.1 Image and preprocessing data (Dynamic)

Parameter	Resolution	Quantization	Accuracy	Source
Radiometric and geometric corrected gray count values Visible (0.52-0.75 μm) & SWIR (1.55-1.70 μm)	pixel	10 bit	--	Derived from raw data by DP (data processing)

Radiometric and geometric corrected gray count values of TIR-1 channel (10.2-11.2 μm)	pixel	10 bit	-	Derived from raw data by DP
Gray value to brightness temperature conversion table	-	-	0.3 K	Derived by DP
Geolocation file	Pixel	-	1 pixel	Derived by DP

6.3.2 Other Auxillary data and Model Inputs

Source	Product	Frequency	Role in algorithm	Purpose
AWiFS	Land cover map	Each product	Modify NDSI value	Improve accuracy
Reflectance library	Reflectance in visible and SWIR region	As per requirement	NDSI threshold value before launch	Development and validation of algorithm
AWiFS/INSAT3A	Water mask	Each product	Remove water bodies	Improve accuracy

6.4 Algorithm Functional Specifications

6.4.1 Overview

A grouped-criteria technique incorporating NDSI and threshold-based criterion for the algorithm was selected for the following reasons:

- 1) Similar algorithm is developed for AWiFS sensor of Resourcesat-1. Its accuracy has been tested over a variety of surface covers relative to snow cover maps prepared from other techniques. Similar algorithm is also being used to generate snow maps of MODIS data.
- 2) The technique can map snow under mountain shadow and independent of local solar illumination angle. It makes this algorithm highly suitable for mountainous terrain as Himalayas (Kulkarni et. al. 2006).
- 3) INSAT 3D Met payloads have a channel between 1.55 to 1.75 μm with 1 km spatial resolution. Similar channel is not available on GOES satellite. In addition, channel number 1 and 2 are having 1 km spatial resolution. Therefore, product can be generated at 1 km resolution.
- 4) The algorithm will be further improved using NDVI and brightness temperature to identify snow under forest and cloud, respectively. In addition, Spectral range of band 1 of INSAT 3 D and AWiFS band 2 are different, threshold values needs to be

evaluated. This will be initially established using Spectral Reflectance library of Space Applications Centre and then sensitivity analysis of INSAT-3D data.

- 5) It runs automatically, without human intervention. It is straightforward, computationally frugal, and thus easy for the user to understand exactly how the product is generated.

Snow has strong visible reflectance and strong short-wave IR absorbing characteristics. The Normalized Difference Snow Index (NDSI) is an effective way to distinguish snow from many other surface features. Both sunlit and some shadowed snow is mapped effectively. A similar index for vegetation, the Normalized Difference Vegetation Index (NDVI) has been proven to be effective for monitoring global vegetation conditions throughout the year (Tucker, 1979 and 1986). Additionally, some snow/cloud discrimination is accomplished using the NDSI.

Other promising techniques, such as traditional supervised multispectral classifications, spectral-mixture modeling, or neural-network analyses have not yet been shown to be usable for automatic application at the mountainous region. They are also computationally intensive. Training or the interaction of an interpreter is required for successful application of techniques such as neural-network analysis. These techniques may progress to regional applications and possibly even global application in future years.

6.4.1.1 Theoretical Background

6.4.1.1.1 Snow cover map

The snow-cover mapping algorithm will be designed to identify snow in each 1 km pixel. A regional, daily snow product will be produced. A 10-day composite snow cover product will be generated by compositing successive days of snow cover products. This will yield maximum snow extent for the 10 day period. If a pixel were snow covered on any orbit during that period, then that pixel will be mapped as snow covered even if it were snow-free on all of the other orbits during the 10-day period. Other coverage and persistence statistics will also be included to assist analysis of the data product.

There has been much discussion concerning the optimum composite period for the snow maps (Kulkarni et. al, 2006). While weekly composites would correspond with the NOAA/NESDIS maps and the NOHRSC maps, some modelers are interested in longer composition periods, e.g., 7 days to one month. 8-day composites were chosen because this period optimizes the ground coverage from the MODIS instrument. In India, the hydrological data analysis is carried out on 10-daily basis; therefore 10-day composite will be prepared. If a researcher wants to produce a composite product for any period other than a 10-day period, from our daily product, this can be done using the daily data.

6.4.1.1.2 Normalized Difference Snow Index (NDSI)

The NDSI is useful for the identification of snow and for separating snow and most cumulus clouds. The NDSI is a measure of the relative magnitude of the characteristic reflectance difference between the visible and short-wave IR reflectance of snow. The NDSI is insensitive to a wide range of illumination conditions (Kulkarni et al., 2006). The NDSI is analogous to the normalized-difference vegetation index (NDVI) (Tucker, 1979 and 1986; Townshend and Tucker, 1984). NDSI can be computed as given below;

$$\text{NDSI} = (\text{Visible}_{\text{INSAT B1}} - \text{SWIR}_{\text{INSAT B2}}) / (\text{Visible}_{\text{INSAT B1}} + \text{SWIR}_{\text{INSAT B2}})$$

Pixels that are approximately 75% or greater covered by snow were found to have NDSI values more than 0.4 in our field investigation at Dhundi test site in Himachal Pradesh (Negi et. al., 2006). These NDSI thresholds have been verified from detailed analysis of numerous AWIFS scenes, comparisons with supervised-classification techniques and NDSI technique. (Kulkarni et. al, 2004). Pure snow has a high NDSI but NDSI decreases as other features are mixed in a pixel. Snow in mixed pixels has an NDSI that is less than that for pure snow. Pure snow can be distinguished by its high NDSI value (Negi et. al., 2006). Since Bandwidth of AWIFS band 1 and INSAT 3D imager is different, initially NDSI threshold value will be established using Field Spectral Data Library of Space Applications Centre (Singh, et. al., 2005 and Negi, et. al., 2006). This will be further evaluated during post launch period, by carrying out sensitivity analysis (Kulkarni et. al. 2006).

In forested locations, many snow covered pixels have an NDSI lower than 0.4. To correctly classify these forests as snow covered, a lower NDSI threshold is necessary (Negi et. al., 2006). NDVI and NDSI will be used together in order to discriminate between snow-free and snow covered forests. Forested pixels have higher NDVI values compared with non-forested pixels. Thus by using the NDSI and NDVI in combination, it is possible to lower the NDSI threshold in forested areas without compromising the algorithm performance for other land covers. Since appropriate bands are not available in INSAT 3D payload, mask will be generated using AWIFS sensor.

The NDSI-NDVI field is designed to capture as much of the variation in NDSI-NDVI values observed in the snow covered forests as possible while minimizing inclusion of non-forested pixels. It was designed to include forest-covered pixels that have NDSI values lower than 0.4, yet have NDVI values lower than would be expected for snow-free conditions (Klein et al., 1998).

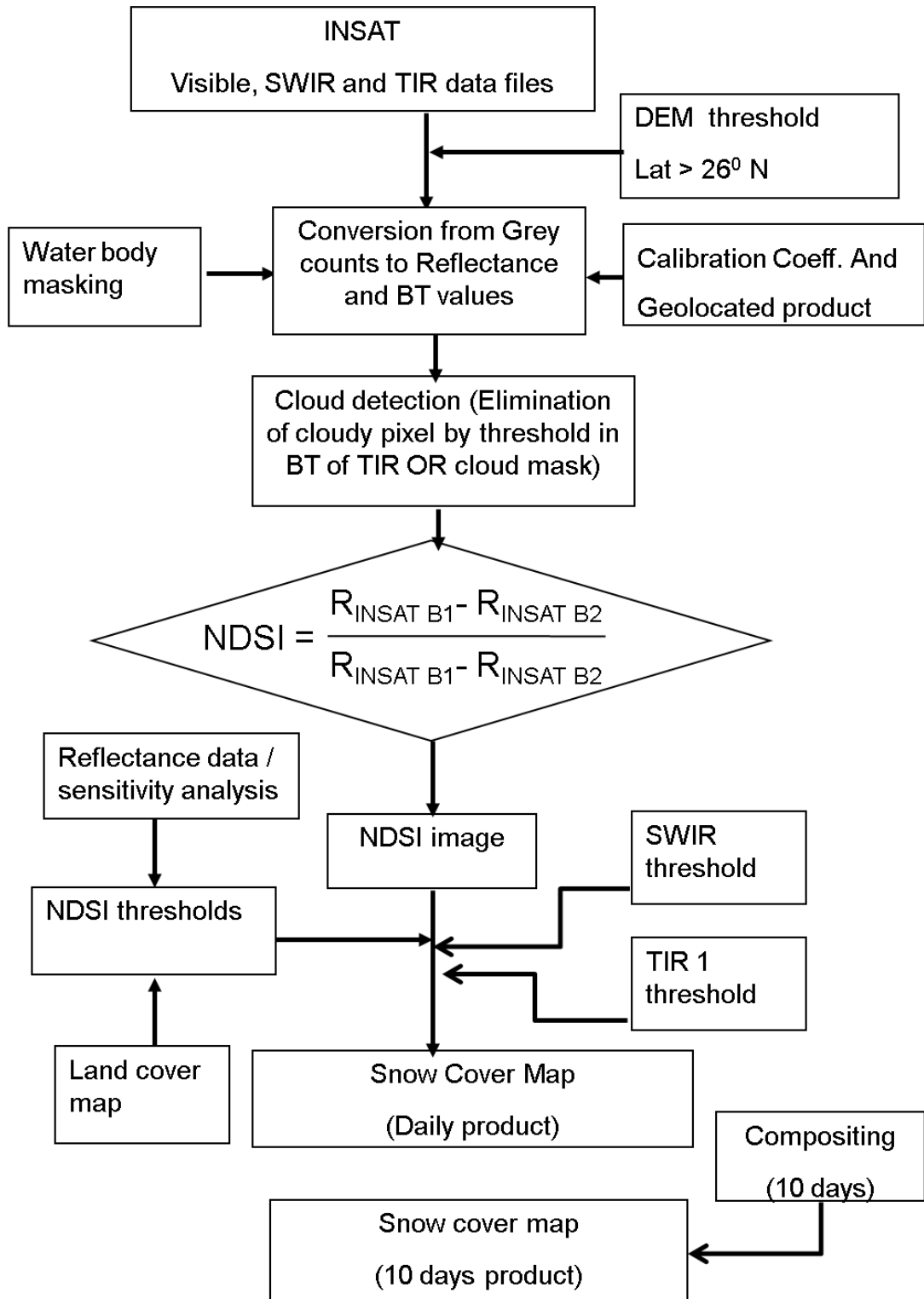
Since water may also have an NDSI 0.4, therefore permanent mask is necessary to separate water from snow.

6.4.1.1.3 Snow / Cloud Discrimination

Snow/cloud-discrimination techniques are based on differences between cloud and snow reflectance and emittance characteristics. Clouds are highly variable and may be detected by their generally high reflectance in the visible and near-IR parts of the electromagnetic spectrum (Kulkarni et al, 2002), whereas the reflectance of snow drops in the short-wave infrared part of the spectrum.

While the NDSI can separate snow from most obscuring clouds, it does not always identify or discriminate optically-thin cirrus clouds from snow. Analyses of AWIFS and MODIS data show that NDSI can map snow under cirrus clouds at least some of the time. Cirrus clouds have high reflectance in SWIR region than snow which requires fine tuning of threshold value and will be used as an additional criterion in present approach. This algorithm will further be improved due to availability of thermal bands in INSAT 3D Met payload. Appropriate brightness temperature threshold will be used to separate cloud from snow (Romanov, et. al., 2003) or cloud removal will also be tested using cloud mask product subject to its availability as an additional INSAT 3D derived product. This will be additional criteria than in build criteria of NDSI.

6.4.1.1.4 Flow Chart



6.4.1.1.5 Sensitivity analysis to establish NDSI threshold

In order to establish credible threshold value of NDSI for snow cover mapping, a sensitivity test of individual threshold values were carried out. NDSI threshold values were changed from 0 to 1 at an interval of 0.05. If pixel is having NDSI value equal or more than threshold value then it is classified as snow. Then loss in areal extent due to increase in threshold value are converted into percent and plotted on Y-axis . X-axis indicate NDSI threshold. In general, areal extent decreases as NDSI value increases from 0 to 1. But amount of change varies from constant to rapid. In case of AWIFS scene of winter, constant drop in area in the order of 3% was observed as threshold value changes from 0 to 0.4. After threshold of 0.4 drop in area (Snow pixels) is moderate to rapid. Visual analysis suggests that all snow cover areas including snow in forest and mountain shadow can be mapped if threshold value is 0.4. In order to establish validity of this observation, the similar investigations were carried out from December to May at an interval of one month. The NDSI threshold will be fine tuned after the availability of INSAT 3D derived snow cover product.

6.4.2 Operational Implementation

6.4.1.2 Step 1 : Conversion from gray count to Reflectance and BT:

In this step, the DN values will be converted into Radiance, Reflectance and Brightness temperature using calibration coefficient available with INSAT 3D data. The radiometrically processed data will also be geolocated and this will provide a radiometrically and geometrically corrected product to be used further in algorithm.

6.4.1.3 Step 2 : Cloud elimination

This step includes the cloud screening from the INSAT 3D image. Cloud screening is based on temperature data/or cloud mask along with cloud removal using SWIR threshold value, and will help to clear cloudy pixels.

6.4.1.4 Step 3 : Generation of NDSI image

Normalized Difference Snow Index will be computed using the normalized ratio of visible and SWIR channel as given below;

$$\text{NDSI} = (\text{R}_{\text{INSAT B1}} - \text{R}_{\text{INSAT B2}}) / (\text{R}_{\text{INSAT B1}} + \text{R}_{\text{INSAT B2}})$$

Where R is the reflectance of the respective channel.

6.5 Outputs

Parameter	Unit	Min	Max	Accuracy	Resolution
SCM	Km ²	-	-	-	Pixel level

6.5.1 Format of the output and the domain

Geolocated Snow map & Areal extent of snow cover in Himalayan region.

6.6 Validation and Error Analysis

6.6.1 Validation Activities

6.6.1.1 Comparison of INSAT 3D snow maps with AWIFS and MODIS operational snow maps

INSAT-derived snow maps will continue to be compared with snow cover maps generated by AWIFS. In addition, comparisons will be made between MODIS maps. Comparison of Snowmap results with these independently-produced snow data sets will allow errors to be identified that will permit us to determine the accuracy of the global maps relative to one another. There are several hemispheric-scale satellite-derived snow-cover maps available, but none has been fully validated.

6.6.1.2. Mapping Snow in Densely-Forested Areas

A significant limitation in mapping the extent of snow cover occurs in situations of mixed pixels where snow cover is obscured by dense forest cover. The snow covered forested landscape is actually never completely snow covered because the tree branches, trunks and canopies often do not get or stay snow covered. Often, in boreal forests, snow that falls on the coniferous tree canopy will not stay on the canopy for the entire winter due to sublimation. Thus, even in a continuously snow covered area, much of the forested landscape will not be snow covered. It may be very difficult, even with field measurements and high-resolution air photos, to determine what percentage of the area is snow covered. Additionally, when viewing at off-nadir angles the tree branches, canopies, etc., will obscure even more of the snow than when viewing at near-nadir angles.

Dense forests cover much of the Earth's land surface. Snow accumulates to greater depths and melts later in the spring in the boreal forests than in adjacent areas (Foster et al., 1991). Though the boreal forests are always snow covered in the winter, within dense forests, snow that falls onto the ground through the canopy may not be visible from above. Some snow stays in the tree canopy and may thus be visible, but the snow often does not stay in the canopy during the entire winter. Snow in trees often sublimates before falling to the ground. Therefore, NDSI values will be appropriately modified to identify snow under forest cover.

6.6.2 Estimate of Errors in Snow cover Mapping

It is recognized that NDSI will perform better in some land covers than in others. Specifically, results using the NDSI algorithm with AWIFS data above snow line show 100 percent snow cover when they were known by field measurements to be 100 percent snow covered. In forested areas, errors may be much larger.

An estimate of the errors inherent in using Snow cover map in different land covers will be made using data from focused field missions, for example: agricultural (e.g. in the Kullu district.), forest free (e.g. Lahaul and Spiti district of Himachal Pradesh), forest (e.g. Forested region of Beas basin). Errors have been determined for the following land covers: forests, mixed agriculture and forest, barren/sparsely-vegetated, shrub land, wetlands, and glacial region. These land covers were selected because they cover a wide range of conditions encountered in snow covered parts of the Himalaya.

6.7 Future Scope

This algorithm will be further modified, in conjunction with NDVI and infrared brightness temperature to identify snow in forest covers and identify cloud pixels, respectively.

6.8 References

- 1) Clarke, A.D. and K.J. Noone, 1985. Soot in the Arctic snowpack: a cause for perturbations in radiative transfer. *Atmospheric Environment*, 19, 2045-2053.
- 2) Chaponniere, A., P. Maisongrade, B. Duchemin, L. Hanich, G. Boulet, R. Escadafal and S. Elouaddat, 2005. A combined high and low spatial resolution approach for mapping snow covered areas in the Atlas mountains, *International J. of Remote Sensing*, 26(13), 2755-2777.
- 3) Foster, J. L., and Chang, A. T. C., 1993. Snow Cover. In "Atlas of Satellite Observations Related to Global Change." Eds. R. L. Burney, C. L. Parkinson, and J. L. Foster, 361-370. Cambridge University Press, Cambridge.
- 4) Hall, D.K., G.A. Riggs and V.V. Salomonson, 1995. Development of methods for mapping global snow cover using moderate resolution imaging spectroradiometer data, *Remote Sensing of Environment*, 54, 127-140.
- 5) Hall D.K., R.E.J. Kelly, G.A. Riggs, A.T.C. Chang and J.L. Foster, 2001. Assessment of the relative accuracy of hemispheric-scale snow-cover maps, *Annals of Glaciology*, 34, 24-30.
- 6) Hall, D.K., V.V. Salomonson, G.A. Riggs, N. DiGirolamo and K.J. Bayr, 2002, MODIS snow cover products, *Remote Sensing of Environment*, 83, 181-194.
- 7) Klein, A.G. and J. Stroeve, 2001. Development and validation of a snow albedo algorithm for the MODIS instrument, *Annals of Glaciology*, 34, 38-44.
- 8) Kulkarni A. V., S. K. Singh, P. Mathur and V. D. Mishra, 2006. Algorithm to monitor snow cover using AWIFS data of Resourcesat for the Himalayan region, *International J. of Remote Sensing*, 27(12), 2449-2457.
- 9) Kulkarni A. V., P. Mathur, S. K. Singh, B. P. Rathore and N. Thakur, 2004. Remote sensing based techniques for snow cover monitoring for the Himalayan region, Proc. International Symposium on Snow Monitoring and Avalanches, Manali, 399-405.
- 10) Kulkarni, A.V. and B. P. Rathore, 2003. Snow cover monitoring in Baspa basin using IRS WiFS data, *Mausam*, 54(1), 335-34.
- 11) Kulkarni A.V, J. Srinivasulu, S. S. Manjul and P. Mathur, 2002. Field based spectral reflectance to develop NDSI method for snow cover monitoring, *Journal of Indian Society of Remote Sensing*, 30 (1 & 2), 73-80.
- 12) Kulkarni A.V, S. S. Randhawa, B. P. Rathore, I. M. Bahuguna and R.K. Sood, 2002. A snow and glacier melt runoff model to estimate hydropower potential, *Journal of Indian Society of Remote Sensing* 30 (4), 221-228.
- 13) Kulkarni A.V, P. Mathur, B.P. Rathore, Suja Alex, N. Thakur and Manoj Kumar, 2002. Effect of Global warming on snow ablation pattern in the Himalayas, *Current Science*, 83(2), 120-123.
- 14) Kulkarni A.V and I. M. Bahuguna, 2001. Role of Satellite images in snow and glacial investigations, *GSI Special Publication Number 53*, 233-240.

- 15) Kulkarni A. V., B. P. Rathore, Suja Alex, P. Mathur, N. Thakur and Manoj Kumar, 2001. Snow cover monitoring in Beas basin using IRS WiFS data, Proceedings of National Snow Science Meet, SASE, Manali, 151-155.
- 16) Kulkarni A.V., P. Basak, S.S. Randhawa and R.K. Sood, 1999. Estimation of seasonal snow cover contributing into snow melt runoff models in winter season, Proceedings of National Snow Science Workshop 1999 (NSSW-99) organized by Snow and Avalanche Study Establishment, Manali, 151-155.
- 17) Manjul S.S., A.V. Kulkarni and Suja Alex, 2000, Spectral reflectance of snow in visible, near-infrared and short wave infrared region, Scientific Note no. SAC/RESA/MWRD-GLI/SN/14/2000, 12p.
- 18) Negi, H. S., A. V. Kulkarni, R. P. Prajapati, S.K. Singh and J. K. Sharma, 2006. Effect of contamination and mixed objects on snow reflectance using spectroradiometer, Scientific Report number RSAM/SAC/RESIPA/MWRG-GLI/SN25/2006, Space Applications Centre, Ahmedabad, India, 24p.
- 19) Nolin, A.W. and S. Liang, 2000. Progress in Bidirectional reflectance modeling and applications for surface particulate media: snow and soils, *Remote Sensing Reviews*, 18, 307-342.
- 20) O'Brien, H.W. and R.H. Munis, 1975. Red and near-infrared spectral reflectance of snow. In: Operational Applications of Satellite Snow cover Observations, Ed. A. Rango, NASA SP-391 (Washington, D.C.: NASA), 345-360.
- 21) Romanov P. and Tarpley D. 2003. Automated monitoring of snow cover over south America using GOES imager data. *International. J. of Remote Sensing*, 24(5), 1119-1125.
- 22) Romanov P., Gutman G. and Csiszar I. 2000. Automated monitoring of snow cover over North America with multispectral satellite data. *J. of Applied Meteorology*, 39, 1866-1880.
- 23) Romanov P., Tarpley D., Gutman G. and Carroll T. 2003. Mapping and monitoring of snow cover fraction over North America, *J. of Geophysical Research*, vol 108, D16, 8619, 14-1to 14-15.
- 24) Singh, S. K., H. S. Negi, Babu Govindh Raj K., A. V. Kulkarni and J. K. Sharma, 2005. Spectral reflectance investigations of snow and other objects using ASD radiometer. RSAM/SAC/RESIPA/MWRG-GLI/SN 23/2005, 43p
- 25) Srinivasulu J. and A. V. Kulkarni, 2004. A Satellite based Spectral Reflectance Model for Snow and Glacier Studies in the Himalayan Terrain, *Proc. of the Indian Acad. Sci. (Earth and Planet. Sci.)* 113 (1), 117-128.
- 26) Townshend, J.R.G. and C.J. Tucker, 1984. Objective assessment of Advanced Very High Resolution Radiometer data for land cover mapping, *International J. of Remote Sensing*, 5, 497-504.
- 27) Tucker, C.J., 1979. Red and photographic infrared linear combinations for monitoring vegetation, *Remote Sensing of Environment*, 8, 127-150.
- 28) Tucker, C.J., 1986. Maximum normalized difference vegetation index images for sub-Saharan Africa for 1983-1985, *International J. of Remote Sensing*, 7, 1383-1384.

7. Snow Depth

S.No.	Product Name	Spatial Resolution	Temporal Resolution
1	3DIMG_L2C_SND	TBD	TBD

Snow Depth Estimation

7.1 Algorithm Configuration Information

7.1.1 Algorithm Name

Snow Depth Estimation (SND)

(Ref : IMD RFP Section 11.9)

7.1.2 Algorithm Identifier

3DIMG_L2C_SND

7.1.3 Algorithm Specification

Version	Date	Prepared by	Description
1.0	14.02.2007	A.V. Kulkarni And S.K. Singh	SD Baseline Document

EXECUTIVE SUMMARY

Algorithms needs be developed to estimate snow depth using INSAT 3D Met payload. Important step in estimation of snow depth is generation of snow fraction map. Since Himalayan region is highly mountainous, the data processing would initially need calibration, georeferencing, atmospheric correction, snow pixel detection, cloud masking, local illumination angle correction, diffuse radiation correction, BDRF correction and orthorectification. This will be followed by Linear or non-linear mixing modeling to estimate snow fraction in each pixel. The mixing modeling would need large spectral reflectance library of snow and other land features of Himalayan region, to identify end members of snow and snow free terrain.

Next important step in the investigation is to develop a relationship between snow fraction and depth. This would need field snow depth data. In North America this relationship was developed using 1400 field observatories. Relationship was found useful; if snow depth is less than 27 cm. Field data needs to be collected from Indian Meteorological Department.

7.2 Introduction

7.2.1 Overview and background

The purpose of the snow-depth estimation algorithm is to generate Himalayan snow depth product from INSAT 3D data. The algorithm based on correlation between depth of the snow pack and satellite derived sub pixel fractional snow cover (Romanov and Tarpley, 2004). However, this relationship was developed for non-forested, open prairie (plain terrain) region of North America. The accuracy of snow depth retrievals was found 30% of observed snow depth for snow depth below 30 cm. The satellite derived sub pixel fractional snow cover is independent of snow depth, if snow depth is more than 30 cm (Romanov and Tarpley, 2004).

Snow covers almost 40 per cent of the Earth's land surface during Northern Hemisphere winter. This makes snow albedo and area an important component of the Earth's radiation balance (Foster and Chang, 1993). Large areas in the Himalayas are also covered by snow

during wintertime. Area of snow can change significantly during winter and spring. This can affect stream flow during spring and summer of the rivers originating in the Higher Himalayas. In order to make optimum utilization of snow information for hydrological, climatological and disaster purpose, snow depth is an important parameter. In addition, snow pack ablation is highly sensitive to climatic variation. Increase in atmospheric temperature can influence snowmelt and stream runoff pattern (Kulkarni, et al. 2002a). Therefore, mapping of areal extent and reflectance of snow is an important parameter for various climatological and hydrological applications. In addition, extent of snow cover can also be used as an input for avalanche investigation.

Snow was first observed by satellite in eastern Canada from the TIROS-1 satellite in April 1960. Since then, the potential for operational satellite-based mapping has been enhanced by the development of higher temporal-frequency and satellite sensors with higher spatial resolution. In addition, satellite sensors with better radiometric resolutions, such as MODIS and AWIFS have been used successfully for snow mapping (Hall et al. 2002; Kulkarni et. al. 2006). This is possibly due to distinct spectral reflectance characteristics of snow in visible and short wave infrared region. Information generated from satellite observations has been extensively used for snowmelt runoff modeling (Kulkarni et al. 2002b). Remote sensing technique has been extensively used for snow cover monitoring in the Himalayan region with the help of numerous satellite sensors (Kulkarni and Rathore. 2003). Various analysis techniques as visual, hybrid (Visual and supervised classification) have been used to estimate areal extent of snow cover (Kulkarni and Rathore, 2003). However, major difficulty in snow cover monitoring using automated technique in the Himalayan region is mountain shadow and confusing signature of snow and cloud in the visible and near infrared region. Because of above-mentioned reasons, combination of digital and visual interpretation technique is needed to monitor snow cover. This makes snow cover mapping cumbersome and time consuming. To over come this problem normalized difference snow index method is developed and discussed in this paper. In optical region snow reflectance is higher as compared to other land features as grass, rock and water. However, in SWIR region snow reflectance is lower than rock and vegetation (Kulkarni et. al. 2002c). Therefore, snow on satellite images appears white in visible and black in SWIR region. This characteristic can be effectively used to develop Normalized Difference Snow Index (NDSI) for snow cover mapping (Hall et al. 1995).

7.2.1.1 Remote Sensing of Snow Cover and Depth

One of the earliest method was used for snow cover monitoring was visual interpretation. During this investigation Large Format Optical Enlarger was used and investigation was carried out using band 2 of Landsat MSS and IRS LISS-I sensor. The investigation was extensively used for snow cover monitoring in Malan, Tosh and many small basins in the Himalayas (Kulkarni, et. al. 2004).

This technique was further modified with advancement of Digital Analysis Technique and availability of higher frequency satellite data such as WiFS of IRS and VHRR of NOAA satellite. In this technique combination of visual and digital analysis technique was used. This was necessary because mountain shadows in the months from November to February normally make it difficult to used only digital technique for snow cover delineation. From the month of March mountain shadows are negligible and snow extent can be estimated from

supervised classification technique. This technique has been extensively used to map snow cover in Western Himalaya, Baspa and Satluj basins (Kulkarni and Rathore, 2003).

Another important difficulty in snow cover monitoring is cloud cover. It is further compounded due to similar reflectance characteristics of snow and cloud. The discrimination between snow and cloud can be done by using various techniques such as textural analysis, association with shadow and by using multi temporal analysis. In Himalayas and in present investigation, snow/cloud discrimination was done by using texture, where snow shows characteristic mountainous pattern and it can not be seen, when area is covered by cloud cover. In visible and near infrared region reflectance of snow and cloud is very high. Therefore discrimination between snow and cloud is not possible. This is because of similar reflectance characteristics in this region. In spectral range between 1.55-1.75 m, 2.1-2.35 m and 3.55-3.93 m have shown potential for snow/cloud discrimination. In these bands snow shows lower reflectance than cloud. Spectral region between 1.55-1.75 μm has been successfully used to separate some types of clouds from snow (Kulkarni et. al., 2006).

7.2.1.2 Estimation of Snow Reflectance in Himalaya

In order to estimate snow fraction important step is estimation of reflectance. Reflectance of fresh snow is very high in the visible part of the electromagnetic spectrum, but decreases in the near-IR especially as grain size increases (O'Brien and Munis, 1975; Warren and Wiscombe, 1980; Srinivasulu et. al. 2002). In addition, soot from industrial pollution becomes incorporated into the snowpack and this may decrease albedo and enhance snowmelt (Clarke and Noone, 1985; Negi, et. al. 2006). Both because of natural aging and other factors (e.g. soot or volcanic ash deposition), the reflectance of snow decreases over time. Fresh snow can have a reflectance (integrated over the reflective part of the spectrum) up to about 80 percent but its reflectance may decrease to below 40 percent after snow crystals metamorphose.

One of the parameter, which can influence satellite obtained reflectance is terrain topography. The relative magnitudes of terrain slope and its aspect with respect to the sun's position will determine the amount of direct solar radiation incident on an undulating surface. The analysis carried out over the Beas Basin, Himachal Pradesh, India, indicated a variation of 22% in the amount of incident solar radiation for an increase of 10° in terrain slope (Srinivasulu and Kulkarni, 2003).

Various parameters required to estimate reflectance are mean solar exo-atmospheric spectral irradiances in the sensor bands, digital elevation information, solar declination, mean earth-sun distance on a Julian day, and the calibration parameters of the sensor, such as maximum and minimum radiances in the sensor bands. The terrain topography parameters, viz., terrain slope and aspect are derived from the digital elevation information of the terrain. The local illumination angle for each pixel, which determines the amount of direct solar radiation incident on a sloped surface, is computed using both the sun and terrain geometry.

Markham and Barker equation for computing reflectance from a flat area cannot be valid for the Himalayan region where the terrain is highly undulating. To estimate reflectance from a rugged terrain, cosine of the local illumination angle, not the cosine of solar zenith angle, has to be used as given below:

$$\rho_\lambda = \pi L_\lambda d^2 / E_{\text{sun}\lambda} \cos\theta_i$$

Where, d is the mean earth-sun distance on a Julian day (AU), and θ_i is the local illumination angle (degree), the angle between the Sun's rays and the surface normal and is calculated by using the relation given by Robinson (1966).

Snow, like all natural surfaces, is an anisotropic reflector (Salomonson and Marlatt, 1968; Dirmhirn and Eaton, 1975; Steffen, 1987; Nolin and Liang, 2000). The reflectance from snow is greatest in the forward direction and is largely specular. While freshly fallen snow can be nearly a Lambertian reflecting surface, as snow metamorphoses the specular component characteristic of forward scattering increases. This means, reflectance of snow will change depending upon view and illumination geometry. This can be described by Bidirectional reflectance distribution Function (BRDF) (George Joseph, 2005).

7.2.2 Objective

The purpose of the snow-depth estimation algorithm is to generate Himalayan snow depth product from INSAT 3D data. The algorithm based on correlation between depth of the snow pack and satellite derived sub pixel fractional snow cover (Romanov and Tarpley, 2004).

However, this relationship was developed for non-forested, open prairie (plain terrain) region of North America. Therefore, this algorithm needs further development for application in mountainous Himalayan Terrain. This involves reflectance correction using local illumination angle, diffuse radiation from sidewalls and Bidirectional reflectance distribution Function (BRDF). BRDF is necessary as snow reflectance in anisotropic with aging.

7.3 Inputs

7.3.1 Image and preprocessing data (Dynamic)

Parameter	Resolution	Quantization	Accuracy	Source
Radiometric and geometric corrected gray count values Visible (0.52-0.75 μm) & SWIR (1.55-1.70 μm)	pixel	10 bit	--	Derived from raw data by DP (data processing)
Radiometric and geometric corrected gray count values of TIR-1 channel (10.2-11.2 μm)	pixel	10 bit	-	Derived from raw data by DP
Gray value to brightness temperature conversion table	-	-	0.3 K	Derived by DP
Geolocation file	Pixel	-	1 pixel	Derived by DP

7.3.2 Other Auxillary data and Model Inputs

Source	Product	Role in algorithm	Purpose
Field Data	Snow Depth	Development of Snow fraction and snow depth based approach	Developing and validating.
Sensor parameter	Sun-solar geometry	Deriving snow fraction map	Generation of snow cover map
Topographic map	Digital Elevation Model	Terrain parameters	Computation of Slope and aspect of terrain.
AOD, O3, and other gases	Transmittance coefficient	Atmospheric correction	To minimize atmospheric contribution
AWiFS	Land cover map	Modify NDSI value	Improve accuracy
Reflectance library	Reflectance in visible and SWIR region	NDSI threshold value before launce	Development and validation of algorithm
AWiFS	Water mask	Remove water bodies	Improve accuracy

7.4 Algorithm Functional Specifications

7.4.1 Overview

First step in this study is estimation of snow pixels. A grouped-criteria technique incorporating a NDSI and threshold-based criterion for the algorithm will be used due to the following reasons:

- 1) Similar algorithm is developed for AWiFS sensor of Resourcesat. Its accuracy has been tested over a variety of surface covers relative to snow cover maps prepared from other techniques. Similar algorithm is also being used to generate snow maps using MODIS data.
- 2) The technique can map snow under mountain shadow and independent of local solar illumination angle. It makes this algorithm highly suitable for mountainous terrain as Himalayas.
- 3) INSAT 3D Met payloads have a channel between 1.55 to 1.75 μm with 1 km spatial resolution. Similar channel is not available on GOES satellite. In addition, channel number 1 and 2 are having 1 km spatial resolution. Therefore, product can be generated at 1 km resolution.
- 4) It runs automatically, without human intervention. It is straightforward, computationally frugal, and thus easy for the user to understand exactly how the product is generated.

Snow has strong visible reflectance and strong short-wave IR absorbing characteristics. The Normalized Difference Snow Index (NDSI) is an effective way to distinguish snow from

many other surface features. Both sunlit and some shadowed snow is mapped effectively. A similar index for vegetation, the Normalized Difference Vegetation Index (NDVI) has been proven to be effective for monitoring global vegetation conditions throughout the year (Tucker, 1979 and 1986). Additionally, some snow/cloud discrimination is accomplished using the NDSI.

Other promising techniques, such as traditional supervised multispectral classifications, spectral-mixture modeling, or neural-network analyses have not yet been shown to be usable for automatic application at the global scale. They are also computationally intensive. Training or the interaction of an interpreter is required for successful application of techniques such as neural-network analysis. These techniques may progress to regional applications and possibly even global application in future years.

7.4.1.1 Theoretical Background

7.4.1.1.1 Identification of Snow pixels

The snow-cover mapping algorithm will be designed to identify snow in each 1 km pixel. A regional, daily snow product will be produced. An 10-day composited snow cover product will be generated by compositing successive days of snow cover products. This will yield maximum snow extent for the 10 day period. If a pixel were snow covered on any orbit during that period, then that pixel will be mapped as snow covered even if it were snow-free on all of the other orbits during the 10-day period. Other coverage and persistence statistics will also be included to assist analysis of the data product.

There has been much discussion concerning the optimum composite period for the snow maps (Kulkarni et. al, 2006). While weekly composites would correspond with the NOAA/NESDIS maps and the NOHRSC maps, some modelers are interested in longer composition periods, e.g., 7 days to one month. 8-day composites were chosen because this period optimizes the ground coverage from the MODIS instrument. The repeat period of the satellite is 16 days. In India, the hydrological data analysis is carried out on 10-daily basis; therefore 10-day composite will be prepared. If a researcher wants to produce a composite product for any period other than a 10-day period, from our daily product, this can be done using the daily data.

7.4.1.1.2 Normalized Difference Snow Index (NDSI)

The NDSI is useful for the identification of snow and for separating snow and most cumulus clouds. The NDSI is a measure of the relative magnitude of the characteristic reflectance difference between the visible and short-wave IR reflectance of snow. The NDSI is insensitive to a wide range of illumination conditions, is partially normalized for atmospheric effects, and does not depend on reflectance in a single band (Kulkarni 2006). The NDSI is analogous to the normalized-difference vegetation index (NDVI) (Tucker, 1979 and 1986; Townshend and Tucker, 1984).

$$\text{NDSI} = (\text{INSAT Band 1} - \text{INSAT Band 2}) / (\text{INSAT Band 1} + \text{INSAT Band 2})$$

Pixels that are approximately 25 % or greater covered by snow have been found to have NDSI values 0.4 in our field investigation at Dhundi test site in Himachal Pradesh (Negi et. al., 2006). Since water may also have an NDSI 0.4, therefore permanent mask is necessary to separate water from snow.

These NDSI thresholds have been verified from detailed analysis of numerous AWIFS scenes, comparisons with supervised-classification techniques and NDSI technique. (Kulkarni et. al. 2004). Pure snow has a high NDSI but NDSI decreases as other features are mixed in a pixel. Snow in mixed pixels has an NDSI that is less than that for pure snow. Pure snow can be distinguished by its high NDSI value (Negi et. al., 2006).

In forested locations, many snow covered pixels have an NDSI lower than 0.4. To correctly classify these forests as snow covered, a lower NDSI threshold is necessary (negi et. al., 2006; Hall et al, 1998). The normalized difference vegetation index (NDVI) and the NDSI are used together in order to discriminate between snow-free and snow covered forests. Forested pixels have higher NDVI values compared with non-forested pixels. Thus by using the NDSI and NDVI in combination, it is possible to lower the NDSI threshold in forested areas without compromising the algorithm performance in other land covers. Since appropriate bands are not available in INSAT 3D payload, mask will be generated using AWIFS sensor.

The NDSI-NDVI field is designed to capture as much of the variation in NDSI-NDVI values observed in the snow covered forests as possible while minimizing inclusion of non-forested pixels. It was designed to include forest-covered pixels that have NDSI values lower than 0.4, yet have NDVI values lower than would be expected for snow-free conditions (Klein et al., 1998).

7.4.1.1.3 Snow / Cloud Discrimination

Snow/cloud-discrimination techniques are based on differences between cloud and snow reflectance and emittance characteristics. Clouds are highly variable and may be detected by their generally-high reflectance in the visible and near-IR parts of the electromagnetic spectrum (Kulkarni et al, 2002), whereas the reflectance of snow drops in the short-wave infrared part of the spectrum.

While the NDSI can separate snow from most obscuring clouds, it does not always identify or discriminate optically-thin cirrus clouds from snow. Analyses of AWIFS and MODIS data show that NDSI can map snow under cirrus clouds at least some of the time. This algorithm will be further improves, as INSAT 3D Met payload is having thermal bands. Appropriate brightness temperature threshold will be used to separate cloud from snow (Romanov, et. al., 2003). This will be additional criteria than in build criteria of NDSI.

7.4.1.1.4 Estimation of Snow Reflectance

Various parameters required to estimate reflectance are mean solar exo-atmospheric spectral irradiances in the sensor bands, digital elevation information, solar declination, mean earth-sun distance on a Julian day, and the calibration parameters of the sensor, such as maximum and minimum radiances in the sensor bands. The terrain topography parameters, viz., terrain slope and aspect are derived from the digital elevation information of the terrain. The local illumination angle for each pixel, which determines the amount of direct solar radiation incident on a sloped surface, is computed using both the sun and terrain geometry.

Markham and Barker equation for computing reflectance from a flat area cannot be valid for the Himalayan region where the terrain is highly undulating. To estimate reflectance from a rugged terrain, cosine of the local illumination angle, not the cosine of solar zenith angle, has to be used as given below:

$$\rho_\lambda = \pi L_\lambda d^2 / E_{\text{sun}\lambda} \cos\theta_i$$

Where, d is the mean earth-sun distance on a Julian day (AU), and θ_i is the local illumination angle (degree), the angle between the Sun's rays and the surface normal and is calculated by using the relation given by Robinson (1966).

Snow, like all natural surfaces, is an anisotropic reflector (Salomonson and Marlatt, 1968; Dirmhirn and Eaton, 1975; Steffen, 1987; Nolin and Liang, 2000). The reflectance from snow is greatest in the forward direction and is largely specular. While freshly fallen snow can be nearly a Lambertian reflecting surface, as snow metamorphoses the specular component characteristic of forward scattering increases. This means, reflectance of snow will change depending upon view and illumination geometry. This can be described by Bidirectional reflectance distribution Function (BRDF) (George Joseph, 2005).

$$F(\theta_i, \phi_i, \theta_r, \phi_r) = dL_r(\theta_i, \phi_i, \theta_r, \phi_r) / L_i \cos \theta_i dw_i$$

Where,

θ_i = Zenith angle of incident ray

ϕ_i = Azimuth angle of incident ray

θ_r = Zenith angle of reflected ray

ϕ_r = Azimuth angle of reflected ray

L_i = Incident radiance

dL_r = Reflected radiance in solid angle

dw_i = Solid angle

7.4.1.1.5 SNOW FRACTION RETRIEVAL

To calculate snow fraction (F), technique similar to a linear mixture technique can be used (Romanov and Tarpley, 2004). This techniques need two end members representing the visible reflectance of a completely snow-covered and completely snow-free land surface, R_{snow} and R_{land} , respectively.

$$F = (R - R_{\text{land}}) / (R_{\text{snow}} - R_{\text{land}})$$

Where, R is the observed visible reflectance of the scene. The reflectance of snow free land in every grid cell of the map will be established from satellite data obtained during snow free season. The reflectance of snow assumed to be independent of location and determined empirically from satellite data or from field reflectance observations. Previous investigations have shown that snow fraction retrievals was unreliable over mountainous area due to frequent specular reflectance effects on satellite observed visible reflectance (Romanov and Tarpley, 2004). Attempt will be made to resolve this problem by using concepts mentioned above as local illumination angle correction, Bidirectional reflectance distribution Function and multiple data analysis in a day.

7.4.1.1.6 RELATIONSHIP BETWEEN SNOW FRACTION AND DEPTH

Romanov and Tarpley, (2004) have developed a statistical relationship between satellite observed snow fraction and field observed snow depth. For this purpose field snow depth data of 1400 locations in Great Plains of USA and Canadian Prairies were analyzed. During matching observations, to reduce the effect of possible inhomogeneity of the snow depth distribution and inaccuracy of gecoding, snow fraction was averaged 3×3 grid. For development of this technique, forested region was exclude. A statistical relationship was developed between snow fraction and depth (Romanov and Tarpley, 2004).

$$D = e^{aF} - 1$$

Where, D (cm) is the snow depth, F (%) is the snow fraction and a is a parameter. The best approximation of snow fraction and snow depth was achieve with $a = 0.0333$. This means 100 percent snow fraction can give snow depth around 27 cm. This could be major limitation in the Himalaya, as snow depth is normally very high due orographic effect and avalanche accumulation of snow.

In order to apply this concept in the Himalaya, daily snow depth data needs to be collected from IMD and SASE observatories and region specific relationship needs to be developed. This relationship should be developed using historical INSAT, MODIS and snow depth data.

7.4.1.2 Flow Chart

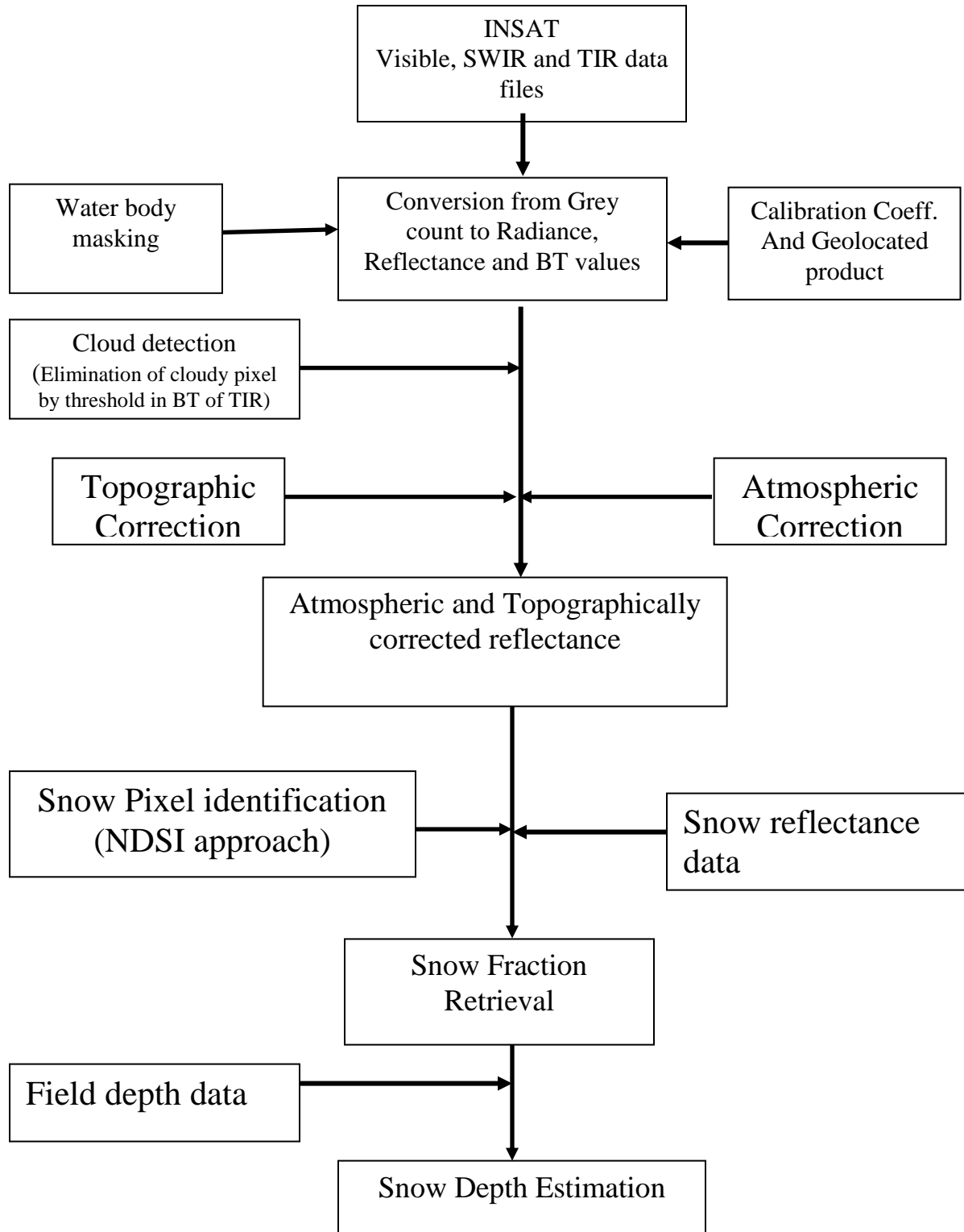


Figure 1. Flow chart to estimate Snow Depth estimation using INSAT 3D.

7.4.2 Operational Implementation

7.4.2.1 Step 1: Conversion from gray count to BT

In this step, the DN values will be converted into Radiance, Reflectance and Brightness temperature using calibration coefficient available with INSAT 3D data. The radiometrically-processed data will also be geolocated and this will provide a radiometrically and geometrically corrected product for further analysis.

7.4.2.2 Step 2: Cloud elimination

This step includes the cloud screening from the INSAT 3D image. Cloud screening is based on the temperature data and will help to clear cloudy pixels, which possibly are not feasible to screen out using visible and SWIR channel based NDSI image.

7.4.2.3 Step 3: Topographic and Atmospheric correction

In this step, DEM data will be used to compute the terrain parameters like slope and aspect of the terrain, which will further be used to compute the local illumination angle. Atmospheric correction algorithm will be applied to compute the atmospherically corrected radiance and reflectance values with standard procedures. This step will provide us the atmospherically and topographically corrected radiances and reflectance.

7.4.2.4 Step 4: Snow pixel identification

Snow pixel identification will be done by using NDSI based approach which uses the normalized ratio of visible and SWIR wavelength reflectance. This prepares a binary map of either snow or non-snow pixels.

7.4.2.5 Snow fraction retrieval

Fractional snow map will be prepared by using linear mixing approach. This considers land and pure snow as end members and compute the snow fraction of any particular pixel using reflectance value.

7.4.2.6 Snow Depth Estimation

A statistical relationship was developed between snow fraction and depth (Romanov and Tarpley, 2004). Snow depth will be estimated by using this relationship for each pixel.

7.5 Outputs

Parameter	Unit	Min	Max	Accuracy	Resolution
SD	cm	-	-	-	1 x 1 deg

7.5.1 format of the output and the domain

Geolocated Snow depth map.
40 S to 40 N; 30 E to 120 E.

7.6 Validation

7.6.1 Comparison of INSAT 3D snow depth with field observations:

INSAT-derived snow depth will continue to be compared with snow depth obtained from field locations. Sites, which were used for development of snow depth algorithm, will be used during validation, however both the activities will be carried out at different time frame.

7.6.2 Estimate of Errors in Snow Depth Mapping

Standard statistical methods will be used to assess error of estimation, as snow depth data is available from field and satellite.

7.7 Technical issues:

The snow depth of this method is limited to 27 cm of snow depth in prairie region which is expected to deteriorate further for highly rugged Himalayan mountain. It is required to develop the exponential relationship for Himalayan region based on snow depth.

7.8 Future Scope

In future scope the developed statistical relationship of snow depth with fractional snow will be modified for Himalayan region as and when data will be available. Indian Meteorological Department will provide field data of snow depth and snow fraction.

7.9 References

1. Clarke, A.D. and K.J. Noone, 1985: Soot in the Arctic snowpack: a cause for perturbations in radiative transfer. *Atmospheric Environment*, 19, pp 2045-2053.
2. Dirmhirn, I. and F.D. Eaton, 1975: Some characteristics of the albedo of snow. *Journal of Applied Meteorology*, 14, pp 375-379.
3. Foster, J. L., and Chang, A. T. C. (1993). Snow Cover. In "Atlas of Satellite Observations Related to Global Change." (R. L. Burney, C. L. Parkinson, and J. L. Foster, Eds.), pp. 361-370. Cambridge University Press, Cambridge.
4. George Joseph, 2003, Fundamental of Remote Sensing, Universities Press, Hyderabad, 371.
5. Hall, D.K., G.A. Riggs and V.V. Salomonson, 1995: Development of methods for mapping global snow cover using moderate resolution imaging spectroradiometer data, *Remote Sensing of Environment*, 54, pp 127-140.
6. Hall, D.K., J.L. Foster, D.L. Verbyla, A.G. Klein and C.S. Benson, 1998: Assessment of snow-cover mapping accuracy in a variety of vegetation-cover densities in central Alaska, *Remote Sensing of Environment*, 66:129-137.
7. Hall, D.K., V.V. Salomonson, G.A. Riggs, N. DiGirolamo and K.J. Bayr, MODIS snow cover products, *Remote Sensing of Environment*, submitted.
8. Klein, A.G., D.K. Hall and G.A. Riggs, 1998: Improving snow cover mapping in forests through the use of a canopy reflectance model, *Hydrological Processes*, 12:1723-1744 .

9. Kulkarni A. V., S. K. Singh, P. Mathur and V. D. Mishra, 2006, Algorithm to monitor snow cover using AWiFS data of RESOURCESAT for the Himalayan region, *Intl. Journal of Remote Sensing*, 27(12), 2449-2457.
10. Kulkarni A. V., P. Mathur, S. K. Singh, B. P. Rathore and N. Thakur, 2004, Remote sensing based techniques for snow cover monitoring for the Himalayan region, *Proc. International Symposium on Snow Monitoring and Avalanches*, Manali, 399-405.
11. Kulkarni, A.V. and B. P. Rathore, 2003. Snow cover monitoring in Baspa basin using IRS WiFS data, *Mausam* 54(1), 335-34.
12. Kulkarni A.V, J. Srinivasulu, S. S. Manjul and P. Mathur, 2002c, Field based spectral reflectance to develop NDSI method for snow cover monitoring, *Journal of Indian Society of Remote Sensing* 30 (1 & 2), 73-80.
13. Kulkarni A.V, S. S. Randhwara, B. P. Rathore, I. M. Bahuguna and R.K. Sood, 2002a. A snow and glacier melt runoff model to estimate hydropower potential, *Journal of Indian Society of Remote Sensing* 30 (4), 221-228.
14. Kulkarni A.V, P. Mathur, B.P. Rathore, Suja Alex, N. Thakur and Manoj Kumar, 2002b. Effect of Global warming on snow ablation pattern in the Himalayas, *Current Science* 83(2), 120-123.
15. Markham, B.L. and J.L. Barker, 1986: Landsat MSS and TM post-calibration dynamic ranges, exoatmospheric reflectances and at-satellite temperatures, *EOSAT Technical Notes*, No. 1, August, pp 3-8.
16. Negi, H. S., A. V. Kulkarni, R. P. Prajapati, S.K. Singh and J. K. Sharma, 2006, Effect of contamination and mixed objects on snow reflectance using spectroradiometer, Scientific Report number RSAM/SAC/RESIPA/MWRG-GLI/SN25/2006, Space Applications Centre, Ahmedabad, India, 24p
17. Nolin, A.W. and S. Liang, 2000: Progress in Bidirectional reflectance modeling and applications for surface particulate media: snow and soils, *Remote Sensing Reviews*, 18:307-342.
18. O'Brien, H.W. and R.H. Munis, 1975: Red and near-infrared spectral reflectance of snow. In: *Operational Applications of Satellite Snow cover Observations*, edited by A. Rango, NASA SP-391 (Washington, D.C.: NASA), pp 345-360.
19. Robinson N., 1966, Solar radiation, Elsevier, Amsterdam, p 347.
20. Romanov P. and Tarpley D. 2004: Estimation of snow depth over open prairie environments using GOES imager observations, *Hydrological processes*, 18, 1073-1087.
21. Romanov P. and Tarpley D. 2003, Automated monitoring of snow cover over south America using GOES imager data. *Int. J. of Remote Sensing*, 24(5), 1119-1125.
22. Salomonson, V.V. and D.C. Marlatt, 1968: Anisotropic solar reflectance over white sand, snow and stratus clouds. *Journal of Applied Meteorology*, 7, pp 475-483.
23. Srinivasulu J. and A. V. Kulkarni, 2004, A Satellite based Spectral Reflectance Model for Snow and Glacier Studies in the Himalayan Terrain, *Proc. of the Indian Acad. Sci. (Earth and Planet. Sci.)* 113 (1), 117-128.
24. Steffen, K., 1987, Bidirectional reflectance of snow. In B.E. Goodison, R.G. Barry, and J.Dozier, (editors): *Large scale effects of seasonal snow cover*. Proceedings of the IAHS Symposium held in Vancouver on 19-22 August 1987 (Vancouver, Canada: IAHS), pp 415-425.

25. Townshend, J.R.G. and C.J. Tucker, 1984: Objective assessment of Advanced Very High Resolution Radiometer data for land cover mapping, International Journal of Remote Sensing, 5:497-504.
26. Tucker, C.J., 1979: Red and photographic infrared linear combinations for monitoring vegetation, Remote Sensing of Environment, 8, pp 127-150.
27. Tucker, C.J., 1986: Maximum normalized difference vegetation index images for sub-Saharan Africa for 1983-1985, International Journal of Remote Sensing, 7, pp 1383-1384.
28. Warren, S.G. and W.J. Wiscombe, 1980: A model for the spectral albedo of snow II: snow containing atmospheric aerosols, Journal of the Atmospheric Sciences, 37, pp 2734-2745.

8. Fire

S.No.	Product Name	Spatial Resolution	Temporal Resolution
1	3DIMG_L2P_FIR	Point (approx. 4x4 km area)	30 minutes

8. Fire Identification

8.1 Algorithm Configuration Information

8.1.1 Algorithm Name

Fire Identification (FIR)
(Ref : IMD RFP Section 11.13)

8.1.2 Algorithm Identifier

3DIMG_L2P_FIR

8.1.3 Algorithm Specification

Version	Date	Prepared by	Description
1.0	14.02.2007	C. P. Singh, Bipasha Paul Shukla	Fire Identification Baseline Document

8.2 Introduction

In this document, we offer some background to the fire identification problem, list the INSAT-3D instrument characteristics, describe the theoretical basis of the fire identification algorithm, discuss inputs required, output deliverables and the practical aspects of the algorithm implementation, and outline the planned validation approach, the technical issues and the future scope.

8.2.1 Overview and background

Forest fire management in tropical countries is one of the major issues. Forest fire quite frequently occurs during summer seasons in tropical countries. A study by forest survey of India has revealed that 51% of the forest area in Assam and Gujarat, 93% in Arunachal Pradesh, 67% in Bihar, 69% in Himachal Pradesh, 46 % in Jammu and Kashmir, 45% in Karnataka, 76% in Madhya Pradesh, 94% in Meghalaya and Orissa, 87% in Nagaland, 58% in Uttar Pradesh and 33% in W. Bengal is subject to annual fires.

One of the most important critical elements of the forest fire management system (FFMS) in the country is the real time detection onset of fire and it's monitoring; study the rate, direction and quantitative estimation of fire spread and amount of smoke emission. Satellite data with suitable spectral bands for fire detection (Visible, SWIR, MIR and Thermal IR bands), daily or twice a day's repetitivity (day and night) and bare minimum spatial resolution, which can locate the fire, can play an important role in development of country's FFMS. Geostationary satellite such as GOES with automated biomass burning algorithm (ABBA) have matured enough for providing information on large-scale forest fires on a regular basis (Prins *et al*, 1992, 1994, 1998). INSAT-3D imager data with 1 km resolution in Visible and SWIR bands and 4 km. in MIR and in TIR-I and TIR-II will help in detecting and monitoring of large scale forest fires, smoke and burn scar.

The purpose of this document is to present an algorithm for retrieving forest fire areas from INSAT-3D multi-wavelength thermal radiation measurements in clear skies. The INSAT-3D fire products will be built on the experience of fire assessment using the MODIS, NOAA-AVHRR and GOES systems. The fire products will include an identification of the occurrence of thermal anomalies, and an estimate the total emitted

energy from the fire. The products will be made available at full resolution (4 km) and as spatial summaries and temporal composites. Daytime and nighttime fire distributions products will be identified.

The fire products will be developed on the basis of convergence of evidence from different spectral information. The INSAT-3D fire products will provide information on the location of a fire, its emitted energy, and an estimate of area burned. The fire products will be made available through IMD as daily 4 km resolution and spatially and temporally summarized products (10 km, and 8 day and monthly), more suited for use by the broader environmental management community as well as modelling community.

8.2.2 Objective

The basic purpose of this document is to propose an algorithm for identifying fire using INSAT 3D imager data. This algorithm is supposed to form the basis of real time application of INSAT 3D data in the identification of fire.

8.3 Inputs

Inputs to the algorithm will include geo-referenced radiant temperature (in deg Kelvin) for MIR,TIR-I,TIR-II, along with satellite viewing geometry (solar zenith angle, satellite zenith angle, azimuth angle). Additionally there is a requirement for temperature data from all IMD-stations, which will help in defining thresholds. Cloud and land/sea mask data will also be used. All these inputs are specifically categorised in the following subsections:

8.3.1 Static Data

About 10 years temperature data from all IMD-stations (as stated in table below), interpolated to geo-referenced raster format (GeoTIFF) at 4x4 km spatial resolution for entire India. This will be useful in defining the background temperature for different temperature zones.

Parameter	Resolution	Quantization	Accuracy	Source
Temperature	Pixel (4x4 km spatial resolution)	10 bit	--	Derived from Temperature data obtained from IMD

8.3.2 Image and preprocessing data (Dynamic)

The following table gives a list of inputs required for algorithm input and calibration:

Parameter	Resolution	Quantization	Accuracy	Source
Radiometric and geometric corrected gray count values of MIR channel (3.9)	pixel	10 bit	--	Derived from raw data by DP (data processing)
Radiometric and geometric corrected gray count values of TIR-I channel (10.5)	pixel	10 bit	-	Derived from raw data by DP
Radiometric and geometric corrected gray count values of TIR-II channel (11.5)	pixel	10 bit	-	Derived from raw data by DP
Gray value to brightness temperature (MIR, TIR-1, TIR-2) conversion table	-	-	0.3 K	Derived by DP
Geolocation file	Pixel	-	1 pixel	Derived by DP

8.4 Algorithm Functional Specifications

The INSAT-3D fire detection and characterization techniques are planned to be fully automated for the production of daily fire information at country level. In order to detect the presence of fire in a non-interactive fashion, a set of detection multiband thresholding criteria different for the day and night fire observations are prescribed. These criteria are based on the apparent temperature of the fire pixel and the difference between the fire pixel and its background temperature. In this section we describe the theoretical basis and algorithm overview for identification of fire.

8.4.1 Overview

8.4.1.1 Theoretical Background

- Any object above absolute zero (0 K; -273.16° C; -459.69° F) emits EMR.
- As temp. increases the maxima shifts towards shorter wave length.

- $\lambda_{\text{max}}=2897/T$; μm (Wien's displacement law) can give max. W.L. at which the exitance is maximum & is related to Temp. (e.g, $\lambda_{\text{max}}=9.66 \mu\text{m}$ at 300°K)

INSAT MIR Channel (3.70 to 3.95 μm) is located near the spectral maximum for radiative emission for objects radiating at temperature around 400 to 1200 K. this temperature is closed to the temperature of burning forest biomass. INSAT, TIR-I Channel (10.20 μm – 11.30 μm) and TIR-II (11.5 μm to 12.5 μm) are located near the spectral maxima for normal environment temperature i.e. around 300 K (fig.1). Therefore, both these channels will be useful in fire detection algorithms.

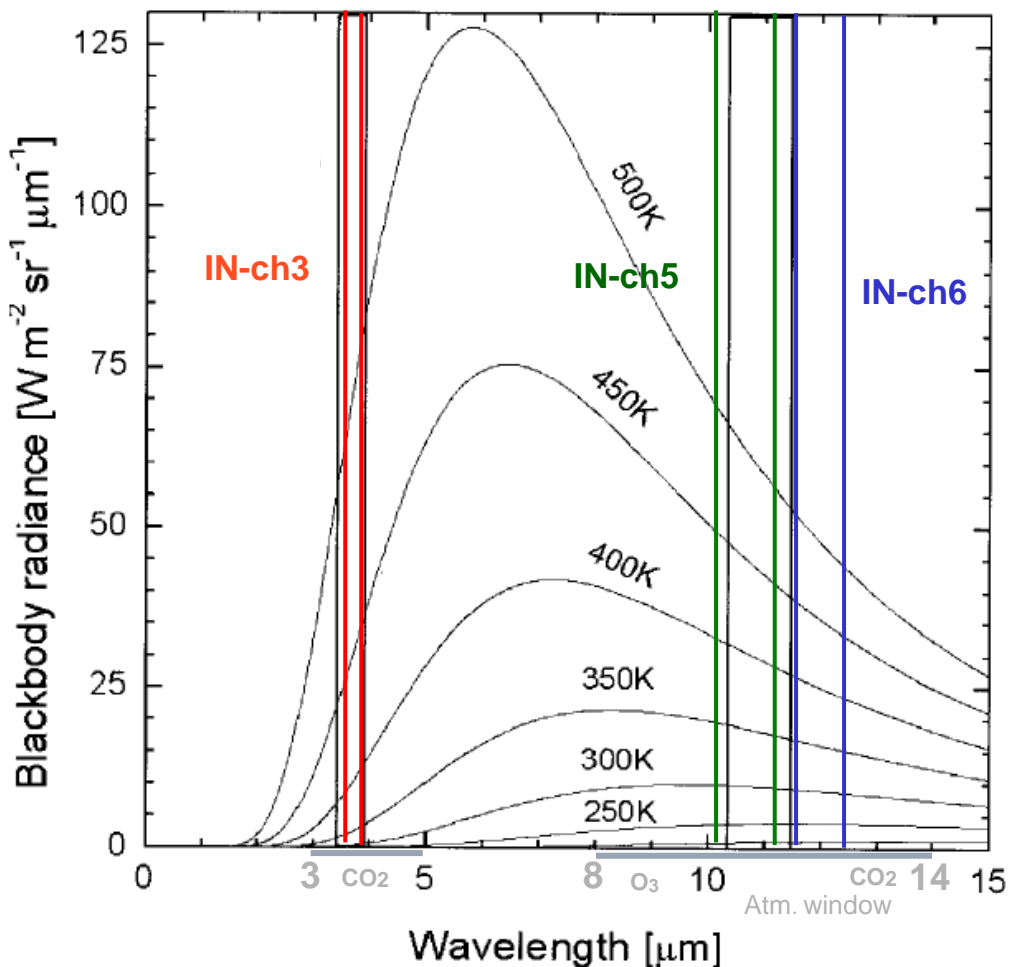


Figure 1. Plank Function and the location of AVHRR channel 3 and 4 and INSAT-3D Channel 3, 5 and 6

Fire detection algorithms using daily NOAA –AVHRR images developed by Li. *et al.*, (2000) and latest version of Fire Identification, Mapping and Monitoring algorithms (FIMMA) developed by NOAA/NESDIS will be evaluated. Pixel will be flagged as containing fire if the values of its brightness temperature and or reflectance exceeds or falls below certain predetermined threshold values, which are fixed during development

phase. Visible and SWIR bands will be utilized for masking clouds and water bodies. Contextual Algorithm (Giglio, *et al.*, 1999; and Kaufman, *et al.*, 1998) is proposed at this stage.

A fire location represents the approximate location of the fire pixels and do not represent the actual fire size, which is usually much smaller than pixel size (4 km.). The INSAT at Nadir is 4x4 Km, for MIR and TIR, which is quite large, but the fire phenomenon is usually much smaller than that. Studies at Cooperative Institute of Meteorological Satellite Studies (CIMSS) at the University of Wisconsin have shown that the sub – satellite point, and smoldering at 450 K, in case of GOES (IFOV: 4x4Km) is approximately 0.5 to 1 acre in size in relatively non-cloudy conditions.

Robinson (1991) has shown that due to very high amplification over background at 3.7 μm for forest fires occupying even a small fraction of a percent of an AVHRR pixel can substantially increase the mid IR brightness of the entire pixel. Therefore, fire (active fire) can be monitored at very low spatial resolution.

8.4.1.2 Algorithm Overview

The fire detection algorithm proposed here employs multi-thresholding contextual technique, which includes multi band thresholds, and compares with the background. The algorithm will first mask out ocean, desert, water and cloud pixels and then proceed further. The contextual algorithms identify a fire pixel based on the level of contrast between the potential fire pixel and its “background” pixels (the definition of background varies according to kernel size). As opposed to the fixed threshold techniques, which must be defined for given regions and seasons, the contextual algorithm is supposed to be flexible and effective in different environmental conditions. Potential fire pixels will be identified using a less restrictive version of the threshold algorithm. These threshold values will be determined through visual inspection of known fire/non-fire pixels. An initial threshold reduces the number of candidate pixels to be applied to the contextual algorithm. The contextual algorithm is based on detecting the contrast between a pixel and its background. A pixel's background can be defined as the 15x15 window surrounding the subject pixel. Because of the large areal extent of many interior Indian wildfires, it is necessary to have such a large window size to define the background values. If a background window size is too small (for example, 3x3), there is a good chance that large wildfires occupying several pixels will elevate the background values rendering the fire undetectable.

The algorithm is a three-step process:

First, the temperatures of channels 3, 5, & 6 of INSAT-3D from pixels adjacent to the test pixel will be averaged; these values will be utilized in a separate algorithm to estimate background temperature and adjusted temperature values for channels 3 & 5.

Second, a user-defined minimum fire temperature of interest will be specified.

Third, if the adjusted temperature value for channel 3 is greater than the threshold channel 3 temperature, the pixel is classified as fire. The fire identification algorithm flowchart is given in next subsection:

8.4.1.3 Flow Chart

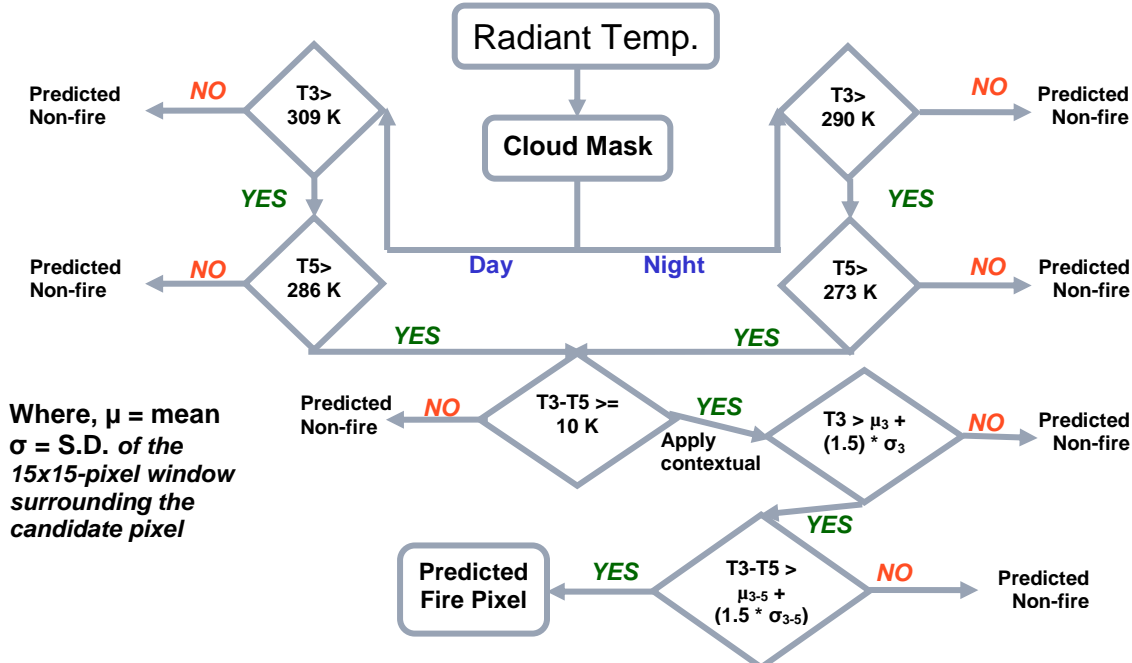


Figure.2. Contextual Algorithm Flowchart

(Note: The temperature values are indicative only. The actual value will be decided after analyzing the ground data for different regions and seasons)

8.4.2 Operational retrieval Implementation

The operational implementation of the retrieval process can be enumerated as follows:

Step 1 : Conversion of gray counts to radiance and radiant temperatures

Step 2 : Cloud, Land/Sea, desert and major inland water bodies masking

Step 3: Solar logic flag: pixel is sunlit if the solar zenith angle is $>0^\circ$ and $<86.5^\circ$ to partition day and night pixels and have dynamic thresholds for MIR channel ($3.9\mu\text{m}$). [e.g. $T_3 = (300+15*\cos(\text{solar zenith angle}))\text{ K}$].

Step 4: Defining of thresholds for background temperature using historical IMD data and building thresholds for different parts of the country and for different seasons. Training dataset of actual forest fires over the Indian region for MIR, TIR-I and TIR-II channels. The methodology to be followed is to first assume initial value of thresholds and then fine tune them, using visual inspection.

Step 5: Implementation of three step tests (mentioned above in section 1.4.2)

Step 6: Contextual Fire detection algorithm

8.5 Outputs

Generation of fire map.

8.5.1 Format of the output and the domain

Output: lat , lon, Fire flag (Getiff Image)

Fire flag: 1 - Fire pixels, 0 - Non-fire pixels

8.6 Validation

This gives an outline of proposed validation methodology.

8.6.1 Data required

Radiometric and geometric corrected radiant temperature of corresponding INSAT-3D channels (given in table below) of MODIS sensor acquired over Indian region for fire event.

Channel number	Central wavelength (μm)	Purpose
1	0.65	Sun glint and coastal false alarm rejection; cloud masking.
2	0.86	Bright surface, sun glint, and coastal false alarm rejection; cloud masking.
7	2.1	Sun glint and coastal false alarm rejection.
21	4.0	High-range channel for active fire detection.
22	4.0	Low-range channel for active fire detection.
31	11.0	Active fire detection, cloud masking.
32	12.0	Cloud masking.

(Source: Giglio, *et al*, 2003)

8.6.2 Methods of validation

- Validation through comparison with images acquired over forest fire events from other sensors.
- Validation through temporal monitoring.
- Verification by ground truth data.

8.7 Technical issues (limitation etc.)

Accuracy of the product will depend on the accuracy of the input radiance. Further some limitations in the present study are listed as:

- (i) It is assumed that an adequate knowledge of the background temperature prevailing in India in all season and geographic regions are known and correct.
- (ii) False fire alarm will be mostly controlled. However, fine tuning in first year of operation may be required.

- (iii) Fire pixel flagged and will represent approximate locations of fire and do not represent the actual fire size.
- (iv) Fires below threshold (Small cool fires) and those burning below thick overgrowth may go undetected.

8.8 Future Scope

Further tuning of thresholds by inclusion of more training datasets.

8.9 References

1. Giglio, L., J. D. Kendall and C. O. Justice, 1999: Evaluation of global fire detection algorithms using simulated AVHRR infrared data. Int. Joun. of remote Sensing, 20, 1947 - 1985.
2. Giglio L., J. Descloires, C. O. Justice, Y. J. Kaufman, 2003 : An Enhanced Contextual Fire Detection Algorithm for MODIS. Remote Sensing of Environment, 87, 273 – 282.
3. Kaufman, Y. J., Justice, C. O., Flynn, L. P., Kendall, J.D., Prins, E.M., Giglio, L., Ward, D. E., Menzel, W.P. and Setzer, A. W., 1998: potential global fire monitoring from EOS –MODIS. J. Geo. Res., 103, 32215 – 32238.
4. Li, Z., S. Nadson, and J. Cihlar., 2000: Satellite – Based detection of Canadian boreal forest fires: development and applications of the algorithms. Int. Joun. of remote Sensing, Vol. 21 (16), pp. 3057 -3069.
5. Prins, E.M., and W.P. Menzel, 1992 : Geostationary Satellite detection of biomass burning in South America. Int. Joun. of remote Sensing, 13, 2783-2799.
6. Prins, E.M., and W.P. Menzel, 1994 : Trends in South American biomass burning detected with the GOES visible infrared spin scan radiometer atmospheric sounder from 1983 to 1991. J. Geo. Res., 99, 16719-16735.
7. Prins, E.M., J.M. Feltz, W.P. Menzel and D.E. Ward, 1998 : An overview of GOES-8 diurnal fire and smoke results for SCAR-B and the 1995 fire season in South America. Accepted by SCAR-B Special Issue, J.Geo. Res., 103, 31821-31835.
8. Robinson, J. M., 1991: Fire from space: global fire evaluation using infrared remote sensing, Int. Joun. of remote Sensing. 12 (1), 3 -24.

9. Smoke

S.No.	Product Name	Spatial Resolution	Temporal Resolution
1	3DIMG_L2P_SMK	Point (approx. 4x4 km area)	30 minutes

9. Smoke Identification (SI)

9.1 Algorithm Configuration Information

9.1.1 Algorithm Name

Smoke Identification (SI)

(Ref : IMD RFP Section 11.13)

9.1.2 Algorithm Identifier

3DIMG_L2P_SMK

9.1.3 Algorithm Specification

Version	Date	Prepared by	Description
1.0	14.02.2007	Bipasha Paul Shukla C. P. Singh	Smoke Identification Baseline Document

9.2 Introduction

In this document, we offer some background to the smoke identification problem, list the INSAT-3D instrument characteristics, describe the theoretical basis of the smoke identification algorithm, discuss inputs required, output deliverables and the practical aspects of the algorithm implementation, and outline the planned validation approach, the technical issues and the future scope.

9.2.1 Overview and Background

Smoke is a form of particulate matter, which contains liquid or solid particles of the size ranging from 1–200 μm . It is formed by combustion or other chemical processes. Each year more than 100 million tons of smoke aerosols are released into the atmosphere as a result of biomass burning. More than 80percent of this burning is in the tropical regions [1]. Smoke plumes can travel over hundreds or even thousands of kilometers horizontally and also reach up to stratosphere under certain atmospheric circulation conditions. Thus smoke can have an impact far beyond the region of fire activity. Smoke play a major role on the radiation balance of the earth-atmosphere system. Smoke particles scatter and absorb incoming solar radiation, thereby having a two-fold impact, i.e. a cooling effect at the surface, but warming effect on the atmosphere. Since the magnitude of the scattering effect outweighs that of absorption, smoke has a net cooling effect at the top of the atmosphere-surface system. This is often called the direct effect of smoke aerosols [1].

Smoke can also modify the short wave reflective properties of clouds by acting as cloud condensation nuclei [2]. Under a limited supply of water vapor, an increased number of nuclei result in smaller cloud droplets that have higher reflectivity than larger cloud droplets .This effect called the indirect radiative forcing, is difficult to quantify and has large uncertainties associated with the sign and magnitudes.

Understanding such numerous and complex effects of smoke on weather and climate requires a good knowledge of the spatial and temporal variation of smoke and its optical properties, which is only feasible by means of satellite observation. Identification of smoke on satellite

imagery is a prerequisite to study and retrieve physical, chemical, and optical properties of smoke.

9.2.2 Objective

The basic purpose of this document is to propose an algorithm for identifying smoke using INSAT 3D imager data. This algorithm is supposed to form the basis of real time application of INSAT 3D data in the identification of smoke.

9.3 Inputs

Inputs to the algorithm will include geo-referenced, corrected Albedo, Digital counts for Visible channel and geo-referenced Brightness temperature for MIR,TIR1, TIR2, along with satellite viewing geometry (solar zenith angle, satellite zenith angle, azimuth angle). Additionally there is a requirement for dataset of forest fires acquired over India for defining thresholds.

All these inputs are specifically categorized in the following subsections.

9.3.1 Static Data

Radiometric and geometric corrected dataset of forest fires acquired over Indian region for the channels of corresponding INSAT-3D channels (given in table below) of MODIS sensor.

Table 2: STATIC DATA

Channel Number (MODIS)	Channel Number (INSAT3D)	Central wavelength (μm)
1	1	0.65
21	3	4.0
22	3	4.0
31	5	11.0
32	6	12.0

9.3.2 Image and preprocessing data (Dynamic)

The following table gives a list of inputs required for algorithm input and calibration:

Table 3: IMAGE AND CALIBRATION INPUTS

Parameter	Resolution	Quantization	Accuracy	Source
Radiometric and geometric corrected gray count values of VIS channel (6.5)	pixel	10 bit	--	Derived from raw data by DP (data processing)
Radiometric and geometric corrected gray count values of MIR channel (3.9)	pixel	10 bit	--	Derived from raw data by DP (data processing)
Radiometric and geometric corrected gray count values of TIR-I channel (10.5)	pixel	10 bit	-	Derived from raw data by DP
Radiometric and geometric corrected gray count values of TIR-II channel (11.5)	pixel	10 bit	-	Derived from raw data by DP
Gray value to brightness temperature (MIR, TIR-1, TIR-2) conversion table	-	-	0.3 K	Derived by DP
Gray value to albedo (VIS) conversion table	-	-	0.3 K	Derived by DP
Geolocation file	Pixel	-	1 pixel	Derived by DP

9.3.3 Other Auxillary data and Model Inputs

Table 4: AUXILARY DATA

Parameter	Resolution	Quantization	Accuracy	Source
Solar Zenith Angle	pixel	-	--	Derived by DP
Satellite Zenith Angle	pixel	-	--	Derived by DP
Azimuth angle	pixel	-	-	Derived by DP

9.4 Algorithm Functional Specifications

Automatic detection of smoke pixels in a satellite imagery calls for development of algorithm employing multi-thresholding techniques and utilizing multi-band satellite data. In this section we describe the theoretical basis and algorithm overview for identification of smoke.

9.4.1 Overview

9.4.1.1 Theoretical Background

Identification of smoke through satellite observations is a challenge in itself. The large spectral overlap in the spectral signature smoke and other scene types such as clouds and background surfaces has complicated the problem. Till date, very few studies have been done to discriminate smoke in a satellite imagery. The most commonly used method of identifying smoke is to assign different colors to different channels or channel combinations. The resulting false-color images can provide visual separation of smoke from other objects. For example, Kaufman et al. [2] assigned AVHRR channel 1 to red, channel 2 to green, and inverse channel 4 to blue, generating a composite image showing smoke plumes [3]. The Hazard Mapping System (HMS) developed in 2001 by the National Oceanic and Atmospheric Administrations (NOAA) National Environmental Satellite and Data Information Service (NESDIS) also generated the smoke outlines manually, primarily utilizing animated visible band satellite imagery.

Smoke plumes and their path can also be traced using temporal satellite imagery, through image processing techniques. But this methodology is a manual detection technique and can hardly be used for automatic detection of smoke in satellite imageries. Some sporadic efforts in the direction of distinguishing smoke in satellite imagery has been made in the past. The Geostationary Operational Environmental Satellite GOES-8 employed the automated smoke/aerosol detection algorithm (ASADA) to monitor biomass burning in South America [4], while some attempts for automatic detection of smoke using artificial neural networks and threshold approaches applied to AVHRR imagery was made by Li et al [3]

In general, smoke is composed of many small particles suspended in the air. These particles scatter and absorb (attenuate) different spectra of electromagnetic radiation. This absorption reduces transmittance of that radiation through the smoke. The effect of smoke aerosol as function of wavelength forms the crux of its satellite detection algorithm. Smoke has a large effect in the visible part of the spectrum, decreasing in magnitude with wavelength from the blue to the red region. In the near IR the effect is smaller than the variation in the surface reflectance between the smoke free area and the area affected by smoke. The smoke effect is not observable in the mid IR ($2.2 \mu\text{m}$) region due to the large ratio of the wavelength of radiation to the size of particles.

Thus using visible channel it is possible to distinguish smoke plumes over land. But the diffusion processes associated with smoke and clouds lead to fuzzy boundaries between them. Hence although the reflectance of smoke is generally less than that of clouds, the latter has so large a range of variation that it is difficult to use it to discriminate smoke pixels from cloudy pixels. Thus the biggest challenge in smoke detection is to isolate smoke from a smoke/Haze/ Cloud mix in a satellite imagery. Discrimination between smoke and clouds is generally made on the basis of cloud classification.

The channels Visible, MIR, TIR-1, TIR-2 of the INSAT-3D imager exhibit some distinction in the characteristics of smoke, clouds and underlying surface which is the basis of smoke identification.

Algorithm Overview

The smoke detection algorithm proposed here employs multi-thresholding technique, which includes single and multi band difference thresholds, corrected albedo calculations, sun glint mask and cloud edge detection. It first eliminates Smoke/ Cloud/ Haze free pixels and then screens out different kinds of cloudy pixels to arrive at smoke pixels. In general, the reflectance and brightness temperature of dense smoke have intermediate values between those of clouds and land. The reflectance of smoke is usually less than that of clouds, but higher than that of the underlying surface, while the converse is true for brightness temperature So double sided thresholding is applied in form of these five pass tests.

First pass Test:

A first pass thresholding is done on the visible channel counts to limit values indicative of haze/cloud mix.

Second pass Test:

Second pass is albedo thresholding to further screen out cloud/ surface reflectance over land and water.

Albedo Calculation for the VIS channel

$$A = \frac{\pi L_r}{F_0 \cos(\theta_0)} \quad (1)$$

where A is the albedo, L_r is the radiance, θ_0 is the solar zenith angle and F_0 is the incident radiance if the satellite were to look directly at the sun, which is computed as:

$$F_0 = \frac{\int_0^\infty S_\lambda w_\lambda d\lambda}{\int_0^\infty w_\lambda d\lambda} \quad (2)$$

where S_λ is the spectral irradiance of the sun and w_λ is the spectral response function for the channel.

Third pass Test:

Since sun glint often produces the same signature as smoke in visible imagery, regions with reflected solar angles less than a threshold value are not processed to avoid those areas affected by sun glint.

Fourth pass Test:

Thresholding on brightness temperature of MIR, TIR-1 and difference of these two channels is implemented to screen out opaque cirrus and stratus clouds. Since clouds usually have cold tops, they have low brightness temperatures in TIR-1 channel. Further the large difference in the brightness temperatures between the MIR and the TIR-1 channels due to the reflection of solar energy at $3.9\mu\text{m}$ is successful in screening out water clouds.

Fifth pass Test:

Thresholds are placed on the brightness temperature of TIR-1, TIR-2 and difference of these two channels is implemented to screen out low level moisture and cirrus clouds. Thresholding based on differences between brightness temperatures of TIR-1 and TIR-2 are widely used for cloud screening and is often referred to as the split window technique.

Pseudo Channel Index (PCI) Test :

Even after applying the above tests , misclassification between smoke and clouds is possible. For further screening, pseudo channel (CLD) is made use of and defined as:

$$CLD = \frac{(TIR2) - (Visible)}{(TIR2) + (Visible)} \quad (3)$$

where TIR2 and Visible refer to the radiation received in 12 μm and 0.65 μm channels respectively [5].

Owing to their different signatures in the pseudo channel, smoke plumes and clouds can be discriminated using a CLD threshold. Although in earlier studies CLD and Normalized Difference Vegetation Index (NDVI) feature space analysis was used for categorization of smoke and cloud, it was found to generate false alarms and was eventually improved by using multi-temporal change detection technique. However, in this study, it has been found that combining CLD with conventional multi-threshold test also improves the robustness of smoke detection. Thus pixels are further required to pass the following test,

$$CLD > C_1 \quad (4)$$

where ' C_1 ' is the threshold value for smoke plumes.

If a pixel passes all these 5 tests, surrounding pixels are checked to screen out cloud edge pixels.A flow diagram is given to illustrate the flow of the smoke detection algorithm.

9.4.1.2 Flow Chart

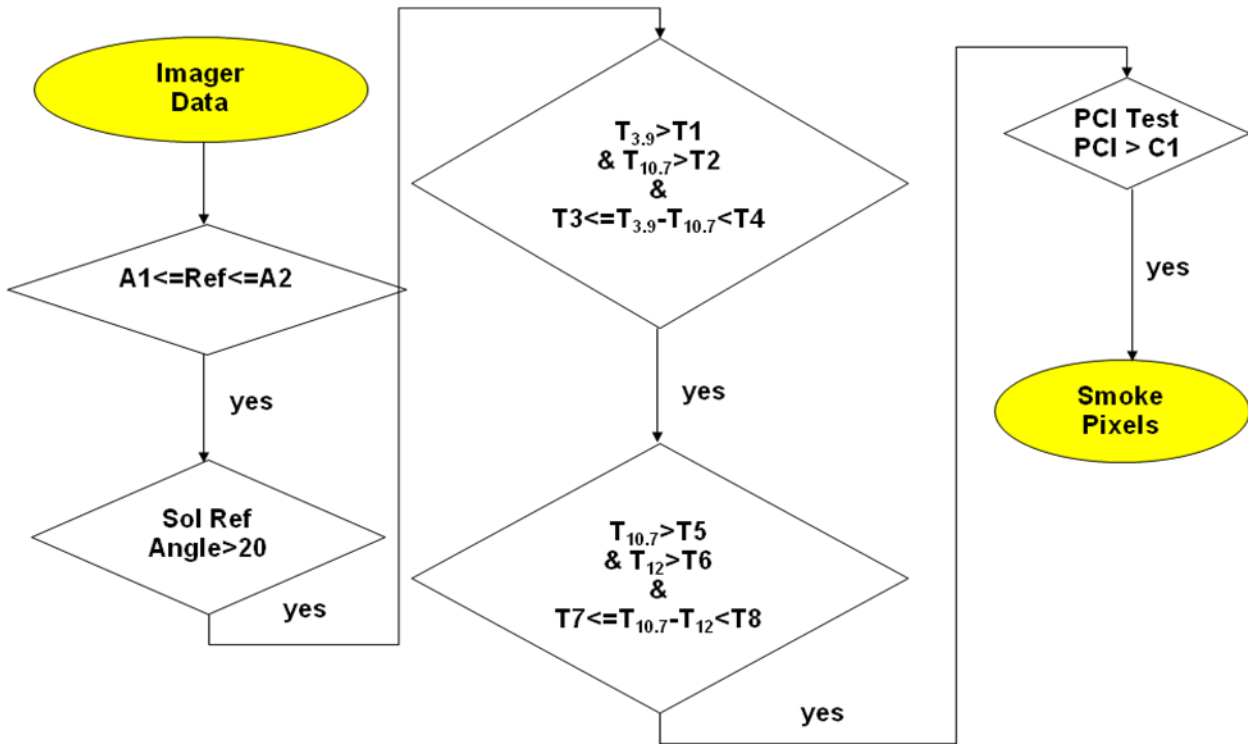


Figure 1: FLOW DIAGRAM FOR SMOKE DETECTION ALGORITHM

9.4.2 Operational retrieval implementation

The operational implementation of the retrieval process can be enumerated as follows:

1. Conversion of gray counts to radiance and brightness temperatures

2. Conversion of gray counts to Albedo for the VIS channel

This is done with the help of conversion tables.

3. Calculation of solar reflectance angle

To exclude sun glint processing path is taken for solar reflectance angle θ_r greater than threshold value (approximately 20deg)[4], where

$$\cos(\theta_r) = \sin(\theta)\sin(\theta_0)\cos(\phi) + \cos(\theta)\cos(\theta_0) \quad (3)$$

where θ is the viewing zenith angle, ϕ is the azimuth angle and, θ_0 is the Solar Zenith Angle.

4. Defining of thresholds

Using training dataset of forest fires over the Indian region for VIS, MIR , TIR-1 and TIR-2 channels, thresholds have to be defined for tests listed above. The methodology

to be followed is to first assume initial value of thresholds based on literature and then fine tune them, using visual inspection.

5. Implementation of five pass tests

6. Cloud edge detection algorithm

A difference image is produced from 10.7 and 3.9- μm channels and an adjacent pixel test is performed to detect cloud edges.

9.5 Output

Generation of smoke map

9.5.1 Format of the output and the domain

Output: **lat , lon, Smoke flag**

Smoke flag: 1 - Smoke pixels, 0 - Non-smoke pixels

Domain : 40 S to 40 N, 30 E to 120 E

9.6 Validation

This gives an outline of proposed validation methodology.

9.6.1 Data Required

Data from different sensors required for validation

Acquisition Time	Sensor	Area
Forest fire event	MODIS, AVHRR	Indian region

9.6.2 Method of Validation

1. Validation through comparison with images acquired over forest fire events from other sensors.
2. Validation through temporal monitoring.
3. Validation by matching with neighbourhood fire pixels, which is generated through fire identification algorithm (FI)

9.7 Technical Issues

Accuracy of the product will depend on the accuracy of the input radiance. Further some

limitations in the present study are listed as:

1. False classification due to noisy pixels.
2. Only daytime detection is possible.
3. Algorithm will be sensitive to the dataset used for defining the thresholds.
4. Cloud and smoke mixed pixels can give rise to misclassification.

9.8 Future work

1. Further tuning of thresholds by inclusion of more training datasets.

2. Incorporation of land cover classification data in the algorithm to aid in screening.

9.9 References

1. S. A.Christopher and J.Zhang , 2002: Int. J. Remote Sensing, Vol. 23, No. 22, pp 4931-4944.
2. Y. J. Kaufman, C. J. Tucker, and I. Fung, Remote sensing of biomass burningin the tropics, J. Geophys. Res., vol. 95, pp. 99279939, 1990.
3. Zhanqing Li, Alexandre Khananian, Robert H. Fraser, and Josef Cihlar,2001: Automatic Detection of Fire Smoke Using Artificial Neural Networks and Threshold Approaches Applied to AVHRR Imagery,IEEE Transactions on Geoscience and Remote science, Vol. 39, No. 9,1859-1870.
4. E. M.Prins, J. M. Feltz, W. P. Menzel, and D. E. Ward, 1998: An overview of GOES-8 diurnal fire and smoke results for SCAR-B and the 1995 fire season in South America, Jour. of Geo. Res., 103, D24, pp. 31,821-31,836.
5. Shukla, Bipasha Paul and Pal, P. K., 2009, Automatic smoke detection using satellite imagery: preparatory to smoke detection from Insat-3D',International Journal of Remote Sensing,30:1,9 -22.

10. Aerosol

S.No.	Product Name	Spatial Resolution	Temporal Resolution
1	3DIMG_L2G_AOD	0.10X0.10 degree	30 minutes

10. Aerosol Optical Depth (AOD) Retrieval

10.1 Algorithm Configuration Information

10.1.1 Algorithm Name

Aerosol Optical Depth (AOD)

(Ref : IMD RFP Section 11.13)

10.1.2 Algorithm Identifier

3DIMG_L2G_AOD

10.1.3 Algorithm Specification

Version	Date	Prepared by	Description
1.0	14.02.2007	Prakash Chauhan	AOD Baseline Document
1.1	17.08.2012	Prakash Chauhan Nivedita Sanwlani Arvind Sahay	

10.2 Introduction

10.2.1 Overview and background

Aerosols play an important role in numerous aspects of human life. Aerosols have large-scale effects, such as their impact on climate by redistributing solar radiation (Herman and Browning 1975; Charlson *et al.* 1991; Haywood *et al.* 1999) and interacting with clouds (Platnick and Twomey 1994; Kaufman *et al.* 2002). Aerosol information is also critical for atmospheric correction algorithms for multi-spectral satellite sensors and military operations. The climate effects of atmospheric aerosols may be comparable to CO₂ greenhouse effects, but with opposite sign and larger uncertainty (Hansen and Lacis, 1990). Aerosols have a significant impact on human life beyond the climate element. When in the lower troposphere, aerosols cause poor air quality, reduction of visibility, and public health hazards. Satellite remote sensing provides a means to derive aerosol distribution at global and regional scales.

This Algorithm Theoretical Basis Document (ATBD) describes the algorithm used to retrieve the Aerosol Optical Thickness (AOT) for the INSAT-3D Imager instrument operating from a geostationary platform. The output product description is summarized in Table 1.

Specifically, this document identifies the sources of input data, both INSAT-3D imager and non-INSAT-3D imager data, required for retrieval; provides the physical theory and mathematical background underlying the use of this information in the retrievals; includes implementation details; and describes assumptions and limitations of the proposed approach.

Table 1: Summary of Aerosol optical Depth (AOD) product

Parameter Name	Units	Horizontal Cell Size	Comments
Aerosol Optical depth at 650 nm	Dimensionless	4.0 Km for both Land and oceans	Retrieved for all the pixels except areas of clouds

10.2.2 Objective

The objective of this algorithm is to calculate the aerosol optical thickness, proportional to the total aerosol loading of the ambient aerosol, over both land and ocean for Indian region on twice daily basis. As clouds block the surface reflectance, the aerosol optical thickness cannot be found for cloudy pixels. Retrievals are only performed during the daytime due to the lack of light in the visible channel of INSAT-3D imager data during the nighttime. The overall objectives of the aerosol retrieval is:

To determine the aerosol optical thickness, at 650 nm and 4 Km spatial resolution over both land and ocean surfaces with root mean square (RMS) error of ± 0.1 . Optical thickness (τ) is related to transmission (t) by $t=\exp(-\tau)$. Optical thickness retrievals apply only under clear and daytime conditions.

10.3 Inputs

10.3.1 Static Data

Parameter	Resolution	Quantization	Accuracy	Source
Digital Elevation model	5 minutes	--	--	ETOPO5
Spectral Response Function (SRF) for Imager bands	1nm	--	--	Sensor Group of Space Applications Centre, Ahmedabad

10.3.2 Image and preprocessing data (Dynamic)

Parameter	Resolution	Quantization	Accuracy	Source
Radiometric and geometric corrected radiance values of visible channel (0.55-0.75 μ m)	4 Km	10 bit	--	Derived from raw data by DP (data processing)
Radiometric and geometric corrected gray count values of TIR-1 channel (10.5)	4 Km	10 bit	-	Derived from raw data by DP
Radiometric and geometric corrected gray	4 Km	10 bit	-	Derived from raw data by DP

count values of TIR-2 channel (11.5)				
Geolocation file Along with sun zenith & azimuth and sensor zenith and azimuth information	Pixel	-	1 pixel	Derived by DP
At least 20 data data for Visible band should be available for 1030 and 1330 hrs for the generation of Clear composite reflectance image for initial period	4 Km			

10.3.3 Other Auxillary data and Model Inputs

Parameter	Resolution	Quantization	Accuracy	Source
Total Column Ozone concentration	50 Km	--	--	NCEP or INSAT-3D SOUNDER
Surface pressure	50 Km	--	--	NCEP or GTS through IMD

10.4 Algorithm Functional Specifications

10.4.1 Overview

It has been demonstrated that aerosol optical thickness can be retrieved from solar-reflected radiance, and that aerosol size distribution information is carried in the spectral dependence of aerosol optical thickness. Thus, satellite reflectance measurement limited to one (GOES) or two channels (Advanced Very High Resolution Radiometer [AVHRR]) were used first to derive the total aerosol content by assuming a given aerosol model.

The relatively homogeneous surface of the ocean enables the direct application of the look up table (LUT) approach to find the aerosol optical thickness. Using the observed

reflectance at the top of the atmosphere (TOA) in coordination with ancillary information on the wind speed, water vapor, surface pressure, surface elevation, and ozone, the corrected reflectances are inverted into a maritime LUT to find values of optical thickness.

The approach over land is more complicated, in that dark, vegetated surfaces are required for aerosol optical depth retrieval. A near-IR band is used to identify dark, vegetated pixels, then the surface reflectance in the visible bands is calculated from the observed reflectance in the near-IR band. The optical thickness is initially calculated assuming a continental aerosol model. The suspended matter information is used to choose a better aerosol model and more accurate values of optical thickness (Kaufmann *et al.* 1997).

In spite of advances in aerosol remote sensing over land, most retrievals are limited to once or twice per day, as by the morning and afternoon passes of the orbiting polar satellites. Aerosols, however, show diurnal variations that would be missed by such sparse observations. While studies of aerosol optical depth from Sun photometers show little systematic trends (Smirnov *et al.* 2002), surface observations of scattering show significant diurnal patterns. It is required to understand aerosol plume movement to track and forecast plume movement in the interest of human health. Therefore, it is important to monitor the temporal aspects of aerosol.

The INSAT-3D imager data from geostationary platform has the potential to provide aerosol observations over land and ocean with multiple observations per day. Many studies have demonstrated the potential of Geostationary Operational Environmental Satellite (GOES) series of imager sensors to provide quantitative estimates of aerosol optical depth. Their sensitivity studies, however, concluded that retrievals depend on aerosol optical property assumptions and surface reflectance. Studies using geostationary satellites (e.g. GOES-8) and larger validation networks (e.g. Aerosol Robotic Network—AERONET) supported those initial findings. Specifically, Zhang *et al.* (2001) and Knapp *et al.* (2002) showed that aerosol monitoring from GOES is possible for South America. However, this region has optimal retrieval conditions: surface cover with little variability (i.e. rainforest) and large aerosol optical depths (from biomass burning).

Recent study by Knapp *et al.* (2005) has shown operational potential of GOES series of sensors for the monitoring of aerosol optical depth over land. A method is proposed by Knapp *et al* (2005) to correct surface effects and retrieve aerosol optical depth using visible reflectance measurements from the Geostationary Operational Environmental Satellite (GOES). The surface contribution is determined from temporal compositing of visible imagery, where darker pixels correspond to less atmospheric attenuation and surface reflectance is deduced from the composite using radiative transfer. The method is applied to GOES-8 imagery over the eastern US. Retrieved surface reflectance is compared with separate retrievals using a priori ground based observations of aerosol optical depth.

10.4.1.1 Theoretical Background

The INSAT-3D imager data will be used to perform the surface reflectance and aerosol optical depth (τ) retrievals and mask for clouds. It measures top of the atmosphere (TOA) radiance in six channels: three at infrared wavelengths, one in the visible wavelength and one sensitive to both solar and Earth-emitted radiance. Primarily, the visible channel

(0.52–0.72 mm full width at half maximum) is sensitive to aerosol scattering, so the remaining channels are used for cloud masking. The cloud mask algorithm is based on the Clouds from the Advanced Very High Resolution Radiometer (AVHRR) (CLAVR) algorithm (Stowe *et al.* 1999) which uses spectral and spatial thresholds to test for the presence of clouds.

The retrieval of aerosol information from INSAT-3D imager data is a two-step process:

- 1) Cloud masking
- 2) Composite the visible images to estimate the surface reflectance, and
- 3) Use the surface reflectance with an image to retrieve the aerosol optical depth.

Cloud Masking

Clouds are generally characterized by higher reflectance and lower temperature than the underlying earth surface. As such, simple visible and infrared window threshold approaches offer considerable skill in cloud detection. Following threshold based tests will be performed to detect the cloudy pixels.

a) Visible and *Mid-wave Infrared Window Reflectance Threshold Test*

The reflectance threshold test using visible band of INSTA-3D along with 3.9 micron channel where values > 6% are considered to be cloudy, will be used.

b) *IR Window Temperature Threshold and Difference Tests*

Simple thresholds based cloud screening test will be established over land and oceanic features using the TIR data of the INSAT-3D.

Surface Reflectance Retrieval

Estimating the surface contribution to the TOA INSAT-3D Imager visible reflectance is difficult since observations will have atmospheric contamination. For instance, a visible observation from INSAT-3D Imager on a cloudless day with low aerosol burden will still have: gaseous absorption (primarily, ozone and water vapour); Rayleigh scattering; and residual aerosol extinction. This atmospheric component to the TOA reflectance needs to be removed to retrieve the surface reflectance. While studies have shown it is possible to estimate the surface component from observations in the near-infrared (e.g. 2.1 μm) where aerosol and Rayleigh scattering are very low, the INSAT-3D imager lacks an observation at this wavelength. Therefore, a compositing method will be used to estimate the surface reflectance.

The visible imagery is composited to determine the surface contribution to the top-of-the-atmosphere (TOA) reflectance. For each pixel in the visible image, the darkest observation over the course of some time period is called the composite clear reflectance. By using this value to obtain the surface reflectance, one assumes: that aerosol would increase the reflectance and cloud shadows will be rare. The length of the time period is somewhat subjective. In general, a long enough time period is needed for at least one cloud-free observation. Knapp et. al. (2005) used a two week (i.e., 14 day) period. A radiative transfer model, the second simulation of satellite signal in the solar spectrum (6S) will be used to convert the TOA observed reflectance to a surface reflectance. This atmospheric correction removes Rayleigh scattering and gaseous

absorption, leaving the Lambertian surface reflectance. This is then used in following calculations to retrieve aerosol optical depth in the subsequent aerosol optical depth retrieval.

Cloud shadows, however, can contaminate the composite reflectance. At high solar zenith angles (i.e. during early morning and late afternoon), high clouds may cast large shadows. In the shadow regions, the direct downward solar radiance is obscured at the surface, thereby reducing the surface reflectance. The second darkest observation will be used in the composite clear reflectance (CCR) method to reduce the effect of cloud shadows. By selecting the second darkest pixel, a cloud shadow would need to be present on at least two days during the period to affect the composite.

The accuracy of the composite depends on the length of time used to create it. For instance, enough cloud-free observations must exist with little aerosol influence for the surface reflectance to be accurate. Areas of persistent aerosol or cloud cover will be likely to have caused errors in the retrieved surface reflectance because the atmospheric component remains large in such situations.

Atmospheric effects—*aerosol extinction, Rayleigh scattering and gaseous absorption*—will be removed from the composite using the second simulation of the satellite signal in the solar spectrum (6S) radiative transfer model. This will retrieve the surface reflectance, ρ_{sfc} .

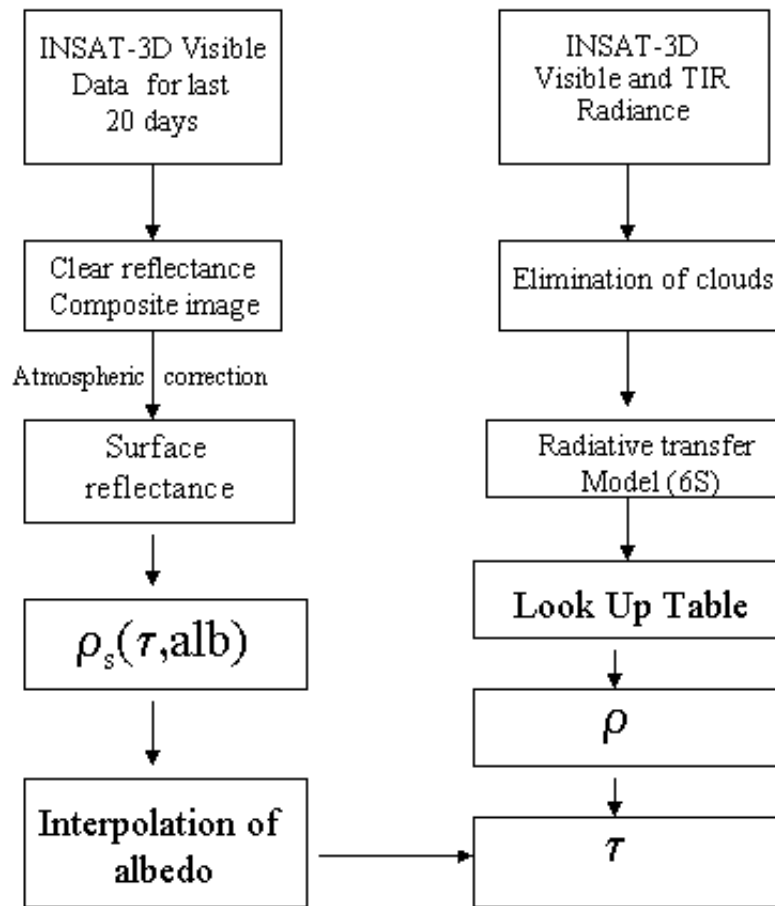
Some aerosols are still present in the composite reflectance; their radiative effect must be removed as well. This aerosol will be simulated using rural and dust aerosol model, given its ability to simulate the aerosol signal over the Indian region. This will represent the aerosol extinction still present in a composite reflectance. The amount of background aerosol is difficult to determine because it varies with season, length of CCR and time of day. However, it has been reported that background aerosol can vary from 0.02 to 0.08.

Aerosol Optical Depth Retrieval

The aerosol optical depth retrieval is performed using a INSAT-3D imager visible image and the retrieved surface reflectance (from the previous step). In this retrieval, the optical depth of the rural and dust model in the 6S radiative transfer model is increased until the theoretical reflectance matches that in the INSAT-3D imager observation.

The second simulation (6S) model will be used to simulate ρ_{sat} observations. Satellite altitude INSAT-3D imager visible band (0.55-0.75 μm) radiances will be simulated as a function of geometric angles determining the satellite viewing geometry and time of the day, surface reflectance R , and aerosol optical depth (varying from 0 to 3) at 650 nm. The aerosol optical depth will be retrieved using a look up table (LUT). The retrieval method then will depend on the interpolation within the LUT, finding the t which corresponds to the observed ρ_{sat} . The uncertainties in such a retrieval is dependent upon the accuracy of the model parameters

10.4.1.2 Flow Chart



10.4.2 Operational Implementation

- 10.4.2.1 Step 1 : Conversion from gray count to Visible radiance and BT
- 10.4.2.2 Step 2 : Cloud and sun glint elimination
- 10.4.2.3 Step 3 : Generation of surface reflectance image using darkest observations using last 20 days data
- 10.4.2.4 Step 4: Atmospheric correction of INSAT-3D visible image for molecular scattering and gaseous absorption
- 10.4.2.5 Step 5 : Correction for surface reflectance
- 10.4.2.6 Step 6: Use LUTs for the inversion of aerosol optical depth (AOD)

10.5 Outputs

Parameter	Unit	Min	Max	Accuracy	Resolution
Aerosol optical depth at 650 nm	Dimensionless	0	2	15-20%	4 Km

10.5.1 format of the output and the domain

Lat , Lon, AOD ,

Domain :

40 to 40 N, 30 E to 120 E

10.6 Validation

10.6.1 Data required

Parameter	Resolution	Quantization	Accuracy	Source
AERONET spectral AOD data	<i>In-situ</i> point observation	--	--	AERONET sites in India Kanpur, Goa and Dharwar
Spectral AOD using handheld sunphotometer	<i>In-situ</i> point observation	--	--	Data collection campaigns will be organized
MODIS AOD products	1 degree X 1 degree			Data available through internet

10.6.2 Methods of validation

AERONET data for Validation

Post-launch routine ground-based observations can be made using AERONET, and any of the several miscellaneous techniques, including the diffuse/direct method, aureole meters, and polarization measurements. AeRoNet (Aerosol Robotic Network) is a network of ground-based sun-photometers established and maintained by Brent Holben of Code 923 of the NASA Goddard Space Flight Center and Tom Eck of Raytheon ITSS. The sun-photometers measure the spectral aerosol optical thickness and sky radiance. In India 3 Aeronet sites namely Kanpur, Goa and Dharwar are providing systematic in-situ AOD measurements. Data from these sites will be used for validation of INSAT-3D derived AODs.

Post-Launch Special Field Experiments

Many of the present satellite observations are augmented by special field campaigns to provide ground-truth data for the satellite-derived measurements. The INSAT-3D Imager derived aerosol optical thickness measurements will be validated using hand-held sun-

photometer. The details of these campaigns (timing, location, instrumentation, etc.) will be decided later on.

Post-Launch Satellite-Based Inter-comparisons

INSAT-3D Imager derived aerosol optical depths may be validated by comparing them with aerosol optical depths derived by other satellite sensors, such as MODIS. The basic inter-comparison technique involves three steps: 1) identification of locations where both sensors fly over at nearly the same time; 2) extraction of data for storage in an inter-comparison archive; 3) analysis of the differences between the measurements.

10.7 Technical issues (Limitation etc.)

Accuracy of the product depends on the accuracy of the radiation model to simulate the satellite radiances. However the following limitations of the present study have to be kept in mind.

- i) Characterization of surface reflectivity is critical of the study. Use of darkest observation for last 20 days provides mean reflectivity.

10.8 Future Scope

- i) In future algorithms making use of INSAT-3D imager data for SWIR and MIR bands can also be attempted for characterization of surface reflectivity.

10.9 References

1. Bergin, M.H., Cass, G.R., Xu, J., Fang, C., Zeng, L.M., Yu, T., Salmon, L.G. , Kiang, C.S., Tang, X.Y., Zhang, H. and Chameides, W.L., 2001, Aerosol radiative, physical, and chemical properties in Beijing during June 1999. *Journal of Geophysical Research*, 106, pp. 17 969–17 980.
2. Charston, R.J., Langer, J., Rodhe, H., Levoy, C.B. and Warren, S.G., 1991, Perturbation of the northern hemisphere radiative balance by backscattering from anthropogenic sulfate aerosols. *Tellus*, 43AB, pp. 152–163.
3. Hansen, J. E., and A. A. Lacis, 1990, Sun and dust versus greenhouse gases: An assessment of their relative roles in global climate change. *Nature*, 346, 713-719.
4. Haywood, J. and Boucher, O., 2000, Estimates of the direct and indirect radiative forcing due to tropospheric aerosols: a review. *Reviews of Geophysics*, 38, pp. 513–543.
5. Herman, B.M. and Browning, S.R., 1975, The effect of aerosols on the Earth-atmosphere albedo. *Journal of Atmospheric Science*, 32, pp. 1430–1445.
6. Kaufman, Y.J., Tanre', D., Remer, L.A., Vermote, E.F., Chu, A. and Holben, B.N., 1997, Operational remote sensing of tropospheric aerosol over land from EOS moderate resolution imaging spectroradiometer. *Journal of Geophysical Research*, 102, pp. 17051–17067.
7. Kaufman, Y.J., Tanre, D. and Boucher, O., 2002, A satellite view of aerosols in the climate system. *Nature*, 419, pp. 215–223.
8. Knapp, K.R., Vonder Harr, T.H. and Kaufman, Y.J., 2002, Aerosol optical depth retrieval from GOES-8: uncertainty study and retrieval validation over South America. *Journal of Geophysical Research*, 107, 10.1029/2001JD000505.

9. Knapp, K. R., Frouin, R, Kondragunta, and Prados, A., 2005, Toward aerosol optical depth retrievals over land from GOES visible radiances: determining surface reflectance, *International Journal of Remote Sensing*.
10. Platnick, S. and Twomey, S., 1994, Remote sensing the susceptibility of cloud albedo to changes in drop concentration. *Atmospheric Research*, 34, pp. 85–98.
11. Smirnov, A., Holben, B.N., Dubovik, O.V., O'Neill, N.T., Eck, T.F., Westphal, D.L., Goroch, A.K., Pietras, C. and Slutsker, I., 2002, Atmospheric aerosol optical properties in the Persian Gulf. *Journal of Atmospheric Science*, 59, pp. 620–634.
12. Stowe, L.L., Davis, P.A. and McClain, E.P., 1999, Scientific basis and initial evaluation of the CLAVR-1 global clear/cloud classification algorithm for the advanced very high resolution radiometer. *Journal of Atmospheric and Oceanic Technology*, 16, pp. 656–681.
13. Zhang, J., Christopher, S.A. and Holben, B., 2001, Intercomparison of aerosol optical thickness derived from GOES 8 imager and ground-based Sun photometers. *Journal of Geophysical Research*, 106, pp. 7387–7397.

11. Atmospheric Motion Vector Winds (TIR 1)

S.No.	Product Name	Spatial Resolution	Temporal Resolution
1	3DIMG_L2P_IRW	Point	30 minutes

11. Cloud Motion Wind Vectors (CMV)

11.1 Algorithm Configuration Information

11.1.1 Algorithm Name

Atmospheric Motion Vectors Winds (TIR 1)

(Ref : IMD RFP Section 11.14)

11.1.2 Algorithm Identifier

3DIMG_L2P_IRW

11.1.3 Algorithm Specification

Version	Date	Prepared by	Description
1.0	14.02.2007	C.M. Kishtawal S.K. Deb	CMV Baseline Document
2.0	21.08.2012	C. M. Kishtawal S. K Deb	CMV Baseline Document (Verson 2)
3.0	21.07.2014	C. M. Kishtawal S. K. Deb	CMV Baseline Document (Verson 3)

11.2 Introduction

The purpose of this document is to present an algorithm for retrieving Cloud Motion Vectors (CMVs) from INSAT-3D thermal infrared imager channel and its validation procedure. The INSAT-3D will have two IR window channels (10.5-11.5 μm , and 11.5-12.5 μm). In this document some background and general characteristic of satellite-derived CMV and INSAT-3D IR channel characteristics; the methodology employed to derive the vector fields, theoretical basis and practical aspects of this algorithm and outlined the planned validation approach.

11.2.1 Overview and background

Spatio-temporal analysis of meteorological events is an important part of routine numerical weather analysis. In that context, a cloud tracking method is presented here for a sequence of geostationary satellite images. Given a pair of remotely sensed images, captured at a fixed time interval (typically, 30 min), the objective is to derive motion vectors associated with the cloud mass. This correspondence process is a useful precursor to cloud motion vector (CMV) studies and spatio-temporal analysis of cloud life cycles. The spatio-temporal life cycle includes the generation, dissipation and assimilation of clouds that can be observed in a sequence of geostationary satellite images. During the 1970's and early 1980's, cloud motion winds were produced in major operational centers like NESDIS (National Environmental Satellite Data and Information Service) using a combination of automated and manual techniques. Early automated techniques supplied quality low-level vectors but often yielded inconsistent quality for mid- and high-level motions. Height assignment was automatic but often contained errors for semitransparent cirrus clouds. In the subsequent years, due to the developments in image-processing and pattern recognition techniques (Merill et al., 1991), it

was possible to design fully automatic techniques for CMV retrieval, and NESDIS began its application in 1992. In later time, several new developments were made to make accurate retrievals of cloud motion winds. For example, CO₂ slicing algorithm was replaced by H₂O intercept algorithm for assigning the height to semitransparent tracers. Other improvements were (i) automated correction of navigation inconsistencies within the imageries (ii) inclusion of spatial filters in tracer selection methodology to filter undesirable scenes.

11.2.2 Objective

The main objective of this study is to derive the Cloud Motion Vectors (CMVs) over land and sea using multiple half hourly IR images. The region over which the winds are derived should be in the range of 50° from sub-satellite point.

11.3 Inputs

11.3.1 Static Data

Parameter	Resolution	Source
Continental boundary data	4 km	DP (IMD data)

11.3.2 Image and preprocessing data (Dynamic)

Parameter	Resolution	Quantization	Accuracy	Source
Radiometric and geometric corrected gray count values of split window IR channel (10.5-11.5 μm and 11.5-12.5 μm) and WV channel (6.7 μm) (All the data is required in fixed lat-lon grid for continuous 8-images separated by 30 minutes time interval)	pixel	10 bit	--	Derived from raw data by DP (data processing)
Gray value to brightness temperature conversion table	-	-	0.3 K	Derived by DP
Geo-location file	Pixel	-	4 km	Derived by DP

11.3.3 Other Auxiliary data and Model Inputs

Parameter	Resolution	Accuracy	Source
Numerical model forecast of wind for all levels	1 degree	2 m/s (speed) 20° (direction)	IMD
All levels model forecast Temperature		1° K	

11.4 Algorithm Functional Specifications

11.4.1 Overview

11.4.1.1 Methodology

11.4.1.1.1 Tracer selection

At the National Environmental Satellite, Data, and Information Service (NESDIS), the initial cloud features are selected by locating the highest pixel brightness values for each target domain and computing the local gradients around those locations ([Nieman et al., 1997](#)). Any gradients greater than 15K are assigned as target locations, and prospective targets also undergo a spatial coherence analysis ([Coakley and Bretherton, 1982](#)) to filter out unwanted targets. Water vapor tracers are generally identified using the local bi-directional gradients in a template of specified size and compared with empirically determined thresholds to identify the features with sufficient variability ([Velden et al., 1997](#)) and those that pass the threshold value are identified as tracers for cloud-free environments. The pixel with maximum bi-directional gradient is the location of the tracer. At the European Organization for the Exploitation of Meteorological Satellites (EUMETSAT), the tracers in the Meteosat (first-generation satellites) images are selected using multispectral histogram analysis ([Tomassini, 1981](#)), which extracts the dominating scenes in an image segment corresponding to the area of 32 X 32 IR pixels at the sub-satellite point. Later the selected templates undergo a spatial coherence analysis ([Coakley and Bretherton, 1982](#)) to filter the image, to enhance the upper-level cloud. Because the spatial resolution of the infrared channel of Kalpana-1 (8 km) is coarser relative to GOES (5 km) or Meteosat-7 (5 km), we used a 20 X 20 window (called a template) to identify features in Kalpana-1 images. However in case of INSAT-3D (4 km) we used 32 x 32 template window. The features are selected by computing local image anomaly in a 32 x 32 template window, both in cloudy and cloud free regions. The local image anomaly is calculated using the following formula:

$$a = \sum_i \sum_j |I(i, j) - \bar{I}| \quad (1)$$

Where $I(i, j)$ represent the grey value for (i, j) pixel of a template window and bar represents the mean of grey values within that template. The anomaly-based tracers are generally produced by a smooth feature field in comparison to the gradient-based features. This difference can help in reducing the tracking errors ([Deb et al., 2008](#)). As per the location of the tracer, the template window is re-located with tracer position at the centre. A schematic diagram is shown in [Fig. 2](#)

11.4.1.1.2 Height assignment

The height assignments of the selected tracers selected based on the above criterion are derived using the following widely used methods viz. such as the infrared window (WIN) technique or the water vapor histogram method (HIST), the H₂O intercept method ([Nieman et al., 1993](#)) and the cloud base method ([LeMarshall, 1993](#)). Once final height is selected a few gross error checks are also applied. A brief description of each method is following:

2.1 Infrared Window Channel (WIN) and Water Vapor Histogram Methods (HIST):

In this method the height assignment using a single satellite channel is made by comparing either infrared window or water vapor brightness temperature (BT) values with NWP model

forecast temperature profiles. Cloud heights are determined by interpolating the cloud temperature, which is an average of coldest 20% of pixels, to the interpolated model guess field at the target location. A 6-h NWP model forecast from National Center for Environmental Prediction (NCEP) Global Forecast System (GFS) is the source of temperature profile. This method works well with opaque clouds. However, movement of opaque clouds usually does not accurately represent atmospheric motion at the assigned level ([Nieman et al., 1993](#)), resulting in a lower derived wind speed than observed. Semitransparent clouds or sub-pixel clouds give more accurate representation of the actual movement of the atmosphere at a particular level. Estimation of this level is very difficult in these cases since determination of the cloud top BT is affected by an unknown cloud emissivity or the percentage of cloud versus clear sky, respectively. The BT values are warmer than observed in these cases, thus leading to estimated cloud heights that are too high in pressure (too low in altitude), typically resulting in an overestimation of the wind speed at the estimated cloud height.

2.2 Water Vapor–Infrared Window Intercept Method (H₂O):

Height assignments derived with this method are based upon the fact that radiances from two different spectral bands are linearly related for different cloud amounts within the field of view at a specified height. Observed radiance measurements are a function of clear sky and opaque cloud radiances.

$$R(N) = (1 - nE)R_{cl}(N) + nER_{bcd}(N, P_c) \quad (2)$$

Opaque cloud radiance can be calculated from:

$$R_{bcd}(N, P_c) = R_{cl}(N) - \int_{P_c}^{P_s} t(N, p) \frac{db[N, T(p)]}{dp} dp \quad (3)$$

where R_{bcd} is the opaque ("black") cloud radiance, R_{cl} is the clear sky radiance, $t(N, p)$ is the fractional transmittance of radiation of spectral band N emitted from the atmospheric pressure p arriving at the top of the atmosphere ($p=0$), n is the fraction of FOV covered with cloud, P_s is the surface pressure, P_c is the cloud pressure, and $b[N, T(p)]$ is the Planck radiance of the spectral band N for a temperature $T(p)$. The second part of the above equation represents the radiance decrease from clear sky conditions introduced by an opaque cloud at a pressure level p . This calculation is dependent upon an "accurate" estimation of the current atmospheric temperature and moisture structure, which are provided by a NWP model forecast profile. By comparing the observed radiances with the calculated radiances (for an observed atmosphere defined by the model guess profiles), an estimation of the cloud height can be derived for a completely opaque cloud. In the **Fig. 1**, observed WV and IR radiances at each field of view (FOV) points are plotted with the calculated radiances at different heights for opaque clouds in the atmosphere (curved line). The straight line connects the center points of the warmest and coldest clusters, which approximate the observed surface and cloud conditions.

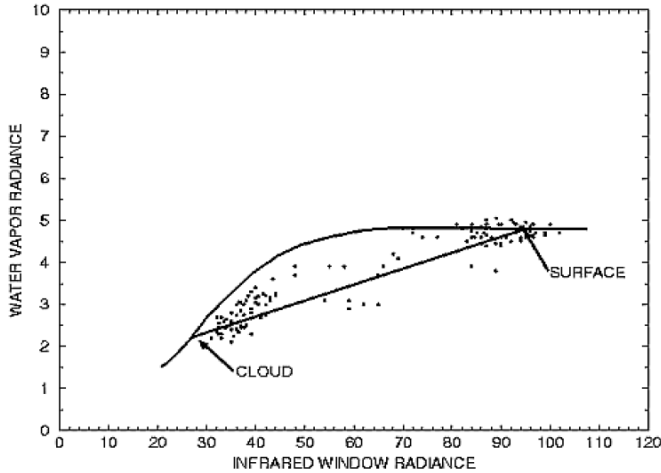


Fig 1: Measured radiances ($\text{mW m}^{-2} \text{ sr}^{-1} \text{ cm}$) for fields of view partially filled with clouds (Nieman et al., 1993)

By extrapolating this line to intersect the calculated radiance curve, where the cloud amount is one (representing an opaque cloud), the cloud top temperature/pressure can be determined. The cluster determination algorithm used is a modified version of the bivariate asymmetric Gaussian histogram analysis (Rossow et al., 1985; Tomassini, 1981), and involves ten steps. These steps are outlined in detail in Nieman et al., 1993. Calculated water vapor radiances can be in error due to incorrect NWP model forecast profiles. This error would lead to calculated radiances being systematically higher or lower than observed radiances. When the calculated radiances are systematically lower, an adjustment is applied to the radiances obtained using the above equation. When the calculated radiances are greater than observed radiances, no adjustment is applied since it is assumed that the lower measured radiance is due to cloud contamination. The accuracy of this method can be affected by the amount of water vapor in the atmosphere. Dry atmospheric conditions lead to a steeper slope between the IR and WV radiances, leading to an overestimate in the target height (lower pressure value). The NCEP GFS model forecast are used here as guess fields.

2.3 Cloud Base Method (BASE):

Wind speeds for low-level cumulus clouds (cloud top pressures greater than 600 hPa or altitudes lower than 600 hPa) have been found to be best represented by the movement at the cloud base level instead of the mid or upper levels of the cloud (Hasler et al., 1979). A method was developed at the Australian Bureau of Meteorology (LeMarshall, 1993) to estimate this height using the Infrared Window channel. This method first constructs a histogram of the BT values over a selected region surrounding the cloud target being examined. This histogram is then smoothed and Hermite polynomials are fitted to the histogram to separate the distribution into two components; a cloudy and clear sky region. Assuming the distributions are normal, the cloud base height can be estimated. The mid cloud temperature is determined by examining the second derivative histogram of the cloudy distribution, while the cloud top temperature is estimated to be located at the coldest 5% of the cloudy distribution. The cloud base temperature is estimated to be located the same distance from the mid cloud temperature as the cloud top temperature. The calculated cloud base temperature is converted to a pressure using model field interpolated to the target

location. As mentioned previously, this height assignment method is only applied to those targets which are calculated to have a cloud top pressure of greater than 600 hPa (i.e. altitude lower than 600 hPa). This "initial" target cloud top height is provided by one of the previous Infrared Window height assignment methods. The BASE method is used to adjust only these winds, and is not utilized for water vapor winds or winds with pressures less than 600 hPa (i.e. altitudes higher than 600 hPa).

Once the infrared tracers heights using the above three algorithms and water vapor tracers heights using the HIST and H₂O methods have been calculated, the best height among the available heights is determined. The lowest pressure (highest altitude) value of all the calculated height values is used as the final pressure height. However, if for a specific infrared tracer final height is WIN and a valid BASE height is available, then the BASE height is used as the final height.

11.4.1.1.3 Tracking

If a traceable feature is found in the first image and corresponding height of the selected tracers are estimated, the match of this template is searched in the second image within a bigger "search window", centered at the same point as the template window. To optimize the search window size, the first guess model wind direction at the tracer location is also considered. The search area is optimized within ± 30 degree from the model wind direction at that level of atmosphere. The 32 X 32 template in the second image that lies within the search window should have the same class as the template in the first image; otherwise the template in the second window is rejected. The cross-correlation technique is used operationally for tracking the tracer between two images in most operational centers. However, in this study the degrees of matching between two successive images are calculated by the Nash-Sutcliffe model efficiency ([Nash and Sutcliffe, 1970](#)) coefficient (E). It is defined as

$$E = 1 - \frac{\sum_{i=1}^n (I_t - I_s)^2}{\sum_{i=1}^n (I_t - \bar{I}_t)^2} \quad (4)$$

Where I_t and I_s are the variance of the grey values for template window and search window and \bar{I}_t is the average of variance of template window. Here n is 32 x 32 and this is the size of template window and corresponding template of same size in the searching area. The size of the searching area in the subsequent image is taken as 64 x 64. The coefficient E is normalized to values between $-\infty$ and +1. An efficiency $E = 1$ corresponds to a perfect match, $E = 0$ means that search window is as accurate as mean of the template window and $E < 0$ implies the lack of matching between template and search window. The closer the model efficiency to 1, the more accurate the matching between the windows. A cut-off value of $E=0.8$ is defined, below which a matching of target is not considered. The Nash-Sutcliffe model efficiency coefficient (E) is normalized and its value lies between $-\infty$ and 1, towards the higher end (e.g. as $E \rightarrow 1.0$), the value of E approaches r^2 , where r is the correlation coefficient. Thus a value of $E=1$ is exactly equivalent to a correlation of 1.0 between two objects. The maximum value of E is chosen as the best fit for tracking. One of the main advantages of this matching technique is that it reduces the possibility of multiple maxima, because the parameter E has a higher sensitivity to differences between two features

compared to maximum cross correlation coefficient (MCC). Thus, when the degree of mismatch between two objects increases, the value of E falls more sharply compared to that of MCC, making E a better index for matching two objects. The application of this tracking method in estimation of water vapor winds has shown some improvement over Indian Ocean region ([Deb et al., 2008](#)).

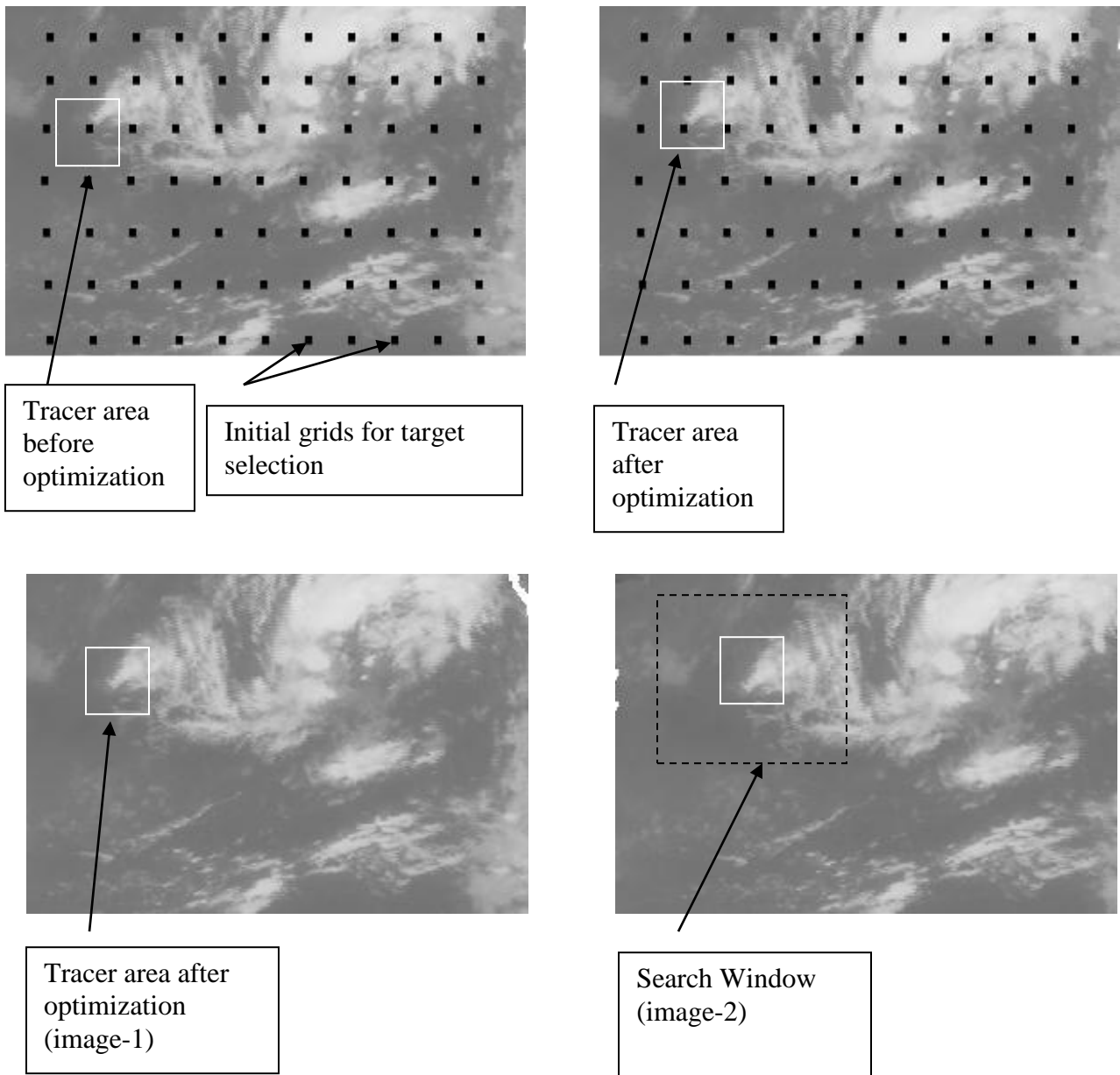


Fig.2 : Steps involved in tracer selection and tracking

11.4.1.1.4: Wind buffer generation and Quality control

Quality indicator of a derived wind vectors is traditionally represented as the degree of the coherence of a given vector with its surrounding. In most of the operational centers the AMVs are derived from three successive satellite images and the quality control of the retrieved winds are done either through Quality Indicator (QI) ([Holmlund, 1998](#)) followed at EUMETSAT or through 3-dimensional recursive filter function followed at NESDIS ([Nieman et al., 1997](#)) or both the algorithms together. In the present study a new technique of wind buffer generation and subsequently QI procedure followed at EUMETSAT is proposed. In this technique, a wind buffer is created using previous eight images between a pair of images (viz. between 1-2, 2-3, 3-4, 4-5, 5-6, 6-7 and 7-8) and stored in a file (**Fig. 3**). The previous eight images were considered to maintain the minimum 4-hour decorrelation timescale during retrieval ([Kaur et al., 2011](#)). In quality control procedure consists of a coherence analysis which forms the basis for acceptance/rejection of a vector and degree of coherence computed is used to assign quality flags to the derived vector. The value of quality flag falls sharply by an exponential function, as the disagreement of a given vector with its surroundings increases. Here each vector wind is represented by a complex number $V_{i,j}^c = u_{i,j} + i v_{i,j}$. For every new vector under consideration, (from current image-pair), its vector difference from the buffer is computed at the same as well as 3 X 3 neighborhood (**Fig. 3**), provided, the vectors to be compared show similar brightness characteristics (to maintain the similar height).

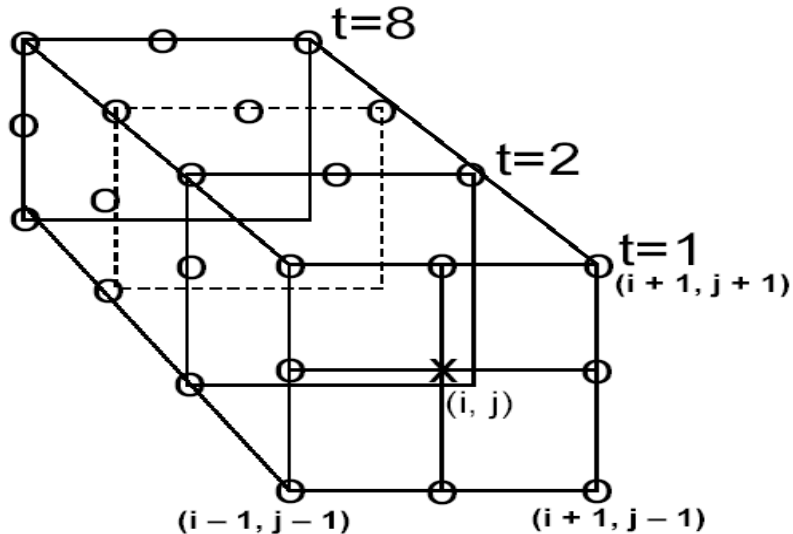


Fig 3: A schematic diagram of quality control process.

Here X (cross sign) at the centre of first box represents the current vector under consideration and O (circle sign) represents spatial and temporal neighborhood vectors. The vector differences (magnitude of complex numbers) are calculated as $\{V_{dif}\}_{i,j,t} = V^c - \{V\}_{i,j,t}$. Here V^c represents the current vector at (i, j) point and $\{V\}_{i,j,t}$ neighborhood vectors with $-1 \leq i \leq 1, -1 \leq j \leq 1$ and temporal scale t varies from 1 to 8. If all spatial and temporal

neighborhood vectors are present, then the difference set will contain 72 vectors (9 spatial neighborhoods with 8 temporal scales). However, all vectors may not be there all the times. The quality control process begins if at least 10 vector differences V_{dif} , excluding the difference corresponding to current (i, j) , are present in the set. In the next step, set of vector differences $\{V_{dif}\}$ is arranged in ascending order. The quality control process begins is the average of 10 V_{dif} is greater than 2.5 m/s. In the next step, the QI value for each vector is determined by using EUMETSAT procedure where four different tests are performed, which is normalized by a tanh-function that returns the value between 0 and 1. A weighted average of these individual quality indicators is then used for screening of poor quality vectors from final output. If any vector is not present in the immediate two pairs, then in-stead of rejecting, search process goes to the previous time steps of the wind buffer and if still it is not present it goes to next previous times steps and so on.

If S is the mean “speed” of a vector computed from two pair of images, then different quality functions are computed as below :

Direction Consistency Function:

$$DCF = 1.0 - \left[\tanh\left(\frac{\Delta\theta}{A_1 \exp(-S/B_1) + C_1}\right) \right]^{D_1}$$

Speed Consistency Function:

$$SCF = 1.0 - \left[\tanh\left(\frac{\Delta S}{\text{MAX}(A_2 S, B_2) + C_2}\right) \right]^{D_2}$$

Vector Consistency Function:

$$VCF = 1.0 - \left[\tanh\left(\frac{\Delta V}{\text{MAX}(A_3 S, B_3) + C_3}\right) \right]^{D_3}$$

Spacial Consistency Function:

$$PCF = 1.0 - \left[\tanh\left(\frac{\Delta V_m}{\text{MAX}(A_4 S, B_4) + C_4}\right) \right]^{D_4}$$

In the above formulation, $\Delta\theta, \Delta S, \Delta V$ represent the difference of direction (degrees), difference of speed, and the length of the difference vector between first and second satellite wind component. ΔV_m is the length of difference vector between satellite wind component and its best neighbor. The best neighbor is determined by the smallest vector difference. Quantities A_N, B_N, C_N , and D_N are constants. The final quality indicator of a wind vector is given as

$$\text{QI} = \frac{DCF + SCF + VCF + PCF}{4.0}$$

All the vectors with $\text{QI} < 0.6$ are rejected.

In the conventional triplet based methodology requires that a vector is available in both sets (i.e. in 1-2 and 2-3), if not so, such vectors are rejected, because they don't get “support”.

Hundreds of “isolated” vectors thus get eliminated, even though they represent the real situation. In the current method, the vector under consideration receives support from the past eight images. This method produces higher number of valid retrieval in the low-level and captures upper-level meridional flow very prominently. To explain this more explicitly, if we take eight satellite images each with 30-minute interval starting at 00:00 UTC to 03:30 UTC, then winds retrieved using each-image pair are stored as buffer in a file and represented as wind buffer generated at 03:30 UTC. The buffer generated at 03:30 UTC is used for quality control for wind retrieved using 03:30 UTC and 04:00 UTC images and the second image time is given as actual observation time of retrieved wind. For example winds retrieved using 03:30 UTC wind buffer and 03:30 UTC and 04:00 UTC images is given as 04:00 UTC observation time. As a whole to complete the process once it requires nine images. Similarly the buffer is updated at every 30-minute with the latest available image and process is repeated for next cycle of wind retrieval. This method produces higher number of valid retrieval in all levels and captures upper-level meridional flow very prominently.

11.4.2 Operational Implementation

11.4.2.1 Step 1 : Conversion from gray count to BT

- In this step a radiation model will be used to convert the instrument measured radiances into brightness temperature. This requires an accurate definition of the spectral response of the satellite.

11.4.2.2 Step 2: Tracer selection from image

- Cloud tracer selection will be done by evaluating the maximum local gradients surrounding each pixel in the target array and selecting the maximum brightness temperature of the window.

11.4.2.3 Step 3: Height assignment

- Assign height of the tracer using IR window technique. In this case the brightness temperature in the target window will be averaged and matched with collocated numerical model temperature profile. The level of optimum fit will be assigned as initial height.
- Re-assign the height using H₂O intercept technique for semi-transparent tracers.
- Re-assign the height using cloud-base height assignment technique.
- Assign correct height after implementing all the height assignment technique mentioned above.

11.4.2.4 Step 4: Tracking

- The tracking employs a simple search for the mean absolute difference of the radiance difference between the target and search arrays in subsequent half hourly images. This search will be done in the direction of $\pm 30^\circ$ of model wind.

11.4.2.5 Step 5: Wind buffer generation & quality control

- The wind buffer is created using previous eight images between pairs of images (viz. the winds retrieved between 1-2, 2-3, 3-4, 4-5, 5-6, 6-7 and 7-8) and stored in a file. The selection of eight images is consistent with decorrelation timescales of winds over tropical region.

- Use quality control criteria for selecting wind using the wind buffer.
- Calculate wind speed and direction.

11.5 Outputs

Parameter	Unit	Min	Max	Accuracy	Resolution
U and V component of CMV	m/sec	0	90	5-6 m/sec (upper level) 4-5 m/sec (lower level)	--
Domain of output : 0°E – 130°E :: 60°S – 60°N					

11.5.1 Format of the output and the domain

As output of CMV the following parameters will be provided to IMD:

- Zonal and meridional components of the wind vectors.
- Latitudinal and longitudinal position.
- Height of CMV

The format of the final product will be like this:

Parameter	Lat.	Lon.	Level	U-component	V-component	Quality Flag	Wind Speed(m/s)	Wind direction (clockwise from North)
Unit	Deg N	Deg E	hPa	m/s	m/s	0.0 to 0.9	m/s	Deg

11.6 Validation

11.6.1 Data required

Parameter	Type	Source
Wind	Collocated Radiosonde Profiles	IMD

11.6.2 Methods of validation

The evaluation of CMV should be taken into both qualitative and quantitative measures. Quantitative assessment of the CMV product is possible from statistical analyses and impact on NWP. The traditional method of validation is matching observations with collocated radiosondes. The statistical validation will be done according to the CGMS winds evaluation reporting guidelines. These statistics can provide a fixed measure of product quality over time and can be employed in determining observation weight in objective data assimilation. At the CGMS XXIII the Working Group on Satellite Tracked Winds recommended that evaluation of operational wind production quality should be

accomplished with a new standardized reporting method. The recommended three parts to the report.

- i) Monthly means of speed bias and rms vector difference between radiosondes and satellite winds for low (>700 hPa), medium (700-400 hPa), and high (< 400 hPa) levels together with the radiosonde mean wind speed. This should be done for three latitude bands: north of 20 N, the tropical belt (20 N to 20 S), and south of 20 S.
- ii) Trends of the evaluation statistics for the monthly cloud motion vectors and water vapor motion vectors through the last 12 months.
- iii) Information on recent significant changes in the wind retrieval algorithm.

The vector Difference (VD) between an individual wind report (i) and the collocated radiosonde report used for verification is given by

$$(VD) = [(U_i - U_r)^2 + (V_i - V_r)^2]^{1/2}$$

The speed bias is given by

$$(BIAS)_i = 1/N \sum_{i=1}^N [(U_i^2 + V_i^2)^{1/2} - (U_r^2 + V_r^2)^{1/2}]$$

The mean vector difference (MVD) traditionally reported is

$$(MVD) = 1/N \sum_{i=1}^N (VD)_i$$

And the standard deviation (SD) about the mean vector difference traditionally reported is

$$(SD) = [1/N \sum_{i=1}^N ((Vd_i) - (MVD))^2]^{1/2}$$

The root-mean-square error (RMSE) traditionally reported is the square root of the sum of the squares of the mean vector difference and the standard deviation about the mean vector difference,

$$(RMSE) = [(MVD)^2 + (SD)^2]^{1/2}$$

It must be noted that this definition of the mean vector difference is not the same as the mean component difference. The mean difference is calculated from the sum of the squares of the deviations of each component (u and v) of the wind vector.

$$(\Delta U^2) = \sum_{i=1}^N (U_i - U_r)^2$$

$$(\Delta V^2) = \sum_{i=1}^N (V_i - V_r)^2$$

$$(MCD) = [(\Delta U^2) + (\Delta V^2)]^{1/2} \neq (MVD)$$

To avoid confusion, a common terminology will be accepted. It is suggested to report mean vector difference (MVD) and standard deviation (SD). The standard accuracy according to CGMS guideline for CMV is that the root mean square error (RMSE) for WV winds should be 7m/s respectively with respect to radiosonde observations. The mean bias for both sets of winds should be about zero.

11.7 Technical Issues (Limitations etc)

Accuracy of the product depends on the accuracy of the registration of the images. If the registration has an error of 1 pixel, then error of the final product will be increased. However the following limitations of the present study have to be kept in mind. The spatially coherent, high resolution coverage of upper tropospheric winds are possible from geostationary satellite remote sensing of water vapor. CMV are comparable in quality to operational upper-level cloud-motion vectors. However, the retrieved vectors in regions are lacking in defining moisture structure, though they have the ability to obtain track-able information in extremely dry air masses and regions of strong subsidence is limited. The individual vectors represent single level reports; however, upper level vertical winds profiles are possible by using multi-spectral observations.

1. Sensitivity of error in height assignment to the error in wind speed retrieval

This sensitivity will depend upon the structure of wind circulation over different vertical levels as well as different geographical regions. For example, in the vicinity of atmospheric jets, the retrieved wind vectors will be highly sensitive to the errors in the assigned pressure levels. Based on some standard analysis (e.g. NCEP reanalysis of 6-hourly sampling), we will provide a quantitative assessment of the vertical and spatial structure of this sensitivity.

2. Numerical model to be used for AMV height assignment

We plan to use IMD's operational regional model output during height assignment procedure. However, if the domain of this regional model is smaller than the area of AMV retrieval, either IMD may be requested to increase the domain of its operational model, or a lower-quality solution based on the output of coarser-resolution GCM will be generated over the regions not covered by IMD's regional model.

3. Whether RT model to be used in real-time for height assignment

To use RT model in real-time height-assignment application is generally required to find the optimum solution. However, it is computationally expensive and may increase the AMV turn-around time very significantly. Efforts are currently underway to develop an empirical version of RT model that can be used for simulation of IR and water-vapor channel radiances for a variety of cloud heights. The inverse of this empirical model will then be used in real-time applications.

4. Comparison of maximum-correlation and minimum-difference methods for tracking of cloud-tracers.

The comparison have been made for a large number of image samples and it was found that the efficiencies of minimum-difference method (MDM) and maximum

cross correlation (MCC) methods are comparable, while the MDM method is significantly faster than MCC.

11.8 References

1. Bedka KM, Mecikalski JR (2005) Application of satellite-derived atmospheric motion vectors for estimating meso-scale flows. *Journal of Applied Meteorology* 44: 1761-1772.
2. Deb SK, Kishtawal CM, Pal PK (2010). Impact of *Kalpana-1* derived water vapor winds on Indian Ocean Tropical cyclones forecast. *Monthly Weather Review* 138 (3): 987-1003.
3. Deb SK, Kishtawal CM, Pal PK, Joshi PC (2008) A modified tracer selection and tracking procedure to derive winds using Water vapor imagers. *Journal of Applied Meteorology and Climatology* 47: 3252-3263.
4. Deb SK, Kishtawal CM, Kaur Inderpreet, Pal PK, Kiran Kumar AS (2012a). Multiplet based Technique to derive Atmospheric winds from Kalpana-1, *The Proceedings 11th International Wind Workshop*, 20-24 February, 2012, Auckland, New Zealand
5. Deb SK, Kaur Inderpreet, Kishtawal CM, Pal PK (2012b). Atmospheric Motion Vectors from Kalpana-1: An ISRO Status, *The Proceedings 11th International Wind Workshop*, 20-24 February, 2012, Auckland, New Zealand
6. Hasler AF, Skillman WC, Shenk WE, Steranka J (1979) In situ aircraft verification of the quality of satellite cloud winds over oceanic regions. *Journal of Applied Meteorology* 18: 1481–1489.
7. Holmlund K (1998) The utilization of statistical properties of satellite-derived Atmospheric Motion Vectors to derive quality indicators. *Weather Forecasting* 13:1093-1104.
8. Kelly G (2004) Observing system experiments of all main data types in the ECMWF operational system. 3rd WMO Numerical Weather Prediction OSE Workshop, Alpbach, Austria, WMO, Tech Rep. 1228: pp 32-36.
9. Kishtawal CM, Deb SK, Pal PK, Joshi PC (2009) Estimation of Atmospheric Motion Vectors from Kalpana-1 imagers. *Journal of Applied Meteorology and Climatology* 48: 2410-2421.
10. Kaur Inderpreet, Kishtawal CM, Deb SK, Kumar Raj (2012) Temporal Scales of Satellite Derived Atmospheric Winds over the Asian Monsoon Region. *IEEE. Geoscience and Remote Sensing Letters*. 9 (2): 317-320.
11. LeMarshall J, Pescod N, Khaw A, Allen G (1993) The real-time generation and application of cloud-drift winds in the Australian region. *Australian Meteorological Magazine* 42: 89–103.
12. Merrill, R. T., Menzel W. P, Baker W, Lynch J. and Legg E, (1991): A report on the recent demonstration of NOAA's upgraded capability to derive cloud motion satellite winds. *Bull. Amer. Meteor. Soc.*, 72, 372-376.
13. Nieman SJ, Schmetz J, Menzel WP (1993) A comparison of several techniques to assign heights to cloud tracers. *Journal of Applied Meteorology* 32:1559–1568.
14. Nieman S, Menzel WP, Hayden CM, Gray D, Wanlong S, Velden C, Daniels J (1997) Fully automated cloud-driftwinds in NESDIS operations. *Bulletin of American Meteorological Society* 78: 1121–1133.

15. Rossow WB, Mosher F, Kinsella E, Arking A, Debois M, Harrison E, Minnis P, Ruprecht E, Seze G, Simmer C, Smith E (1985) ISCCP clouds algorithm inter-comparison. *Journal of Climate and Applied Meteorology* 24: 877-903.
16. Schmetz J, Holmlund K, Hoffman J, Strauss B, Mason B, Gaertner V, Koch A, van de Berg L (1993) Operational cloud-motion winds from Meteosat infrared images. *Journal of Applied Meteorology* 32: 1206–1225.
17. Tokuno M (1996) Operational system for extracting cloud motion and water vapor motion winds from GMS-5 image data. Proc. Third Int. Winds Workshop, EUM P18, Ascona, Switzerland, EUMETSAT, 21–30.
18. Tokuno M (1998) Collocation area for comparison of satellite winds and radiosondes. Proc. Fourth Int. Winds Workshop, EUM P24, Saanenmoser, Switzerland, EUMETSAT 21–28.
19. Tomassini C (1981) Objective analysis of cloud fields. Proc. Satellite Meteorology of the Mediterranean ESA, SP-159: pp.73-78.
20. Velden CS, Hayden CM, Nieman SJ, Menzel WP, Wanzong S, Goerss JS (1997) Upper-tropospheric winds derived from geostationary satellite water vapor observations. *Bulletin of American Meteorological Society* 78:173–195.

12. Atmospheric Motion Vector Winds (WV)

S.No.	Product Name	Spatial Resolution	Temporal Resolution
1	3DIMG_L2P_WVW	Point	30 minutes

12. Water Vapor Wind Vector

12.1 Algorithm Configuration Information

12.1.1 Algorithm Name

Atmospheric Motion Vector Winds (WV)

(Ref : IMD RFP Section 11.15)

12.1.2 Algorithm Identifier

3DIMG_L2P_WVV

12.1.3 Algorithm Specification

Version	Date	Prepared by	Description
1.0	14.02.2007	S. K. Deb, C. M. Kishtawal, P. K. Pal	WVWV Baseline Document
2.0	21.08.2012	S. K. Deb, C. M. Kishtawal, P. K. Pal	WVWV Baseline Document (Version 2)
3.0	21.07.2014	S. K. Deb, C. M. Kishtawal, P. K. Pal	WVWV Baseline Document (Version 2)

12.2 Introduction

The purpose of this document is to present an algorithm for retrieving Water Vapor Wind Vector (WVWV) from INSAT-3D water channel and its validation procedure. The INSAT-3D will have one water vapor channel (6.3 -7.1 (m). In this document some background and general characteristic of satellite-derived WVWV products, the methodology employed to derive the vector fields, theoretical basis and practical aspects of this algorithm and outlined the planned validation approach.

12.2.1 Overview and background

In early nineties, forecasters have used extensively the water vapor radiances from geo-stationary satellites qualitatively (Weldon and Holmes 1991). In quantitative studies, the first attempt was made by Hayden and Stewart (Hayden and Stewart 1987) by manually tracking moisture features in automated image sequences. Later studies (Laurent 1993, Velden 1993, Holmlund 1993) on this area have shown much maturity with ability of automated wind extraction methods for producing spatially coherent Water Vapor Wind Vector (WVWV) fields comparable in quality to operational cloud-tracked winds. The successful implementation of University of Wisconsin-Madison Co-operative Institute for Meteorological Satellite Studies (CIMSS) automated wind-extraction algorithm operationally at National Environmental Satellite Data and Information Service (NESDIS) have shown considerable improvement in this regards (Nieman et. al 1997). However, the quality control (QC) of WVWV fields still demanded intensive manual intervention. In 1992, NESDIS began the use of first version of new automated winds (CIMSS) software

package and producing full disk wind set without manual intervention since 1997 by suitably selecting tracers (filtering undesirable scenes) and assigning heights using several methods. The tracking features in subsequent imagery was automated using advanced pattern matching techniques (Merrill et al. 1991) and an automated quality control algorithm was also implemented. Laurent (1993) reports on Water Vapor (WV) wind extraction from Meteosat image data that is carried out under operational conditions. Subsequent years further development has been made by adding quality indicators (Holmlund 1998) to supply the users with additional information about the products. The U.S Geo-stationary Operational Environmental Satellites (GOES-8 etc series) are equipped with one imager and two sounder water vapor channels. As of GOES-12 the spatial resolution of the WV imager has been improved from 8Km to 4 Km at the sub-satellite point, and the radiometer is spectrally wider with a central wavelength of 6.5 micro m instead 6.7 micro m. The sounders look progressively deeper into the troposphere as the spectral band wavelength moves away from the 6.3micro m absorption band center. (Menzel et al 1998). This facts opens the opportunity for a 3-dimensional reconstruction of atmospheric motions (Menzel 2001). Water vapor winds from image data taken by the WV channel aboard the Japanese satellite Geo-stationary Meteorological Satellite (GMS)-5 have been produced since 1995, and clear-sky WV segments have been separated since 1998 (Tokuno 1996, 1998). Tokuno et al. (2002) state that the appropriate height assignment of clear-sky WV motion vectors is still an unresolved task.

Geo-stationary satellites of the Fengyun-2 series are operated by the National Satellite Meteorological Center of China since 1997 (Xu et al. 1998). These satellites are equipped with a water vapor channel as well. The method to evaluate atmospheric motion vectors compromises new features (Xu et al. 2002) that are unconventional relative to the earlier schemes applied to the data from Meteosat or GOES.

The study Buche et al. (2006) has shown improvement in Water Vapor structure displacements both in smooth and shallow scenes by using proper filters. He then tested a series of height assignment methods using altitude-based parameters such as wind shear and brightness contrast of pixels. This study reveals that for the cases of strong wind shear the methods that use the effective brightness temperature from the coldest pixels lead to better height assignments than do others that are based on the contribution function explicitly.

12.2.2 Objective

The main objective of this study is to derive the water vapor wind vectors over land and sea using multiple half hourly Water Vapor images. The region over which the winds are derived should be in the range of 500 from sub-satellite point.

12.3 Inputs

12.3.1 Static Data

Parameter	Resolution	Source
Continental boundary data	4 km	DP (IMD data)
Land Sea mask	8 km	

12.3.2 Image and preprocessing data (Dynamic)

Parameter	Resolution	Quantization	Accuracy	Source
Radiometric and geometric corrected gray count values of WV channel (6.7)	pixel	10 bit	--	Derived from raw data by DP (data processing)
Radiometric and geometric corrected gray count values of IR channel (10.5)	pixel	10 bit	--	Derived from raw data by DP (data processing)
Gray value to brightness temperature conversion table	-	-	0.3 K	Derived by DP
Geolocation file	Pixel	-	4 km	Derived by DP

12.3.3 Other Auxiliary data and Model Inputs

Parameter	Resolution	Accuracy	Source
Numerical model forecast of wind for all levels	0.5 degree	2 m/s (speed) 20° (direction)	IMD
All levels model forecast temperature		1 K	

12.4 Algorithm Functional Specifications

12.4.1 Overview

The procedure for deriving Water Vapor Wind Vector (WVWV) will be followed the basic methods employed for cloud tracking described in *Merrill 1989, 1991* with some upgrade in *Velden et al. 1997*. The vertical distribution of WVWV is dependent on several key factors: 1) characteristics of the spectral channel, such as central wavelength and band width; 2) air-mass characteristics, such as cloudiness and vertical moisture profile; 3) season (less moisture in the cool season leads to lower mean heights); and 4) latitude (higher moisture content and tropopause in the tropics leads to higher mean heights). In regard to the first point, the operational geo-stationary weather satellites with water vapor channels (GOES, Meteosat, and GMS) have similar features. The coverage attainable from WVWV is quite uniform in most cases, since the observed displacement

of a large portion of the targeted features is a result of pure moisture advection and adequately represents the instantaneous wind. The coverage is especially complete in the summertime tropics due to the presence of abundant moisture. However there are situations when extraction of useful WVWV information is difficult, if not impossible. These situations are summarized as: 1) very dry air masses lacking in moisture features, which prohibits good target selection; 2) regions of strong vertical motion, in which a coherent radiance signal can be significantly attenuated over the tracking interval; 3) uniform moisture fields lacking in contrast; 4) strong vertical shear zones, which can be deform targets over the tracking interval; and 5) rapidly amplifying extra-tropical troughs, which contain a large phase speed component. The above conditions represent relatively rare situations when considering full-disk coverage. As a whole the coverage and quality of WVWV will vary depending on atmospheric factors such as moisture availability and structure, vertical shear, and instrument characteristics such as detector precision and resolution.

12.4.1.1 Methodology

The main components for the process of WVWV detection are the following:

- Tracer selection
- Height assignment
- Tracking
- Wind buffer generation and Quality control

Before going to details, a crux of such approaches is given in the following steps:

- The tracer whose displacement is to be detected in subsequent WV image frames is selected.
- Let the source image s and target image t is registered to same scale. For every given $m \times m$ (typically 32×32 pixels) sub-image c_s of the tracer in image s , an $n \times n$ ($n > m$) search window w_t is selected in t . The center co-ordinates of c_s and w_t are identical as s and t are registered to the same scale.
- Given c_s and w_t , the problem of detection of WVWV is to find out best correlation measure between c_s and any one of $m \times m$ sub-image within w_t . The vector originating from the center co-ordinate of c_s to the center of best-matched $m \times m$ sub-image of w_t gives the WVWV.
- The correlation measures are some sort of similarity measure between time varying sub-images. This similarity measures can be accomplished either by maximum cross-correlation or sum of the squared difference measure or by Nash-Sutcliffe model efficiency function (Deb et al. 2008).

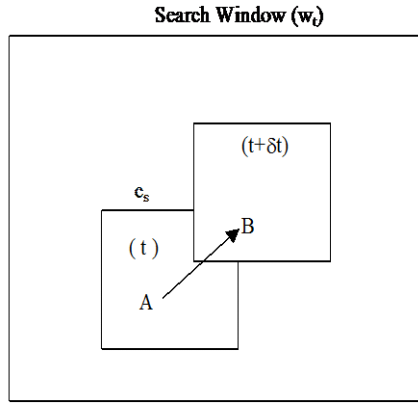


Figure 1: The schematic for WVVW detection process

The description of each step is given in the following:

12.4.1.1.1 Tracer selection:

At the National Environmental Satellite, Data, and Information Service (NESDIS), the initial cloud features are selected by locating the highest pixel brightness values for each target domain and computing the local gradients around those locations ([Nieman et al., 1997](#)). Any gradients greater than 15K are assigned as target locations, and prospective targets also undergo a spatial coherence analysis ([Coakley and Bretherton, 1982](#)) to filter out unwanted targets. Water vapor tracers are generally identified using the local bi-directional gradients in a template of specified size and compared with empirically determined thresholds to identify the features with sufficient variability ([Velden et al., 1997](#)) and those that pass the threshold value are identified as tracers for cloud-free environments. The pixel with maximum bi-directional gradient is the location of the tracer. At the European Organization for the Exploitation of Meteorological Satellites (EUMETSAT), the tracers in the Meteosat (first-generation satellites) images are selected using multispectral histogram analysis ([Tomassini, 1981](#)), which extracts the dominating scenes in an image segment corresponding to the area of 32 X 32 IR pixels at the sub-satellite point. Later the selected templates undergo a spatial coherence analysis ([Coakley and Bretherton, 1982](#)) to filter the image, to enhance the upper-level cloud. Because the spatial resolution of the water vapor channel of Kalpana-1 (8 km) is coarser relative to GOES (5 km) or Meteosat-7 (5 km), we used a 20 X 20 window (called a template) to identify features in Kalpana-1 images. However in case of INSAT-3D (4 km) we used 32 x 32 template window. The features are selected by computing local image anomaly in a 32 x 32 template window, both in cloudy and cloud free regions. The local image anomaly is calculated using the following formula:

$$a = \sum_i \sum_j |I(i, j) - \bar{I}| \quad (1)$$

Where $I(i, j)$ represent the grey value for (i, j) pixel of a template window and bar represents the mean of grey values within that template. The anomaly-based tracers are generally produced by a smooth feature field in comparison to the gradient-based features. This difference can help in reducing the tracking errors ([Deb et al., 2008](#)).

12.4.1.1.2 Height assignment

The height assignments of the selected tracers corresponding to each retrieved vectors are derived using the following widely used methods viz. the water vapor histogram method (HIST) and the H₂O intercept method ([Nieman et al., 1993](#)). Once final height is selected a few gross error checks are also applied. A brief description of each method is following:

a. Water Vapor Histogram Methods (HIST):

In this method the height assignment using a single satellite channel is made by comparing either infrared window or water vapor brightness temperature (BT) values with NWP model forecast temperature profiles. Cloud heights are determined by interpolating the cloud temperature, which is an average of coldest 20% of pixels, to the interpolated model guess field at the target location. A 6-h NWP model forecast from National Center for Environmental Prediction (NCEP) Global Forecast System (GFS) is the source of temperature profile. This method works well with opaque clouds. However, movement of opaque clouds usually does not accurately represent atmospheric motion at the assigned level ([Nieman et al., 1993](#)), resulting in a lower derived wind speed than observed. Semitransparent clouds or sub-pixel clouds give more accurate representation of the actual movement of the atmosphere at a particular level. Estimation of this level is very difficult in these cases since determination of the cloud top BT is affected by an unknown cloud emissivity or the percentage of cloud versus clear sky, respectively. The BT values are warmer than observed in these cases, thus leading to estimated cloud heights that are too high in pressure (too low in altitude), typically resulting in an overestimation of the wind speed at the estimated cloud height.

b. Water Vapor–Infrared Window Intercept Method (H₂O):

Height assignments derived with this method are based upon the fact that radiances from two different spectral bands are linearly related for different cloud amounts within the field of view at a specified height. Observed radiance measurements are a function of clear sky and opaque cloud radiances.

$$R(N) = (1 - nE)R_{cl}(N) + nER_{bcd}(N, P_c) \quad (2)$$

Opaque cloud radiance can be calculated from:

$$R_{bcd}(N, P_c) = R_{cl}(N) - \int_{P_c}^{P_s} t(N, p) \frac{db[N, T(p)]}{dp} dp \quad (3)$$

where R_{bcd} is the opaque ("black") cloud radiance, R_{cl} is the clear sky radiance, $t(N, p)$ is the fractional transmittance of radiation of spectral band N emitted from the atmospheric pressure p arriving at the top of the atmosphere ($p=0$), n is the fraction of FOV covered with cloud, P_s is the surface pressure, P_c is the cloud pressure, and $b[N, T(p)]$ is the Planck radiance of the spectral band N for a temperature $T(p)$. The second part of the above equation represents the radiance decrease from clear sky conditions introduced by an opaque cloud at a pressure level p . This calculation is dependent upon an "accurate" estimation of the current atmospheric temperature and moisture structure, which are provided by a NWP model forecast profile. By comparing the observed radiances with the calculated radiances (for an observed atmosphere defined by the model guess profiles), an estimation of the cloud height can be derived for a completely opaque cloud. In the [Fig. 2](#), observed WV and IR radiances at each field of view (FOV) points are plotted with the calculated radiances at different

heights for opaque clouds in the atmosphere (curved line). The straight line connects the center points of the warmest and coldest clusters, which approximate the observed surface and cloud conditions.

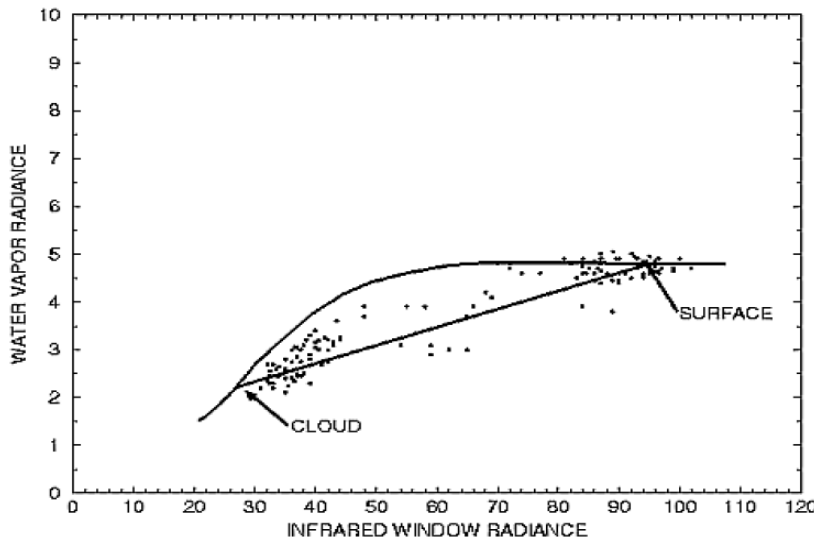


Fig 2: Measured radiances ($\text{mW m}^{-2} \text{ sr}^{-1} \text{ cm}^{-1}$) for fields of view partially filled with clouds
([Nieman et al., 1993](#))

By extrapolating this line to intersect the calculated radiance curve, where the cloud amount is one (representing an opaque cloud), the cloud top temperature/pressure can be determined. The cluster determination algorithm used is a modified version of the bivariate asymmetric Gaussian histogram analysis ([Rossow et al., 1985; Tomassini, 1981](#)), and involves ten steps. These steps are outlined in detail in [Nieman et al., 1993](#). Calculated water vapor radiances can be in error due to incorrect NWP model forecast profiles. This error would lead to calculated radiances being systematically higher or lower than observed radiances. When the calculated radiances are systematically lower, an adjustment is applied to the radiances obtained using the above equation. When the calculated radiances are greater than observed radiances, no adjustment is applied since it is assumed that the lower measured radiance is due to cloud contamination. The accuracy of this method can be affected by the amount of water vapor in the atmosphere. Dry atmospheric conditions lead to a steeper slope between the IR and WV radiances, leading to an overestimate in the target height (lower pressure value). The NCEP GFS model forecast are used here as guess fields.

Once the water vapor tracers heights using the above two algorithms have been calculated, the best height among the available heights is determined. The lowest pressure (highest altitude) value of all the calculated height values is used as the final pressure height.

12.4.1.1.3 Tracking:

If a traceable feature is found in the first image and corresponding height of the selected tracers are estimated, the match of this template is searched in the second image within a bigger “search window”, centered at the same point as the template window. To optimize the search window size, the first guess model wind direction at the tracer location is also considered. The search area is optimized within ± 30 degree from the model wind direction at that level of atmosphere. The 32×32 template in the second image that lies within the search window should have the same class as the template in the first image; otherwise the

template in the second window is rejected. The cross-correlation technique is used operationally for tracking the tracer between two images in most operational centers. However, in this study the degrees of matching between two successive images are calculated by the Nash-Sutcliffe model efficiency ([Nash and Sutcliffe, 1970](#)) coefficient (E). It is defined as

$$E = 1 - \frac{\sum_{i=1}^n (I_t - I_s)^2}{\sum_{i=1}^n (I_t - \bar{I}_t)^2} \quad (4)$$

Where I_t and I_s are the variance of the grey values for template window and search window and \bar{I}_t is the average of variance of template window. Here n is 32×32 and this is the size of template window and corresponding template of same size in the searching area. The size of the searching area in the subsequent image is taken as 64×64 . The coefficient E is normalized to values between $-\infty$ and $+1$. An efficiency $E = 1$ corresponds to a perfect match, $E = 0$ means that search window is as accurate as mean of the template window and $E < 0$ implies the lack of matching between template and search window. The closer the model efficiency to 1, the more accurate the matching between the windows. A cut-off value of $E=0.8$ is defined, below which a matching of target is not considered. The Nash-Sutcliffe model efficiency coefficient (E) is normalized and its value lies between $-\infty$ and 1, towards the higher end (e.g. as $E \rightarrow 1.0$), the value of E approaches r^2 , where r is the correlation coefficient. Thus a value of $E=1$ is exactly equivalent to a correlation of 1.0 between two objects. The maximum value of E is chosen as the best fit for tracking. One of the main advantages of this matching technique is that it reduces the possibility of multiple maxima, because the parameter E has a higher sensitivity to differences between two features compared to maximum cross correlation coefficient (MCC). Thus, when the degree of mismatch between two objects increases, the value of E falls more sharply compared to that of MCC, making E a better index for matching two objects. The application of this tracking method in estimation of water vapor winds has shown some improvement over Indian Ocean region ([Deb et al., 2008](#)).

12.4.1.4: Wind buffer generation and Quality control

Quality indicator of a derived wind vectors is traditionally represented as the degree of the coherence of a given vector with its surrounding. In most of the operational centers the AMVs are derived from three successive satellite images and the quality control of the retrieved winds are done either through Quality Indicator ([Holmlund, 1998](#)) followed at EUMETSAT or through 3-dimensional recursive filter function followed at NESDIS ([Nieman et al., 1997](#)) or both the algorithms together. In the present study a new technique of wind buffer generation and quality control procedure is proposed and implemented first time in AMV retrieval. In this technique, a wind buffer is created using previous eight images between a pair of images (viz. between 1-2, 2-3, 3-4, 4-5, 5-6, 6-7 and 7-8) and stored in a file (**Fig. 3**). The previous eight images were considered to maintain the minimum 4-hour decorrelation timescale during retrieval ([Kaur et al., 2011](#)). In quality control procedure consists of a coherence analysis which forms the basis for acceptance/rejection of a vector and degree of coherence computed is used to assign quality flags to the derived vector. The value of quality flag falls sharply by an exponential function, as the disagreement of a given vector with its surroundings increases. Here each vector wind is represented by a complex

number $V_{i,j}^c = u_{i,j} + i v_{i,j}$. For every new vector under consideration, (from current image-pair), its vector difference from the buffer is computed at the same as well as 3 X 3 neighborhood (**Fig. 3**), provided, the vectors to be compared show similar brightness characteristics (to maintain the similar height).

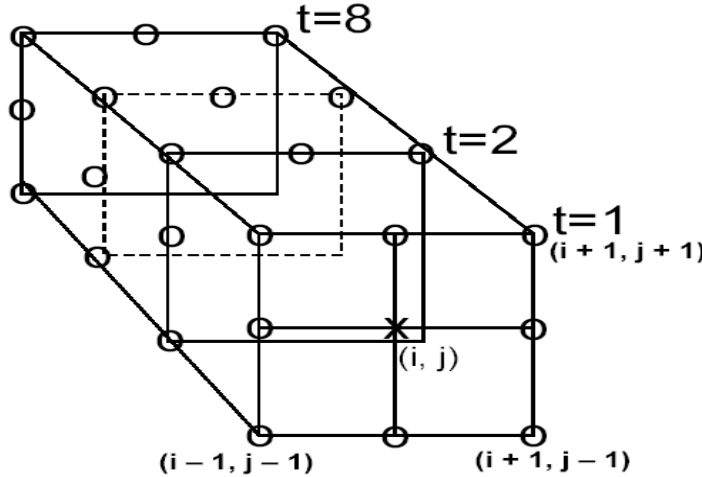


Fig 3: A schematic diagram of quality control process.

Here X (cross sign) at the centre of first box represents the current vector under consideration and O (circle sign) represents spatial and temporal neighborhood vectors. The vector differences (magnitude of complex numbers) are calculated as $\{V_{dif}\}_{i,j,t} = V^c - \{V\}_{i,j,t}$. Here V^c represents the current vector at (i, j) point and $\{V\}_{i,j,t}$ neighborhood vectors with $-1 \leq i \leq 1, -1 \leq j \leq 1$ and temporal scale t varies from 1 to 8. If all spatial and temporal neighborhood vectors are present, then the difference set will contain 72 vectors (9 spatial neighborhoods with 8 temporal scales). However, all vectors may not be there all the times. The quality control process begins if at least 10 vector differences V_{dif} , excluding the difference corresponding to current (i, j) , are present in the set. In the next step, set of vector differences $\{V_{dif}\}$ is arranged in ascending order. The quality control process begins if the average of 10 V_{dif} is greater than 2.5 m/s. In the next step, the QI value for each vector is determined by using EUMETSAT procedure where four different tests are performed, which is normalized by a tanh-function that returns the value between 0 and 1. A weighted average of these individual quality indicators is then used for screening of poor quality vectors from final output. If any vector is not present in the immediate two pairs, then instead of rejecting, search process goes to the previous time steps of the wind buffer and if still it is not present it goes to next previous time steps and so on.

If S is the mean “speed” of a vector computed from two pair of images, then different quality functions are computed as below :

Direction Consistency Function:

$$DCF = 1.0 - \left[\tanh\left(\frac{\Delta\theta}{A_1 \exp(-S/B_1) + C_1}\right) \right]^{D_1}$$

Speed Consistency Function:

$$SCF = 1.0 - \left[\tanh\left(\frac{\Delta S}{MAX(A_2 S, B_2) + C_2}\right)\right]^{D_2}$$

Vector Consistency Function:

$$VCF = 1.0 - \left[\tanh\left(\frac{\Delta V}{MAX(A_3 S, B_3) + C_3}\right)\right]^{D_3}$$

Spacial Consistency Function:

$$PCF = 1.0 - \left[\tanh\left(\frac{\Delta V_m}{MAX(A_4 S, B_4) + C_2}\right)\right]^{D_4}$$

In the above formulation, $\Delta\theta, \Delta S, \Delta V$ represent the difference of direction (degrees), difference of speed, and the length of the difference vector between first and second satellite wind component. ΔV_m is the length of difference vector between satellite wind component and its best neighbor. The best neighbor is determined by the smallest vector difference. Quantities A_N, B_N, C_N , and D_N are constants. The final quality indicator of a wind vector is given as

$$QI = \frac{DCF + SCF + VCF + PCF}{4.0}$$

All the vectors with $QI < 0.6$ are rejected.

In the conventional triplet based methodology requires that a vector is available in both sets (i.e. in 1-2 and 2-3), if not so, such vectors are rejected, because they don't get "support". Hundreds of "isolated" vectors thus get eliminated, even though they represent the real situation. In the current method, the vector under consideration receives support from the past eight images. This method produces higher number of valid retrieval in the low-level and captures upper-level meridional flow very prominently. To explain this more explicitly, if we take eight satellite images each with 30-minute interval starting at 00:00 UTC to 03:30 UTC, then winds retrieved using each-image pair are stored as buffer in a file and represented as wind buffer generated at 03:30 UTC. The buffer generated at 03:30 UTC is used for quality control for wind retrieved using 03:30 UTC and 04:00 UTC images and the second image time is given as actual observation time of retrieved wind. For example winds retrieved using 03:30 UTC wind buffer and 03:30 UTC and 04:00 UTC images is given as 04:00 UTC observation time. As a whole to complete the process once it requires nine images. Similarly the buffer is updated at every 30-minute with the latest available image and process is repeated for next cycle of wind retrieval. This method produces higher number of valid retrieval in all levels and captures upper-level meridional flow very prominently.

The height assignment of WVWV is a long-standing problem in this regard. In cloud free regions, the radiometric signal from pure water vapor structure is a result of emittance over a finite layer. It is further complicated by radiance contributions from multiple moist layer (*Weldon and Holmes 1991*). Here the challenge is to assign a height that best represents the motion of the feature. In the first step, the instrument measured radiances is converted into brightness temperature, which requires an accurate definition of the spectral response of the

instrument. It is important to note that the different instruments are sensing radiation from slightly different parts of the H₂O absorption band. Sampling the center of the absorption band (around 6.3μm) yields radiation from upper levels of the troposphere. Sampling away from the center of the absorption band yields radiation from lower levels of the troposphere.

Once the target is selected for tracking, the brightness temperature in the target area is averaged and this value will be matched with a collocated model guess temperature profile. The level of optimum fit will be used to assign an initial pressure height.

12.4.2 Operational Implementation

1.4.2.1 Step 1 : Conversion from gray count to BT

- In this step a radiation model will be used to convert the instrument measured radiances into brightness temperature. This requires an accurate definition of the spectral response of the satellite.
- It is important that the different instruments are sensing radiation from slightly different parts of H₂O absorption band. Sampling the centre of the absorption band yields radiation from the upper levels of the troposphere, similarly sampling away from the centre of the absorption band yields radiation from lower levels of the atmosphere

12.4.2.2 Step 2: Tracer selection from image

- Water-vapor images tracer selection will be done by evaluating local image anomaly surrounding each pixel in the target array and selecting the maximum brightness temperature of the window exceeding some thresholds value.

12.4.2.3 Step 3: Height assignment

- Assign height of the selected tracer using water vapor histogram technique. In this case the brightness temperature in the target window will be averaged and matched with collocated numerical model temperature profile. The level of optimum fit will be assigned as initial height.
- Re-assign the height using H₂O intercept technique for semi-transparent tracers.
- Assign correct height after implementing all the height assignment technique mentioned above.

12.4.2.4 Step 4: Tracking

- The tracking employs a simple search for the minimum in the sum of squares of the radiance difference between the target and search arrays in subsequent half hourly images. This search will be done in the direction of ± 30° of model wind.

12.4.2.5 Step 5: Wind buffer generation & quality control

- The wind buffer is created using previous eight images between pairs of images (viz. the winds retrieved between 1-2, 2-3, 3-4, 4-5, 5-6, 6-7 and 7-8) and stored in a file. The selection of eight images is consistent with decorrelation timescales of winds over tropical region.
- Use quality control criteria for selecting wind using the wind buffer.
- Again calculate wind speed and direction.

12.5 Outputs

Parameter	Unit	Min	Max	Accuracy	Resolution
U and V component of WVVWV	m/sec	0	70	5 -6 m/s	0.5 – 2.5 deg
Domain of output : 30°E – 130°E :: 50° S – 50° N					

12.5.1 Format of the output and the domain

As output of WVVWV the following parameters will be provided to IMD:

- Zonal and meridional components of the wind vectors.
- Latitudinal and longitudinal position.
- Height of WVVWV

The format of the final product will be like this:

Parameter	Lat.	Long.	Level	U-component	V-component	Quality Flag	Wind Speed (m/s)	Wind direction (clockwise from North)
Unit	Deg N	Deg E	hPa	m/s	m/s	0.0 to 0.9	m/s	Deg

12.6 Validation

12.6.1 Data required

Parameter	Type	Source
Wind	Collocated Rawinsonde	IMD

12.6.2 Methods of validation

The evaluation of WVVWV should be taken into both qualitative and quantitative measures. Quantitative assessment of the WVVWV product is possible from statistical analyses and impact on NWP. The traditional method of validation is matching observations with collocated Rawinsondes. The statistical validation will be done according to the CGMS winds evaluation reporting guidelines. These statistics can provide a fixed measure of product quality over time and can be employed in determining observation weight in objective data assimilation. At the CGMS XXIII the Working Group on Satellite Tracked Winds recommended that evaluation of operational wind production quality should be accomplished with a new standardized reporting method. The recommended three parts to the report.

- (i) Monthly means of speed bias and rms vector difference between Rawinsondes and satellite winds for low (>700 hPa), medium (700-400 hPa), and high (< 400 hPa) levels together with the Rawinsonde mean wind speed. This should be done for three latitude bands: north of 20 N, the tropical belt (20 N to 20 S), and south of 20 S.

- (ii) Trends of the evaluation statistics for the monthly cloud motion vectors and water vapor motion vectors through the last 12 months.
- (iii) Information on recent significant changes in the wind retrieval algorithm.

The Vector Difference (VD) between an individual wind (i) and the collocated Rawinsonde (r) used for verification is given by

$$(VD) = [(U_i - U_r)^2 + (V_i - V_r)^2]^{1/2}$$

The speed bias is given by

$$(BIAS)_i = 1/N \sum_{i=1}^N [(U_i^2 + V_i^2)^{1/2} - (U_r^2 + V_r^2)^{1/2}]$$

The mean vector difference (MVD) traditionally reported is

$$(MVD) = 1/N \sum_{i=1}^N (VD)_i$$

And the standard deviation (SD) about the mean vector difference traditionally reported is

$$(SD) = [1/N \sum_{i=1}^N ((VD) - (MVD))^2]^{1/2}$$

The root-mean-square error (RMSE) traditionally reported is the square root of the sum of the squares of the mean vector difference and the standard deviation about the mean vector difference,

$$(RMSE) = [(MVD)^2 + (SD)^2]^{1/2}$$

It must be noted that this definition of the mean vector difference is not the same as the mean component difference. The mean difference is calculated from the sum of the squares of the deviations of each component (u and v) of the wind vector.

$$(\Delta U^2) = \sum_{i=1}^N (U_i - U_r)^2$$

$$(\Delta V^2) = \sum_{i=1}^N (V_i - V_r)^2$$

$$(MCD) = [(\Delta U^2) + (\Delta V^2)]^{1/2} \neq (MVD)$$

To avoid confusion, a common terminology will be accepted. It is suggested to report mean vector difference (MVD) and standard deviation (SD). The standard accuracy according to CGMS guideline for WVWV is that the root mean square error (RMSE) for WV winds should be 7m/s respectively with respect to Rawinsonde observations. The mean bias for both sets of winds should be about zero.

12.7 Technical Issues (Limitations etc)

Accuracy of the product depends on the accuracy of the registration of the images. Assuming the registration has an error of 1 pixel then error of the final product will be of 5 m/sec. However the following limitations of the present study have to be kept in mind. The spatially coherent, high-resolution coverage of upper tropospheric winds are possible from geostationary satellite remote sensing of water vapor. WVWV are comparable in quality to operational upper-level cloud-motion vectors. However, the retrieved vectors in regions are lacking in defining moisture structure, though they have the ability to obtain track-able information in extremely dry air masses and regions of strong subsidence is limited. The individual vectors represent single level reports; however, upper level vertical winds profiles are possible by using multi-spectral observations.

12.8 References

1. Bedka KM, Mecikalski JR (2005) Application of satellite-derived atmospheric motion vectors for estimating meso-scale flows. *Journal of Applied Meteorology* 44: 1761-1772.
2. Buche, G., H. Karbstein, A. Kummer, and H. Fischer, 2006: Water Vapor structure displacements from Cloud-free Meteosat scenes and their interpretation for the wind field.,*J. Appl. Meteor.*, 45, 556-575.
3. Deb SK, Kishtawal CM, Pal PK (2010). Impact of *Kalpana-1* derived water vapor winds on Indian Ocean Tropical cyclones forecast. *Monthly Weather Review* 138 (3): 987-1003.
4. Deb SK, Kishtawal CM, Pal PK, Joshi PC (2008) A modified tracer selection and tracking procedure to derive winds using Water vapor imagers. *Journal of Applied Meteorology and Climatology* 47: 3252-3263.
5. Deb SK, Kishtawal CM, Kaur Inderpreet, Pal PK, Kiran Kumar AS (2012a). Multiplet based Technique to derive Atmospheric winds from Kalpana-1, *The Proceedings 11th International Wind Workshop*, 20-24 February, 2012, Auckland, New Zealand.
6. Deb SK, Kaur Inderpreet, Kishtawal CM, Pal PK (2012b). Atmospheric Motion Vectors from Kalpana-1: An ISRO Status, *The Proceedings 11th International Wind Workshop*, 20-24 February, 2012, Auckland, New Zealand
7. Hayden, C. M and T. R. Stewart, 1987: Three-dimensional recursive filter objective analysis of meteorological fields. Eighth Conf. on Numerical Weather Prediction, Baltimore, MD, Amer. Meteor. Soc., 185-190.
8. Hayden, C. M., and R. J. Purser, 1995: Recursive filter objective analysis of meteorological fields: Applications to NESDIS operational processing. *J. Appl. Meteor.*, 34, 3-15.
9. Holmlund, K., 1993: Operational water vapor wind vectors from Meteosat imagery. Second Workshop on Wind Extraction from Operational Satellite Data, Tokyo, Japan, EUMETSAT, 77-84.
10. Holmlund, K., 1998: The utilization of statistical properties of satellite-derived atmospheric motion vectors to derive quality indicators, *Wea Forecasting*, 13, 1093-1104.

11. Kelly G (2004) Observing system experiments of all main data types in the ECMWF operational system. 3rd WMO Numerical Weather Prediction OSE Workshop, Alpbach, Austria, WMO, Tech Rep. 1228: pp 32-36.
12. Kishtawal CM, Deb SK, Pal PK, Joshi PC (2009) Estimation of Atmospheric Motion Vectors from Kalpana-1 imagers. *Journal of Applied Meteorology and Climatology* 48: 2410-2421.
13. Kaur Inderpreet, Kishtawal CM, Deb SK, Kumar Raj (2012) Temporal Scales of Satellite Derived Atmospheric Winds over the Asian Monsoon Region. *IEEE. Geoscience and Remote Sensing Letters*. 9 (2): 317-320.
14. Laurent, H., 1993: Wind extraction from Meteosat water vapor channel image data. *J. Appl. Meteor.*, 32. 1124-1133.
15. Merrill, R. T., W. P. Menzel, W. Baker, J. Lynch and E. Legg, 1991: A report on the recent demonstration of NOAA's upgraded capability to derive cloud motion satellite winds. *Bull. Amer. Meteor. Soc.*, 72, 372-376.
16. Merrill, R. T., 1989: Advances in the automated production of wind estimates from geostationary satellite imagery. Preprints, Fourth Conf. on Satellite Meteorology and Oceanography, San Diegom CA, Amer. Meteor. Soc, 246-249.
17. Merrill, R. T., Menzel W. P, Baker W, Lynch J. and Legg E, (1991): A report on the recent demonstration of NOAA's upgraded capability to derive cloud motion satellite winds. *Bull. Amer. Meteor. Soc.*, 72, 372-376.
18. Menzel W. P. 2001: Cloud tracking with satellite imagery: From the pioneering work of Ted Fujita to present. *Bull. Amer. Meteor. Soc.*, 82, 33-47.
19. Menzel, W. P., F. C. Holt, T. J. Schmit, R. M. Aune, A. J. Schreiner, G. S. Wade and D. G. Gray, 1998: Application of GOES-8/9 soundings to weather forecasting and nowcasting., *Bull. Amer. Meteor. Soc*, 79, 2059-2077.
20. Nieman, S. J., W. P. Menzel, C.M. Hayden, D. Gray, S. Wanlong, C. S. Velden, and J. Daniels, 1997: Fully automated cloud-drift winds in NESDIA operations. *Bull. Amer. Metror. Soc.*, *Bull. Amer. Meteor. Soc.*,78, 1121-1133.
21. Nieman S, Menzel WP, Hayden CM, Gray D, Wanlong S, Velden C, Daniels J (1997) Fully automated cloud-driftwinds in NESDIS operations. *Bulletin of American Meteorological Society* 78: 1121–1133.
22. Rossow WB, Mosher F, Kinsella E, Arking A, Debois M, Harrison E, Minnis P, Ruprecht E, Seze G, Simmer C, Smith E (1985) ISCCP clouds algorithm inter-comparison. *Journal of Climate and Applied Meteorology* 24: 877-903.
23. Schmetz J, Holmlund K, Hoffman J, Strauss B, Mason B, Gaertner V, Koch A, van de Berg L (1993) Operational cloud-motion winds from Meteosat infrared images. *Journal of Applied Meteorology* 32: 1206–1225.
24. Tokuno, M., 1996: Operational system for extracting cloud motion and water vapor motion winds from GMS-5 image data. Proc. Third Int. Winds Workshop, Vol EUM p18, Ascona, Switzerland, EUMETSAT, 21-30.
25. Tokuno, M., 1998: Improvements in the method to extract operationsl cloud motion winds and water vapor motion winds of GMS-5 system. Proc. Fourth Int. Winds Workshop, Vol. EUM P-24, Saanenmoser, Switerland, EUMETSAT, 61-68.
26. Tokuno, M., R. Kumabe, and Y. Kajino, 2002: Recent advances to experimental GMS atmospheric motion vector processing system at MSC/JMA. Proc. Sixth Int. Winds Workshop, Vol EUM P35, Madison, WI, EUMETSAT, 25-32.

27. Tomassini C (1981) Objective analysis of cloud fields. Proc. Satellite Meteorology of the Mediterranean ESA, SP-159: pp.73-78.
28. Velden, C. S., 1993: Investigation of water vapor motion winds from geostationary satellites. Second Workshop on Wind Extraction from Operational Satellite Data, Tokyo, Japan, EUMETSAT, 99-104.
29. Velden, C. S., C. M. Hayden, S. J. Nieman, W. P. Menzel, S. Wanzong, J. S. Goerss, 1997: Upper-tropospheric winds derived from geo-stationary satellite water vapor observations., Bull. Amer. Meteor. Soc., 78(2), 173-195.
30. Weldon, R. B., and S. J. Holmes, 1991: Water vapor imagery: Interpretation and applications to weather analysis and forecasting. NOAA Tech Rep. NESDIS 67, 213 pp.
31. Xu, J., Q. Zhang, X. Fang, and J. Liu, 1998: Cloud motion winds from FY-2 and GMS-5 meteorological satellites. Proc. Fourth. Int. Winds Workshop. Vol EUM P24, Saanenmoser, Switzerland, EUMETSAT, 41-48.
32. Xu, J., K. Holmlund, Q. Zhang, and J. Schmetz, 2002: Comparison of two schemes for derivation of atmospheric motion vectors. J. Geophys. Res, 107, 4196. doi:10.1029/2001JD000744.

13. Atmospheric Motion Vector Winds (VIS)

S.No.	Product Name	Spatial Resolution	Temporal Resolution
1	3DIMG_L2P_VSW	Point	30 minutes

13. Visible Wind Vectors (VIS)

13.1 Algorithm Configuration Information

13.1.1 Algorithm Name

Atmospheric Motion Vector Winds (VIS)

(Ref : IMD RFP Section 11.14)

13.1.2 Algorithm Identifier

3DIMG_L2P_VSW

13.1.3 Algorithm Specification

Version	Date	Prepared by	Description
1.0	22.08.2012	S.K. Deb C.M. Kishtawal Inderpreet Kaur	Visible winds Baseline Document
2.0	21.07.2014	S.K. Deb, C.M. Kishtawal	Visible winds Baseline Document (Version 2)

13.2 Introduction

The purpose of this document is to present an algorithm for retrieving Visible Winds (VIS) from INSAT-3D imager channel and its validation procedure. The INSAT-3D will have one visible channel (0.55 – 0.75 (m). In this document some background and general characteristic of satellite-derived winds from visible channels and INSAT-3D visible channel characteristics; the methodology employed to derive the vector fields, theoretical basis and practical aspects of this algorithm and outlined the planned validation approach.

13.2.1 Overview and background

Spatio-temporal analysis of meteorological events is an important part of routine numerical weather analysis. In that context, a cloud tracking method is presented here for a sequence of geostationary satellite images. Given a pair of remotely sensed images, captured at a fixed time interval (typically, 30 min), the objective is to derive motion vectors associated with the cloud mass. This correspondence process is a useful precursor to cloud motion vector studies and spatio-temporal analysis of cloud life cycles. The spatio-temporal life cycle includes the generation, dissipation and assimilation of clouds that can be observed in a sequence of geostationary satellite images. During the 1970's and early 1980's, cloud motion winds were produced in major operational centers like NESDIS (National Environmental Satellite Data and Information Service) using a combination of automated and manual techniques. Early automated techniques supplied quality low-level vectors from visible channels but often yielded in consistent quality for mid- and high-level motions. Height assignment for the visible winds is done with collocated infrared images using infrared window technique. In the subsequent years, due to the developments in image-processing and pattern recognition techniques (Merill et al., 1991), it was possible to design fully automatic techniques for wind retrieval, and NESDIS began its application in 1992. In later time, several new developments were made to make accurate retrievals of winds from satellite images.

13.2.2 Objective

The main objective of this study is to derive the Visible Winds (VIS) over sea using multiple successive half hourly VIS images. The region over which the winds are derived should be in the range of 500 from sub-satellite point.

13.3 Inputs

13.3.1 Static Data

Parameter	Resolution	Source
Continental boundary data	1 km	DP (IMD data)

13.3.2 Image and preprocessing data (Dynamic)

Parameter	Resolution	Quantization	Accuracy	Source
Radiometric and geometric corrected gray count values of split window IR channel (10.5-11.5 μm and 11.5-12.5 μm) and VIS channel (0.65 μm) (All the data is required in fixed lat-lon grid for continuous 8-images separated by 30 minutes time interval)	pixel	10 bit	--	Derived from raw data by DP (data processing)
Gray value to brightness temperature conversion table	-	-	0.3 K	Derived by DP
Geo-location file	Pixel	-	1 km	Derived by DP

13.3.3 Other Auxiliary data and Model Inputs

Parameter	Resolution	Accuracy	Source
Numerical model forecast of wind for all levels	1 degree or 0.5 degree	2 m/s (speed) 20° (direction)	IMD
All levels model forecast Temperature		1° K	

13.4 Algorithm Functional Specifications

13.4.1 Overview

13.4.1.1 Methodology

13.4.1.1.1 Tracer selection and Tracking

At the National Environmental Satellite, Data, and Information Service (NESDIS), the initial cloud features are selected by locating the highest pixel brightness values for each target domain and computing the local gradients around those locations ([Nieman et al., 1997](#)). Any gradients greater than 15°K are assigned as target locations, and prospective targets also undergo a spatial coherence analysis ([Coakley and Bretherton, 1982](#)) to filter out unwanted targets. Water vapor tracers are generally identified using the local bi-directional gradients in a template of specified size and compared with empirically determined thresholds to identify the features with sufficient variability ([Velden et al., 1997](#)) and those that pass the threshold value are identified as tracers for cloud-free environments. The pixel with maximum bi-directional gradient is the location of the tracer. At the European Organization for the Exploitation of Meteorological Satellites (EUMETSAT), the tracers in the Meteosat (first-generation satellites) images are selected using multispectral histogram analysis ([Tomassini, 1981](#)), which extracts the dominating scenes in an image segment. Later the selected templates undergo a spatial coherence analysis ([Coakley and Bretherton, 1982](#)) to filter the image, to enhance the upper-level cloud. In the present study the features are selected by computing local image anomaly in a 32×32 template window, both in cloudy regions of the visible images. The local image anomaly is calculated using the following formula:

$$a = \sum_i \sum_j |I(i, j) - \bar{I}| \quad (1)$$

Where $I(i, j)$ represent the grey value for (i, j) pixel of a template window and bar represents the mean of grey values within that template. The anomaly-based tracers are generally produced by a smooth feature field in comparison to the gradient-based features. This difference can help in reducing the tracking errors ([Deb et al., 2008](#)).

13.4.1.1.2 Height assignment

The height assignments of the selected tracers selected based on the above criterion are derived using the collocated infrared images with the following widely used methods viz. such as the infrared window (WIN) technique and the cloud base method ([LeMarshall, 1993](#)). Once final height is selected a few gross error checks are also applied. A brief description of each method is following:

2.4 Infrared Window Channel (WIN):

In this method the height assignment using a single satellite channel is made by comparing either infrared window brightness temperature (BT) values with NWP model forecast temperature profiles. Cloud heights are determined by interpolating the cloud temperature, which is an average of coldest 20% of pixels, to the interpolated model guess field at the target location. A 6-h NWP model forecast from National Center for Environmental Prediction (NCEP) Global Forecast System (GFS) is the source of temperature profile. This method works well with opaque clouds. However, movement of opaque clouds usually does not accurately represent atmospheric motion at the assigned level ([Nieman et al., 1993](#)), resulting in a lower derived wind speed than observed.

2.5 Cloud Base Method (BASE):

Wind speeds for low-level cumulus clouds (cloud top pressures greater than 600 hPa or altitudes lower than 600 hPa) have been found to be best represented by the movement at the cloud base level instead of the mid or upper levels of the cloud ([Hasler et al., 1979](#)). A method was developed at the Australian Bureau of Meteorology ([LeMarshall, 1993](#)) to estimate this height using the Infrared Window channel. This method first constructs a histogram of the BT values over a selected region surrounding the cloud target being examined. This histogram is then smoothed and Hermite polynomials are fitted to the histogram to separate the distribution into two components; a cloudy and clear sky region. Assuming the distributions are normal, the cloud base height can be estimated. The mid cloud temperature is determined by examining the second derivative histogram of the cloudy distribution, while the cloud top temperature is estimated to be located at the coldest 5% of the cloudy distribution. The cloud base temperature is estimated to be located the same distance from the mid cloud temperature as the cloud top temperature. The calculated cloud base temperature is converted to a pressure using model field interpolated to the target location. As mentioned previously, this height assignment method is only applied to those targets which are calculated to have a cloud top pressure of greater than 600 hPa (i.e. altitude lower than 600 hPa). This "initial" target cloud top height is provided by one of the previous Infrared Window height assignment methods. The BASE method is used to adjust only these winds, and is not utilized for water vapor winds or winds with pressures less than 600 hPa (i.e. altitudes higher than 600 hPa).

Once the visible tracers heights using the above two algorithms have been calculated, the best height among the available heights is determined. The lowest pressure (highest altitude) value of all the calculated height values is used as the final pressure height. However, if for a specific visible tracer final height is WIN and a valid BASE height is available, then the BASE height is used as the final height.

13.4.1.3 Tracking

If a traceable feature is found in the first image and corresponding height of the selected tracers are estimated, the match of this template is searched in the second image within a bigger “search window”, centered at the same point as the template window. To optimize the search window size, the first guess model wind direction at the tracer location is also considered. The search area is optimized within ± 30 degree from the model wind direction at that level of atmosphere. The 32 X 32 template in the second image that lies within the search window should have the same class as the template in the first image; otherwise the template in the second window is rejected. The cross-correlation technique is used operationally for tracking the tracer between two images in most operational centers. However, in this study the degrees of matching between two successive images are calculated by the Nash-Sutcliffe model efficiency ([Nash and Sutcliffe, 1970](#)) coefficient (E). It is defined as

$$E = 1 - \frac{\sum_{i=1}^n (I_t - I_s)^2}{\sum_{i=1}^n (I_t - \bar{I}_t)^2} \quad (2)$$

Where I_t and I_s are the variance of the grey values for template window and search window and \bar{I}_t is the average of variance of template window. Here n is 32×32 and this is the size of template window and corresponding template of same size in the searching area. The size of the searching area in the subsequent image is taken as 64×64 . The coefficient E is normalized to values between $-\infty$ and $+1$. An efficiency $E = 1$ corresponds to a perfect match, $E = 0$ means that search window is as accurate as mean of the template window and $E < 0$ implies the lack of matching between template and search window. The closer the model efficiency to 1, the more accurate the matching between the windows. A cut-off value of $E=0.8$ is defined, below which a matching of target is not considered. The Nash-Sutcliffe model efficiency coefficient (E) is normalized and its value lies between $-\infty$ and 1, towards the higher end (e.g. as $E \rightarrow 1.0$), the value of E approaches r^2 , where r is the correlation coefficient. Thus a value of $E=1$ is exactly equivalent to a correlation of 1.0 between two objects. The maximum value of E is chosen as the best fit for tracking. One of the main advantages of this matching technique is that it reduces the possibility of multiple maxima, because the parameter E has a higher sensitivity to differences between two features compared to maximum cross correlation coefficient (MCC). Thus, when the degree of mismatch between two objects increases, the value of E falls more sharply compared to that of MCC, making E a better index for matching two objects. The application of this tracking method in estimation of water vapor winds has shown some improvement over Indian Ocean region ([Deb et al., 2008](#)).

13.4.1.1.4: Wind buffer generation and Quality control

Quality indicator of a derived wind vectors is traditionally represented as the degree of the coherence of a given vector with its surrounding. In most of the operational centers the AMVs are derived from three successive satellite images and the quality control of the retrieved winds are done either through Quality Indicator (QI) ([Holmlund, 1998](#)) followed at EUMETSAT or through 3-dimensional recursive filter function followed at NESDIS ([Nieman et al., 1997](#)) or both the algorithms together. In the present study a new technique of wind buffer generation and subsequently QI procedure followed at EUMETSAT is proposed. In this technique, a wind buffer is created using previous eight images between a pair of images (viz. between 1-2, 2-3, 3-4, 4-5, 5-6, 6-7 and 7-8) and stored in a file (**Fig. 1**). The previous eight images were considered to maintain the minimum 4-hour decorrelation timescale during retrieval ([Kaur et al., 2011](#)). In quality control procedure consists of a coherence analysis which forms the basis for acceptance/rejection of a vector and degree of coherence computed is used to assign quality flags to the derived vector. The value of quality flag falls sharply by an exponential function, as the disagreement of a given vector with its surroundings increases. Here each vector wind is represented by a complex number $V_{i,j}^c = u_{i,j} + i v_{i,j}$. For every new vector under consideration, (from current image-pair), its vector difference from the buffer is computed at the same as well as 3×3 neighborhood (**Fig. 1**), provided, the vectors to be compared show similar brightness characteristics (to maintain the similar height).

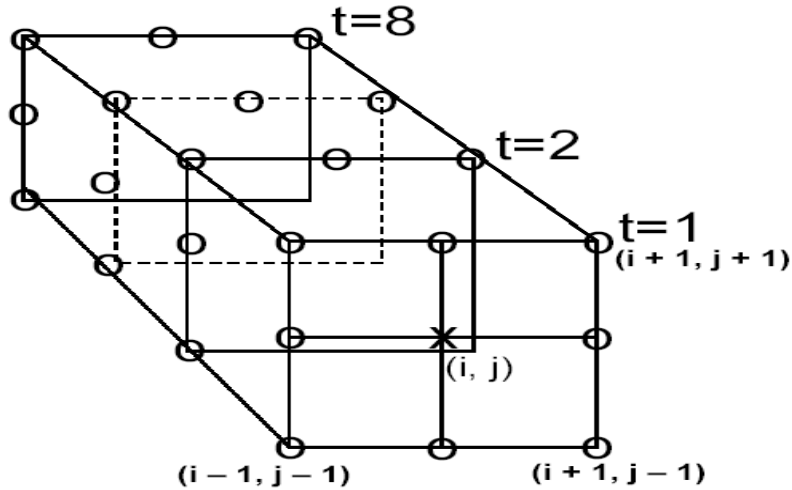


Fig 1: A schematic diagram of quality control process.

Here X (cross sign) at the centre of first box represents the current vector under consideration and O (circle sign) represents spatial and temporal neighborhood vectors. The vector differences (magnitude of complex numbers) are calculated as $\{V_{dif}\}_{i,j,t} = V^c - \{V\}_{i,j,t}$. Here

V^c represents the current vector at (i, j) point and $\{V\}_{i,j,t}$ neighborhood vectors with $-1 \leq i \leq 1, -1 \leq j \leq 1$ and temporal scale t varies from 1 to 8. If all spatial and temporal neighborhood vectors are present, then the difference set will contain 72 vectors (9 spatial neighborhoods with 8 temporal scales). However, all vectors may not be there all the times. The quality control process begins if at least 10 vector differences V_{dif} , excluding the difference corresponding to current (i, j) , are present in the set. In the next step, set of vector differences $\{V_{dif}\}$ is arranged in ascending order. The quality control process begins if the average of 10 V_{dif} is greater than 2.5 m/s. In the next step, the QI value for each vector is determined by using EUMETSAT procedure where four different tests are performed, which is normalized by a tanh-function that returns the value between 0 and 1. A weighted average of these individual quality indicators is then used for screening of poor quality vectors from final output. If any vector is not present in the immediate two pairs, then instead of rejecting, search process goes to the previous time steps of the wind buffer and if still it is not present it goes to next previous time steps and so on.

If S is the mean “speed” of a vector computed from two pair of images, then different quality functions are computed as below :

Direction Consistency Function:

$$DCF = 1.0 - \left[\tanh\left(\frac{\Delta\theta}{A_1 \exp(-S/B_1) + C_1}\right) \right]^{D_1}$$

Speed Consistency Function:

$$SCF = 1.0 - \left[\tanh\left(\frac{\Delta S}{\text{MAX}(A_2 S, B_2) + C_2}\right) \right]^{D_2}$$

Vector Consistency Function:

$$VCF = 1.0 - \left[\tanh\left(\frac{\Delta V}{MAX(A_3S, B_3) + C_3}\right) \right]^{D_3}$$

Spacial Consistency Function:

$$PCF = 1.0 - \left[\tanh\left(\frac{\Delta V_m}{MAX(A_4S, B_4) + C_2}\right) \right]^{D_4}$$

In the above formulation, $\Delta\theta, \Delta S, \Delta V$ represent the difference of direction (degrees), difference of speed, and the length of the difference vector between first and second satellite wind component. ΔV_m is the length of difference vector between satellite wind component and its best neighbor. The best neighbor is determined by the smallest vector difference. Quantities A_N, B_N, C_N , and D_N are constants. The final quality indicator of a wind vector is given as

$$QI = \frac{DCF + SCF + VCF + PCF}{4.0}$$

All the vectors with $QI < 0.6$ are rejected.

In the conventional triplet based methodology requires that a vector is available in both sets (i.e. in 1-2 and 2-3), if not so, such vectors are rejected, because they don't get "support". Hundreds of "isolated" vectors thus get eliminated, even though they represent the real situation. In the current method, the vector under consideration receives support from the past eight images. This method produces higher number of valid retrieval in the low-level and captures upper-level meridional flow very prominently. To explain this more explicitly, if we take eight satellite images each with 30-minute interval starting at 00:00 UTC to 03:30 UTC, then winds retrieved using each-image pair are stored as buffer in a file and represented as wind buffer generated at 03:30 UTC. The buffer generated at 03:30 UTC is used for quality control for wind retrieved using 03:30 UTC and 04:00 UTC images and the second image time is given as actual observation time of retrieved wind. For example winds retrieved using 03:30 UTC wind buffer and 03:30 UTC and 04:00 UTC images is given as 04:00 UTC observation time. As a whole to complete the process once it requires nine images. Similarly the buffer is updated at every 30-minute with the latest available image and process is repeated for next cycle of wind retrieval. This method produces higher number of valid retrieval in all levels and captures upper-level meridional flow very prominently.

13.4.2 Operational Implementation

13.4.2.1 Step 1: Tracer selection from image

- Cloud tracer selection will be done by evaluating the local image anomaly surrounding each pixel in the target array and selecting the maximum brightness temperature of the window.

13.4.2.2 Step 2: Height assignment

- Assign height of the selected tracer using IR window technique. In this case the brightness temperature in the target window will be averaged and matched with collocated numerical model temperature profile. The level of optimum fit will be assigned as initial height.

- Re-assign the height using cloud-base height assignment technique.
- Assign correct height after implementing all the height assignment technique mentioned above.

13.4.2.3 Step 3: Tracking

- The tracking employs a simple search for the mean absolute difference of the radiance difference between the target and search arrays in subsequent half hourly images. This search will be done in the direction of $\pm 30^\circ$ of model wind.

13.4.2.4 Step 4: Wind buffer generation & quality control

- The wind buffer is created using previous eight images between pairs of images (viz. the winds retrieved between 1-2, 2-3, 3-4, 4-5, 5-6, 6-7 and 7-8) and stored in a file. The selection of eight images is consistent with decorrelation timescales of winds over tropical region.
- Use quality control criteria for selecting wind using the wind buffer.
- Calculate wind speed and direction.

13.5 Outputs

Parameter	Unit	Min	Max	Accuracy	Resolution
U and V component of CMV	m/sec	0	90	5-6 m/sec (upper level) 4-5 m/sec (lower level)	--

Domain of output : $30^\circ\text{E} - 130^\circ\text{E} :: 50^\circ\text{S} - 50^\circ\text{N}$

13.5.1 Format of the output and the domain

As output of VIS wind the following parameters will be provided to IMD:

- Zonal and meridional components of the wind vectors.
- Latitudinal and longitudinal position.
- Height of wind

The format of the final product will be like this:

Parameter	Lat.	Lon.	Level	U-component	V-component	Quality Flag	Wind Speed(m/s)	Wind direction (clockwise from North)
Unit	Deg N	Deg E	hPa	m/s	m/s	0.0 to 0.9	m/s	Deg

13.6 Validation

13.6.1 Data required

Parameter	Type	Source
Wind	Collocated Radiosonde Profiles	IMD

13.6.2 Methods of validation

The evaluation of VIS winds should be taken into both qualitative and quantitative measures. Quantitative assessment of the VIS winds product is possible from statistical analyses and impact on NWP. The traditional method of validation is matching observations with collocated radiosondes. The statistical validation will be done according to the CGMS winds evaluation reporting guidelines. These statistics can provide a fixed measure of product quality over time and can be employed in determining observation weight in objective data assimilation. At the CGMS XXIII the Working Group on Satellite Tracked Winds recommended that evaluation of operational wind production quality should be accomplished with a new standardized reporting method. The recommended three parts to the report.

- i) Monthly means of speed bias and rms vector difference between radiosondes and satellite winds for low (>700 hPa), medium (700-400 hPa), and high (< 400 hPa) levels together with the radiosonde mean wind speed. This should be done for three latitude bands: north of 20 N, the tropical belt (20 N to 20 S), and south of 20 S.
- ii) Trends of the evaluation statistics for the monthly cloud motion vectors and water vapor motion vectors through the last 12 months.
- iii) Information on recent significant changes in the wind retrieval algorithm.

The vector Difference (VD) between an individual wind report (i) and the collocated radiosonde report used for verification is given by

$$(VD) = [(Ui - Ur)^2 + (Vi - Vr)^2]^{1/2}$$

The speed bias is given by

$$(BIAS)i = 1/N \sum_{i=1}^N [(Ui^2 + Vi^2)^{1/2} - (Ur^2 + Vr^2)^{1/2}]$$

The mean vector difference (MVD) traditionally reported is

$$(MVD) = 1/N \sum_{i=1}^N (VD)i$$

And the standard deviation (SD) about the mean vector difference traditionally reported is

$$(SD) = [1/N \sum_{i=1}^N ((Vdi) - (MVD))^2]^{1/2}$$

The root-mean-square error (RMSE) traditionally reported is the square root of the sum of the squares of the mean vector difference and the standard deviation about the mean vector difference,

$$(RMSE) = [(MVD)^2 + (SD)^2]^{1/2}$$

It must be noted that this definition of the mean vector difference is not the same as the mean component difference. The mean difference is calculated from the sum of the squares of the deviations of each component (u and v) of the wind vector.

$$(\Delta U^2) = \sum_{i=1}^N (U_i - U_r)^2$$

$$(\Delta V^2) = \sum_{i=1}^N (V_i - V_r)^2$$

To avoid confusion, the mean vector difference (MCD) is given by $d(MCD) = [(\Delta U^2) + (\Delta V^2)]^{1/2} \neq (MVD)$. It is suggested to report mean vector difference (MVD) instead of MCD . The standard accuracy according to CGMS guideline for CMV is that the root mean square error (RMSE) for WV winds should be 7m/s respectively with respect to radiosonde observations. The mean bias for both sets of winds should be about zero.

13.7 Technical Issues (Limitations etc)

Accuracy of the product depends on the accuracy of the registration of the images. If the registration has an error of 1 pixel, then error of the final product will be increased. However the following limitations of the present study have to be kept in mind. The spatially coherent, high resolution coverage of upper tropospheric winds are possible from geostationary satellite remote sensing of water vapor. VIS wind are comparable in quality to operational upper-level cloud-motion vectors. However, the retrieved vectors in regions are lacking in defining moisture structure, though they have the ability to obtain trackable information in extremely dry air masses and regions of strong subsidence is limited. The individual vectors represent single level reports; however, upper level vertical winds profiles are possible by using multi-spectral observations.

1. Sensitivity of error in height assignment to the error in wind speed retrieval

This sensitivity will depend upon the structure of wind circulation over different vertical levels as well as different geographical regions. For example, in the vicinity of atmospheric jets, the retrieved wind vectors will be highly sensitive to the errors in the assigned pressure levels. Based on some standard analysis (e.g. NCEP reanalysis of 6-hourly sampling), we will provide a quantitative assessment of the vertical and spatial structure of this sensitivity.

2. Numerical model to be used for AMV height assignment

We plan to use IMD's operational regional model output during height assignment procedure. However, if the domain of this regional model is smaller than the area of AMV retrieval, either IMD may be requested to increase the domain of its operational model, or a lower-quality solution based on the output of coarser-resolution GCM will be generated over the regions not covered by IMD's regional model.

3. Whether RT model to be used in real-time for height assignment

To use RT model in real-time height-assignment application is generally required to find the optimum solution. However, it is computationally expensive and may increase the AMV turn-around time very significantly. Efforts are currently underway to develop an empirical version of RT model that can be used for simulation of IR

and water-vapor channel radiances for a variety of cloud heights. The inverse of this empirical model will then be used in real-time applications.

4. Comparison of maximum-correlation and minimum-difference methods for tracking of cloud-tracers.

The comparison have been made for a large number of image samples and it was found that the efficiencies of minimum-difference method (MDM) and maximum cross correlation (MCC) methods are comparable, while the MDM method is significantly faster than MCC.

13.8 References

1. Bedka KM, Mecikalski JR (2005) Application of satellite-derived atmospheric motion vectors for estimating meso-scale flows. *Journal of Applied Meteorology* 44: 1761-1772.
2. Deb SK, Kishtawal CM, Pal PK (2010). Impact of *Kalpana-1* derived water vapor winds on Indian Ocean Tropical cyclones forecast. *Monthly Weather Review* 138 (3): 987-1003.
3. Deb SK, Kishtawal CM, Pal PK, Joshi PC (2008) A modified tracer selection and tracking procedure to derive winds using Water vapor imagers. *Journal of Applied Meteorology and Climatology* 47: 3252-3263.
4. Deb SK, Kishtawal CM, Kaur Inderpreet, Pal PK, Kiran Kumar AS (2012a). Multiplet based Technique to derive Atmospheric winds from Kalpana-1, *The Proceedings 11th International Wind Workshop*, 20-24 February, 2012, Auckland, New Zealand.
5. Deb SK, Kaur Inderpreet, Kishtawal CM, Pal PK (2012b). Atmospheric Motion Vectors from Kalpana-1: An ISRO Status, *The Proceedings 11th International Wind Workshop*, 20-24 February, 2012, Auckland, New Zealand
6. Hasler AF, Skillman WC, Shenk WE, Steranka J (1979) In situ aircraft verification of the quality of satellite cloud winds over oceanic regions. *Journal of Applied Meteorology* 18: 1481–1489.
7. Holmlund K (1998) The utilization of statistical properties of satellite-derived Atmospheric Motion Vectors to derive quality indicators. *Weather Forecasting* 13:1093-1104.
8. Kelly G (2004) Observing system experiments of all main data types in the ECMWF operational system. 3rd WMO Numerical Weather Prediction OSE Workshop, Alpbach, Austria, WMO, Tech Rep. 1228: pp 32-36.
9. Kishtawal CM, Deb SK, Pal PK, Joshi PC (2009) Estimation of Atmospheric Motion Vectors from Kalpana-1 imagers. *Journal of Applied Meteorology and Climatology* 48: 2410-2421.
10. Kaur Inderpreet, Kishtawal CM, Deb SK, Kumar Raj (2012) Temporal Scales of Satellite Derived Atmospheric Winds over the Asian Monsoon Region. *IEEE. Geoscience and Remote Sensing Letters*. 9 (2): 317-320.
11. LeMarshall J, Pescod N, Khaw A, Allen G (1993) The real-time generation and application of cloud-drift winds in the Australian region. *Australian Meteorological Magazine* 42: 89–103.

12. Merrill, R. T., Menzel W. P, Baker W, Lynch J. and Legg E, (1991): A report on the recent demonstration of NOAA's upgraded capability to derive cloud motion satellite winds. *Bull. Amer. Meteor. Soc.*, 72, 372-376.
13. Nieman SJ, Schmetz J, Menzel WP (1993) A comparison of several techniques to assign heights to cloud tracers. *Journal of Applied Meteorology* 32:1559–1568.
14. Nieman S, Menzel WP, Hayden CM, Gray D, Wanzong S, Velden C, Daniels J (1997) Fully automated cloud-driftwinds in NESDIS operations. *Bulletin of American Meteorological Society* 78: 1121–1133.
15. Rossow WB, Mosher F, Kinsella E, Arking A, Debois M, Harrison E, Minnis P, Ruprecht E, Seze G, Simmer C, Smith E (1985) ISCCP clouds algorithm inter-comparison. *Journal of Climate and Applied Meteorology* 24: 877-903.
16. Schmetz J, Holmlund K, Hoffman J, Strauss B, Mason B, Gaertner V, Koch A, van de Berg L (1993) Operational cloud-motion winds from Meteosat infrared images. *Journal of Applied Meteorology* 32: 1206–1225.
17. Tokuno M (1996) Operational system for extracting cloud motion and water vapor motion winds from GMS-5 image data. Proc. Third Int. Winds Workshop, EUM P18, Ascona, Switzerland, EUMETSAT, 21–30.
18. Tokuno M (1998) Collocation area for comparison of satellite winds and radiosondes. Proc. Fourth Int. Winds Workshop, EUM P24, Saanenmoser, Switzerland, EUMETSAT 21–28.
19. Tomassini C (1981) Objective analysis of cloud fields. Proc. Satellite Meteorology of the Mediterranean ESA, SP-159: pp.73-78.
20. Velden CS, Hayden CM, Nieman SJ, Menzel WP, Wanzong S, Goerss JS (1997) Upper-tropospheric winds derived from geostationary satellite water vapor observations. *Bulletin of American Meteorological Society* 78:173–195.

14. Atmospheric Motion Vector Winds (MIR)

S.No.	Product Name	Spatial Resolution	Temporal Resolution
1	3DIMG_L2P_MRW	Point	30 minutes

14. Mid Infrared Wind Vectors (MIR)

14.1 Algorithm Configuration Information

14.1.1 Algorithm Name

Atmospheric Motion Vector Winds (MIR)
(Ref : IMD RFP Section 11.14)

14.1.2 Algorithm Identifier

3DIMG_L2P_MRW

14.1.3 Algorithm Specification

Version	Date	Prepared by	Description
1.0	21.07.2014	S.K. Deb, C.M. Kishtawal	Mid-Infrared winds Baseline Document (Version 1)

14.2 Introduction

The purpose of this document is to present an algorithm for retrieving Mid-Infrared Winds (MIR) from INSAT-3D thermal infrared imager channel and its validation procedure. The INSAT-3D will have one MIR channel ($3.8 - 4.0 \mu\text{m}$). In this document some background and general characteristic of satellite-derived winds from mid-infrared channels characteristics; the methodology employed to derive the vector fields, theoretical basis and practical aspects of this algorithm and outlined the planned validation approach.

14.2.1 Overview and background

Spatio-temporal analysis of meteorological events is an important part of routine numerical weather analysis. In that context, a cloud tracking method is presented here for a sequence of geostationary satellite images. Given a pair of remotely sensed images, captured at a fixed time interval (typically, 30 min), the objective is to derive motion vectors associated with the cloud mass. This correspondence process is a useful precursor to cloud motion vector studies and spatio-temporal analysis of cloud life cycles. The spatio-temporal life cycle includes the generation, dissipation and assimilation of clouds that can be observed in a sequence of geostationary satellite images. During the 1970's and early 1980's, cloud motion winds were produced in major operational centers like NESDIS (National Environmental Satellite Data and Information Service) using a combination of automated and manual techniques. Early automated techniques supplied quality low-level vectors from mid-infrared channel but often yielded in consistent quality for mid- and high-level motions. Height assignment for the mid-infrared winds is done with collocated infrared images using infrared window technique. In the subsequent years, due to the developments in image-processing and pattern recognition techniques (Merill *et al.*, 1991), it was possible to design fully automatic techniques for wind retrieval, and NESDIS began its application in 1992. In later time, several new developments were made to make accurate retrievals of winds from satellite images.

Generally, atmospheric motion vectors (AMVs) wind coverage has been diurnally consistent in the mid to upper-levels (100-600 hPa) by the use of $6.7 \mu\text{m}$ water vapor and $10.7 \mu\text{m}$ long-

wave infrared (LWIR) channels. However, in the low-levels (600-950 hPa), AMVs are retrieved using a combination of the visible and LWIR channels, depending on the time of day. The visible channel provides far superior low-level tracer detection than the LWIR channel. This is due to its finer spatial resolution and decreased susceptibility to attenuation by low-level moisture. Unfortunately, nighttime low-level satellite wind coverage typically decreases sharply when visible channel is not available. This creates a situation of overall reduced wind information for the user during night-time. Using the mid-infrared (MIR) 3.9 μm channel on the INSAT-3D satellite, MIR cloud-drift winds have been developed to provide improved nighttime low-level satellite wind coverage. The MIR channel is slightly more sensitive to warmer temperatures and less sensitive to thin cirrus than the 10.7 μm long-wave infrared (LWIR) channel traditionally used to track low-level clouds at night. This allows for a higher detectability rate of low-level (600-950 hPa) cloud tracers in the MIR channel. Improved low-level nighttime wind coverage can provide forecasters with more wind data as well as reduce the diurnal inconsistencies that may be a challenge to data assimilation into models.

14.2.2 Objective

The main objective of this study is to derive the Mid-Infrared Winds (MIR) over sea using multiple successive half hourly MIR images. The region over which the winds are derived should be in the range of 50° from sub-satellite point.

14.3 Inputs

14.3.1 Static Data

Parameter	Resolution	Source
Continental boundary Data	1 km	DP (IMD data)

14.3.2 Image and preprocessing data (Dynamic)

Parameter	Resolution	Quantization	Accuracy	Source
Radiometric and geometric corrected gray count values of split window IR channel (10.5-11.5 μm and 11.5-12.5 μm) and MIR channel (3.9 μm) (All the data is required in fixed lat-lon grid for continuous 8-images separated by 30 minutes time interval)	pixel	10 bit	--	Derived from raw data by DP (data processing)
Gray value to brightness temperature conversion table	-	-	0.3 K	Derived by DP
Geo-location file	Pixel	-	1 Km	Derived by DP

14.3.3 Other Auxiliary data and Model Inputs

Parameter	Resolution	Accuracy	Source
Numerical model forecast of wind for all levels	1 degree or 0.5 degree	2 m/s (speed) 20° (direction)	IMD
All levels model forecast Temperature		1° K	

14.4 Algorithm Functional Specifications

14.4.1 Overview

14.4.1.1 Methodology

14.4.1.1.1 Solar Contamination in MIR Channel

The MIIR channel is susceptible to solar contamination during daytime due to its proximity to the visible spectrum. Cirrus clouds are somewhat reflective of solar radiation and cumulus clouds are highly reflective in the MIR channel. Since low-level cumulus clouds are the main source of targets for low-level cloud-drift winds, this reflectance causes tracking problems due to saturation effects. The reflected solar energy received at the INSAT-3D sensor from the cumulus clouds can make them appear to be warmer than even the underlying ocean surface at times. This makes tracer selection extremely difficult and erroneous. Therefore, the usefulness of this channel for winds derivation to be limited to nighttime applications because of its sensitivity to solar contamination.

14.4.1.1.2 MIR Image Enhancements

The MIR channel is characterized by relatively small gradients in brightness temperatures in the warmer low levels. This limits the ability of the tracking algorithm to detect viable cloud targets and resultant tracers over time. A technique was developed at CIMSS ([Velden and Dunion 2001](#)) to enhance the MIR imagery by stretching the brightness temperature contrast in the warmer end of the spectrum (low levels). Specifically, the brightness temperature range from 50-160 is stretched. This enhancement greatly improves the gradients in the low-levels at the cost of confining the mid to upper-level gradients in the image. Therefore, tracer detection is strictly limited to cloud tracers ≥ 600 hPa (based on brightness temperature determined heights). The image enhancement technique is performed on the MIR images used to track the cloud features.

14.4.1.1.3 Tracer selection

At the National Environmental Satellite, Data, and Information Service (NESDIS), the initial cloud features are selected by locating the highest pixel brightness values for each target domain and computing the local gradients around those locations ([Nieman et al., 1997](#)). Any gradients greater than 15°K are assigned as target locations, and prospective targets also undergo a spatial coherence analysis ([Coakley and Bretherton, 1982](#)) to filter out unwanted targets. Water vapor tracers are generally identified using the local bi-directional gradients in a template of specified size and compared with empirically determined thresholds to identify

the features with sufficient variability ([Velden et al., 1997](#)) and those that pass the threshold value are identified as tracers for cloud-free environments. The pixel with maximum bi-directional gradient is the location of the tracer. At the European Organization for the Exploitation of Meteorological Satellites (EUMETSAT), the tracers in the Meteosat (first-generation satellites) images are selected using multispectral histogram analysis ([Tomassini, 1981](#)), which extracts the dominating scenes in an image segment. Later the selected templates undergo a spatial coherence analysis ([Coakley and Bretherton, 1982](#)) to filter the image, to enhance the upper-level cloud. In the present study the features are selected by computing local image anomaly in a 32 x 32 template window, both in cloudy regions of the mid-infrared images. The local image anomaly is calculated using the following formula:

$$a = \sum_i \sum_j |I(i, j) - \bar{I}| \quad (1)$$

Where $I(i, j)$ represent the grey value for (i, j) pixel of a template window and bar represents the mean of grey values within that template. The anomaly-based tracers are generally produced by a smooth feature field in comparison to the gradient-based features. This difference can help in reducing the tracking errors ([Deb et al., 2008](#)).

14.4.1.1.4 Height assignment

The height assignments of the selected tracers selected based on the above criterion are derived using the collocated infrared images with the following widely used methods viz. such as the infrared window (WIN) technique and the cloud base method ([LeMarshall, 1993](#)). Once final height is selected a few gross error checks are also applied. A brief description of each method is following:

Infrared Window Channel (WIN):

In this method the height assignment using a single satellite channel is made by comparing either infrared window brightness temperature (BT) values with NWP model forecast temperature profiles. Cloud heights are determined by interpolating the cloud temperature, which is an average of coldest 20% of pixels, to the interpolated model guess field at the target location. A 6-h NWP model forecast from National Center for Environmental Prediction (NCEP) Global Forecast System (GFS) is the source of temperature profile. This method works well with opaque clouds. However, movement of opaque clouds usually does not accurately represent atmospheric motion at the assigned level ([Nieman et al., 1993](#)), resulting in a lower derived wind speed than observed.

Cloud Base Method (BASE):

Wind speeds for low-level cumulus clouds (cloud top pressures greater than 600 hPa or altitudes lower than 600 hPa) have been found to be best represented by the movement at the cloud base level instead of the mid or upper levels of the cloud ([Hasler et al., 1979](#)). A method was developed at the Australian Bureau of Meteorology ([LeMarshall, 1993](#)) to estimate this height using the Infrared Window channel. This method first constructs a histogram of the BT values over a selected region surrounding the cloud target being examined. This histogram is then smoothed and Hermite polynomials are fitted to the histogram to separate the distribution into two components; a cloudy and clear sky region. Assuming the distributions are normal, the cloud base height can be estimated. The mid cloud temperature is determined by examining the second derivative histogram of the cloudy

distribution, while the cloud top temperature is estimated to be located at the coldest 5% of the cloudy distribution. The cloud base temperature is estimated to be located the same distance from the mid cloud temperature as the cloud top temperature. The calculated cloud base temperature is converted to a pressure using model field interpolated to the target location. As mentioned previously, this height assignment method is only applied to those targets which are calculated to have a cloud top pressure of greater than 600 hPa (i.e. altitude lower than 600 hPa). This "initial" target cloud top height is provided by one of the previous Infrared Window height assignment methods. The BASE method is used to adjust only these winds, and is not utilized for water vapor winds or winds with pressures less than 600 hPa (i.e. altitudes higher than 600 hPa).

Once the mid-infrared tracers heights using the above two algorithms have been calculated, the best height among the available heights is determined. The lowest pressure (highest altitude) value of all the calculated height values is used as the final pressure height. However, if for a specific tracer final height is WIN and a valid BASE height is available, then the BASE height is used as the final height.

14.4.1.1.5 Tracking

If a traceable feature is found in the first image and corresponding height of the selected tracers are estimated, the match of this template is searched in the second image within a bigger "search window", centered at the same point as the template window. To optimize the search window size, the first guess model wind direction at the tracer location is also considered. The search area is optimized within ± 30 degree from the model wind direction at that level of atmosphere. The 32 X 32 template in the second image that lies within the search window should have the same class as the template in the first image; otherwise the template in the second window is rejected. The cross-correlation technique is used operationally for tracking the tracer between two images in most operational centers. However, in this study the degrees of matching between two successive images are calculated by the Nash-Sutcliffe model efficiency ([Nash and Sutcliffe, 1970](#)) coefficient (E). It is defined as

$$E = 1 - \frac{\sum_{i=1}^n (I_t - I_s)^2}{\sum_{i=1}^n (I_t - \bar{I}_t)^2} \quad (2)$$

Where I_t and I_s are the variance of the grey values for template window and search window and \bar{I}_t is the average of variance of template window. Here n is 32 x 32 and this is the size of template window and corresponding template of same size in the searching area. The size of the searching area in the subsequent image is taken as 64 x 64. The coefficient E is normalized to values between $-\infty$ and +1. An efficiency $E = 1$ corresponds to a perfect match, $E = 0$ means that search window is as accurate as mean of the template window and $E < 0$ implies the lack of matching between template and search window. The closer the model efficiency to 1, the more accurate the matching between the windows. A cut-off value of $E=0.8$ is defined, below which a matching of target is not considered. The Nash-Sutcliffe model efficiency coefficient (E) is normalized and its value lies between $-\infty$ and 1, towards the higher end (e.g. as $E \rightarrow 1.0$), the value of E approaches r^2 , where r is the correlation

coefficient. Thus a value of $E=1$ is exactly equivalent to a correlation of 1.0 between two objects. The maximum value of E is chosen as the best fit for tracking. One of the main advantages of this matching technique is that it reduces the possibility of multiple maxima, because the parameter E has a higher sensitivity to differences between two features compared to maximum cross correlation coefficient (MCC). Thus, when the degree of mismatch between two objects increases, the value of E falls more sharply compared to that of MCC, making E a better index for matching two objects. The application of this tracking method in estimation of water vapor winds has shown some improvement over Indian Ocean region ([Deb et al., 2008](#)).

14.4.1.6 Wind buffer generation and Quality control

Quality indicator of a derived wind vectors is traditionally represented as the degree of the coherence of a given vector with its surrounding. In most of the operational centers the AMVs are derived from three successive satellite images and the quality control of the retrieved winds are done either through Quality Indicator (QI) ([Holmlund, 1998](#)) followed at EUMETSAT or through 3-dimensional recursive filter function followed at NESDIS ([Nieman et al., 1997](#)) or both the algorithms together. In the present study a new technique of wind buffer generation and subsequently QI procedure followed at EUMETSAT is proposed. In this technique, a wind buffer is created using previous eight images between a pair of images (viz. between 1-2, 2-3, 3-4, 4-5, 5-6, 6-7 and 7-8) and stored in a file (**Fig. 1**). The previous eight images were considered to maintain the minimum 4-hour decorrelation timescale during retrieval ([Kaur et al., 2011](#)). In quality control procedure consists of a coherence analysis which forms the basis for acceptance/rejection of a vector and degree of coherence computed is used to assign quality flags to the derived vector. The value of quality flag falls sharply by an exponential function, as the disagreement of a given vector with its surroundings increases. Here each vector wind is represented by a complex number $V_{i,j}^c = u_{i,j} + i v_{i,j}$. For every new vector under consideration, (from current image-pair), its vector difference from the buffer is computed at the same as well as 3 X 3 neighborhood (**Fig. 1**), provided, the vectors to be compared show similar brightness characteristics (to maintain the similar height).

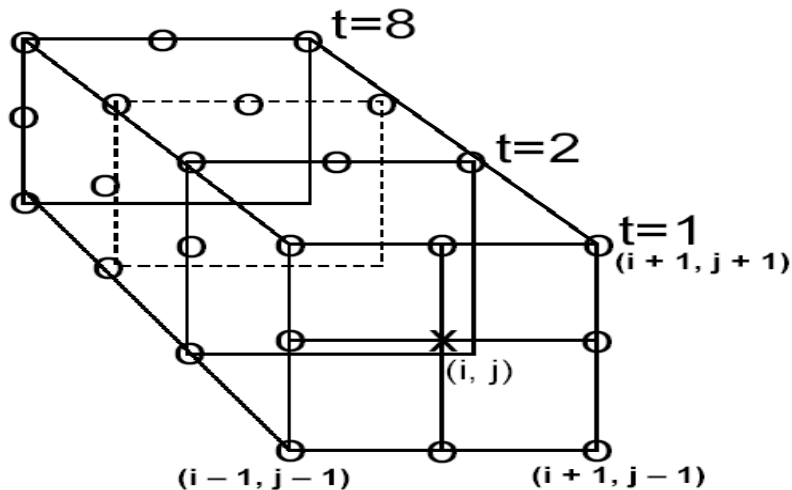


Fig 1: A schematic diagram of quality control process.

Here X (cross sign) at the centre of first box represents the current vector under consideration and O (circle sign) represents spatial and temporal neighborhood vectors. The vector differences (magnitude of complex numbers) are calculated as $\{V_{dif}\}_{i,j,t} = V^c - \{V\}_{i,j,t}$. Here V^c represents the current vector at (i, j) point and $\{V\}_{i,j,t}$ neighborhood vectors with $-1 \leq i \leq 1, -1 \leq j \leq 1$ and temporal scale t varies from 1 to 8. If all spatial and temporal neighborhood vectors are present, then the difference set will contain 72 vectors (9 spatial neighborhoods with 8 temporal scales). However, all vectors may not be there all the times. The quality control process begins if at least 10 vector differences V_{dif} , excluding the difference corresponding to current (i, j), are present in the set. In the next step, set of vector differences $\{V_{dif}\}$ is arranged in ascending order. The quality control process begins if the average of 10 V_{dif} is greater than 2.5 m/s. In the next step, the QI value for each vector is determined by using EUMETSAT procedure where four different tests are performed, which is normalized by a tanh-function that returns the value between 0 and 1. A weighted average of these individual quality indicators is then used for screening of poor quality vectors from final output. If any vector is not present in the immediate two pairs, then instead of rejecting, search process goes to the previous time steps of the wind buffer and if still it is not present it goes to next previous time steps and so on.

If S is the mean “speed” of a vector computed from two pair of images, then different quality functions are computed as below :

Direction Consistency Function:

$$DCF = 1.0 - \left[\tanh\left(\frac{\Delta\theta}{A_1 \exp(-S/B_1) + C_1}\right)\right]^{D_1}$$

Speed Consistency Function:

$$SCF = 1.0 - \left[\tanh\left(\frac{\Delta S}{\text{MAX}(A_2 S, B_2) + C_2}\right)\right]^{D_2}$$

Vector Consistency Function:

$$VCF = 1.0 - \left[\tanh\left(\frac{\Delta V}{\text{MAX}(A_3 S, B_3) + C_3}\right)\right]^{D_3}$$

Spacial Consistency Function:

$$PCF = 1.0 - \left[\tanh\left(\frac{\Delta V_m}{\text{MAX}(A_4 S, B_4) + C_2}\right)\right]^{D_4}$$

In the above formulation, $\Delta\theta, \Delta S, \Delta V$ represent the difference of direction (degrees), difference of speed, and the length of the difference vector between first and second satellite wind component. ΔV_m is the length of difference vector between satellite wind component and its best neighbor. The best neighbor is determined by the smallest vector difference.

Quantities A_N, B_N, C_N , and D_N are constants. The final quality indicator of a wind vector is given as

$$\text{QI} = \frac{DCF + SCF + VCF + PCF}{4.0}$$

All the vectors with $\text{QI} < 0.6$ are rejected.

In the conventional triplet based methodology requires that a vector is available in both sets (i.e. in 1-2 and 2-3), if not so, such vectors are rejected, because they don't get "support". Hundreds of "isolated" vectors thus get eliminated, even though they represent the real situation. In the current method, the vector under consideration receives support from the past eight images. This method produces higher number of valid retrieval in the low-level and captures upper-level meridional flow very prominently. To explain this more explicitly, if we take eight satellite images each with 30-minute interval starting at 00:00 UTC to 03:30 UTC, then winds retrieved using each-image pair are stored as buffer in a file and represented as wind buffer generated at 03:30 UTC. The buffer generated at 03:30 UTC is used for quality control for wind retrieved using 03:30 UTC and 04:00 UTC images and the second image time is given as actual observation time of retrieved wind. For example winds retrieved using 03:30 UTC wind buffer and 03:30 UTC and 04:00 UTC images is given as 04:00 UTC observation time. As a whole to complete the process once it requires nine images. Similarly the buffer is updated at every 30-minute with the latest available image and process is repeated for next cycle of wind retrieval. This method produces higher number of valid retrieval in all levels and captures upper-level meridional flow very prominently.

14.4.2 Operational Implementation

14.4.2.1 Step 1: Tracer selection from image

- Cloud tracer selection will be done by evaluating the local image anomaly surrounding each pixel in the target array and selecting the maximum brightness temperature of the window.

14.4.2.2 Step 2: Height assignment

- Assign height of the selected tracer using IR window technique. In this case the brightness temperature in the target window will be averaged and matched with collocated numerical model temperature profile. The level of optimum fit will be assigned as initial height.
- Re-assign the height using cloud-base height assignment technique.
- Assign correct height after implementing all the height assignment technique mentioned above.

14.4.2.3 Step 3: Tracking

- The tracking employs a simple search for the mean absolute difference of the radiance difference between the target and search arrays in subsequent half hourly images. This search will be done in the direction of $\pm 30^\circ$ of model wind.

14.4.2.4 Step 4: Wind buffer generation & quality control

- The wind buffer is created using previous eight images between pairs of images (viz. the winds retrieved between 1-2, 2-3, 3-4, 4-5, 5-6, 6-7 and 7-8) and stored

in a file. The selection of eight images is consistent with decorrelation timescales of winds over tropical region.

- Use quality control criteria for selecting wind using the wind buffer.
- Calculate wind speed and direction.

14.5 Outputs

Parameter	Unit	Min	Max	Accuracy	Resolution
U and V component of CMV	m/sec	0	90	5-6 m/sec (upper level) 4-5 m/sec (lower level)	--

Domain of output : 30°E – 130°E :: 50°S – 50° N

14.5.1 Format of the output and the domain

As output of MIR wind the following parameters will be provided to IMD:

- Zonal and meridional components of the wind vectors.
- Latitudinal and longitudinal position.
- Height of wind

The format of the final product will be like this:

Parameter	Lat.	Lon.	Level	U-component	V-component	Quality Flag	Wind Speed(m/s)	Wind direction (clockwise from North)
Unit	Deg N	Deg E	hPa	m/s	m/s	0.0 to 0.9	m/s	Deg

14.6 Validation

14.6.1 Data required

Parameter	Type	
Wind	Collocated Radiosonde Profiles	IMD

14.6.2 Methods of validation

The evaluation of MIR winds should be taken into both qualitative and quantitative measures. Quantitative assessment of the MIR winds product is possible from statistical analyses and impact on NWP. The traditional method of validation is matching observations with collocated radiosondes. The statistical validation will be done according to the CGMS winds evaluation reporting guidelines. These statistics can provide a fixed measure of product quality over time and can be employed in determining observation

weight in objective data assimilation. At the CGMS XXIII the Working Group on Satellite Tracked Winds recommended that evaluation of operational wind production quality should be accomplished with a new standardized reporting method. The recommended three parts of the report.

- i) Monthly means of speed bias and rms vector difference between radiosondes and satellite winds for low (>700 hPa), medium (700-400 hPa), and high (< 400 hPa) levels together with the radiosonde mean wind speed. This should be done for three latitude bands: north of 20 N, the tropical belt (20 N to 20 S), and south of 20 S.
- ii) Trends of the evaluation statistics for the monthly cloud motion vectors and water vapor motion vectors through the last 12 months.
- iii) Information on recent significant changes in the wind retrieval algorithm.

The vector Difference (VD) between an individual wind report (i) and the collocated radiosonde report used for verification is given by

$$(VD) = [(U_i - U_r)^2 + (V_i - V_r)^2]^{1/2}$$

The speed bias is given by

$$(BIAS)_i = 1/N \sum_{i=1}^N [(U_i^2 + V_i^2)^{1/2} - (U_r^2 + V_r^2)^{1/2}]$$

The mean vector difference (MVD) traditionally reported is

$$(MVD) = 1/N \sum_{i=1}^N (VD)_i$$

And the standard deviation (SD) about the mean vector difference traditionally reported is

$$(SD) = [1/N \sum_{i=1}^N ((Vd_i) - (MVD))^2]^{1/2}$$

The root-mean-square error (RMSE) traditionally reported is the square root of the sum of the squares of the mean vector difference and the standard deviation about the mean vector difference,

$$(RMSE) = [(MVD)^2 + (SD)^2]^{1/2}$$

It must be noted that this definition of the mean vector difference is not the same as the mean component difference. The mean difference is calculated from the sum of the squares of the deviations of each component (u and v) of the wind vector.

$$(\Delta U^2) = \sum_{i=1}^N (U_i - U_r)^2$$

$$(\Delta V^2) = \sum_{i=1}^N (V_i - V_r)^2$$

$$(MCD) = [(\Delta U^2) + (\Delta V^2)]^{1/2} \neq (MVD)$$

To avoid confusion, a common terminology will be accepted. It is suggested to report mean vector difference (MVD) and standard deviation (SD). The standard accuracy according to CGMS guideline for CMV is that the root mean square error (RMSE) for WV winds should be 7m/s respectively with respect to radiosonde observations. The mean bias for both sets of winds should be about zero.

14.7 Technical Issues (Limitations etc)

Accuracy of the product depends on the accuracy of the registration of the images. If the registration has an error of 1 pixel, then error of the final product will be increased. However the following limitations of the present study have to be kept in mind. The spatially coherent, high resolution coverage of upper tropospheric winds is possible from geostationary satellite remote sensing of water vapor. MIR wind is comparable in quality to operational upper-level cloud-motion vectors. However, the retrieved vectors in regions are lacking in defining moisture structure, though they have the ability to obtain trackable information in extremely dry air masses and regions of strong subsidence is limited. The individual vectors represent single level reports; however, upper level vertical winds profiles are possible by using multi-spectral observations.

1. Sensitivity of error in height assignment to the error in wind speed retrieval

This sensitivity will depend upon the structure of wind circulation over different vertical levels as well as different geographical regions. For example, in the vicinity of atmospheric jets, the retrieved wind vectors will be highly sensitive to the errors in the assigned pressure levels. Based on some standard analysis (e.g. NCEP reanalysis of 6-hourly sampling), we will provide a quantitative assessment of the vertical and spatial structure of this sensitivity.

2. Numerical model to be used for AMV height assignment

We plan to use IMD's operational regional model output during height assignment procedure. However, if the domain of this regional model is smaller than the area of AMV retrieval, either IMD may be requested to increase the domain of its operational model, or a lower-quality solution based on the output of coarser-resolution GCM will be generated over the regions not covered by IMD's regional model.

3. Whether RT model to be used in real-time for height assignment

To use RT model in real-time height-assignment application is generally required to find the optimum solution. However, it is computationally expensive and may increase the AMV turn-around time very significantly. Efforts are currently underway to develop an empirical version of RT model that can be used for simulation of IR and water-vapor channel radiances for a variety of cloud heights. The inverse of this empirical model will then be used in real-time applications.

4. Comparison of maximum-correlation and minimum-difference methods for tracking of cloud-tracers.

The comparison have been made for a large number of image samples and it was found that the efficiencies of minimum-difference method (MDM) and maximum cross correlation (MCC) methods are comparable, while the MDM method is significantly faster than MCC.

14.8 References

1. Bedka KM, Mecikalski JR (2005) Application of satellite-derived atmospheric motion vectors for estimating meso-scale flows. *Journal of Applied Meteorology* 44: 1761-1772.
2. Deb SK, Kishtawal CM, Pal PK (2010). Impact of *Kalpana-1* derived water vapor winds on Indian Ocean Tropical cyclones forecast. *Monthly Weather Review* 138 (3): 987-1003.
3. Deb SK, Kishtawal CM, Pal PK, Joshi PC (2008) A modified tracer selection and tracking procedure to derive winds using Water vapor imagers. *Journal of Applied Meteorology and Climatology* 47: 3252-3263.
4. Deb SK, Kishtawal CM, Kaur Inderpreet, Pal PK, Kiran Kumar AS (2012a). Multiplet based Technique to derive Atmospheric winds from Kalpana-1, *The Proceedings 11th International Wind Workshop*, 20-24 February, 2012, Auckland, New Zealand.
5. Deb SK, Kaur Inderpreet, Kishtawal CM, Pal PK (2012b). Atmospheric Motion Vectors from Kalpana-1: An ISRO Status, *The Proceedings 11th International Wind Workshop*, 20-24 February, 2012, Auckland, New Zealand
6. Hasler AF, Skillman WC, Shenk WE, Steranka J (1979) In situ aircraft verification of the quality of satellite cloud winds over oceanic regions. *Journal of Applied Meteorology* 18: 1481–1489.
7. Holmlund K (1998) The utilization of statistical properties of satellite-derived Atmospheric Motion Vectors to derive quality indicators. *Weather Forecasting* 13:1093-1104.
8. Kelly G (2004) Observing system experiments of all main data types in the ECMWF operational system. 3rd WMO Numerical Weather Prediction OSE Workshop, Alpbach, Austria, WMO, Tech Rep. 1228: pp 32-36.
9. Kishtawal CM, Deb SK, Pal PK, Joshi PC (2009) Estimation of Atmospheric Motion Vectors from Kalpana-1 imagers. *Journal of Applied Meteorology and Climatology* 48: 2410-2421.
10. Kaur Inderpreet, Kishtawal CM, Deb SK, Kumar Raj (2012) Temporal Scales of Satellite Derived Atmospheric Winds over the Asian Monsoon Region. *IEEE. Geoscience and Remote Sensing Letters*. 9 (2): 317-320.
11. LeMarshall J, Pescod N, Khaw A, Allen G (1993) The real-time generation and application of cloud-drift winds in the Australian region. *Australian Meteorological Magazine* 42: 89–103.
12. Merrill, R. T., Menzel W. P, Baker W, Lynch J. and Legg E, (1991): A report on the recent demonstration of NOAA's upgraded capability to derive cloud motion satellite winds. *Bull. Amer. Meteor. Soc.*, 72, 372-376.

13. Nieman SJ, Schmetz J, Menzel WP (1993) A comparison of several techniques to assign heights to cloud tracers. *Journal of Applied Meteorology* 32:1559–1568.
14. Nieman S, Menzel WP, Hayden CM, Gray D, Wanzong S, Velden C, Daniels J (1997) Fully automated cloud-driftwinds in NESDIS operations. *Bulletin of American Meteorological Society* 78: 1121–1133.
15. Rossow WB, Mosher F, Kinsella E, Arking A, Debois M, Harrison E, Minnis P, Ruprecht E, Seze G, Simmer C, Smith E (1985) ISCCP clouds algorithm inter-comparison. *Journal of Climate and Applied Meteorology* 24: 877-903.
16. Schmetz J, Holmlund K, Hoffman J, Strauss B, Mason B, Gaertner V, Koch A, van de Berg L (1993) Operational cloud-motion winds from Meteosat infrared images. *Journal of Applied Meteorology* 32: 1206–1225.
17. Tokuno M (1996) Operational system for extracting cloud motion and water vapor motion winds from GMS-5 image data. Proc. Third Int. Winds Workshop, EUM P18, Ascona, Switzerland, EUMETSAT, 21–30.
18. Tokuno M (1998) Collocation area for comparison of satellite winds and radiosondes. Proc. Fourth Int. Winds Workshop, EUM P24, Saanenmoser, Switzerland, EUMETSAT 21–28.
19. Tomassini C (1981) Objective analysis of cloud fields. Proc. Satellite Meteorology of the Mediterranean ESA, SP-159: pp.73-78.
20. Velden CS, Hayden CM, Nieman SJ, Menzel WP, Wanzong S, Goerss JS (1997) Upper-tropospheric winds derived from geostationary satellite water vapor observations. *Bulletin of American Meteorological Society* 78:173–195.
21. Velden, C.S., and J.P. Dunion, 2001: New satellite derived wind products and their applications to tropical cyclone/tropical wave forecasting. Minutes, *55th Interdepartmental Conf.*, Orlando, FL, Office of Federal Coordinator For Meteorological Services and Supporting Research, NOAA, in press.

15. Upper Tropospheric Humidity

S.No.	Product Name	Spatial Resolution	Temporal Resolution
1	3DIMG_L2B_UTH	4 km	30 minutes
2	3DIMG_L2B_UTH_DLY	4 km	Daily

15. Upper Tropospheric Humidity (UTH)

15.1 Algorithm Configuration Information

15.1.1 Algorithm Name

Upper Tropospheric Humidity (UTH)

(Additional parameter to IMD RFF)

15.1.2 Algorithm Identifier

3DIMG_L2B_UTH

3DIMG_L3B_UTH_DLY

15.1.3 Algorithm Specification

Version	Date	Prepared by	Description
1.0	14.02.2007	P. K. Thapliyal M. V. Shukla Shivani Shah	UTH Baseline Document

15.2 Introduction

Upper Tropospheric Humidity (UTH) is an estimate of the mean relative humidity of the atmosphere between approximately 600 hPa and 300 hPa. UTH is basically a measure of weighted mean of relative humidity according to the weighting function of the water vapour channel. Therefore, UTH is more likely a representative of the relative humidity around the atmospheric layer where weighting function of water vapour channel peaks

15.2.1 Overview and background

Upper tropospheric humidity from satellite measurements is useful to monitor changes in water vapour in the upper troposphere on a global and regional scale. Several methods have been developed for retrieving UTH from water vapour channel measurements (Schmetz and Turpeinen, 1988; Soden and Bretherton, 1993, 1996; Stephens et al, 1996). Changes in relative humidity around this layer would contribute maximum to the changes in the radiances received in this channel.

UTH extraction is in principle the calculation of single-column values for the upper tropospheric humidity. The physics involved is the quantitative description of the transfer of the WV channel radiances from the radiation emitting surface through the atmosphere towards the satellite as calculated by radiative transfer model. The transfer calculations are performed for a set of different constant humidity values for the upper tropospheric atmosphere for standard atmosphere representing different months/seasons. Empirical coefficients generated for different months are then used to derive from the IR and WV radiation measured by the satellite to estimate an average of the upper tropospheric humidity that caused the emitted radiation to be attenuated to the values measured. Only the pixels of surface and low cloud clusters are used, excluding the pixels of contamination with medium and high cloud clusters from the processing.

15.2.2 Objective

In this project the algorithm will be developed for computing Upper Tropospheric Humidity (UTH) from WV channels 6.7 μm of VHRR onboard Kalpana -1, INSAT-3A and Imager onboard future INSAT-3D satellite.

15.3 Inputs

15.3.1 Static Data

Parameter	Resolution	Accuracy	Source
Atmospheric profile (2311) of Temperature, Water Vapour, Ozone	-	-	TIGR-3 data base (Chevallier, Che'din, Che'ruey, & Morcrette, 2000)
41 diverse profiles of temperature, water vapour, Ozone	-	-	ECMWF
SeeBor dataset of diverse profiles (~12000)	-	-	Seeman and Borbas, CIMSS/SSEC

15.3.2 Image and preprocessing data (Dynamic)

Parameter	Resolution	Quantization	Accuracy	Source
Radiometric and geometric corrected gray count values of WV channel#2 (5.7-7.1 μm) of INSAT-3A/Kalpana and Channel#4 (6.5-7.1 μm) of INSAT-3D Imager	Pixel	10bit	-	Derived from raw data by DP (data processing)
Radiometric and geometric corrected gray count values of TIR channel#3 (10.5-12.5 μm) for INSAT-3A/Kalpana and Imager Channel#5 (10.2-11.3 μm) for INSAT-3D	pixel	10 bit	-	Derived from raw data by DP
Coefficients for conversion of Gray value to radiances	-	-	-	Derived by DP
Geolocation file	Pixel	-	1 pixel	Derived by DP

15.4 Algorithm Functional Specifications

15.4.1 Overview

Standard tropical atmospheric profile has been used to simulate VHRR radiances using SBDART model. Filter response function for the INSAT-3A/ Kalpana-1 WV channel was provided as input to the SABDART. Standard profile was modified by replacing specific humidity at levels above 600 hPa to represent constant relative humidity ranging from 2 to 100% with the interval of 2%. Satellite zenith angle was varied from 0 to 75 degrees at an interval of 5 degree for each constant relative humidity profile. Radiances were simulated for each set of profile and zenith angle at the top of atmosphere (100 km) from SBDART for VHRR WV channel. Brightness temperature is computed from simulated radiances using the following relationship:

$$Tb_{6.7} = A / \ln\{(B/R) + 1\}$$

Where, A and B are constants, Tb is Brightness Temperature in K and R is Radiance in mW/cm²/Sr/ μ .

A bilinear regression relationship is established between $\ln\{uth/\cos(\theta)\}$ and water vapour channel brightness temperature $Tb_{6.7}$ in the form:

$$\ln\{UTH/\cos(\theta)\} = a + b.Tb_{6.7} \quad \text{---- (1)}$$

Where, θ is the satellite zenith angle of the corresponding pixel, and a and b are the regression coefficients. We obtain the following relationship for the UTH with satellite zenith angle and measured brightness temperature (Fig.1):

$$UTH = \cos(\theta) * \exp(-a_1 * Tb_{6.7} + b_1) \quad \text{for } Tb_{6.7} < 240.0 \quad \text{---- (2a)}$$

(with $R^2 = 0.9965$)

And,

$$UTH = \cos(\theta) * \exp(-a_2 * Tb_{6.7} + b_2) \quad \text{for } Tb_{WV} > 240.0 \quad \text{---- (2b)}$$

(with $R^2 = 0.9989$)

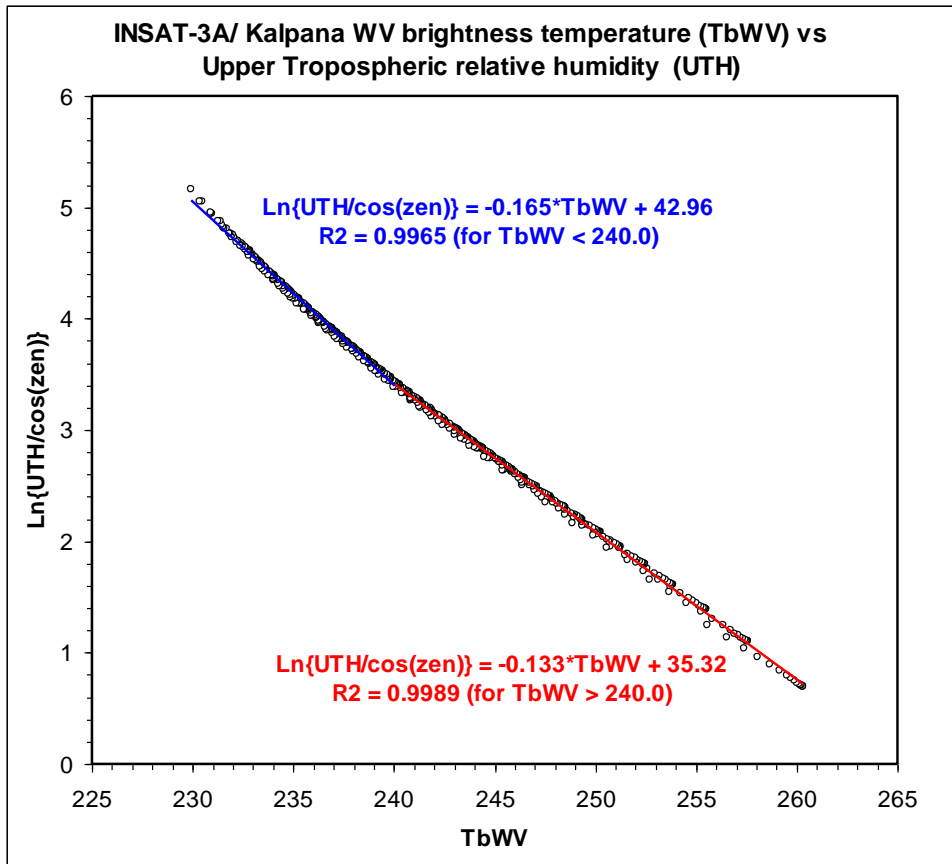


Fig.1 INSAT WV Brightness Temperature vs UTH

The algorithm uses water vapour channel of the INSAT-3A/Kalpana-1 VHRR (5.7-7.1 μ) to estimate the upper tropospheric humidity in absence of middle and upper level clouds. The generation of the UTH product is directly based on the WV brightness temperatures. Each water vapour image is converted into different segments of 16 x 16 pixels as the averaging would reduce the error in measurements and also helps removes the pixels with partial cloud cover. The WV image pixels of each segment not belonging to contamination with medium and high cloud clusters are averaged (if there are any, otherwise no UTH value is derived for such a segment). Presently, pixels with middle and upper clouds are removed using a threshold value of IR brightness temperature of 270 K. Additionally, if UTH value exceeds 110%, then pixel is assumed to be cloud contaminated. However, this approach needs further modification. These segment WV brightness temperatures are used to derive an upper tropospheric relative humidity by using the empirical relation (2).

Brightness temperatures depend strongly upon the satellite zenith angle since it increases the path length for the radiances reaching the satellite. Therefore, zenith angle is computed for each segment to be used with the regression equation. Satellite zenith angles are computed for every pixel using satellite-observer geometry using the following formula:

$$\beta = (\pi/2) - \arccos[\sin(\eta)/\sin(\rho)] \quad \text{--- (3)}$$

where,

$$\rho = \arcsin[R_e/(R_e + H)]$$

$$\eta = \arctan[\sin(\rho) * \sin(\lambda) / (1 - \sin(\rho) * \cos(\lambda))]$$

$$\lambda = \arccos[\sin(\delta_s) * \sin(\delta_t) + \cos(\delta_s) * \cos(\delta_t) * \cos(\Delta L)]$$

R_e = radius of Earth = 6378.16 km

H = Altitude of satellite = 36000 km

$$\Delta L = |L_s - L_t|$$

(δ_t, L_t) is latitude and longitude of the target

(δ_s, L_s) is latitude and longitude of the sub-satellite point

15.4.2 Theoretical Background

In general a satellite sensor observes the total radiances in a spectral interval, which exits the atmosphere in the direction of the satellite sensor. Let Φ_ν represent the spectral response function then radiances observed by satellite sensors is given by:

$$L(p_t, \mu) = \int_{\Delta\nu} \Phi_\nu I_\nu^\uparrow(p_t, \mu) d\nu \quad (4)$$

with $\Delta\nu$ the width of the spectral interval, $\mu = \cos \theta$, with θ the satellite viewing angle and $I_\nu^\uparrow(p_t, \mu)$ the monochromatic radiances at the top of the atmosphere, which is given by:

$$I_\nu^\uparrow(p_t, \mu) = I_\nu^\uparrow(p_b, \mu) \tau_\nu(p_b, p_t, \mu) + \int_{p_b}^{p_t} S_\nu(p, \mu) \frac{d\tau_\nu(p, p_t, \mu)}{dp} dp \quad (5)$$

where p_b represents the pressure at lower boundary, and, S_ν the source function. The transmission (τ) is given by

$$\tau_\nu(p_1, p_2, \mu) = e^{-\frac{\beta_\nu(p_1, p_2)}{\mu}} \quad (6)$$

with β the dimension less optical depth.

Equation (4) requires the specification of a lower boundary condition. Here two cases are considered, namely a simulation for clear scene, and one for a scene with an opaque cloud. In case of clear sky scene $I_\nu^\uparrow(p_b, \mu)$ is the upwelling radiance at the surface given by

$$I_\nu^\uparrow(p_b, \mu) = \varepsilon_\nu B_\nu(T_{sfc}) \quad (7)$$

In case of cloud case simulation, the lower boundary is given by:

$$I_\nu^\uparrow(p_b, \mu) = \varepsilon_\nu B_\nu(T_{cloud}) \quad (8)$$

For an atmosphere in local thermodynamic equilibrium the source function is given by the plank function:

$$B_\nu(T) = 2h\nu^3c^2 \frac{1}{\exp(hc\nu/kT) - 1} \quad (9)$$

which together with Equation (4) gives complete description of radiances at the top of the atmosphere.

15.4.2.1 Radiative Transfer Model

SBDART (Santa Barbara DISORT Atmospheric Radiative Transfer) model developed by Ricchiazzi et al (1998) at University of California will be used for INSAT-3A/Kalpana and INSAT-3D VHRR radiance simulations. SBDART is designed for the analysis of a wide variety of radiative transfer problems encountered in satellite remote sensing and atmospheric energy budget studies. SBDART is based on a collection of highly developed and reliable physical models developed by the atmospheric science community. A brief description to the key components of the model are discussed below:

Cloud Model: Clouds are a major modulator of the earth's climate by reflecting visible radiation and intercepting part of the infrared radiation emitted by the Earth and re-radiating it back to the surface. The computation of radiative transfer within a cloudy atmosphere requires knowledge of the scattering efficiency, the single scattering albedo, and the asymmetry factor, which indicates the strength of forward scattering. SBDART contains an internal database of these parameters for clouds computed with a Mie scattering code and covers a range of particle size effective radius in the range 2 to $128\mu m$. By default, the angular distribution of scattered photons is based on the simple Henyey-Greenstein parameterization, but more detailed scattering functions may be input as desired.

Gas Absorption Model: Standard SBDART uses low-resolution band models developed for the LOWTRAN 7 atmospheric transmission code (Pierluissi and Marogoudakis, 1986). These models provide the clear sky atmospheric transmisson from 0 to 50000 cm^{-1} and include the effects of all radiatively active molecular species found in the earth's atmosphere. The models were derived from detailed line-by-line calculations, which were degraded to 20 cm^{-1} resolutions for use in LOWTRAN. This translates to a wavelength resolution of about 5 nm in the visible and about 200 nm in the thermal infrared. A capability to read high-resolution k-distribution optical depths from a disk file is introduced in SBDART version 2.0 which is less convenient to use than the standard approach. However, it has the advantage of removing limitations in the ultimate spectral resolution available with SBDART.

Extraterrestrial Source Spectra: SBDART has options for three extraterrestrial solar spectrum models: LOWTRAN-7 solar spectrum (Shettle and Fenn, 1975), solar models used in 5s (Tanre, 1988) or MODTRAN-3 solar spectrum.

Standard Atmospheric Models: SBDART has six standard atmospheric profiles from the 5s atmospheric radiation code to model the following typical climatic conditions: tropical, midlatitude summer, midlatitude winter, subarctic summer, subarctic winter and US62. These model atmospheres (McClatchey et al, 1971) have been widely used in the atmospheric research community and provide standard vertical profiles of pressure, temperature, water vapor and ozone density. Optionally users can specify their own model atmosphere, e.g, a radiosonde profile. The concentration of trace gases such as CO₂ or CH₄ are assumed to make up a fixed fraction (which may be specified by the user) of the total particle density.

Standard Aerosol Models: SBDART can compute the radiative effects of several common boundary layer and upper atmosphere aerosol types. In the boundary layer, the

user can select from rural, urban, or maritime aerosols. The total vertical optical depth of boundary layer aerosols is derived from user specified horizontal meteorologic visibility at $0.55\text{ }\mu\text{m}$ and an internal vertical distribution model. In the upper atmosphere up to 5 aerosol layers can be specified, with radiative characteristics that model fresh and aged volcanic, meteoric and the climatological tropospheric background aerosols. The aerosol models included in SBDART were derived from those provided in the 5s and LOWTRAN7.

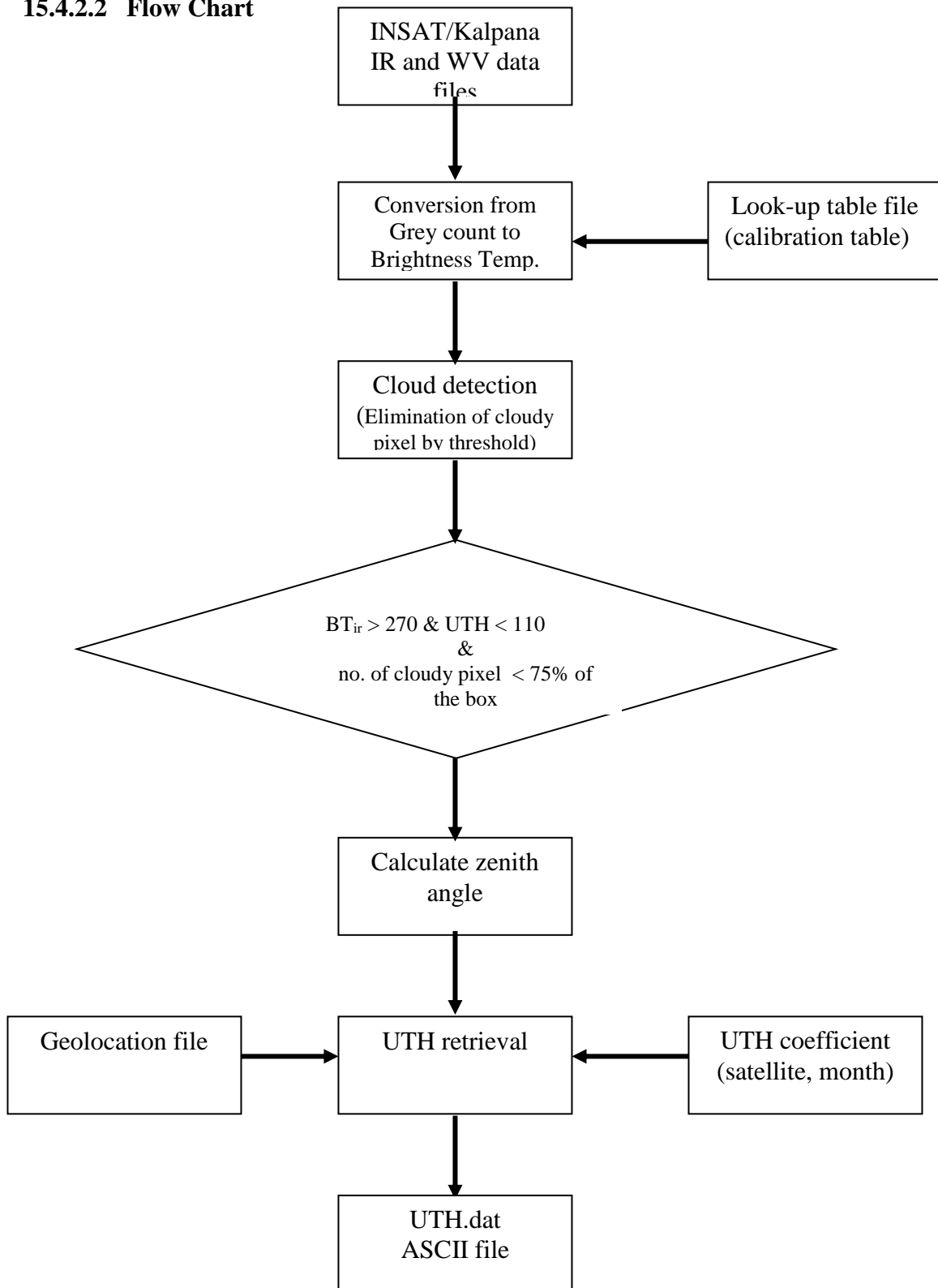
Radiative Transfer Equation Solver: The radiative transfer equation is numerically integrated with DISORT (DIScrete Ordinate Radiative Transfer, Stamnes et al, 1988). The discrete ordinate method provides a numerically stable algorithm to solve the equations of plane-parallel radiative transfer in a vertically inhomogeneous atmosphere. The intensity of both scattered and thermally emitted radiation can be computed at different heights and directions. SBDART is configured to allow up to 65 atmospheric layers and 40 radiation streams (40 zenith angles and 40 azimuthal modes).

Surface Models: The ground surface cover is an important determinant of the overall radiation environment. In SBDART six basic surface types -- ocean water, lake water, vegetation, snow and sand are used to parameterize the spectral reflectivity of the surface. The spectral reflectivity of a large variety of surface conditions is well approximated by combinations of these basic types. For example, the fractions of vegetation, water and sand can be adjusted to generate a new spectral reflectivity representing new/old growth, or deciduous vs. evergreen forest. Combining a small fraction of the spectral reflectivity of water with that of sand yields an overall spectral dependence close to wet soil.

The diverse profiles datasets are used to construct monthly average temperature and humidity profiles over INSAT observation area. Monthly averaged profiles are used to minimize the uncertainties due to seasonal variation of upper tropospheric temperature on UTH computation. For each month the average profile is perturbed by replacing water vapour at each levels between 600-200 hPa to make the relative humidity (RH) a constant value (=2, 4, 6....100%) throughout the layer 600-200hPa and falls off linearly to ~0 from 200 hPa to 100 hPa in each of the perturbed profiles. Temperature and ozone profiles are kept same for each perturbed profile in each month and only water vapour is changed above 600 hPa level. Since each level between 600-200hPa has same RH value, the weighted average value, i.e. UTH is equal to RH for each perturbed profile. Water vapour channel brightness temperatures for each perturbed profile at different zenith angle (0, 5, 10.....60°) are simulated using the Santa Barbara DISORT Atmospheric Radiative Transfer (SBDART) model (Ricchiazzi, Yang, Gautier, & Sowle, 1998). The radiative transfer computations are carried out separately for each satellite (INSAT-3A, Kalpana, and INSAT-3D) using sensor response functions of water vapour channels for simulating realistic satellite radiances. For each profile, the main inputs for the radiative transfer computations are: atmospheric profiles of temperature, water vapour, and ozone concentrations. These simulations are carried out for average profiles corresponding to different months. Regression analysis is carried out separately for each satellite and each months independently and the regression coefficients are obtained between $[UTH/\cos(\theta)]$ and water vapour channel brightness temperature, where θ is zenith angle. These coefficients may be used to retrieve the UTH from satellite observations of water

vapour channel by choosing appropriate coefficient represent the particular satellite and month of observation.

15.4.2.2 Flow Chart



15.4.3 Operational Implementation

15.4.2.1 Step 1 : Conversion of Grey count to Brightness temperature :

The grey count values in the IR and WV geo-corrected files are converted into the brightness temperature values using the static look-up table file, which is generated during characterization of the instruments on the ground before launch. This LUT file is provided along with the data set.

15.4.2.2 Step 2 : Cloud detection:

All the data in the cold space and data falling beyond the 60° radius from the sub-satellite points are excluded from further calculations. Cloudy pixels are identified and these pixels are also excluded from further calculations. The threshold used to eliminate the cloudy pixel is that if brightness temperature of thermal IR window channel is less than or equal to 270 and if the UTH calculated at that pixel is > 110 then it is a cloudy pixel, and hence eliminated. In the 5×5 pixel box, if the number of cloudy pixels is more than 75 % than the whole box is considered as cloudy and excluded from UTH retrieval.

15.4.2.3 Step 3: Zenith angle calculation:

After the cloudy pixels are discarded then the zenith angle is calculated for the pixels using Equation (3).

15.4.2.4 Step 4 : UTH retrieval:

Using the above calculated zenith angle and the UTH coefficients for corresponding satellite and month of the observation, UTH is calculated from Equation (2) using the water vapour channel brightness temperature. UTH is generated for every 5×5 pixel box.

15.5 Outputs

Parameter	Unit	Min	Max	Accuracy	Resolution
UTH	%	0	100	5 % (RMSE)	$0.5^{\circ} \times 0.5^{\circ}$

15.5.1 Format of the output and the domain

Binary file giving details of the time and location of the retrieval, zenith angle, % of clear pixels used in averaging within 5×5 pixel box, and UTH (%).

Domain: 50 S to 50 N, 30 E to 130 E

15.6 Validation

15.6.1 Data required

The following data can be used for comparison and validation of UTH

Data	Resolution	Source
UTH		EUMETSAT
Humidity Profile	Radiosonde observations	IMD
Humidity Profile	1×1 deg	NCEP Reanalysis

15.6.2 Methods of validation

Radiosonde profiles and NCEP analysis profiles of water vapour are converted into upper tropospheric humidity (UTH) estimates using water vapour channel weighting function of the satellite concerned. UTH is weighted average of relative humidity weighted by the water vapour weighting function at each atmospheric level. These estimates of observed UTH are compared with the collocated satellite retrieved UTH.

These estimates of UTH can also be compared with retrieved product of Meteosat satellite located over Indian Ocean region. Because the extracted UTH product is dependent on the WV channel calibration, these UTH/radiosonde comparisons may also provide a method of checking the actual WV calibration coefficients. Brightness temperature observations of satellite WV channels may also be used with simulated brightness temperature from collocated radiosonde profile to compute the bias correction coefficients in the RT model.

15.7 Technical issues (limitation etc.)

Accuracy of the product depends on the accuracy of the radiation model to simulate the satellite radiances. However the following limitations of the present study have to be kept in mind.

- i) It is assumed that upper tropospheric temperature does not deviate by a large amount from the mean monthly profile.
- ii) Satellite receives only a negligible amount of radiance emitted from layers beneath 600 hPa. The atmosphere above 200 hPa is represented by decreasing the relative humidity to 0% at 100 hPa, which seems to be a reasonable assumption consistent with the structure of standard profiles and observations.
- iii) The reason for using mean monthly profiles of water vapour at lower levels as input to the radiative transfer model is that these levels contribute very little to the outgoing radiance.

15.8 Future Scope

These coefficients can be improved with the availability of more accurate radiation models in future. UTH algorithm in future may include the upper tropospheric mean temperature derived from model forecast to minimize the uncertainties due to the temperature variations in the 600-200 hPa layer.

15.9 References

1. McClatchey, R.A., R.W. Fenn, J.E.A. Selby, F.E. Volz, J.S. Garing, 1972: Optical properties of the atmosphere, (third edition), Air Force Cambridge Research Laboratories, Report AFCRL-72-0497.
2. Pierluissi, J.H., and Maragoudakis, C.E. 1986: "Molecular Transmission Band Models for LOWTRAN", AFGL-TR-86-0272, AD A180655.
3. Ricchiazzi, P., Yang, S., Gautier, C., and Sowle, D. (1998): SBDART: A Research and Teaching Software Tool for Plane-Parallel Radiative Transfer in the Earth's Atmosphere, *Bull. Amer. Met. Soc.*, 79 (10), 2101-2114.

4. Schmetz, J., and O.M. Turpeinen, 1988: Estimation of the Upper Tropospheric Relative Humidity Field from METEOSAT Water Vapour Image Data. *J. Appl. Meteor.*, 27, No. 8, 889-899.
5. Shettle, E. P., and R. W. Fenn, 1975: "Models of the atmospheric aerosols and their optical properties." AGARD conference proceedings no. 183, Optical Propagation in the Atmosphere, 700 pages, presented at the Electromagnetic Wave Propagation Panel Symposium, Lyngby, Denmark 27-31 October 1975, sponsored by North Atlantic Treaty Organization, Advisory Group for Aerospace Research.
6. Soden B. J. and F. P. Bretherton (1996): Interpretation of TOVS water vapour radiances in terms of layer-average relative humidities: method and climatology for the upper, middle, and lower troposphere, *J. geophys. Res.*, 101, 9333-9343.
7. Soden B.J. and F. P. Bretherton (1993): Upper tropospheric relative humidity from GOES 6.7 μ m channel: method and climatology for July 1987, *J. geophys. Res.*, 98, 16669-16688.
8. Stamnes, K., S. Tsay, W. Wiscombe and K. Jayaweera, 1988: "Numerically stable algorithm for discrete-ordinate-method radiative transfer in multiple scattering and emitting layered media." *Appl. Opt.*, 27, 2502-2509.
9. Stephens G., D. Jackson and I. Wittmeyer (1996): Global observations of upper tropospheric water vapor derived from TOVS radiance data. *J. Climate*, 9, 305-326.
10. Tanre D., C. Deroo, P. Duhamet, M. Herman, J. Morerette, J. Peros and P. Y. Deschamps (1990) : "Description of a computer code to simulate the satellite signal in the solar spectrum : the 5S code", *Int. J. Rem. Sens.*, Technical note, 11, 659-668.

16. Temperature, Moisture Profile and Total Ozone from Sounder

S.No.	Product Name	Spatial Resolution	Temporal Resolution
1	3DSND_L2B_SA1	10 km	1 hourly
2	3DSND_L2B_SB1	10 km	6 hourly

16. Retrieval of Atmospheric Profiles Of Temperature, Humidity And Ozone

16.1 Algorithm configuration information

16.1.1 Algorithm name:

Atmospheric Profiles Retrieval (ATMPROF)

(Ref : IMD RFP Section 12.1)

16.1.2 Algorithm Identifier:

3DSND_L2B_SA1

3DSND_L2B_SB1

16.1.3 Algorithm Specification

Version	Date	Prepared by	Description
1.0	14.02.2007	P K Thapliyal, M V Shukla, C M Kishtawal and P K Pal	ATBD for Atmospheric profiles retrieval from INSAT-3D Sounder

16.2 Introduction

INSAT-3D will carry an 18-channel infrared Sounder (plus a visible channel) along with a 6 channel Imager.

This algorithm is designed for retrieving vertical profiles of atmospheric temperature and moisture along with total column ozone content in the atmosphere from clear sky infrared radiances in different absorption bands observed through INSAT-3D. INSAT-3D Sounder channels are similar to those in GOES-12 Sounder and many of the spectral bands are similar to High resolution Infrared Radiation Sounder (HIRS) onboard NOAA-ATOVS. Hence, present algorithm for INSAT-3D Sounder is adapted from the operational HIRS and GOES algorithms developed by Cooperative Institute for Meteorological Satellite Studies (CIMSS), University of Wisconsin.

This module also describes the background to retrieval problem, theoretical basis of the retrieval algorithm for vertical profiles, practical aspects of algorithm implementation, and outline of the planned validation approach. INSAT-3D Sounder instrument characteristics are given in the appendix-1 at the end.

16.2.1 Overview and Background:

INSAT-3D Sounder observations will provide vertical profiles of temperature and humidity in clear-sky conditions besides total column ozone and various other derived products. Atmospheric profile retrieval algorithm for INSAT-3D Sounder is a two-step approach. The first step includes generation of accurate hybrid first guess profiles using combination of statistical regression retrieved profiles and model forecast profiles. The second step is nonlinear physical retrieval to improve the resulting first guess profile using Newtonian iterative method.

The retrievals will be performed using clear sky radiances measured by Sounder within a 5x5 field of view (approximately 50 km resolution) over land and ocean for both day and night. Four sets of regression coefficients will be generated. Two sets for land and ocean daytime conditions and the other two sets for land and ocean night-time conditions using a training dataset comprising historical radiosonde observations representing atmospheric conditions over INSAT-3D observation region.

The retrieval algorithm discussed here is adapted from CIMSS algorithm for GOES-Sounder and is primarily based on the retrieval algorithms of Li et al. (2000), Ma et al. (1999), Smith and Woolf (1988) and Hayden (1988). Temperature and moisture profiles at Sounder resolution are required for numerical weather prediction in short to medium range besides various other weather and climate applications. High temporal resolution of sounding data from geostationary satellite INSAT-3D will provide a wealth of new information on atmospheric structure in clear-sky conditions. Retrieval of atmospheric profiles at high spatial and temporal resolutions will immensely improve mesoscale prediction.

16.2.2 History of atmospheric sounding

King (1956) was first to suggest that atmospheric temperature profiles could be inferred from satellite observations of thermal infrared emission and explained the feasibility of retrieving the temperature profile from the satellite intensity scan measurements. Further advances were made for the temperature-sounding concept when Kaplan demonstrated (1959) that vertical profile of temperature could be inferred from the spectral distribution of emission by atmospheric gases. He suggested that observations in the wings of a spectral band sense deeper regions of the atmosphere; whereas observations in the band center see only the very top layer of the atmosphere. Thus by properly selecting a set of sounding spectral channels at different wavelengths in the absorption band, the observed radiances could be used to estimate the vertical temperature profile in the atmosphere.

Following a proposal by Wark (1961) for satellite vertical sounding program to measure atmospheric temperature profiles, the first satellite-sounding instrument (SIRS-A) was launched on NIMBUS-3 in 1969 (Wark et al., 1970). NOAA launched the TIROS Operational Vertical Sounder in 1978 (TOVS, Smith et al. 1979), consisting of High-resolution Infrared Radiation Sounder (HIRS), Microwave Sounding Unit (MSU), and the Stratospheric Sounding Unit (SSU) onboard satellites NOAA-6 to NOAA-14. HIRS provides 17 km spatial resolution at nadir with 19 infrared sounding channels (4-15 μ), whereas MSU provides 109 km resolution at nadir with 4 microwave channels (~50 GHz). SSU has 3 channels in the far IR (~15 μ) for stratospheric measurements. Current NOAA series satellites NOAA-15 and NOAA-16 (and future satellite in the NOAA series) have ATOVS with HIRS/3, and MSU and SSU have been replaced by AMSU-A and AMSU-B to improve the temperature and humidity sounding. HIRS/3 has the same spectral bands as the HIRS/2. AMSU-A uses 15 microwave channels around 23, 30, 50 and 90 GHz of oxygen absorption bands with resolution of 50 km at nadir. AMSU-B uses 5 microwave channels around 90, 150 and 190 GHz with a horizontal resolution of 17 km at nadir.

New generation of infrared atmospheric sounder is the hyper-spectral sounder with thousands of channels instead of few tens of infrared bands. Atmospheric Infra-Red Sounder (AIRS) onboard EOS-Aqua satellite was launched on May 4, 2002 and is providing a wealth of highly accurate atmospheric and surface information using 2378 high-spectral-resolution

infrared ($3.7 - 15.4 \mu$) channels with horizontal resolution of 10 km at nadir. AIRS along with AMSU forms a state-of-art atmospheric sounding tool for temperature profiles with accuracy of 1°C in a 1 km thick layer and humidity profile with an accuracy of 20% in 2 km thick layer in the troposphere. Aqua satellite also has MODIS with very high spatial resolution of 1 km and is providing the vertical profiles of temperature and humidity. Recently, METOP satellite was launched carrying a hyper-spectral sounder IASI onboard with > 8400 channels and mission objective to achieve the temperature and humidity profiles accuracy of 1°C and 10% in 1 km and 2km layers, respectively.

The first sounding instrument in geostationary orbit was the GOES VISSR Atmospheric Sounder (VAS, Smith et al. 1981) launched in 1980. This was followed by GOES-8 Sounder (Menzel and Purdom, 1994) that provides 8 km spatial resolution with 18 infrared sounding channels. Current satellite of this series, GOES-13, is launched recently in May 2006. Future satellite GOES-R of this series to be launched in 2012 will have a Hyperspectral Environmental Suite (HES) to provide high spectral resolution in the infrared and a high spatial resolution mode for mesoscale sounding capability. Advanced Baseline Imager (ABI) onboard GOES-R will be similar to the current polar orbiting EOS-MODIS. NASA and NOAA are planning to launch Geostationary Imaging Fourier Transform Spectrometer (GIFTS) that will revolutionize our ability to measure, understand and predict the earth-atmosphere system.

16.2.3 Objective

Objective of the present module is to describe the algorithms and different aspects associated with the retrieval of temperature, humidity profiles and total column ozone from INSAT-3D Sounder observation in 18 infrared spectral bands. Present document also outlines the validation plan for the retrieved atmospheric profiles.

16.3 Inputs

16.3.1 Static Data

Parameter	Resolution	Accuracy	Source
Land/sea flag	$\sim 2 \text{ km} \times 2 \text{ km}$	--	Global topographic datasets (Available)
Surface Elevation	Each Pixel $10 \text{ km} \times 10 \text{ km}$	--	Global topographic datasets (Available)
Monthly mean spectral surface Emissivity	Each Pixel $10 \text{ km} \times 10 \text{ km}$	--	Univ. of Wisconsin (Available)
Global training dataset for temperature and humidity (Radiosonde/ Analysis Profiles)	Surface to 0.01 hPa levels	--	Univ. of Wisconsin/ IMD (Available)
Global training dataset for ozone profile (Ozonesonde)	Surface to 0.01 hPa levels	--	Univ. of Wisconsin/ IMD (Available)

16.3.2 Sounder data:

Parameter	Resolution	Quantization	Accuracy	Source
Radiometric and Geometric corrected gray count values of	Each Pixel	12-bit	--	Derived from raw

sounder channels #1-19				data by DP
Geolocation information	each pixel		1 pixel	Derived by DP
Coefficients to convert gray values of sounder channels#1-18 to radiances/brightness temperature	-	-	-	Derived by DP
Brightness temperature quality flag for sounder channels	each pixel	-	-	Derived by DP

16.3.3 Other Auxiliary data:

In addition to Sounder data, numerical model forecast and surface observations of temperature and humidity are required to improve the retrieval accuracy.

Parameter	Resolution	Accuracy	Source
Forecast temperature and humidity profiles valid at observation time	1° x 1° at model pressure levels	--	NCEP and/or IMD/NCMRWF
Forecast surface pressure and surface skin temperature valid at observation time	1° x 1°	--	NCEP and/or IMD/NCMRWF
Observed surface pressure, surface air temperature and humidity	AWS locations	--	IMDs Automatic Weather Station (AWS)

16.4 Algorithm Functional Specifications

16.4.1 Overview

In this section, detailed theoretical aspects of the sounding retrieval are discussed. INSAT-3D Sounder retrieval scheme involves two-step approach. In first step, first-guess temperature and humidity profiles are derived based on regression retrieval combined with model forecast. In the second step, accurate temperature and humidity profiles are retrieved based on physical retrieval procedure that uses non-linear Newtonian iterative method to adjust first guess profiles. Ozone profile and integrated amount is retrieved using regression retrieval and used as first guess for the physical retrieval routine.

16.4.1.1 Theoretical Background

Atmospheric sounding is one of the most important applications of satellite measurements in meteorology, which involves retrieving vertical profiles of temperature and trace-gas concentrations, especially water vapor and ozone, using observations at wavelengths that have significant attenuation in atmosphere. For this we need to know the variation of temperature with altitude, and the variation of the density of atmospheric gases with altitude, such as carbon dioxide, water vapor and ozone. Water vapor is important because of its meteorological impact and its importance for atmospheric correction in thermal infrared measurements.

Atmospheric sounding techniques exploit all three phenomena that play important role in radiative transfer: namely absorption, scattering and thermal emission. Most observations are made in the thermal infrared and microwave bands. At infrared wavelengths scattering due to atmospheric gases is negligible, hence it is not considered in the radiative transfer process.

For vertical sounding at infrared wavelengths the significant terms in the radiative transfer equation (RTE) are absorption and thermal emission. This simplification is called Schwartzchild's equation. Here, we will consider only cloud-free conditions. If a sensor views vertically downwards into the atmosphere at a wavelength at which the atmosphere is optically thick, the brightness temperature/radiances that are received by sensor will be characteristic of the atmosphere at a depth below the sensor that is of the order of the absorption length. Thus for bigger absorption coefficient, the absorption length is smaller and hence the temperature signal is received from higher altitude. So by making observations at a number of wavelengths near a broad absorption line, different altitudes in the atmosphere can be investigated. Thermal infrared temperature profilers normally employ the broad and deep CO₂ lines near 15 μm wavelengths.

Radiative transfer equation in the non-scattering case may be written in simple form as:

$$I_{\lambda}(p=0) = \varepsilon_{\lambda} \cdot B_{\lambda}(T_s) \cdot \tau_{\lambda}(p_s \rightarrow 0) + \int_{p_s}^0 B_{\lambda}[T(p)] \cdot \frac{\partial \tau_{\lambda}(p \rightarrow 0)}{\partial p} \cdot dp + (1 - \varepsilon_{\lambda}) \cdot \tau_{\lambda}(p_s \rightarrow 0) \cdot \int_0^{p_s} B_{\lambda}[T(p)] \cdot \frac{\partial \tau_{\lambda}(p \rightarrow p_i)}{\partial p} \cdot dp \quad --- (1)$$

Where,

- ε_{λ} -Surface emissivity
- $\tau_{\lambda}(p \rightarrow 0)$ -Vertical transmittance from level with pressure p to space
- $T(p)$ -vertical profile of temperature and
- $B_{\lambda}[T(p)]$ -corresponding Planck function profile.

This equation implies that the radiance received at a particular wavelength is sum of three terms on the right hand side: first term is upwelling radiance from the surface, second term is direct atmospheric emission term and the third term is reflected downward atmospheric emission reaching at satellite sensor. $(\partial \tau / \partial p)$ is called a weighting function. It weights the Planck function in the atmospheric component of the emitted radiation. It specifies the layer from which the radiation emitted to space originates, and hence it determines the region of the atmosphere that can be sensed from space at this wavelength. Fig.1 shows the transmittance profiles and corresponding weighting functions at three wavelengths for which the atmospheric absorption is different. Since the weighting function is the derivative of the transmittance profile, it will peak higher in the atmosphere for the wavelengths at which the absorption is stronger. In this way, if the atmosphere is observed at a number of carefully chosen wavelengths, whose weighting functions sample the atmosphere, then it is possible to retrieve the Planck's function $B_{\lambda}(T)$ and thereby the temperature T itself.

To explain this form of weighting functions, we consider the emission to space from air parcels of unit volume at different heights in the atmosphere. The radiation emitted to space is determined by three factors: temperature of the air parcel, number density of emitting gas, and transmittance of the atmosphere from the air parcel to space. For the lowest parcel, the atmospheric density is high and so the amount of radiation emitted is high, but most of the radiation is absorbed in the atmosphere above it and very little reaches space. For the highest parcel, the transmittance to space is high, but comparatively little radiation is emitted because

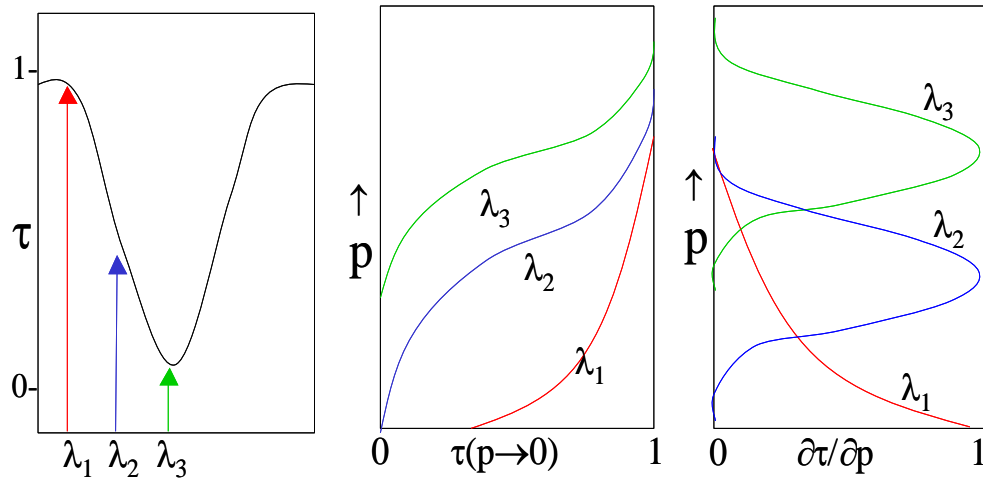


Fig.1: Schematic diagram of layer to space transmittances at three spectral wavelengths

atmospheric density decreases exponentially with height. These two contrasting effects combine in such a way that, at some intermediate height, the contribution of a parcel to the radiation reaching space is a maximum. The variation of the radiance to space as a function of height is shown by the curve on the right of the Fig.1.

Most of the radiation to space originates in a layer around the peak of weighting function. From the knowledge of atmospheric composition and spectroscopic parameters we can calculate where in the atmosphere this layer will be. Then the intensity of the radiation can be interpreted in terms of the mean temperature of the layer. Using radiation at different frequencies for which the absorption strength is different, we can build a group of weighting functions, which provide information on the mean temperatures of many such layers, thus leading to the retrieval of the atmospheric temperature profile from a set of multi-frequency measurements.

It is important to note that the weighting functions are broad, implying that the satellite instrument can sense the mean properties of broad layers very well, but it is only able to sense the characteristics of single levels or narrow layers insofar as they are correlated with the properties of the broad layers. Broad nature of the weighting functions restricts the capability of satellite sounders to detect small-scale vertical structure of the atmospheric. Infrared sounder channels have spectral widths typically hundreds of times greater than the atmospheric absorption lines. Therefore they average frequencies for which the absorption strengths are very different. This has the effect of broadening the weighting functions considerably. By using instruments of much higher spectral resolution, such as interferometers or grating spectrometers (e.g. AIRS, IASI), it is possible to achieve spectral resolutions closer to the widths of the atmospheric absorption lines. In this way instruments with several thousand channels and much sharper weighting functions can be built.

In order for atmospheric temperature to be inferred from measurements of thermal emission, the source of emission must be a relatively abundant gas of known and uniform distribution. Otherwise, the uncertainty in the abundance of the gas will make ambiguous the determination of temperature from the measurements. Carbon dioxide is one such gas in the

atmosphere having uniform known mixing ratio for altitudes below about 100 km, and has emission bands in the spectral regions that are convenient for measurement, e.g. $15\mu\text{m}$.

The forward problem:

The instrument makes measurements of radiance in a number of channels λ_i . For each channel, we can write a radiative transfer equation (excluding reflection term):

This equation expresses the forward problem for the channel, i.e. given the state of the atmosphere; the solution of this equation gives us the radiance incident at the satellite in this channel. Using the radiances measured by the satellite radiometers, we can determine some information directly. For well-mixed gases such CO_2 , we assume that the mixing ratio is known and independent of height. Wavelengths that are sensitive to these gases are used to retrieve atmospheric temperature. For wavelengths sensitive to variable trace gases, such as

$$I_\lambda(p=0) = \varepsilon_\lambda \cdot B_\lambda(T_s) \cdot \tau_\lambda(p_s \rightarrow 0) + \int_{p_s}^0 B_\lambda[T(p)] \cdot \frac{\partial \tau_\lambda(p \rightarrow 0)}{\partial p} \cdot dp \quad --- \quad (2)$$

water vapor and O_3 , we assume that the temperature profile is known and use the radiances to retrieve mixing ratios. Unfortunately, no wavelengths are completely free of absorption by the variable trace gases; this contributes to errors in retrieving temperatures. Also, errors in our knowledge of temperature profiles lead to errors in trace-gas retrievals.

The above equations are strictly applicable only at a single wavelength, but satellite instruments sense a band of wavelengths. So the equation must be integrated over wavelength using the spectral response function for each channel as a weight. This can be very time-consuming. To overcome this problem, regression based fast transmittance models are formulated, in which the atmosphere is divided into predetermined layers, and the transmittance of each layer, averaged over the response function of the radiometer is calculated. Then the functions of temperature, humidity and zenith angle are fitted to the results to generate regression coefficients for the fast model.

The inverse problem:

Inverse problem in the satellite meteorology is to obtain the state of the atmosphere (in terms of its vertical profiles of temperature and constituents) from the radiance measurements. Since we have a limited number of channels the inversion of equation is ill posed or under-constrained. This means that there exist an infinite number of profiles that satisfy a given set of measurements. This is because the atmospheric state (unknown, e.g. temperature profile) is a continuous function of height, and measurements are from a finite number of channels. Inverse problem is to find one that is reasonable and, if possible, to find the profile which is best or most reasonable in some sense. In addition, the measurements always contain some error or "noise". This further increases the ill-posed nature of the problem, and we must find a method of solution that does not amplify the noise to an unacceptable degree. This implies that we need information additional to the measurements in order to reach a solution. For atmospheric remote sensing, additional information is available in the form of numerical model forecast and surface observation analysis.

There are several approaches for solution of this problem:

1. Physical retrieval

2. Statistical retrievals and
3. Hybrid retrieval

In a **physical retrieval**, the forward problem is exploited in an iterative procedure:

1. A first-guess temperature profile is chosen.
2. The weighting functions are calculated.
3. The forward problem is solved to yield estimates of the radiance in each channel.
4. If computed radiances match the observed ones (within noise) then the current profile is accepted as the solution.
5. If convergence is not achieved, the current profile is adjusted.
6. Steps 3-5 are repeated until a solution is found.

An advantage of this approach is that physical processes are clearly evident at each stage. The disadvantages are that the method is computationally intensive and it requires accurate knowledge about the transmittances. It also does not exploit the known statistical properties of the atmosphere.

In **statistical retrieval**, a training dataset, comprising radiosonde observations that are nearly coincident in time and space with satellite soundings are compiled. A relationship between the observed radiances and atmospheric profiles is established. In this approach physical processes are embedded in the statistics.

Advantages of this approach are (1) the actual retrievals are computationally simple (does not use RTE) and (2) it requires no knowledge of the transmittances. It only uses the statistical properties of the atmosphere. The disadvantage is that a large training data set is necessary.

Hybrid retrieval methods are in between the first two approaches. They are much like statistical retrievals, but they do not require a large training dataset. They use weighting functions like physical retrievals, but they do not directly involve integration of the RTE. Hybrid methods are easier to apply than the statistical or physical methods. They require knowledge of the transmittances, and they employ statistical knowledge of the atmosphere.

To summarize, there is no unique solution for the detailed vertical profile of temperature or an absorbing constituent because:

- a. The outgoing radiances arise from relatively deep layers of the atmosphere,
- b. The radiances observed within various spectral channels come from overlapping layers of the atmosphere and are not vertically independent of each other, and
- c. Measurements of outgoing radiance possess errors.

As a consequence, there are a large number of analytical approaches to the profile retrieval problem. The approaches differ both in the procedure for solving the set of spectrally independent radiative transfer equations (e.g. matrix inversion, numerical iteration) and in the type of ancillary data used to constrain the solution to insure a meteorologically meaningful result (e.g. use of atmospheric covariance statistics, use of an a priori estimate of the profile structure). Various methods of sounding retrievals have been reviewed by Fleming and Smith, 1971; Fritz et al., 1972; Rodgers, 1976; Twomey, 1977; and Houghton et al. 1984.

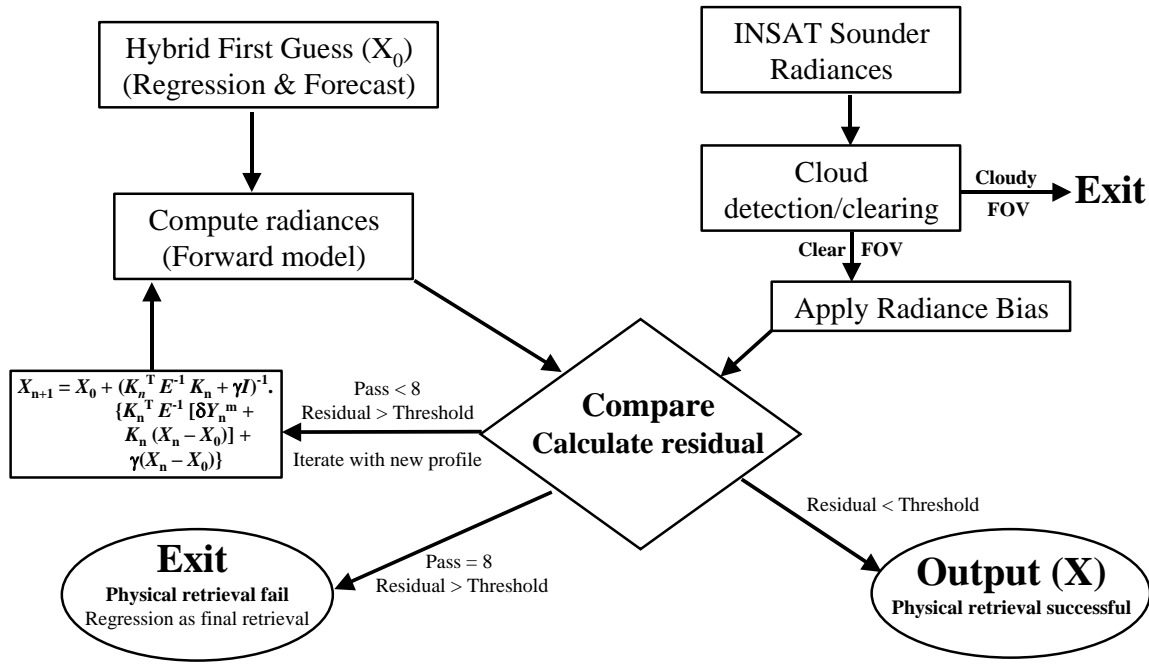
Following sections describe the mathematical basis for two-step procedure, which will be used in the development of retrieval algorithm for atmospheric profiles from INSAT-3D Sounder measurements.

16.4.1.2 Flow Chart:

Present sounder retrieval algorithm includes two steps:

1. Generation of hybrid first-guess profiles using weighted average of regression retrieval

Fig.2: Retrieval Algorithm for INSAT-3D Sounder



and forecast profiles.

2. First-guess profile is adjusted to match the observed radiances in an iterative procedure in physical retrieval routine.

Flow chart of the algorithm is shown in figure-2.

16.4.2 Operational Implementation:

Operational implementation of the retrieval scheme for INSAT-3D Sounder includes the following procedures:

- Development of fast forward radiative transfer model to compute Sounder channels radiances given atmospheric state as input.
- Identification of cloud free pixels
- Derivation of first-guess atmospheric profiles of temperature, humidity and ozone, and surface skin temperature from Sounder radiances using statical regression.
- Retrieval of final profiles through physical retrieval routine, which iteratively adjusts first-guess profiles to match the observed radiances.

16.4.2.1 Fast Forward Radiative Transfer Model:

Remote sensing of atmospheric profiles from satellite is critically dependent on our ability to calculate observed radiances as a function of the atmospheric state. This “forward problem” is the heart of the physically based retrieval algorithms. The high rate of satellite observations requires a forward model fast enough to keep pace with the observations. Though line-by-line models exist to accurately compute atmospheric transmittances, they are far too slow to be practical. Thus fast atmospheric transmittance models are required for operational atmospheric sounding using physical methods. For INSAT-3D Sounder channels we use Pressure Layer Optical Depth (PLOD) model, also known as pressure layer fast algorithm for atmospheric transmittances (PFAAST), developed by Hanon et al (1996). This model has been widely used for profiles retrieval algorithm for GOES, NOAA-TOMS/ATOVS, Aqua-AIRS/MODIS, etc (Li et al. 2000; Li et al. 2001 etc, Ma et al. 1999).

The radiance recorded by the satellite sensor is the convolution of incident spectral radiance function with instrument’s spectral response function (SRF). Computing simulated radiances by calculating the monochromatic radiances and then convolving it with the instrument’s SRF takes too much time to be practical. In fast model PLOD a polychromatic approximation for the transmittances is made which directly computes the approximate convolved radiances. The monochromatic radiance leaving the top of the atmosphere, excluding scattering and reflection, is given by

$$R = \varepsilon_s B(T(s))\tau_z(L) + \sum_{i=1}^L B(T(i)).[\tau_z(i-1) - \tau_z(i)] \quad \text{--- (3)}$$

Where, the atmospheric layers are numbered 1 to L from space to surface respectively. PLOD uses 101 atmospheric levels. $B(T(i))$ is the Planck function emission for layer ‘i’ at temperature $T(i)$ and $\tau_z(i)$ is layer-to-space transmittance from layer ‘i’ to space. ε_s is surface emissivity and $T(s)$ is surface temperature. Applying the polychromatic approximation, we convolve the layer-to-space transmittances and compute the radiances using above equation instead of convolving the monochromatic radiances. PLOD model relates the convolved layer-to-space transmittances to a simple function involving various profile dependent predictors. These predictors are functions of layer pressure, temperature, absorber amount, and viewing angle. Convolved transmittance is given by:

$$-\ln(\tau_{eff}) = \sum_{i=1}^N c_i Q_i \quad \text{--- (4)}$$

τ_{eff} is the effective layer transmittance, Q_i is the profile dependent predictor, and c_i are the fast transmittance coefficients determined by linear regression of the above equation for a set of representative atmospheric profiles. PLOD model uses a regression on $-\ln(\tau)$, i.e. the optical depth (k).

A set of profiles is selected for calculation of the layer-to-space transmittances, which is used for regression in fast coefficient computation. These profiles represent the entire range of atmospheric variation, and should be weighted towards more typical cases. Computation of convolved layer-to-space transmittances is time consuming, thereby restricting the practical limit of number of profiles to be used in the regression. We use 49 regression profiles (6 zenith angles upto 62.5°), which cover most of profile behavior in the INSAT-3D viewing region.

All profiles should cover necessary vertical levels for temperature and absorbing gases. Among absorbing gases only water vapor and ozone are allowed to vary in mixing ratio, and other gases are held “fixed”. Fixed gases include all those whose spatial and temporal variations have a negligible impact on the observed radiances. Monochromatic layer-to-space transmittances computed for fixed and different absorbing gases at different zenith angles are convolved with the instrument SRF. For each layer the effective layer optical depths (k_{fixed} , k_{water} , k_{ozone}) are obtained for fixed and variable absorbing gases. These effective layer optical depths are used in a regression analysis to compute the fast transmittance coefficients (c_i). Choosing the set of predictors for accurate results is mainly a matter of trial and error. PLOD model uses 8 predictors for fixed gases (k_{fixed}), 13 for water vapor (k_{water}), and 9 for ozone (k_{ozone}). These predictors are functions of temperature, water vapor, ozone profiles and sensor viewing angle, and are summarized as follows:

$$\begin{array}{llll} \textbf{k}_{fixed}: & 1) a & 2) a^2 & 3) a.T_r \\ & 5) T_r & 6) (T_r)^2 & 7) a.T_z \\ & & & 8) a.T_z/T_r \end{array}$$

Where, a is secant of the local path angle, T_r is the temperature ratio ($T_{profile}/T_{reference}$), and T_z is the pressure weighted temperature ratio above the layer:

$$T_z(l) = \sum_{i=2}^l P(i). (P(i) - P(i-1)). T_r(i-1) \quad \text{----- (5)}$$

Where $P(i)$ is the average layer pressure for layer ‘ i ’.

k_{water}: For water vapor predictors are divided into two parts: one for total water optical depth above the layer < 5 , i.e.

$$\begin{array}{llll} 1) W.a & 2) \sqrt{W.a} & 3) W.a.dT & 4) (W.a)^2 \\ 5) W.a.dT./dT/ & 6) (W.a)^3 & 7) W_z.a & 8) \sqrt{W.a}.dT \\ 9) {}^4\sqrt{W.a} & 10) (W_z.a)^2 & 11) \sqrt{W_z.a} & \end{array}$$

For total water optical depth > 5 ,

$$12) W.a \quad 13) W.a/(W_z.a)^2$$

W is water amount ratio ($W_{profile}/W_{reference}$), dT is the temperature offset ($T_{profile} - T_{reference}$), and W_z is pressure weighted water amount of W , i.e.

$$W_x(l) = \frac{\sum_{i=1}^l P(i).(P(i) - P(i-1)).W_{profile}(i)}{\sum_{i=1}^l P(i).(P(i) - P(i-1)).W_{reference}(i)} \quad \text{--- (6)}$$

k_{ozone}: Predictors for ozone are:

- | | | | |
|--------------------|-----------------|-----------------------|--------------|
| 1) $O.a$ | 2) $\sqrt{O.a}$ | 3) $O.a.dT$ | 4) $(O.a)^2$ |
| 5) $\sqrt{O.a}.dT$ | 6) $O_z.a$ | 7) $O.a.\sqrt{O_z.a}$ | 8) $O.a.W.a$ |
| 9) $TO_z.O.a$ | | | |

where O is ozone amount ratio ($O_{profile}/O_{reference}$), O_z is the pressure weighted ozone amount ratio above

$$O_z(l) = \sum_{i=2}^l P(i).(P(i) - P(i-1)).O(i-1) \quad \text{--- (7)}$$

and TO_z is pressure and ozone weighted temperature ratio above

$$TO_z(l) = \sum_{i=2}^l P(i).(P(i) - P(i-1)).T_r(i-1).O(i-1) \quad \text{--- (8)}$$

Finally the layer transmittance is given by,

$$\tau_{eff} = \tau_{fixed} * \tau_{water} * \tau_{ozone} \quad \text{----- (9)}$$

16.4.2.2 Cloud detection:

Since atmospheric profiles can be retrieved only over cloud free observations, it is essential to detect the cloudy pixels. For each sounder pixel, a cloud detection algorithm is to be applied to get the clear/cloudy index. Various cloud-detection schemes are developed and implemented for infrared sounders (Smith et al. 1979; McMillen and Dean 1982; Hayden 1988). Each pixel undergoes several tests for clear/cloudy identifications:

- During daytime if visible channel#19 count is greater than a threshold, then the pixel is considered cloudy.
- If longwave window channel (channel#8, 11.0μm) brightness temperature is too cold (< 250) then the pixel is classified cloudy.
- If the longwave window brightness temperature is 4 K cooler than that of the warmest pixel from 8 adjacent pixels, then this pixel is classified as cloudy.
- Different window channels (thermal IR channels 8 and mid IR window channels 17, 18) have different transparency. After atmospheric correction to each channel, few checks are applied to classify the pixel as clear/cloudy. During daytime very high difference in channel 8 and 18 brightness temperature indicates presence of clouds. Thresholds for differences in different channels brightness temperature are to be determined by RT simulations.

- Sounder channel brightness temperatures are simulated for each pixel using numerical model forecast profiles. If difference between simulated and observed sounder brightness temperature for cloud sensitive channels (3, 4, 5, 8, 13, 14, 15) is large (threshold decided by the forward model error and forecast error), then this pixel is classified as cloudy.

If there are at least 9 clear pixels in the field-of-regard (FOR) comprised of 5 x 5 pixels (or 4 clear pixels in the FOR comprised of 3 x 3 pixels), then the average of all pixels brightness temperatures for this FOR is used for clear-sky retrieval. This averaging reduces the random noise of measurements over individual pixels.

16.4.2.3 Regression Retrieval:

A computationally efficient method for determining temperature and moisture profiles from satellite sounding measurements uses previously determined statistical relationships between observed (or modeled) radiances and the corresponding atmospheric profiles. This method is often used to generate a first-guess for a physical retrieval algorithm, as is done in the International TOVS Processing Package (ITPP, Smith et al., 1993) and International ATOVS Processing Package (IAPP, Li et al, 2000). The statistical regression algorithm for atmospheric temperature is described in detail in Smith et. al. (1970).

Regression coefficients are required to correlate observed radiances with vertical profile vectors. This derivation of regression coefficients in turn requires generation of training dataset from radiosonde profiles of temperature, humidity, ozone profiles, surface pressure representing the entire variations. Training dataset generated by CIMSS/SSEC, University of Wisconsin is used, which contains more than 12000 profiles. To include more local data into the training dataset and to create a testing dataset, radiosonde data over INSAT-3D viewing region is collocated and quality checked. These are total ~40,000 profiles spanning over 2 years, twice daily observations. Surface emissivities at each sounder channel wavelength for all profiles are assigned from the global emissivity dataset generated by Seeman et al. (2006) at CIMSS. Sounder radiances/brightness temperature will be simulated using fast radiative transfer model (PLOD) and suitable instrument noise will be added to the simulated radiances. Regression coefficients between atmospheric profile vector, X (T -, q -, O_3 -profiles, T_s), with Sounder observations, Y (brightness temperatures) are computed at different zenith angles from simulated training dataset using:

$$RC = dX \cdot dY^T \cdot (dY \cdot dY^T)^{-1} \quad \text{----- (10)}$$

Where, $dX = X - X_{\text{mean}}$, and $dY = Y - Y_{\text{mean}}$

These regression coefficients can be used to retrieve the atmospheric profiles, X , using the following relation:

$$X = X_{\text{mean}} + RC \cdot (dY_{\text{obs}})^T \quad \text{----- (11)}$$

Emissivity and surface pressure are also used as predictors along with the brightness temperature observations to improve the retrieval accuracy. Quadratic term of all brightness temperatures is used as predictors to account for the moisture non-linearity in the sounder observations. **Separate regression coefficients are generated for land and**

sea for day and night conditions. Regression coefficients are generated for different local zenith angles from nadir to 62.5°.

If any one or more channels in sounder become unusable, then regression coefficients will be recomputed from remaining well-behaved channels and suitable modification will be done in regression retrieval routine. In absence of regression retrieval the first guess will be taken from the model forecast.

Another way to generate profile vectors through regression is by using the matchup file that contains the time and space collocated satellite radiance measurements and radiosonde profiles used for generation of the regression coefficients. This may be attempted after the launch of satellite and when enough collocated data points have been generated to represent the profiles variability. The advantage of the regression retrieval using the theoretically computed regression coefficients over real observations is that it avoids errors due to space and time differences between satellite observation and radiosonde profile observation. Observed matchup data would be very useful for removing the bias error caused by the forward model calculations.

16.4.2.4 Non-Linear Physical Retrieval

Though statistical regression algorithm has the advantage of being computationally efficient, numerically stable, and simple, it does not account for the physical properties of the radiative transfer equation (RTE). Therefore, after computing atmospheric profiles from the regression technique and creating a hybrid first-guess combining with model forecast, a non-linear iterative physical algorithm (Li et al., 2000, Ma et al. 1999, Seeman et al. 2003) is applied to the RTE to improve the solution.

For non-scattering atmosphere in local thermodynamic equilibrium, the radiative transfer equation may be written as: Following derivation by Li et al (1994) the RTE may be

$$I_\lambda(p=0) = \varepsilon_\lambda \cdot B_\lambda(T_s) \cdot \tau_\lambda(p_s \rightarrow 0) + \int_{p_s}^0 B_\lambda[T(p)] \cdot \frac{\partial \tau_\lambda(p \rightarrow 0)}{\partial p} \cdot dp \quad \text{--- (12)}$$

written as linear perturbation form:

$$\delta T_b = K_{ts} \cdot \delta T_s + \sum_{i=1}^{ls} K_t \cdot \delta T(i) + \sum_{i=1}^{ls} K_q \cdot \delta \ln(q(i)) + \sum_{i=1}^{ls} K_o \cdot \delta T(i) \quad \text{--- (13)}$$

or simply,

$$\delta Y = K \cdot \delta X \quad \text{----- (14)}$$

Where, perturbation- δ is with respect to an a priori estimate or mean-conditions. T_b is Sounder channel brightness temperature, and K_{ts} , K_t , K_q and K_o are weighting functions (also known as Jacobian) of surface skin temperature, atmospheric temperature profile, humidity profile and ozone profile respectively. Analytical forms of these weighting functions are derived in Li et al (2000) have the following form:

$$\begin{aligned}
 K_{T_s} &= \beta_s \tau_s \varepsilon, \\
 K_T(p) &= -\beta \frac{\partial \tau}{\partial p} + \beta(1 - \varepsilon) \frac{\partial \tau^*}{\partial p}, \\
 K_q(p) &= \left[(T_s - T_a) \varepsilon \tau_s \beta_s - 2(1 - \varepsilon) \int_0^{p_s} \beta \tau^* \frac{\partial T}{\partial p} dp \right] \frac{\partial \ln \tau_q}{\partial p} + \left\{ \int_p^{p_s} \beta [\tau + (1 - \varepsilon) \tau^*] \frac{\partial T}{\partial p} dp \right\} \frac{\partial \ln \tau_q}{\partial p}, \\
 K_{o_3}(p) &= \left[(T_s - T_a) \varepsilon \tau_s \beta_s - 2(1 - \varepsilon) \int_0^{p_s} \beta \tau^* \frac{\partial T}{\partial p} dp \right] \frac{\partial \ln \tau_{o_3}}{\partial p} + \left\{ \int_p^{p_s} \beta [\tau + (1 - \varepsilon) \tau^*] \frac{\partial T}{\partial p} dp \right\} \frac{\partial \ln \tau_{o_3}}{\partial p},
 \end{aligned}
 \quad \text{----- (15)}$$

Physical retrieval involves minimization of the following cost function (Rodgers 1976):

$$J(X) = [Y^m - Y(X)]^T E^{-1} [Y^m - Y(X)] + (X - X_0)^T H^T (X - X_0) \quad \text{----- (16)}$$

Minimization uses the following non-linear Newtonian iteration:

$$X_{n+1} = X_n + J'(X_n)^{-1} J'(X_n) \quad \text{----- (17)}$$

This gives the following non-linear iterative form (Eyre 1989):

$$X_{n+1} = X_0 + (K_n^T E^{-1} K_n + H)^{-1} \cdot \{ K_n^T E^{-1} [dY_n^m + K_n (X_n - X_0)] \} \quad \text{----- (18)}$$

Where, X is the atmospheric profile to be retrieved, X_0 is the initial state of the atmospheric profile or the first guess, Y^m is the observed brightness temperature vector, E is the observation error covariance matrix that includes instrument noise and forward model error, H is the a priori matrix that constrains the solution, which can be first guess error covariance matrix or another type of matrix. Usually $H = \gamma I$, where γ is the smoothing factor. Therefore,

$$X_{n+1} = X_0 + (K_n^T E^{-1} K_n + \gamma_n I)^{-1} \cdot \{ K_n^T E^{-1} [dY_n^m + K_n (X_n - X_0)] \} \quad \text{----- (19)}$$

Smoothing factor γ is very important in the solution and very difficult to determine. If γ is too large then the solution is over-constrained and large biases could be created in the retrieval, while if γ is too small, the solution is less constrained, and possibly unstable. The value γ is dependent upon the observations, the observation error, and the first guess of the atmospheric profile, and often chosen empirically (Smith et al. 1985; Hayden 1988). Often it is chosen empirically (Susskind 1984; Smith et al. 1985; Hayden 1988). Li et al. (2000) uses discrepancy principle (Li and Huang 1999) to determine γ and is changed in each iteration according to

$$\gamma_{n+1} = q_n \gamma_n \quad \text{----- (20)}$$

q is a factor for γ increasing or decreasing. q is obtained in each iteration by the following condition:

$$q_0 = 1; \text{ if } \|F(X_n) - Y^m\|^2 < \sigma^2 \text{ then } q_n = 1.5 \quad \text{----- (21a)}$$

$$\text{if } \|F(X_n) - Y^m\|^2 > \sigma^2 \text{ then } q_n = 0.8 \quad \text{----- (21b)}$$

Where, $\sigma^2 = \sum e_k^2$, e_k is the observation error of channel k which includes instrument error and forward model error. The q factor is found from empirical experience to ensure

that the solution is stable from one iteration to the next. This factor would be required to tune-up carefully for the INSAT-3D Sounder channels.

Since atmospheric variables correlate between different levels, only a limited number of variables are needed to explain the vertical structure of atmosphere (Smith and woolf 1976). Thus it is computationally efficient to solve the iterative equation. This reduces the number of unknown expansion coefficients to the same order as the number of measured radiances:

$$\delta X = \sum f_i v_i = V \cdot f, \quad i = 1, M \quad \text{----- (22)}$$

Where, v_i is the i^{th} eigenvector, f_i is the i^{th} expansion coefficient, and M denotes the number of terms. V and f represent the eigenvector matrix and coefficient vector, respectively. These eigenvectors are derived from a statistical covariance matrix of a large profile set of temperature, moisture and ozone.

$$\delta Y = K \cdot \delta X = K \cdot V \cdot f = \tilde{K} \cdot f \quad \text{----- (23)}$$

Corresponding iterative equation becomes,

$$\mathbf{f}_{n+1} = (\tilde{K}_n^T E^{-1} \tilde{K}_n + \gamma_n I)^{-1} \cdot \{\tilde{K}_n^T E^{-1} [dY_n^m + \tilde{K}_n f_n]\} \quad \text{----- (24)}$$

Thus the retrieval problem is reduced to finding a set of coefficients that may be used with eigenvectors to update the meteorological variables. Statistical analysis of the GOES radiance information content (similar to INSAT-3D Sounder) reveals that five temperature and three water vapor eigenvectors explain all the variance in the sounder channels occurring above the instrument noise level (Ma et al 1999). Therefore, the physical retrieval problem has been reduced to one of solving for ten unknowns (five temperature eigenvector coefficients, three water vapor eigenvector coefficients, one ozone eigenvector coefficient, plus surface skin temperature perturbation) from 18 INSAT Sounder observations plus two surface observations: surface air temperature and humidity. In absence of the surface observations only sounder observations will be used for observation vector.

At each iterative step in the physical retrieval procedure, convergence tests are carried out for the quality control of the profile retrievals. Following two convergence tests are carried out at each iteration and if one of the test fails, then the retrieval is rejected.

- (i) The expansion coefficient convergence test defines the coefficient distance, d_{n+1} defined by:

$$d_{n+1} = (\mathbf{f}_{n+1} - \mathbf{f}_n)^T \cdot (\tilde{K}_n^T E^{-1} \tilde{K}_n + \gamma_n I)^{-1} (\mathbf{f}_{n+1} - \mathbf{f}_n) \quad \text{----- (25)}$$

This should approach zero as the solution converges. At each iteration, the norm of the coefficient distance d is calculated and compared with previous iteration. If d_{n+1} is smaller or equal to d_n then iteration continues, else γ_n is increased, and d_{n+1} is recalculated for the n^{th} iteration. This procedure of changing γ continues until the norm of d_{n+1} is less than or equal to the norm of d_n , and the iteration further continues towards convergence until the difference between the norm of d_{n+1} and the norm of d_n is less than an experimental threshold (~ 0.1). If the norm of d_{n+1} less than or equal to the norm of d_n is not met by the third increase in γ_n , the retrieval

process is considered to be non-convergent and physical retrieval is assumed to be failed.

(ii) Second convergence criteria is based on the brightness temperature residual test. The *rms* residual is defined by:

$$(r_{n+1})^2 = \sum [Y_k^m - Y_k(X_{n+1})]^2/nch; \quad \text{----- (26)}$$

Where *k* is channel number, *nch* is total channel used in the iterative procedure. If $r_{n+1} \leq r_n$ the iteration continue until r_{n+1} is acceptably small (less than instrument noise).

Ancillary surface information is used as boundary condition for the profile solutions. The surface air temperature and humidity are treated as additional “channels” to assist the better retrieval of near surface atmospheric parameters. These surface observations may be within 30 minutes in time and 50 km in space of sounding time/location. Following two additional equations are added in Eq.23 if surface ancillary information is available:

$$\delta t(ls) = \sum_{i=1}^{nt} f_i^t v_i^t(ls) \quad \text{----- (27a)}$$

and

$$\delta[\ln\{q(ls)\}] = \sum_{i=1}^{nw} f_i^w v_i^w(ls) \quad \text{----- (27b)}$$

Where, $\delta t(ls)$ and $\delta[\ln\{q(ls)\}]$ are surface perturbations between “truth” and their initial estimation (first guess) at the surface level ‘ls’, and *nt* (=5) and *nw* (=3) are number of temperature and water vapor mixing ratio eigenvectors, respectively. f_i^t and f_i^w are expansion coefficients corresponding to the eigenvectors V_i^t and V_i^w , respectively.

16.5 OUTPUT

Following parameters will be retrieved from INSAT-3D Sounder:

Parameter	Resolution	Expected Accuracy
Temperature profile	50 km x 50 km (5 x 5 Pixels) 40-vertical pressure levels*	1 - 2 °C
Water vapor profile	50 km x 50 km (5 x 5 Pixels) 21-vertical pressure levels upto 100 hPa	~30%
Ozone profile	50 km x 50 km (5 x 5 pixels) 40 vertical pressure levels	-
Total Column Ozone	50 km x 50 km (5 x 5 pixels)	~ 5-10 % Dobson unit
Surface skin temperature	50 km x 50 km (5 x 5 pixels)	~ 0.5 – 1 °C

Above parameters will also be retrieved at 40 km (4 x 4 pixels) and 10 km resolution (each pixel).

Vertical Pressure Levels (40) in hPa :

1000, 950, 920, 850, 750, 700, 670, 620, 570, 500, 475, 430, 400, 350, 300, 250, 200, 150, 135, 115, 100, 85, 70, 60, 50, 30, 25, 20, 15, 10, 7, 5, 4, 3, 2, 1.5, 1, 0.5, 0.2, 0.1

Format of the output and the domain

Direct access binary format with each record giving details of time of observations, location, forecast profiles, regression first guess profiles, final physical retrieval output profiles, surface skin temperature, total column ozone, and other auxiliary information. These retrievals will be made within 60 degrees from the sub-satellite point. The output may be in the following format:

Word No.	Record
(1)	Record number
(2)	Retrieval latitude
(3)	Retrieval longitude
(4)	Surface pressure (hPa)
(5)	Surface elevation (meters)
(6)	Surface air temperature from surface observation (K)
(7)	Surface mixing ratio from surface observation (g/kg)
(8)	Year of retrieval (YYYY)
(9)	Month of retrieval (MM, 01-12)
(10)	Day of retrieval (DD, 01-31)
(11)	Hour of retrieval (ZZ, 0-23)
(12)	Minute of retrieval (MM, 0-59)
(13)	Water/land index (0=water,1=land)
(14)	Land fraction
(15)	First guess flag (0=Regression, 1=NCEP/IMD Forecast, 2=Hybrid)
(16-33)	INSAT-3D Sounder IR band#1-18 raw Tb (K)
(34-51)	INSAT-3D Sounder bias corrected IR band#1-18 Tb (K)
(52)	Local zenith angle (degrees)
(53)	Clear/cloud index 0=clear,1=partially cloudy,2=cloudy)
(54-103)	Regression retrieval temperature profile (K) (top to surface)
(104-124)	Regression retrieval water vapor profile (g/kg) (top to surface)
(125-164)	Regression retrieval Ozone profile (ppmv) (top to surface)
(165-204)	First guess temperature profile (K) (top to surface)
(205-225)	First guess water vapor from regression (g/kg) (top to surface)
(226-265)	Physical retrieval temperature (K) (top to surface)
(266-286)	Physical retrieval water vapor (g/kg) (top to surface)
(287-326)	Physical retrieval ozone profile (ppmv) (top to surface)
(327)	Regression retrieval surface skin temperature (K)
(328)	Physical retrieval surface skin temperature (K)
(329)	Total integrated ozone (Dobson)

16.6 Validation

Extensive validation campaign is required during the first six months of the satellite launch. Radiosonde profiles collocated with satellite observations will be generated over clear-sky conditions for different regions representing entire variability in atmospheric profiles. These collocated observations will also be used to correct the biases in the forward model, and then incorporated in the regression and physical retrieval routines for accurate retrievals and convergence.

16.6.1 Radiance bias removal

Atmospheric profile retrieval is based on modifying the surface temperature and atmospheric temperature/moisture profiles in a manner such that brightness temperatures calculated agree with those observed from the satellite, within some uncertainty estimate, for the sounding spectral bands.

For INSAT-3D Sounder we begin with a first guess profile, which is a weighted linear combination of profiles obtained from regression retrieval and NWP model forecast, interpolated in time and space to the location of the satellite measurement. The difference between the observation and the "forward calculation" from the first-guess profile represents the information available in the observation.

However, in practice there are generally bias errors associated with the comparison of observation and the forward calculation. These may be due to calibration error, uncertainties in the filter functions, or imprecision in the transmittance model used in the forward calculation. Consequently, prior to calculating retrieval, bias error for each band is subtracted from the observation. Estimates of the bias error are obtained by examining ensembles of collocated observations and forward calculations where the atmospheric state is well known (i.e. in the vicinity of radiosondes).

16.6.2 Data Required

Parameter	Source
Temperature and humidity profile	Radiosonde observations, IMD
Ozone profile	Ozonesonde observations, IMD
Sounder Channel Observations collocated with radiosonde observations	NOAA, EUMETSAT

Space and time collocated (within 100 km in space and 3 hours in time) profiles of temperature, humidity and ozone may also be obtained from the various other satellite missions, such as Aqua-AIRS/MODIS/AMSU, Metop-IASI, NOAA-ATOVS/AMSU, etc for the purpose of inter-comparison.

16.6.3 Methods of Validation

From the observed collocated profiles of temperature, humidity and ozone for clear sky conditions, brightness temperatures corresponding to Sounder channels will be computed with the help of fast radiative transfer model used in the physical retrieval routine. The computed brightness temperatures are analysed with Sounder-observed brightness temperatures to estimate the bias (slope and intercept of the linear regression equation) for each of the sounder channels. These bias-corrections will be implemented in the regression and physical retrieval routines to remove the bias between sounder observations and fast RT model computations.

For clear sky conditions the observed profiles of temperature, humidity and ozone will be interpolated at the pressure levels of retrieval output (standard 40 pressure levels) and root mean square errors (rmse) from space and time collocated retrieved profiles will be computed at each vertical pressure levels. Separate statistics may be generated for retrievals over land and ocean.

16.7 Technical Issues

Final accuracy of the retrieved profiles will largely depend upon the accuracy of the fast radiative transfer model used in the retrieval procedure. Therefore, fast radiative transfer model needs to be properly validated and the forward model errors should be within instrument noise level.

Ancillary data improves the quality of sounding retrieval near surface. However, such observations are very few over Indian region (INSAT-3D viewing region), therefore, the network of the automatic weather stations (AWS) needs to be strengthened.

IMD has a network of radiosonde observations over India; however, for INSAT-3D validation and bias removal procedure highly accurate profiles are required. Therefore, for a limited period of time (6 months after launch), high quality radiosonde (Vaisala) observations should be available over land as well as ocean (special ship cruises) under clear sky conditions.

Currently, ozone information is available only from single channel in Sounder, therefore, retrieval of ozone profile may not be very accurate and column integrated ozone will be more reliable product.

16.8 Future Scope

With the advancement in the spectroscopic measurements of atmospheric gases it is possible to make improvement in the radiative transfer model. Improved fast radiative transfer models may be coupled with the physical retrieval routine in future, as and when available. Improvements will also be attempted by incorporating improved training dataset in regression retrieval.

Another area for future development is improvement of cloud detection algorithm. This may include synergy of high-resolution Imager data with Sounder observations to detect sub-pixel level cloud contamination.

Initially, the retrieval will be attempted only over cloud-free FOVs. In future, an algorithm will be developed and implemented with retrieval routine to compute the cloud-cleared radiances over partially cloudy pixels.

Retrieval of profiles in overcast conditions (valid above cloud top) will also be attempted in near future.

This algorithm will also be useful for future hyper-spectral missions with suitable modifications.

16.9 References

1. Ackerman, S. A., K. I. Strabala, W. P. Menzel, R. A. Frey, C. C. Moeller, and L. E. Gumley, 1998: Discriminating clear sky from clouds with MODIS. *J. Geophys. Res.*, 103, D24, 32141-32157.
2. Alishouse, J.C., S. Snyder, J. Vongsathorn, and R.R. Ferraro, 1990: Determination of oceanic total precipitable water from the SSM/I. *IEEE Trans. Geo. Rem. Sens.*, 28, 811-816.

3. Bowman, K.P. and A.J. Krueger, "A global climatology of total ozone from the Nimbus-7 Total Ozone Mapping Spectrometer", *J. Geophys. Res.*, 90, 7967-7976, 1985.
4. Eyre, J. R. (1989): Inversion of cloudy satellite sounding radiances by non-linear optimal estimation. I : Theory and simulations for TOVS, *Quart. J. Roy. Meteor. Soc.*, 115, 1001-1026.
5. Eyre, J. R., and H. M. Woolf, 1988: Transmittance of atmospheric gases in the microwave region: a fast model. *Appl. Opt.*, 25, 3244-3249.
6. Eyre, J. R., and H. M. Woolf, 1992: A bias correction scheme for simulated TOVS brightness temperatures. ECMWF Technical Memorandum 186. 28 pp.
7. Ferraro, R.R., F. Weng, N.C. Grody, and A. Basist, 1996: An eight year (1987 - 94) climatology of rainfall, clouds, water vapor, snow cover, and sea-ice derived from SSM/I measurements. *Bull. of Amer. Meteor. Soc.*, 77, 891 - 905.
8. Fleming, H. E. and W. L. Smith, 1971: Inversion techniques for remote sensing of atmospheric temperature profiles. Reprint from Fifth Symposium on Temperature. Instrument Society of America, 400 Stanwix Street, Pittsburgh, Pennsylvania, 2239-2250.
9. Fleming, H. E. and W. L. Smith, 1971: Inversion techniques for remote sensing of atmospheric temperature profiles. Reprint from Fifth Symposium on Temperature. Instrument Society of America, 400 Stanwix Street, Pittsburgh, Pennsylvania, 2239-2250.
10. Fritz, S., D. Q. Wark, H. E. Fleming, W. L. Smith, H. Jacobowitz, D. T. Hilleary, and J. C. Alishouse, 1972: Temperature sounding from satellites. NOAA Technical Report NESS 59.
11. Fritz, S., D. Q. Wark, H. E. Fleming, W. L. Smith, H. Jacobowitz, D. T. Hilleary, and J. C. Alishouse, 1972: Temperature sounding from satellites. NOAA Technical Report NESS 59. U.S. Department of Commerce, National Oceanic and Atmospheric Administration, National Environmental Satellite Service, Washington, D.C., 49 pp.
12. Hannon, S., L. L. Strow, and W. W. McMillan, 1996: Atmospheric Infrared Fast Transmittance Models: A Comparison of Two Approaches. Proceeding of SPIE conference 2830, Optical Spectroscopic Techniques and Instrumentation for Atmospheric and Space Research II.
13. Hannon, S., L. L. Strow, and W. W. McMillan, 1996: Atmospheric Infrared Fast Transmittance Models: A Comparison of Two Approaches. Proceeding of SPIE conference 2830, Optical Spectroscopic Techniques and Instrumentation for Atmospheric and Space Research II.
14. Harris, B. A., and G. Kelly, 2001: A satellite radiance bias correction scheme for radiance assimilation. *Quart. J. Roy. Meteor. Soc.*, 127, 1453-1468.
15. Hayden, C.M., 1988: GOES-VAS simultaneous temperature-moisture retrieval algorithm,. *J. Appl. Meteor.*, 27, 705-733.
16. Hayden, C.M., 1995: Initial evaluation of the GOES-8 sounder. Proceedings of the 9th Conference on Meteorological Observations and Instrumentation, *Amer. Meteor. Soc.*, 385-390.

17. Hayden, C.M., and T.J. Schmit, 1994: GOES-I temperature and moisture retrievals and associated gradient wind estimates. Proceedings of the 7th Conference on satellite Meteorology and Oceanography, Amer. Meteor. Soc., 477-480.
18. Houghton, J. T., F. W. Taylor, and C. D. Rodgers, 1984: Remote Sounding of Atmospheres. Cambridge University Press, Cambridge UK, 343 pp.
19. Kaplan, L. D., 1959: Inference of atmospheric structure from remote radiation measurements, Journal of the Optical Society of America, 49, 1004.
20. King, J. I. F., 1956: The radiative heat transfer of planet earth. Scientific Use of Earth Satellites, University of Michigan Press, Ann Arbor, Michigan, 133-136.
21. Li, J., and H.-L. Huang, 1999: Retrieval of atmospheric profiles from satellite sounder measurements by use of the discrepancy principle, Appl. Optics, Vol. 38, No. 6, 916-923.
22. Li, J., C. C. Schmidt, J. P. Nelson III, T. J. Schmit, and W. P. Menzel, 2001: Estimation of total atmospheric ozone from GOES sounder radiances with high temporal resolution, Journal of Atmospheric and Oceanic Technology, 18, 157-168.
23. Li, J., J.P. Nelson III, T. Schmit, W.P. Menzel, C.C. Schmidt, and H.-L. Huang, 1998: Retrieval of total atmospheric ozone from GOES sounder radiance measurements with high spatial and temporal resolution. Preprints, 1st Intl. Asia-Pacific Symposium on Remote Sensing of the Atmosphere, Environment, and Space, Beijing, China, Intl. Soc. Opt. Engineering.
24. Li, J., W. W. Wolf, W.P. Menzel, W Zhang, H.L. Huang and T.H. Achtor, 2000: Global sounding of the atmosphere from ATOVS measurements: The algorithm and validation, J. Appl. Meteor., 39, 1248-1268.
25. Ma, X.L., T. Schmit and W. Smith, 1999: A non-linear physical retrieval algorithm – Its application to the GOES-8/9 sounder, J. Appl. Meteor, 38, 501-503.
26. McMillen, L.M. and C. Dean, 1982, Evaluation of a new operational technique for producing clear radiances, J. Appl. Meteor., 21, 1005-1014.
27. Menzel, W. P., and J. F. W. Purdom, 1994: Introducing GOES-I: The first of a new generation of geostationary operational environmental satellites, Bull. Amer. Meteor. Soc., 75, 757-781.
28. Nelson III, J.P., J. Li, C.C. Schmidt, T. Schmit, and W.P. Menzel, 1999: Retrieval of total atmospheric ozone from GOES. Preprints, International Symposium on Optical Science Engineering and Instrumentation, Denver, CO, SPIE.
29. Rodgers, C. D., 1976: Retrieval of atmospheric temperature and composition from remote measurements of thermal radiation. Rev. Geophys. Space Phys., 14, 609-624.
30. Seaman, S.W., E. Borbas, B. Knuteson, E Weisz, G Stephenson, H-L Huang, and J Li (2006): A global infrared surface emissivity database for clear sky atmospheric retrievals, Submitted to J. Appl. Meteor.

31. Seeman, S.W., J. Li, W.P. Menzel, and L.E. Gumley, 2003: Operational Retrieval of Atmospheric Temperature, Moisture, and Ozone from MODIS Infrared Radiances, *J. Appl. Meteor.*, 42, 1072-1091.
32. Smith, W. L., H. M. Woolf, C. M. Hayden, and A. J. Schreiner, 1985: The simultaneous export retrieval package, *Tech. Proc. Second Int. TOVS Study Conf.*, Igls, Austria, CIMSS, 224-253.
33. Smith, W. L., H. M. Woolf, S. J. Nieman, and T. H. Achtor, 1993: ITPP-5 - The use of AVHRR and TIGR in TOVS Data Processing. Technical Proceedings of the Seventh International TOVS Study Conference held in Igls, Austria 10 to 16 February 1993, J. R. Eyre Ed., 443-453.
34. Smith, W. L., H.M. Woolf, and W. J. Jacob, 1970: A regression method for obtaining real-time temperature and geopotential height profiles from satellite spectrometer measurements and its application to Nimbus 3 "SIRS" observations. *Mon. Wea. Rev.*, 8, 582-603.
35. Smith, W. L., V. E. Suomi, W. P. Menzel, H. M. Woolf, L. A. Sromovsky, H. E. Revercomb, C. M. Hayden, D. N. Erickson, and F. R. Mosher, 1981: First sounding results from VAS-D. *Bull. Amer. Meteor. Soc.*, 62, 232-236.
36. Smith, W.L., 1968: An improved method for calculating tropospheric temperature and moisture from satellite radiance measurements, *Mon. Wea. Rev.*, 96, 387-396.
37. Smith, W.L., and H.M Woolf, 1976: The use of eigenvectors of statistical covariance matrices for interpreting satellite sounding radiometer observations, *J. Atmos. Sci.*, 33, 1127-1140.
38. Smith, W.L., H.M. Woolf, C.M. Hayden, D.Q. Wark, and L. M. McMillin, 1979: The TIROS-N operational vertical sounder. *Bull. Amer. Meteor. Soc.*, 60, 1177-1187.
39. Susskind, J., J. Rosenfield, D. Reuter, and M. T. Chahine, 1984: Remote sensing of weather and climate parameters from HIRS2/MSU on TIROS-N, *J. Geophys. Res.*, 89, 4677-4697.
40. Twomey, S., 1977: An introduction to the mathematics of inversion in remote sensing and indirect measurements. Elsevier, New York.
41. U.S. Department of Commerce, National Oceanic and Atmospheric Administration, National Environmental Satellite Service, Washington, D.C., 49 pp.
42. Wark, D. Q., 1961: On indirect temperature soundings of the stratosphere from satellites. *J. Geophys. Res.*, 66, 77.
43. Wark, D. Q., D. T. Hilleary, S. P. Anderson, and J. C. Fisher, 1970: Nimbus satellite infrared spectrometer experiments. *IEEE. Trans. Geosci. Electron.*, GE-8, 264-270.

Annexure-1

Instrument Characteristics:

INSAT-3D Sounder has 18 infrared channel and a visible channel to help cloud detection during daytime. Central wavelengths of these channels along with the typical noise sensitivity are summarized in the table-1.

A flat elliptical scan mirror mounted at 45° to the optical axis intercepts the radiation and reflects it on to 310mm reflective telescope. At the telescope, dichroic beam splitters separate the visible spectrum and three IR coarse bands. The three IR bands then pass through the concentric ring of a cold filter wheel maintained at a low temperature (-230°C) to limit the background radiation. Channel filters on the filter wheel provide sequential sampling of defined narrow band spectral channels. There are three concentric rings on the filter wheel, each catering to a coarse band. Each of the rings is further divided in to a number of sectors each housing filter for a channel. Detector arrays for each coarse band consist of four elements arranged in north-south direction. Thus the combined IFOV of the arrays is 280 (E-W) x 1120 (N-S) μR^2 . The IR detectors are mounted inside the radiant cooler and cooled to cryogenic temperature of less than 100K for improving noise performance detectors. The temperature of the detectors is maintained at fixed value using temperature sensors and heaters in a servo-loop.

The scan mirror operates in step and dwell mode to facilitate sequential sounding. The east-west step size of scan mirror will be 280 μR (10km). At each step, the mirror dwells for 0.1 second to allow completion of full spectral coverage through filter wheel drive. After completing acquiring data in all bands, the mirror steps in north south direction by 1120 μR (40 km). The rotation of the filter wheel is synchronized to the mirror stepping so that the mirror remains stationary during the sounding. To optimize efficiency, both forward and reverse scans are used for data collection. In addition to full earth disc coverage, flexible programme modes are provided to cater to different coverage requirements based on dynamics of atmospheric environment. The scan mirror traverses to the space-look position to get cold reference for the IR detectors. The interval between two space-looks is of the order of one minute. The space-look periodicity is decided based on the estimate of the interval required for maintaining stable background and temperature of the IR detector so that the space-look data remains valid during this period. It is proposed to have a provision within the scan mechanism to accept motion compensation signal from AOCS to compensate for the various spacecraft rates, orbit perturbations and effect of the imager mirror slew on the spacecraft. Four detectors per coarse band in north-south direction will generate four soundings per channel for every step and dwell interval of 0.1 second through a complete rotation of the filter-wheel. Thus there are a total of sixteen detectors in the instrument, twelve for IR sounding channels and four for visible channel.

The normal mode of Sounder operation covers 6000km x 6000km field of view and takes approximately 160 minutes. In addition, the instrument is designed with flexible modes of operation for fast and repetitive coverage.

The cold space view is used for signal referencing and as a calibration point for all bands. In-orbit multipoint calibration of the IR channel is carried out through viewing of full

aperture high emissivity internal cavity, whose physical temperature is accurately monitored at multiple locations and transmitted in Sounder data stream.

The detector outputs are individually amplified, integrated in synchronism with the filter wheel movement and digitized to twelve bits by A/D converter. The digitized data along with house keeping and calibration information is formatted, randomized and sent to transmitter as a serial data stream. The data rate is approximately 40 Kbps.

The temperature control of the IR detector mounted on cooled patch as well as that of filter wheel will be achieved through proportional controller.

Table 2: INSAT-3D Sounder Channels Characteristics

Detector	Ch. No.	λ_c (μm)	ν_c (cm^{-1})	$\Delta\lambda(\Delta\nu)$ μm (cm^{-1})	Principal absorbing gas	Purpose
Long wave	1	14.67	682	0.385 (18)	CO_2	Stratosphere temperature
	2	14.31	699	0.305 (15)	CO_2	Tropopause temperature
	3	14.03	713	0.321 (16)	CO_2	Upper-level temperature
	4	13.64	733	0.351 (19)	CO_2	Mid-level temperature
	5	13.33	750	0.352 (20)	CO_2	Low-level temperature
	6	12.59	794	0.541 (34)	water vapor	Total precipitable water
	7	11.98	834	0.768 (53)	water vapor	Surface temp., moisture
Mid wave	8	10.99	910	0.611 (51)	window	Surface temperature
	9	9.69	1032	0.262 (28)	ozone	Total ozone
	10	7.43	1346	0.299 (54)	water vapor	Low-level moisture
	11	7.04	1421	0.426 (86)	water vapor	Mid-level moisture
	12	6.52	1534	0.269 (63)	water vapor	Upper-level moisture
Short wave	13	4.61	2168	0.054 (25)	N_2O	Low-level temperature
	14	4.54	2202	0.053 (26)	N_2O	Mid-level temperature
	15	4.48	2232	0.057 (28)	CO_2	Upper-level temperature
	16	4.15	2408	0.078 (45)	CO_2	Boundary-level temp.
	17	4.01	2496	0.075 (46)	window	Surface temperature
	18	3.79	2642	0.143 (100)	window	Surface temp., moisture

17. Fog

S.No.	Product Name	Spatial Resolution	Temporal Resolution
1	3DIMG_L2C_FOG	4 km approx.	30 minutes

17. FOG

17.1 Algorithm Configuration Information

17.1.1 Algorithm Name

Fog (FOG)

(Ref : IMD RFP Section 11.10)

17.1.2 Algorithm Identifier

3DIMG_L2C_FOG

17.1.3 Algorithm Specification

Version	Date	Prepared by	Description
2.0	July 2014	Sasmita Chaurasia	FOG Baseline Document

17.2 Introduction

17.2.1 Overview and background

Fog is disastrous weather phenomenon especially in terms of traffic safety and air quality. The spatial extend and dynamics cannot be adequately nowcasted using conventional ground measurements (Jacobs et al, 2003). However, the upcoming INSAT-3D data with improved spatial and temporal resolution can be used for near real time detection and mapping of fog.

The detection of fog/low stratus with satellite data has been taken up since many years (Bendix 2002). The general methodology of fog detection involves identification of some threshold radiances or brightness temperature at different wavelengths. Fog is formed when vapor in the lower atmosphere condensed in cold conditions. The fog droplets are much smaller than the cloud droplet. The presence of these droplets affects the atmospheric visibility. The radiation difference between the cloud and fog is due to the spectral response differences of every channel. This provides the basis of fog detection.

17.2.2 Objective

To identify the presence of fog from INSAT-3D data

17.3 Inputs

The following table gives a list of inputs required for algorithm input and calibration

17.3.1 Static Data

Data	Resolution	Unit	Source
Surface elevation above mean sea level	Pixel level	meters	USGS or other gridded data available on internet.

17.3.2 Image and Calibration Inputs

Parameter	Resolution	Quantization	Accuracy	Source
Radiometric and geometric corrected gray count values of VIS channel (6.5)	pixel	10 bit	--	Derived from raw data by DP (data processing)
Radiometric and geometric corrected gray count values of MIR channel (3.9)	pixel	10 bit	--	Derived from raw data by DP (data processing)
Radiometric and geometric corrected gray count values of TIR-I channel (10.5)	pixel	10 bit	-	Derived from raw data by DP
Gray value to brightness temperature (MIR, TIR-1) conversion table	-	-	0.3 K	Derived by DP
Gray value to albedo (VIS) conversion table	-	-	0.3 K	Derived by DP
Geolocation file	Pixel	-	1 pixel	Derived by DP

17.3.3 Other Auxillary data

Parameter	Resolution	Quantization	Accuracy	Source
Solar Zenith Angle	pixel	-	--	Derived by DP
Satellite Zenith Angle	pixel	-	--	Derived by DP
Azimuth Angle	pixel	-	-	Derived by DP
Snow Map	pixel	-	-	Derived under IMDPS

17.4 Algorithm Functional Specifications

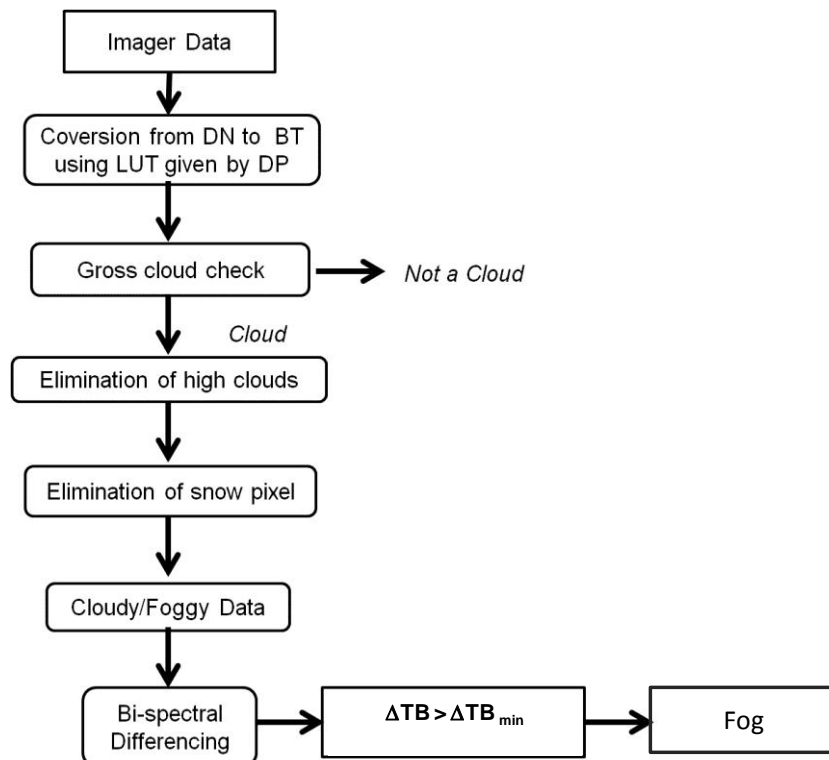
17.4.1 Overview

17.4.1.1 Theoretical Background

Night Time Fog Detection

The difference of brightness temperature corresponding to two spectral channels (3.9 and $10.8\mu\text{m}$) is used for the identification of fog. The theoretical basis for the detection of fog using $3.9\mu\text{m}$ and $\sim 11\mu\text{m}$ channels rely on the particular emissivity properties for fog droplets (Bendix and Bechmann, 1991) in these two channels. The small droplets found in fog are less emissive at $3.9\mu\text{m}$ than at $\sim 11\mu\text{m}$ whereas emissivities are roughly same for larger droplets (Hunt, 1973) in both the channels. The difference between brightness temperatures measured at different wavelength is tested against a threshold value and attributed to the categories of clear/ fog/other clouds etc.. The difference in brightness temperature values below 0.5 K is assumed to be cloud free and above 2.5 K is represented as opaque clouds (Ellord, 1995). However, a threshold of 5.5 K to 7.0 K has been observed for fog developed over the Indo Gangetic plains of India (Chaurasia et al, 2011) ranging from thin to thick fog case using MODIS data. This threshold will change with spatial and spectral resolution of the satellite data used for the detection of fog. Apart from this it also varies from time to time as well as from place to place and types of fog.

Flowchart for nighttime fog detection

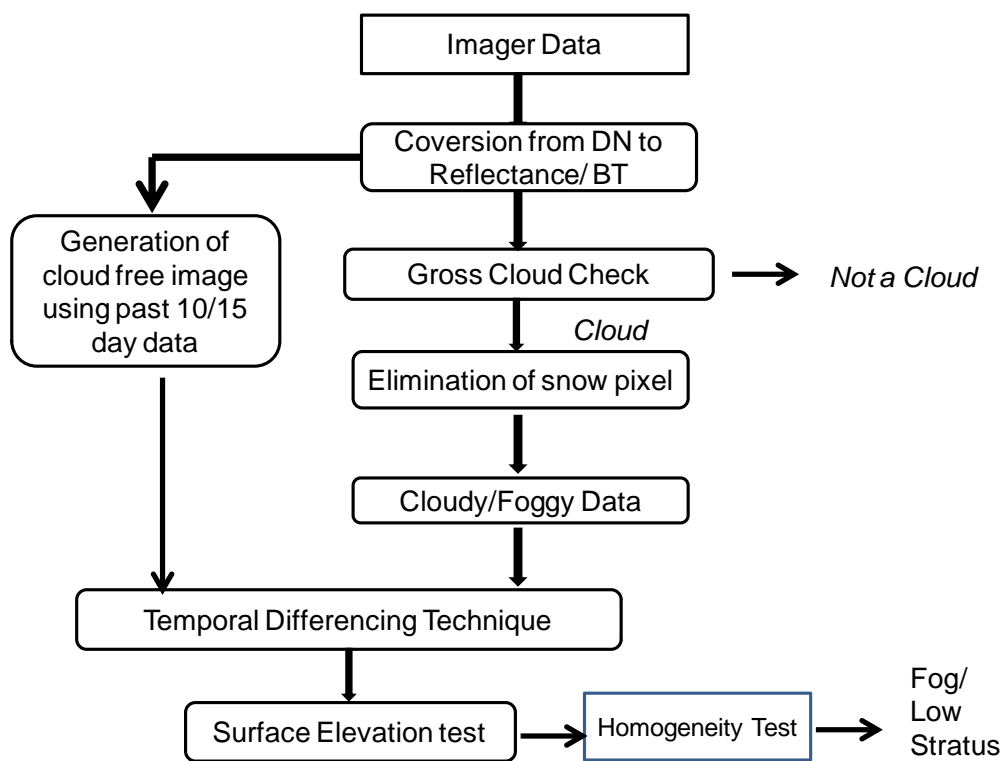


Day Time Fog Detection

The basis of the algorithm is a gross cloud check. This test is based on the assumption that the brightness temperature of high clouds are very low (<270 0K) and the brightness temperature of fog lies between that of land (very high brightness temperature) and high clouds during day time. The high cloud regions are eliminated by using a threshold of brightness temperature of 10.8 μm channel. This threshold is determined dynamically.

Once the region is classified as foggy, the day time detection algorithm is used. The day time algorithm of fog detection is based on the temporal differencing technique (Paul d'Entremont and Gustafson, 2003) which is used operationally to monitor cloud using geostationary data. In this method apart from using thermal channel like TIR1 channel of INSAT-3D for cloud detection, the visible channel (0.55-0.75 μm) is also used. The droplet size of fog being close to the wavelength of visible and infrared radiation, fog has prominent scattering effect. Thus the visible channel plays an important role in detecting day time fog.

17.4.1.2 Flow chart for day time fog detection



17.4.2 Operational Implementation

Night Time Fog Detection

17.4.2.1 Selection of night time data only by using information of solar zenith angle and visible count

17.4.2.2 Conversion of grey count to brightness temperature

- 17.4.2.3** Gross cloud testing using 10.8 μm brightness temperature
- 17.4.2.4** High cloud elimination by using 10.8 μm brightness temperature threshold
- 17.4.2.5** Removal of remaining snow pixel by using 10.8 μm brightness temperature thresholding
- 17.4.2.6** Difference between 10.8 and 3.9 μm channel brightness temperatures.

17.4.2.7 Fog detection

(The minimum value of brightness temperature difference ΔTB_{\min} above which the pixel is flagged to be fog is determined dynamically. It varies for thin, moderate and thick fog).

Day Time Fog Detection (Requires R & D)

- 17.4.2.8** Selection of day time data only by using information of solar zenith angle
- 17.4.2.9** Conversion of grey count of visible to reflectance and TIR channel grey count to brightness temperate
- 17.4.2.10** Gross cloud check (dynamical threshold of 10.8 μm channel brightness temperature).
- 17.4.2.11** Generation of cloud free scene using 15 day data prior to the fog episode for a particular time.
- 17.4.2.12** Use of temporal differencing technique to detect fog
- 17.4.2.13** Elimination of snow pixels and bright land pixel using a threshold for change in reflectance $\Delta\rho$ = (reflectance of sample image – reflectance of clear scene image) for a particular time.
- 17.4.2.14** If the $\Delta\rho$ = (reflectance of sample image – reflectance of clear scene image) for a particular time is greater than a definite threshold, then the pixel is classified as fog.
- 17.4.2.15** Surface homogeneity test is performed. The variation of reflectance is very less over the fog region which is used as a measure to identify fog.

17.5 Outputs

Generation of Fog map

Parameter	Unit	Min	Max	Accuracy	Resolution
FOG (nighttime) and FOG(Day time)	Flag (0 No fog, 1 Fog)	-	-	-	Per pixel Per pixel
	Flag (0 No fog, 1 Fog)	-	-	-	

17.5.1 Format of the output and the domain

Lat, lon, fog (in image format)

Domain: 0 S to 35 N, 60 E to 100 E.

17.6 Validation

17.6.1 Data required

1. Data from different sensors required for validation

Acquisition Time	Sensor	Product	Area
All Day and Night Time during the event	MODIS	Fog Product	Indian region
	MODIS/ INSAT3D	Aerosol Optical Depth	Indian region
	Kalpana CCD data	VHRR/ Kalpana visible data for the day time and FCC of CCD for day time	Indian region

2. Fog observations from ground based network, airport and station data from IMD.

17.6.2 Methods of validation

Validation through cross comparison with other satellite data/products

1. A direct comparison with the fog product of MODIS at different acquisition time over the Indian region.
2. The aerosol optical depth map generated by MODIS and INSAT-3D will be used to validate the presence of highly opaque aerosols as aerosols are also factor influencing fog formation in the Indo-Gangetic plain.
3. The Kalpana visible data and FCC of CCD data at early morning hour can also be used to indicate the presence of fog in the previous night as fog is the deepest before sunrise.

Validation through ground truth

As visibility is one of the important criteria for fog identification the observation from station data (where ever available) can also be used as in-situ observation to validate the fog product. These station data may be available with Airport Meteorological Office (AMO) and India Meteorological Department over different locations.

17.7 Technical issues

Accuracy of the product will depend on the accuracy of the input radiance. Extensive research and development work is required especially for day time fog detection with the help of radiative transfer model simulations. One has to get various fog/low stratus optical properties such as droplet radius etc., perform radiative transfer model simulations at various solar zenith angles, types of atmosphere to arrive at detection algorithms.

17.8 Future Scope

Apart from techniques using visible and thermal channels for the detection of fog, methods to use hyperspectral and multispectral data is required to be developed and implemented.

17.9 References

1. Bendix, J., Reudenbach, CH. & Rollenbeck, R. 2003: The Marburg Satellite Station. *Proceedings 2002 Met. Sat. Users' Conf. Dublin, 2-6 September 2002, EUMETSAT*, 139-146.
2. Ellrod, G. P., 1995: Advances in the detection and analysis of fog at night using GOES multispectral infrared imagery. *Wea. Forecasting*, **10**, 606-619.
3. Hunt GE. 1973. Radiative properties of terrestrial clouds at visible and infra-red thermal window wavelengths. *Quarterly Journal of Royal Meteorological Society* **99**: 346–369.
4. Jacobs, W., V. Nietosvaara, S. C. Michaelides, H. Gmoser (eds.), 2003: COST 722 Phase 1 Report: Very Short Range Forecasting of Fog and Low Clouds: Inventory Phase on Current Knowledge and Requirements by Forecasters and Users. <http://www.lcrs.de>, 184pp.
5. Paul d'Entremont R. and Gustafson, G. G., 2003, Analysis of Geostationary satellite imagery using temporal differencing technique, *Earth Interactions*, **7**, paper no.1, p.1-25.
6. Sasmita Chaurasia, V. sathiyamoorthy, B.P. Shukla, B.Simon, P.C. Joshi and P. K. Pal, 2011, Nighttime fog detection using MODIS data over Northern India, *Meteorological Applications*, DOI: 10.1002/met.248.

18. Land Surface Temperature

S.No.	Product Name	Spatial Resolution	Temporal Resolution
1	3DIMG_L2B_LST	4 km	30 minutes

18. Land Surface Temperature

18.1 Algorithm Configuration Information

18.1.1 Algorithm Name

LST (LST)

18.1.2 Algorithm Identifier

3DIMG_L2B_LST

18.1.3 Algorithm Specification

Version	Date	Prepared by	Description
2.0	July 2014	M. R. Pandya, D. B. Shah and R. P. Singh	LST Baseline Document

18.2 Introduction

18.2.1 Importance of Land surface temperature and its retrieval

Land surface temperature (LST) is one of the key parameters in the land surface processes and climate studies on global and regional scales. It is needed as an input to a variety of climatic, ecological, hydrological and biogeochemical studies. Retrieval of LST from the Earth observation satellite is quite challenging since the land surface is laterally inhomogeneous and is composed of various materials with different geometries. Surface temperatures are derived from satellite based measurements in the thermal infrared (TIR) window channels using either empirical method or physical algorithm.

A number of Earth observation satellites such as EOS-MODIS, ASTER, AATSR, NOAA-AVHRR, Landsat ETM+, GOES-8, GOES-R, MSG-SEVIRI etc have TIR channels to derive LST. Various algorithms and coefficients have been developed for LST retrieval for these systems and reported in the literature over a period of time (Ulivieri *et al.*, 1994, Wan and Dozier, 1996, Sobrino *et al.*, 2000, Sun and Pinker, 2003, Sobrino *et al.*, 2004, Kerr *et al.*, 2004, Sòria and Sobrino, 2007, Sun and Pinker, 2007, Yu *et al.*, 2009).

Indian Earth observation satellites such as INSAT-2E, Kalpana-1, INSAT-3A and INSAT-3D have also TIR channels for surface temperature retrieval purpose. However, little attention has been paid to develop the method for estimating LST from Indian sensors. A Single Channel (SC) algorithm for retrieving LST from the thermal channel (10.5-12.5 μm) of Kalpana-1 (K1) VHRR sensor was developed over India using a radiative transfer model (Pandya *et al.*, 2010, Pandya *et al.*, 2013). In order to exploit the presence of two TIR channels in the INSAT-3D *Imager* sensor for better estimation of LST, a study has been taken up to develop a method to retrieve LST through a split-window (SW) algorithm.

Objective of the present work is to develop an algorithm to retrieve LST using two TIR channels of the *Imager* sensor onboard INSAT-3D satellite using a radiative transfer (RT) model over India. Study also presents the comparison of INSAT-3D LST to the contemporaneous LST products available from the MODIS and K1 satellites.

18.2.2 Imager sensor onboard INSAT-3D

INSAT-3D is the new generation Indian Earth observation satellite launched by ISRO on July 26, 2013. It provides enhanced observations of land, ocean and atmosphere through two payloads namely *Imager* and *Sounder* from the geostationary orbit. The *Imager* payload is designed to sense solar-reflected and radiant energy from the Earth through six channels covering visible (VIS: 0.55-0.75 μm), shortwave infrared (SWIR: 1.55-1.70 μm), middle infrared (MIR: 3.8-4.0 μm), water vapor infrared (WVIR: 6.5-7.1 μm) and thermal infrared (TIR1: 10.3-11.3 μm and TIR2: 11.5-12.5 μm) spectral regions of electromagnetic spectrum having varying spatial resolution ranging from 1 km to 8 km (CDR, 2009). Nominal specifications of spectral and spatial details of the *Imager* payload are provided in table 1.

Table 1: Spectral and spatial specifications of *Imager* payload onboard INSAT-3D satellite (Source: CDR, 2009)

Channel	Range of the Spectral channel	Spatial resolution (at nadir)
VIS	0.55-0.75 μm	1 km
SWIR	1.55-1.70 μm	1 km
MIR	3.80-4.00 μm	4 km
WVIR	6.50-7.10 μm	8 km
TIR1	10.3-11.3 μm	4 km
TIR2	11.5-12.5 μm	4 km

The TIR1 and TIR2 are two thermal channels centered at 10.8 μm and 12.0 μm respectively, which can be used to derive LST through a split-window algorithm. Figure 1 shows the spectral response functions of TIR channels of INSAT-3D *Imager*. The INSAT-3D satellite views the Earth's globe from its location of 84 degree East on the equator. The view zenith angle for INSAT-3D satellite from this particular location was computed by the method developed by Pandya & Dadhwal (1999) and its pattern over India and surroundings is shown in the figure 2.

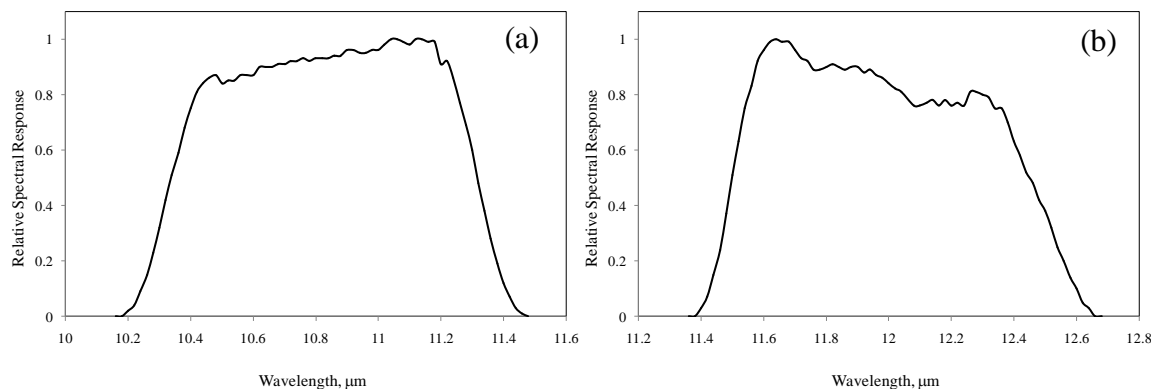


Figure 1. Spectral response functions two thermal infrared bands of INSAT-3D *Imager*
(a) TIR1: 10.3-11.3 μm and (b) TIR2: 11.5-12.5 μm

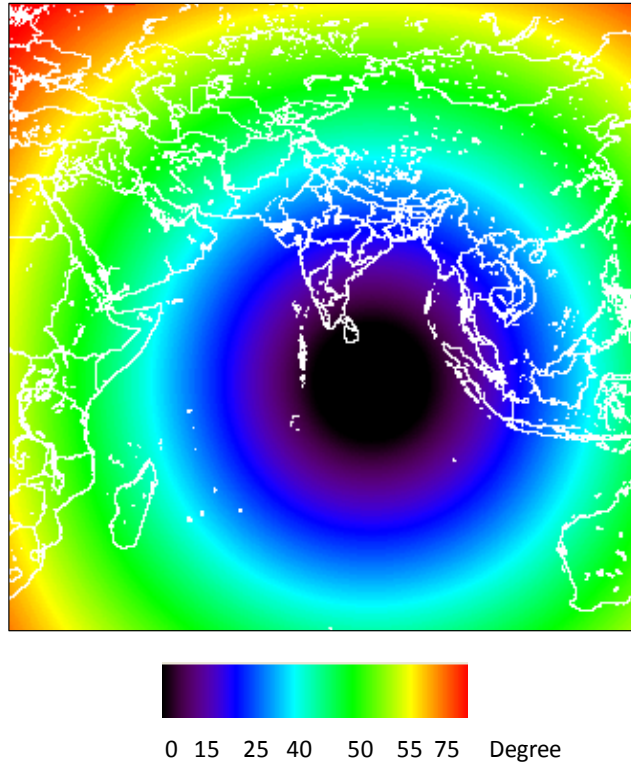


Figure 2. View zenith angle for the INSAT-3D satellite located at 84 degree E

To derive LST from various satellite-based sensors several types of split-window (SW) algorithms have been developed during past three decades; however, SW algorithm for Indian sensor has not been attempted. This document presents a theoretical base study that was carried out to develop a SW algorithm for LST retrieval using TIR observations from the INSAT-3D *Imager*.

18.3 THEORETICAL BACKGROUND

Thermal infrared signal received by satellite sensors is combination of three parameters, namely; (1) surface temperature and surface emissivity, (2) atmospheric emission, absorption and scattering acting upon thermal radiation from the surface, and (3) the solar radiation during daytime. In the absence of atmosphere, estimation of LST of the Earth's surface would be much simpler task. On the other hand, the presence of Earth's atmosphere between the satellite and the surface changes the surface emitted radiances measured by the satellite sensor in several ways, making LST retrieval from satellite based platform a complex task (Dash *et al.* 2002).

The transmission of the surface emitted radiance through the atmosphere to the satellite, and its interaction with the active elements of the atmosphere is expressed as Radiative Transfer Equation (RTE) (Dash *et al.* 2002).

$$B_i(T_i) = \varepsilon_i \cdot B_i(T_s) \cdot \tau_i + (1 - \varepsilon_i) \cdot L_{DW} \cdot \tau_i \quad (1)$$

Where,

B_i = the radiance measured by the satellite based sensor ($\text{W}/\text{m}^2 \cdot \text{sr} \cdot \mu\text{m}$),

T_i = the at-sensor brightness temperature (K)

ε_i = the surface emissivity

$B_i(T_s)$ = Planck radiance at surface temperature T_s

τ_i = atmospheric transmittance

L_i^u = upwelling path radiance

L_{DWR} = downwelling sky radiance at Earth's surface

The first term stands for the surface-emitted radiance after being attenuated by the atmosphere, second term corresponds to the upwelling sky radiance emitted by the atmosphere towards the sensor, and last term represents the downwelling radiation reaching the sensor after being reflected from the Earth's surface. Here all the quantities refer to a spectral integration over the bandwidth of channel i and depend on the view zenith angle.

The Planck radiance $B_i(T_s)$ is expressed as,

$$B_i(T_s) = \frac{c_1}{\lambda_i^5 \left(e^{\frac{c_2}{\lambda_i T_s}} - 1 \right)} \quad (2)$$

with c_1 and c_2 being the Planck's radiation constants, with values of $1.19104 \cdot 10^8 \text{ W} \cdot \mu\text{m}^4 \cdot \text{m}^{-2} \cdot \text{sr}^{-1}$ and $14387.7 \mu\text{m} \cdot \text{K}$, respectively.

Inverting Eq. (1) we get,

$$T_s = B_i^{-1} \left(\frac{B_i(T_i) - L_i^u - (1 - \varepsilon_i) \cdot L_{DWR} \cdot \tau_i}{\varepsilon_i \cdot \tau_i} \right) \quad (3)$$

In this problem, the surface temperature is basically coupled with two factors: the surface emissivity and the atmospheric absorptions. Developing an LST algorithm means to find a solution of decoupling the emissivity and the atmospheric absorption effects from the satellite measured radiance. The surface temperature T_s can be obtained from Eq. 1 and 2 by correcting the atmospheric and emissivity effects and then by calculating T_s by inversion of the Planck's law. However, atmospheric correction of TIR radiances is the most difficult part (Liang, 2004). The use of SW algorithm avoids the atmospheric correction issue. This method uses two thermal bands typically located in the atmospheric window between $10.5-12.5 \mu\text{m}$. The basis of the technique is that the radiance attenuation for atmospheric absorption is proportional to the radiance difference of simultaneous measurements at two different wavelengths, each subject to different amounts of atmospheric absorption. Actually SW algorithm provides atmospheric correction of a brightness temperature measurement in one spectral band (typically centered around $11 \mu\text{m}$) given a brightness temperature measurement in a second "spectrally-close" band (typically centered around $12 \mu\text{m}$) (figure 3). They exploit the differential absorption tendency of two neighbouring spectral bands due to various gases. To estimate LST from satellite observations, most SW algorithms are derived from a first-order Taylor-series linearization of the RT equation in long-wave infrared spectral bands (Yu, 2009).

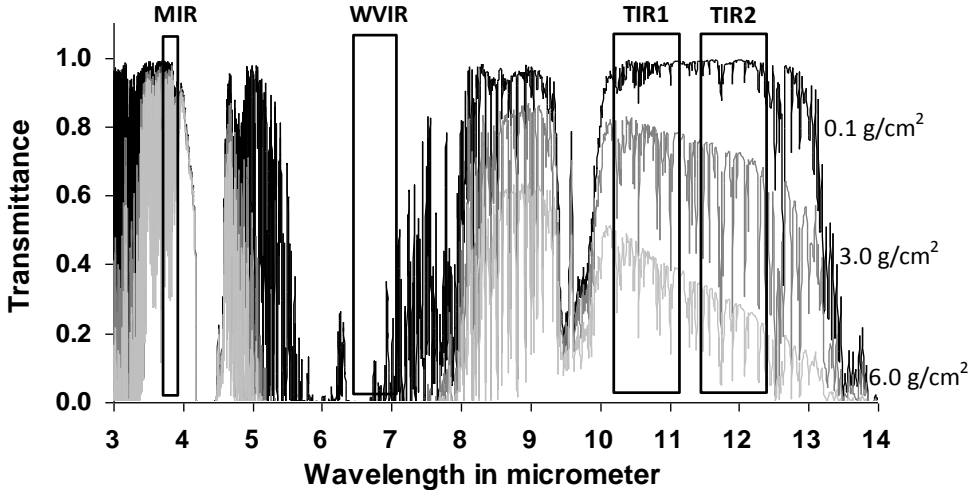


Figure 3: Atmospheric transmission computed for different atmospheric water vapour content using the MODTRAN model for nadir observations with surface temperature of 305K. Positions of four channels of the *Imager* payload are also shown in the graph (source: Pandya *et al.*, 2011a)

The SW technique is particularly favoured for its simplicity and robustness. In most cases, the SW LST algorithms simultaneously convert brightness temperature to skin temperature, given the estimates of the surface spectral emissivity. A review of the SW technique and published SW algorithms can be found in Li *et al.*, (2013). The SW algorithm selected and proposed for this study is given by (Li *et al.*, 2013; Sobrino *et al.*, 1994) equation (4) and it is modified in the present study for varying view zenith angles for the *Imager* sensor (section 3.1),

$$T_s = a_1 + a_2 \cdot T_i + a_3 \cdot (T_i - T_j) + a_4 \cdot (T_i - T_j)^2 + a_5 \cdot (1 - \varepsilon) + a_6 \cdot d\varepsilon \quad (4)$$

Where T_i and T_j are the at-sensor brightness temperatures at the SW bands i and j (in Kelvin), ε is the mean emissivity, $\varepsilon=0.5(\varepsilon_i+\varepsilon_j)$, $\Delta\varepsilon$ is the emissivity difference, $\Delta\varepsilon=(\varepsilon_i-\varepsilon_j)$ and a_1 to a_6 are the SW coefficients to be determined from simulation data.

18.4 Method and Data Used in the Study

18.4.1 Methodology

A flowchart depicting the steps followed in the proposed algorithm is shown in the figure 4. The split-window algorithm requires a forward simulation study for generating split-window coefficients through the RT model using various inputs (details discussed in the next sections). With the use of these split-window coefficients and emissivity information, the radiance observed at the top-of-atmosphere by the INSAT-3D *Imager* sensor is converted into the LST. The LST images generated from the INSAT-3D *Imager* sensor can then be compared with (a) K1-LST products available on MOSDAC archival system and (b) MODIS LST products available through the NASA's archival system. The individual components of this flowchart have been discussed in details in the following sub-sections.

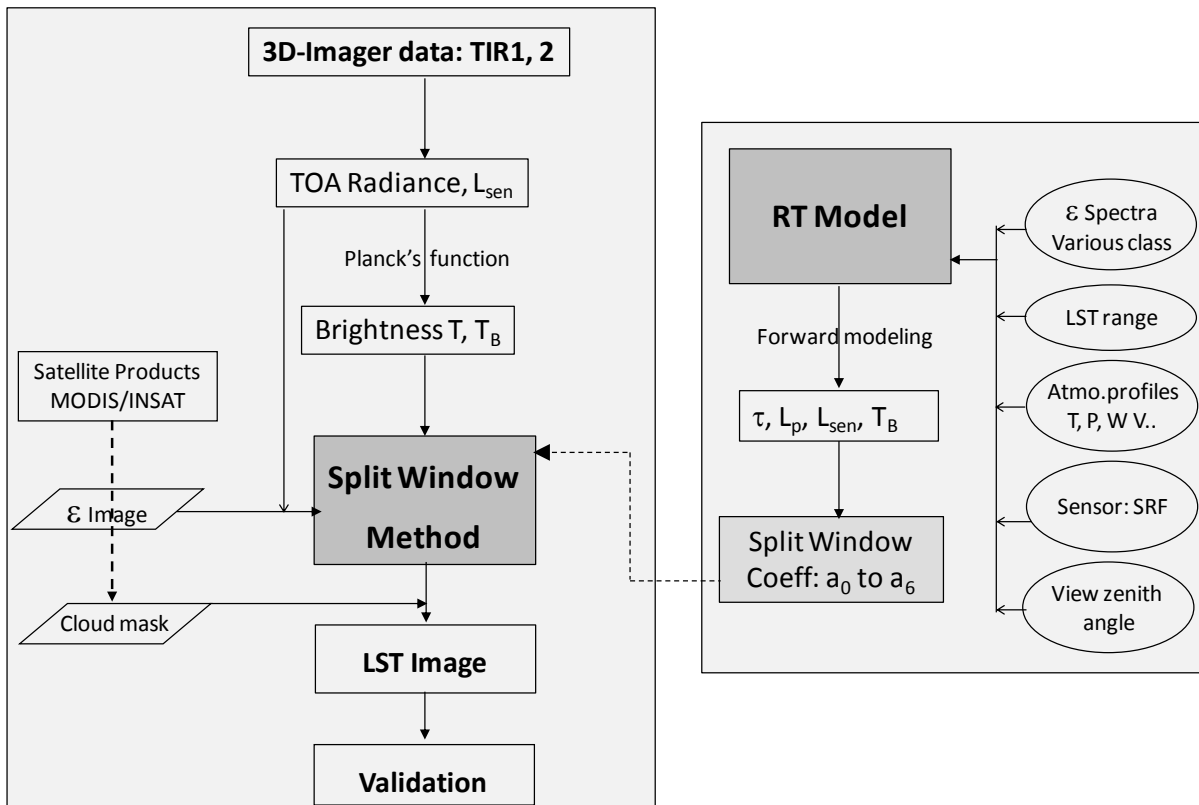


Figure 4: Flowchart showing steps to be followed for retrieval of LST from *Imager* data

18.4.1.1 Split-window method

As discussed in the above section, the basis of SW technique is that the atmospheric attenuation suffered by the surface emitted radiance is proportional to the difference between at-sensor radiances measured simultaneously in two different thermal channels.

Many types of the SW algorithms have been developed for the LST retrieval. In an earlier analysis reported in a paper (Pandya *et al.*, 2011b), various SW algorithms were evaluated for LST retrieval from the INSAT-3D *Imager* sensor. Ten different published SW algorithms (or their slight variants) from the literature were evaluated and compared in the study and the following suitable form of algorithm (Eq. 3) was selected for the *Imager* sensor.

$$T_s = a_1 + a_2 T_i + a_3 (T_i - T_j) + a_4 (T_i - T_j)^2 + a_5 (1 - \varepsilon) + a_6 d\varepsilon$$

This SW expression was then modified from the original formulation for having improved results for correcting path length variation due to high view zenith angle imaging in the case of *Imager* sensor from the geostationary orbit as described in the following sub-section.

18.4.1.2 Modification of split-window method: Correcting for Path Angle Variability

As shown in figure 2, the *Imager* sensor has wide field of view. McClain *et al.* (1985) first pointed out that, at high viewing angles, atmospheric absorption is amplified.

Geometric analysis shows that the atmospheric path length at the sensor's edge-of-scan (for view zenith angle ~65 degree) is at least 2.5 times higher than at nadir. Pandya *et al.* (2011a) have also shown that at-sensor radiance value observed by the *Imager* sensor reduces with increasing view zenith angle by an amount of 7 to 8 percent for 300 K target. This has a significant effect on the satellite measured brightness temperature. For a target on the ground having 300 K temperature and 0.98 emissivity with average atmospheric water vapor of 1.5 g/cm², the at-sensor brightness temperature varies between 297.2 K to 295.5 K for atmospheric path length changing from 1 to 2 corresponding to view zenith angle varying between 0 to 60 degree (figure 5). If a SW algorithm's coefficients are determined for the nadir case, then use of same coefficients for all the view angles can significantly degrade the algorithm accuracy at large view angles. The standard MODIS algorithm addressed this problem (Wan & Dozier, 1996). Here, in the case of *Imager* sensor the view zenith angle can vary nominally up to 50 degree, so we intend to generate a unique set of split-window coefficients for each view angle sub-ranges (e.g., 0°–20°, 20°–30°, 30°–35°, 35°–40°, 40°–45°, 45°–50° and 50°–55°).

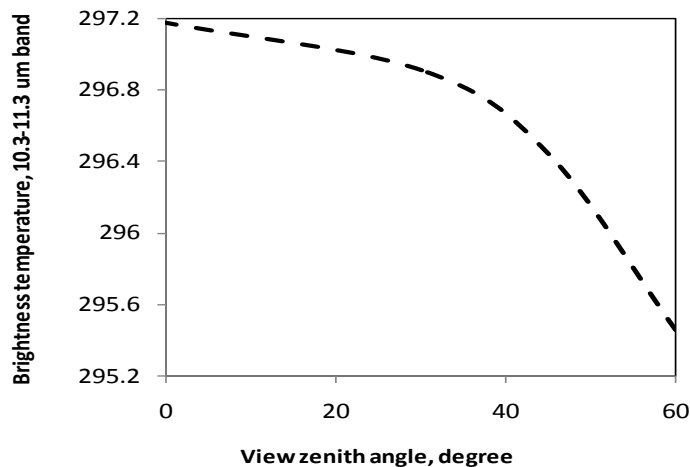


Figure 5. Effect of view zenith angle on the temperature observed at satellite level

18.4.2 Model used

The satellite level signal in the TIR channels of *Imager* sensor was simulated using a RT model – MODTRAN (MODerate spectral resolution atmospheric TRANSmittance) version 4.0. The MODTRAN (Berk *et al.* 1999) was selected for the study because this model has been long publicly available and its heritage traces back to LOWTRAN (Kneizys *et al.* 1988). It is widely used and validated model for variety of remote sensing analysis and applications across the globe. It uses a more accurate and higher resolution molecular band model based on the Atlas of High Resolution Molecular Spectroscopic data (HITRAN) molecular database. With its spectral resolution capability of 2 cm⁻¹, this narrowband model can perform calculations very accurately with less input requirements as discussed by Lacis and Oinas (1991) and Liang (2004). They have shown that using two narrow spectral ranges of H₂O and CO₂ (for a resolution of 10 cm⁻¹, and for total gas pressures above 0.1 atm), the correlation accuracy can be improved to better than 1%. With its spectral resolution capability of cm⁻¹ in frequency it simulates at-sensor radiance and transmittance as a function of: atmospheric inputs (model atmosphere, atmospheric

column parameters, aerosol model etc), surface inputs (emissivity, temperature), viewing geometry and information on spectral channels.

18.4.3 Data used in the study

Various data sets have been used in the present study for generation and validation of LST from the INSAT-3D *Imager* data. This includes the raw *Imager* data sets (at-sensor brightness temperature, latitude-longitude layers), MODIS emissivity products in two spectral channels, K1-LST products and MODIS-LST products. The K1-LST and MODIS-LST products were used for comparing the LST images being generated from the INSAT-3D *Imager* sensor using the proposed method. Table 2 summarizes the data sets used in the present study with their details.

Table 2: Summary of data set used in the study for retrieving LST and its validation

Satellite/ Sensor	Data/ Parameter	Date/ Time
INSAT-3D/ <i>Imager</i>	Brightness Temperature in TIR1 and TIR2 bands, Latitude/Longitude data	40 Images of 29 th Nov. 2013. Full day data, at every half-an hour interval (except 00:00, 17:00 to 20:00 GMT).
Kalpana-1 VHRR	LST product	48 Images of 29 th Nov. 2013. Full day data, at every half-an hour interval.
MODIS/ Aqua, Terra	LST product	Three acquisitions at 05:35, 08:45, 20:55 GMT
MODIS	Emissivity product for two spectral bands located at 11 μm and 12 μm	Two Emissivity mosaics of Indian landmass and surroundings from approximately 20 MODIS tiles from two spectral bands

18.4.4 Theoretical Simulations

In the present study, we have simulated the at-sensor radiances by MODTRAN model in two TIR spectral channels (TIR1 and TIR2) of the *Imager* sensor by varying the following five parameters in the respective spectral regions of interest: (1) Temperature of the atmospheric lower boundary: The simulations for various atmospheric profiles over tropical region (SeeBor dataset) (Borbas *et al.* 2005; Seeman *et al.* 2008) are carried out with the boundary layer temperature ranging from approximately 260-320 K. (2) Atmospheric column water vapour: The water vapour values ranging from 0.1 g/cm² to near saturated level have been used through each atmospheric profile. (3) Surface temperature: The land surface temperature ranging from 260-330 K has been taken keeping tropical region as the context. (4) View zenith angle (VZA): 0 to 60 degree. (5) Land surface emissivity: Emissivity values from the standard International Geosphere Biosphere Program (IGBP) land cover types, major 10 major land cover types (ocean water, snow, sand, crop, shrubs, grass, forest, savanna, wetland, urban) have been considered from the MODTRAN database.

A set of radiosonde and satellite sounder profiles over tropical region from the SeeBor dataset (Borbas *et al.* 2005; Seeman *et al.* 2008) is selected for input in MODTRAN simulations. Figure 6 shows a graph of atmospheric profiles covering the boundary layer atmospheric temperature from 257.4 to 315.3 K and water vapour concentration from 0.1 to 5 g/cm² selected in the present study. Synthetic profiles were also generated from these basic profiles by modulating the surface temperature by ± 10 degree. The attenuation due to atmosphere has been considered because of uniformly mixed gases, namely, CO₂, N₂O, O₃ and CH₄ along with the water vapour in the MODTRAN forward simulations. The contribution due to solar radiation in the MIR channel is not considered in the simulations. All the transmittance and path radiance calculations were performed in the *Imager* thermal IR spectral channels by incorporating the spectral response function (figure 1) of the respective spectral channel.

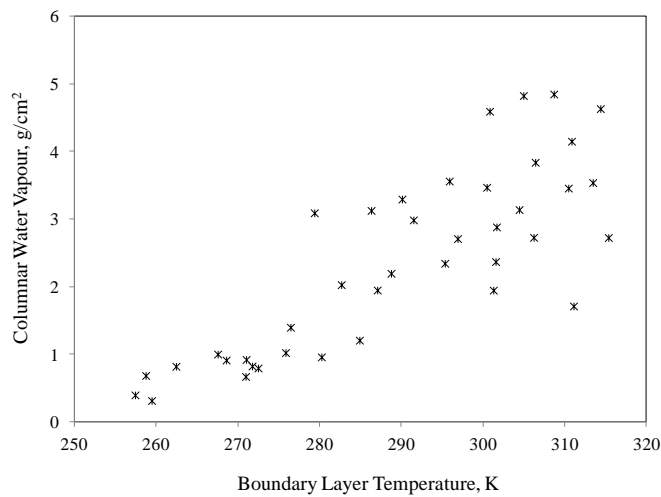


Figure 6. The atmospheric profiles from the SeeBor database used in the study. The water vapour content as a function of boundary layer temperature

The band average emissivity values for various land cover types were used in the simulations with considering relative spectral response functions of INSAT 3D split channels (shown in figure 7).

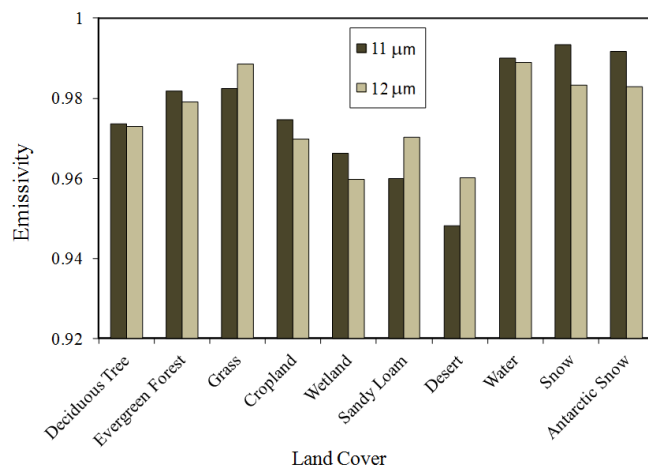


Figure 7. Emissivity for the different surface types considered in the simulation study

Coefficients for SW algorithm are derived from simulation data generated with the RT model MODTRAN. Specifically, the relationship between the model input LST and output top-of-atmosphere (TOA) brightness temperature is fit with an LST algorithm (equation 4) via regression to obtain the required coefficients.

18.5 Results

18.5.1 Derivation of Split-Window Coefficients (SWC)

The satellite-level signals in two TIR channels pertaining to *Imager* sensor were simulated for varying atmospheric and land surface properties discussed in the above sections. In order to determine the SWC a_0 to a_6 in Eq. (4), we divided the VZA into several tractable sub-ranges for improving the fitting accuracy and thus LST retrievals. Simulations were performed for VZA ranging from 0 to 60 degree taking into account the fact that the *Imager* sensor onboard INSAT-3D receives radiance from various VZA having varying atmospheric path length. The SW coefficients (a_1 to a_6) of Eq. (4) can be obtained through statistical regressions method for each VZA sub-range. Seven different sets of SWC were determined for each of this VZA sub-ranges, which are summarized in the table 3 and shown in the figure 8.

Table 3. Split-window coefficients as a function of view zenith angle

View Zenith Angle (°)	a_1	a_2	a_3	a_4	a_5	a_6
0-20	-9.6413	1.036241	1.176646	0.284241	56.24802	-111.024
20-32.5	-10.6691	1.040257	1.134075	0.318362	55.94625	-107.704
32.5-37.5	-10.8886	1.041256	1.129467	0.331893	55.61344	-103.803
37.5-42.5	-11.5068	1.043679	1.101384	0.352332	55.59688	-101.483
42.5-47.5	-12.0646	1.046049	1.101714	0.373722	55.25553	-103.699
47.5-52.5	-12.784	1.049354	1.064926	0.408965	55.26695	-96.7368
52.5 and above	-15.2924	1.058782	1.077231	0.456814	54.46535	-94.9324

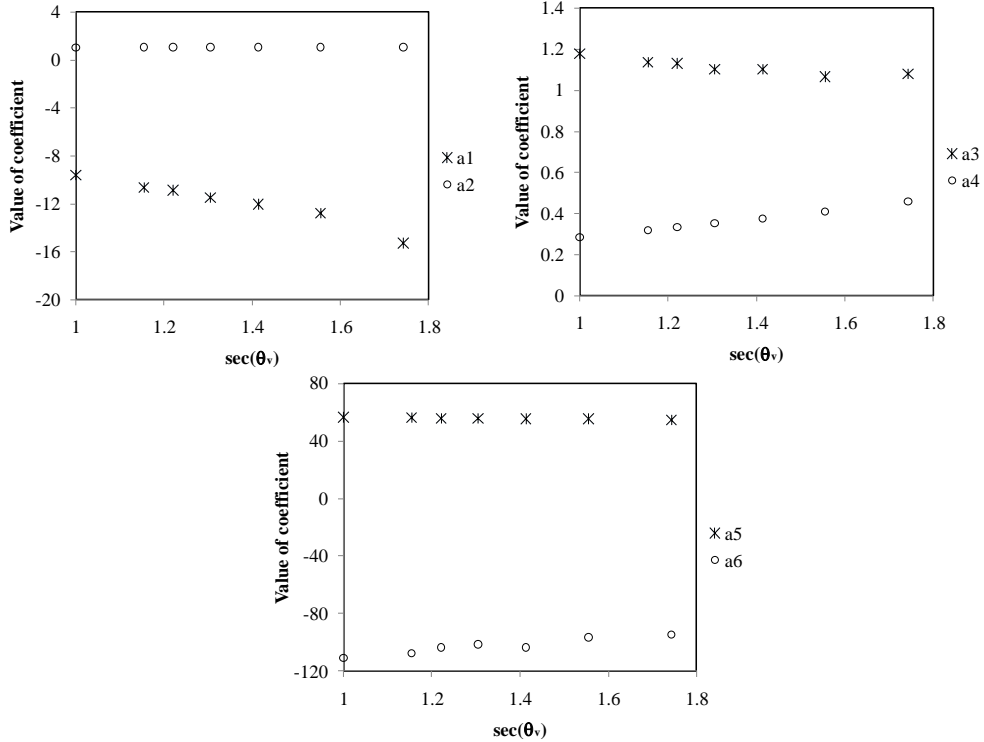


Figure 8. Split-window coefficients shown as a function of view zenith angle

In these calculations LST was treated as free parameter and regression was performed systematically by taking into account the dependency of ε in the algorithm. The R^2 values varied between 0.94 to 0.99 showing good correlation between modelled parameters in the split-window algorithm.

18.5.2 Sensitivity analysis

In order to provide an estimation of the theoretical error on the estimated LST, and also the contribution of the different terms to that error, a sensitivity analysis was performed based on the classical error theory using derivatives. Hence, the contribution to the error on the LST, $e(LST)$ is given by the following terms:

$$e(LST) = \sqrt{\delta_{alg}^2 + \delta_{NEAT}^2 + \delta_\varepsilon^2} \quad (5)$$

where δ_{alg} is the standard error of the algorithm obtained in the minimization (standard error of estimation), δ_{NEAT} is the contribution of the noise equivalent delta temperature ($NE\Delta T$) and δ_ε is the error due to the uncertainty of the surface emissivity. These contributions are, respectively, given by,

$$\delta_{NEAT} = \sqrt{\left(\frac{\partial T_s}{\partial T_i} \right)^2 e^2(T_i) + \left(\frac{\partial T_s}{\partial T_j} \right)^2 e^2(T_j)} \quad (6)$$

$$\delta_\varepsilon = \sqrt{\left(\frac{\partial T_s}{\partial \varepsilon_i} \right)^2 e^2(\varepsilon_i) + \left(\frac{\partial T_s}{\partial \varepsilon_j} \right)^2 e^2(\varepsilon_j)} \quad (7)$$

where e refers to the error of the parameter considered in brackets. The different derivatives of the T_s given by Eq. (5) were calculated. Values of $e(T_i) = e(T_j) = 0.1$ K and $e(\varepsilon_i) = e(\varepsilon_j) = 0.002$ have been considered for the present study. These selected values are considered to be representative of typical errors when working in remote sensing.

The results on the error and sensitivity analysis obtained for each view angle are summarized in table 4, which includes the contribution to the total error of the different terms (δ_{alg} , δ_{NEAT} , and δ_ε) and the total error in LST, $e(LST)$. The errors on LST have been calculated by applying Eq. (5-7) to each of the thousands of simulated data points.

Table 4: Results obtained in the sensitivity analysis

View angle Sub range	δ_{alg} (K)	δ_{NEAT} (K)	δ_ε (K)	$e(LST)$ (K)
0	0.68	0.32	0.32	0.82
30	0.82	0.33	0.32	0.94
35	0.89	0.33	0.30	1.00
40	0.98	0.34	0.30	1.07
45	1.10	0.34	0.30	1.19
50	1.30	0.35	0.29	1.38
55	1.52	0.37	0.28	1.59
Average	1.04	0.34	0.30	1.14

Generally, the accuracy of the SW algorithm is ensured by the standard error of the algorithm (δ_{alg}). In this study, the δ_{alg} values ranged between 0.68 to 1.52 K. An increase in the algorithm error was observed as view angle varied from lower to higher values. In terms of different contributions to $e(LST)$, it is clearly seen that the less contribution is due to the ε uncertainty, with δ_ε values ranging between 0.28 to 0.32 K. The δ_{NEAT} ranged between 0.32 and 0.37 K. In terms of total errors on LST, $e(LST)$, values ranged between 0.82 K to 1.59 K, with an average error of 1.14 K. Looking at the analysis and results summarized in table 3, it is clear that the proposed SW algorithm performs best with overall error of 1 K when view angles vary between 0 to 35 degree. Since major of the Indian landmass is covered with the view angle up to 35 degree by the INSAT-3D *Imager* (figure 2), we expect to obtain overall modeling error less than 1 K.

18.5.3 Application of LST algorithm to INSAT-3D *Imager* data

A total of 40 raw images of INSAT-3D *Imager* sensor for every half an hour time period of 29th Nov. 2013 were obtained for the analysis. From the raw h5 images, the top-of-atmosphere (TOA) radiance data corresponding to two split-window channels (TIR1 and TIR2) and latitude-longitude layers were extracted from it. The TOA radiance data were converted to the brightness temperature values using the calibration coefficients provided in form of look-up-table. Then these brightness temperature layers of two split-window channels were geo-referenced using the latitude and longitude datasets. An example of *Imager* standard false colour composite for a daytime (05:30 GMT) is shown in the figure 9.

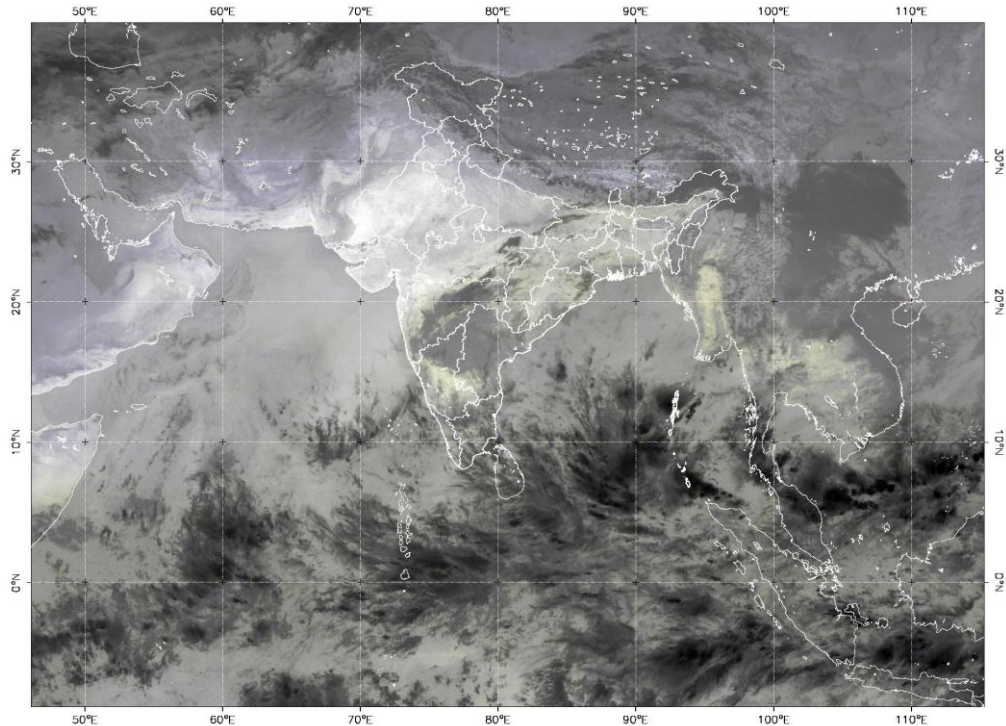


Figure 9. Image composite generated from INSAT-3D *Imager* data using the combination of TIR1, TIR1 and TIR2 channels for Nov. 29, 2013 (05:30 GMT)

Now the TOA brightness temperature images corresponding to the split-window channels were converted into the LST values using the SWC and proposed method. Here a particular set of SWC was used in the SW algorithm depending upon a VZA sub-range, i.e. a unique set of SWC was applied for each of the seven VZA sub-ranges. Figure 10 shows an example of LST image generated by the proposed method. The LST image shown here has been generated by the SW method along with the known emissivity values generated over India with the help of approximately 20 emissivity tiles of MODIS. The LST products have been generated with a typical spatial resolution of 4 km. A specific land-sea mask was applied to obtain only the landmass covered within the image. The cloudy pixels in the LST products are not masked out in the initial stage. The cloud masking was done in later part of the analysis based upon a bi-spectral thresholding method and an example of such LST image is shown in figure 11. To demonstrate the applicability of our SW method, all 40 images were converted to the LST and for detailed analysis and validation, three images were selected corresponding to daytime (05:30 and 09:00 GMT) and night time (21:00 GMT) of 29th Nov. 2013 over India.

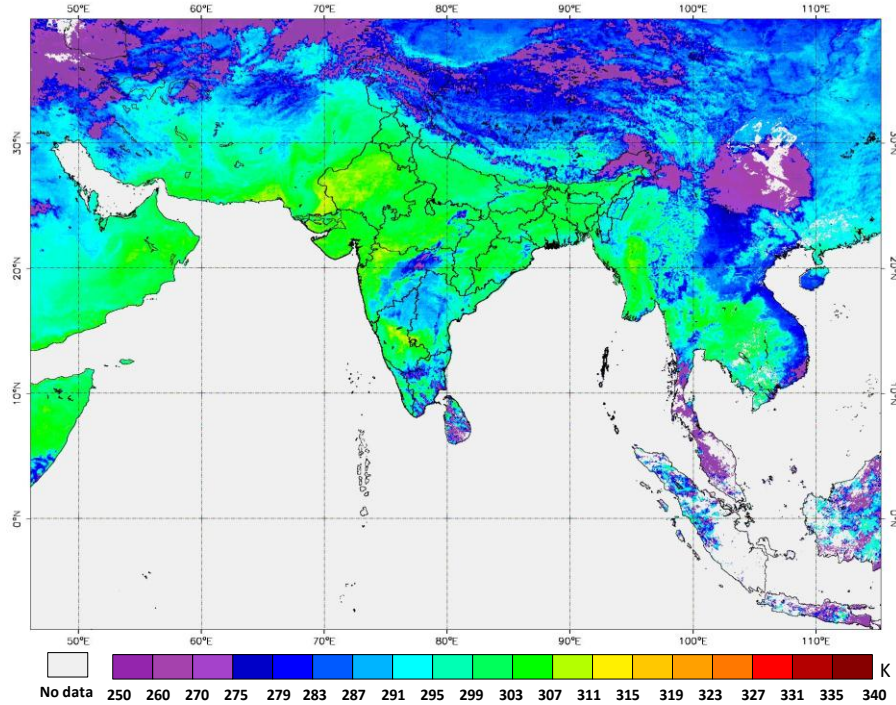


Figure 10: Land surface temperature derived with the proposed split-window method for INSAT-3D Imager for Nov. 29, 2013 (05:30 GMT) without cloud mask

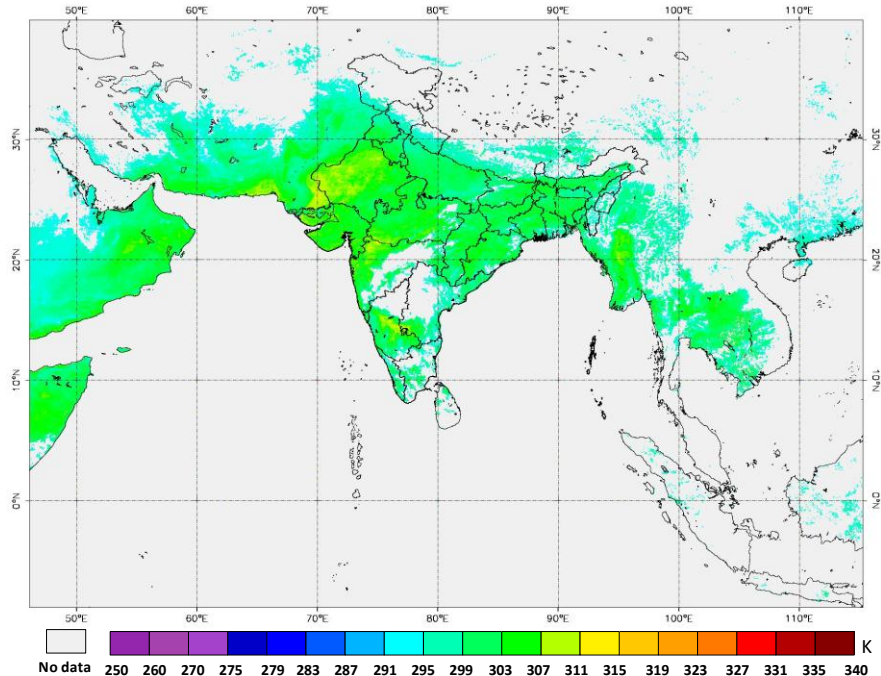


Figure 11: Land surface temperature derived with the proposed split-window method for INSAT-3D Imager for Nov. 29, 2013 (05:30 GMT) with cloud mask

18.5.4 Generation of LST products on diurnal scale

This section presents results on the generation of LST products on the diurnal scale over India and surrounding region. Examples of the 3D-LST images are shown in the figure 12 for diurnal images acquired on Nov. 29, 2013. The 3D-LST images suggest that LST values were captured successfully, which ranged from 275-320 K over the Indian region for this particular day.

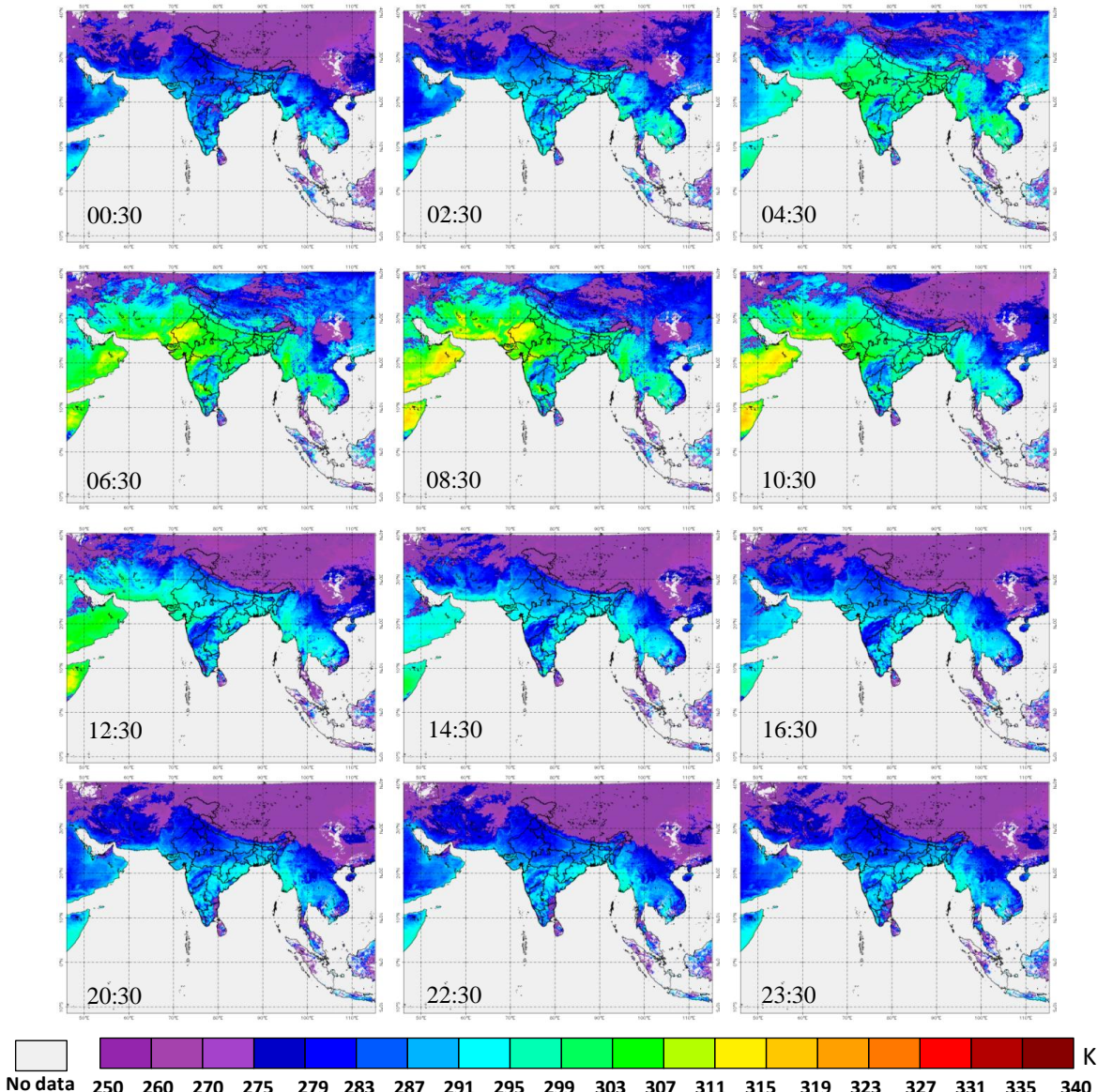


Figure 12. Diurnal LST images generated using a split-window method from INSAT-3D Imager data over India for Nov. 29, 2013

As expected, higher temperatures during daytime were observed mostly in the western arid and semi-arid regions of Rajasthan, Gujarat and Maharashtra states of India as well as major portion of neighbouring countries having arid regions located in the west of India. While lower temperatures were observed in the northern parts of India, which are

were dominated by the winter crop regions. An analysis was carried out to obtain diurnal cycle of typical land covers in the LST profiles. The idea behind generation of LST on this scale is to check whether the model physics works well throughout the day or not. The diurnal patterns of LST over different land covers such as desert, shrub and crop are shown in the figure 13. The patterns resemble to the known behaviour of the LST on these land covers, which confirms that proposed SW method is working well over full day-night cycle.

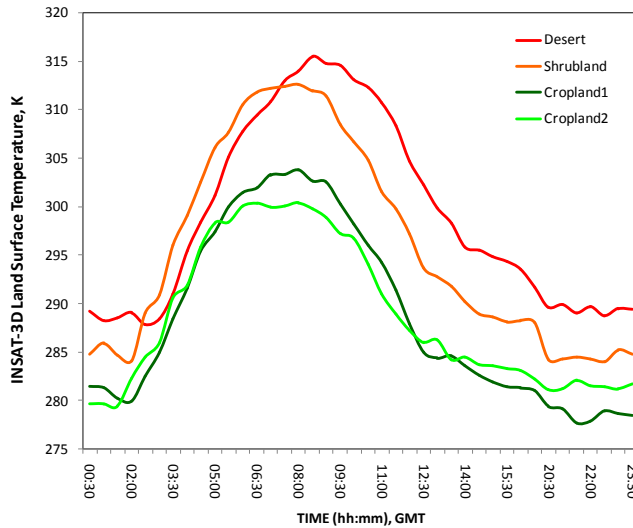


Figure 13. Diurnal patterns of LST derived by the split-window method from the INSAT-3D *Imager* sensor over some representative land covers shown as a function of IST

18.6 Validation of Insat-3d Imager LST with K1/MODIS LST

In order to check the performance of the proposed SW method, LST derived from the INSAT-3D *Imager* LST (3D-LST) with the SW algorithm was compared with (a) the Kalpana-1 VHRR (K1-LST) derived with the single channel algorithm and (b) MODIS LST (MOD-LST) derived with the SW method. Out of all the images, the comparison results obtained for three different times (05:30, 09:00, 21:00 GMT) corresponding to the MODIS satellite pass for a day 29th Nov. 2013 are presented in the following figures and graphs (figure 14-22).

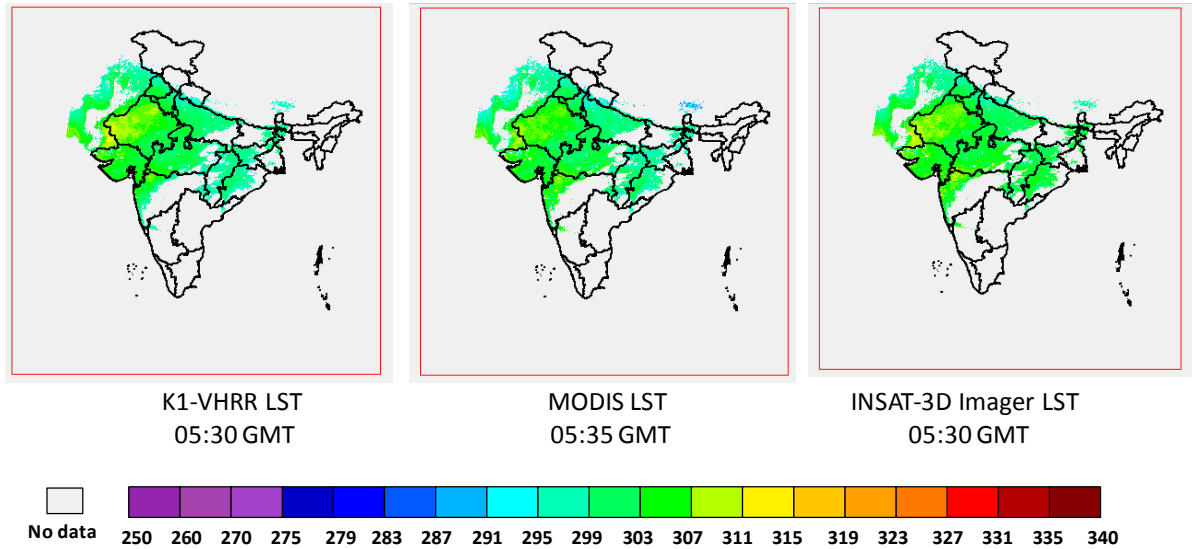


Figure 14. Comparison of INSAT-3D *Imager* LST with the Kalpana-1 VHRR LST and MODIS LST for 05:30 GMT of 29th Nov. 2013 over India

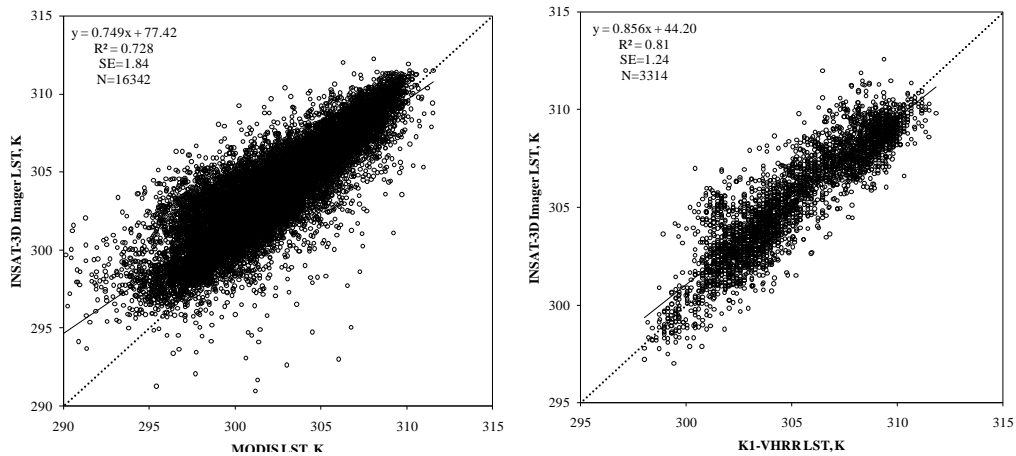


Figure 15. Comparison of INSAT-3D *Imager* LST with MODIS & K1-LST for 05:30 GMT data

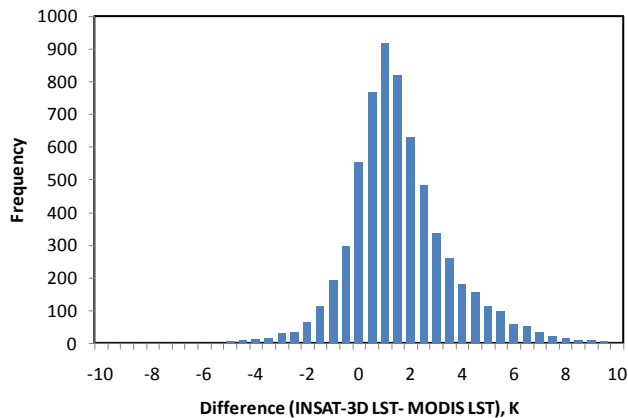


Figure 16. Histogram showing difference between INSAT-3D LST and MODIS LST (5:30 GMT)

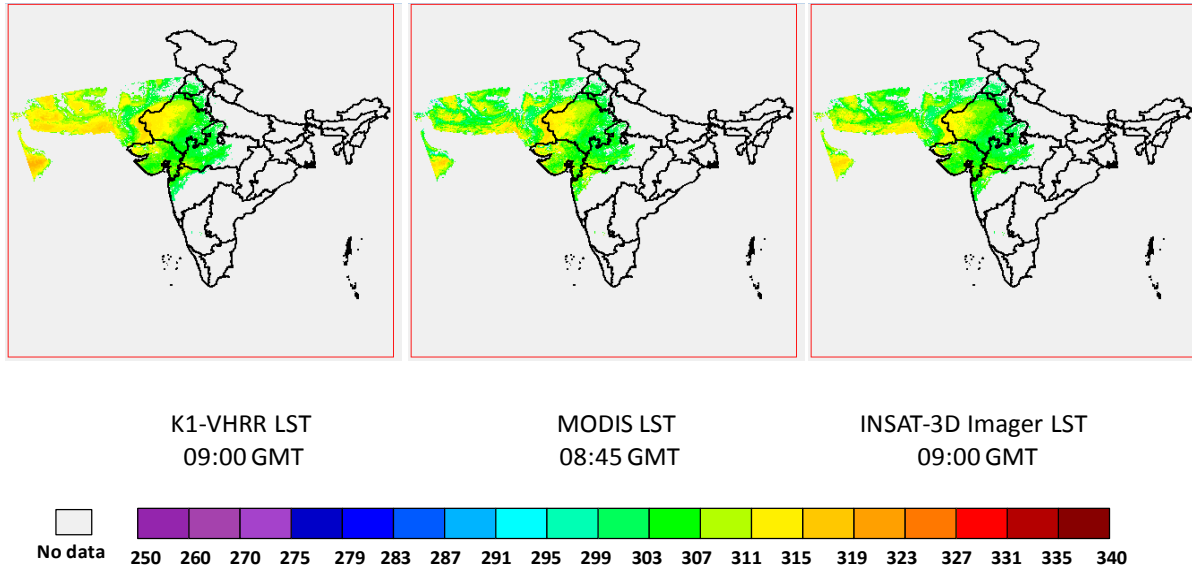


Figure 17. Comparison of INSAT-3D *Imager* LST with the Kalpana-1 VHRR LST and MODIS LST for 09:00 GMT of 29th Nov. 2013 over India

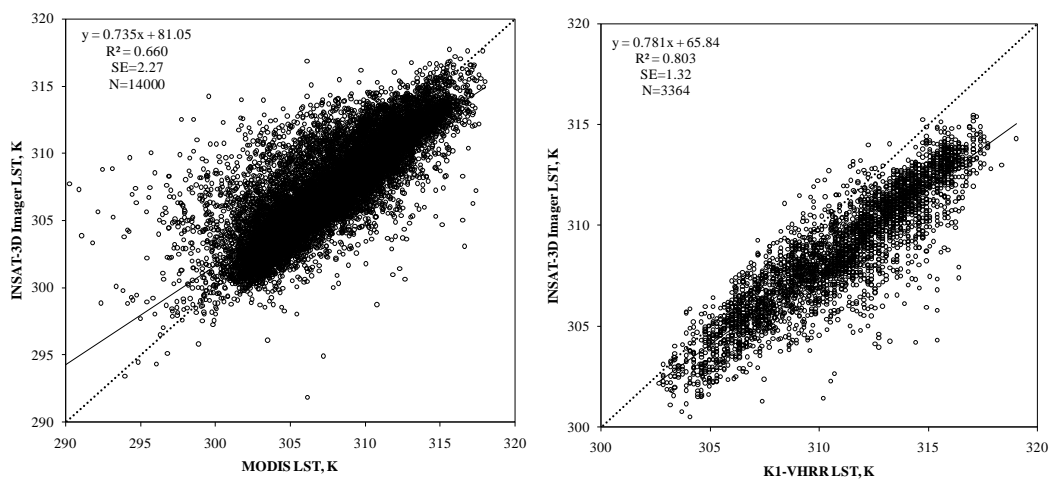


Figure 18. Comparison of INSAT-3D *Imager* LST with MODIS & K1-LST for 09:00 GMT data

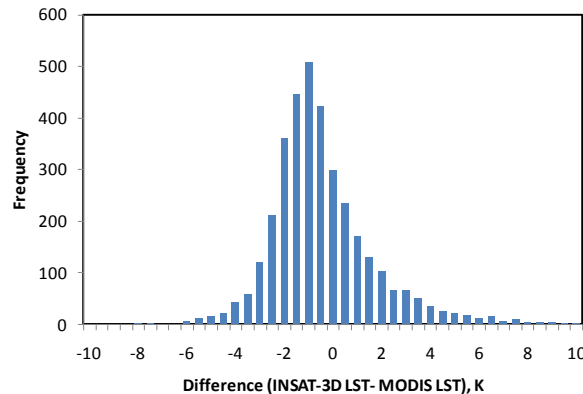


Figure 19. Histogram showing difference between INSAT-3D LST and MODIS LST (9:00 GMT)

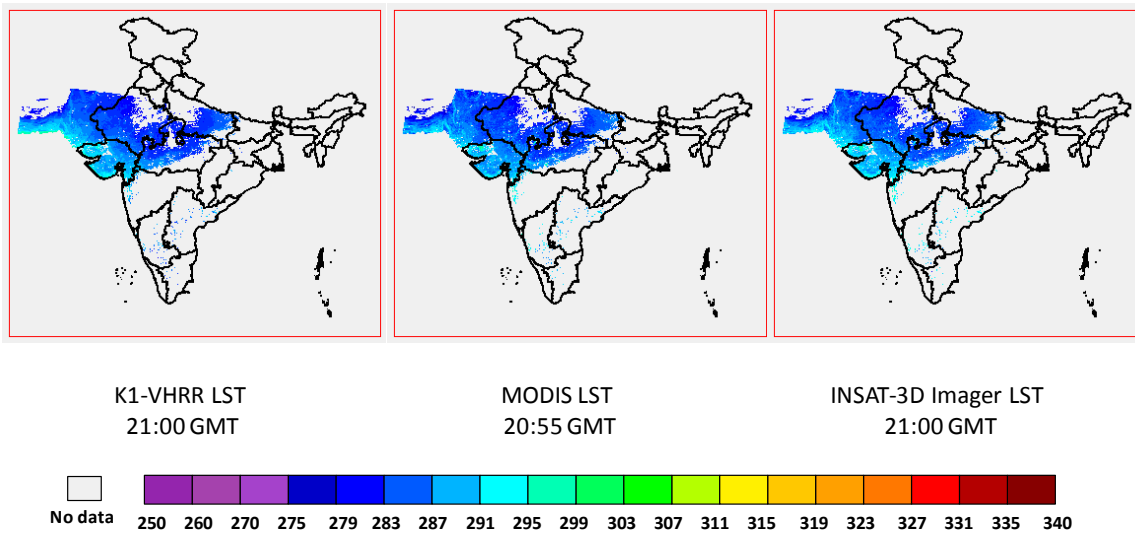


Figure 20. Comparison of INSAT-3D *Imager* LST with the Kalpana-1 VHRR LST and MODIS LST for 21:00 GMT of 29th Nov. 2013 over India

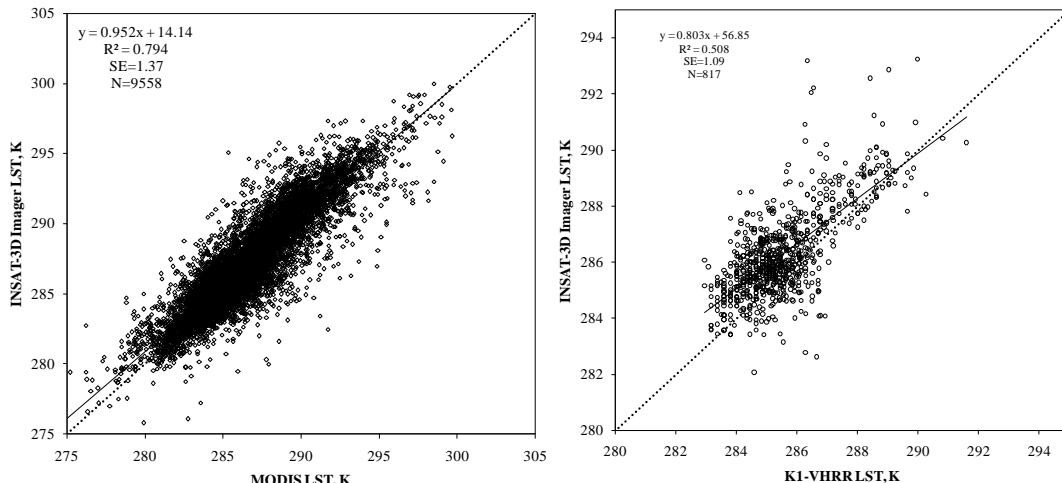


Figure 21. Comparison of INSAT-3D *Imager* LST with MODIS & K1-LST for 21:00 GMT data

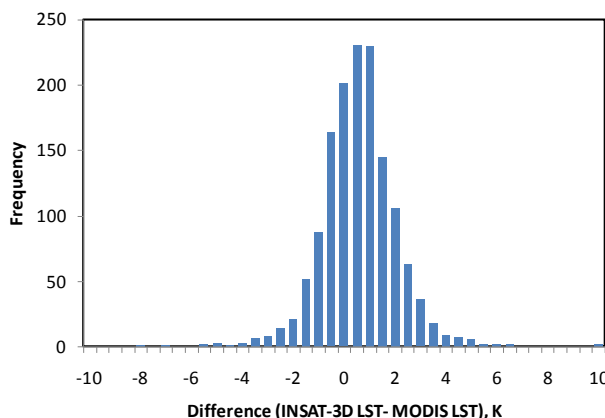


Figure 22. Histogram showing difference between INSAT-3D LST & MODIS LST (21:00 GMT)

Above figures show the inter-comparison of 3D-LST with two other estimates, K1-LST and MOD-LST for three specific time of a day 29th Nov. 2013. The comparison of daytime and nighttime retrievals shows (figure 14, 17 and 20) that the LST values from 3D fairly match with MODIS as well as K1 sensors. The comparison showed a good correlation having R^2 values varying from 0.73 (05:30 GMT), 0.66 (09:00 GMT) and 0.79 (21:00 GMT) for 3D Vs. MODIS and from 0.81 (05:30 GMT), 0.80 (09:00 GMT) and 0.51 (21:00 GMT) for 3D Vs. K1. While, the standard error of estimates (SEE) observed between 3D and MODIS were 1.84 K (05:30 GMT), 2.27K (09:00 GMT) and 1.37 K (21:00 GMT). And the SEE observed between 3D and K1 were 1.24 K (05:30 GMT), 1.37K (09:00 GMT) and 1.10 K (21:00 GMT). It is clear that nighttime retrievals showed an excellent match when the LST ranged between 280 to 300 (figure 21). However, for the daytime satellite-passes when temperatures were generally more than 300 K in this part of the globe, 3D-LST showed a deviation as compared to the MOD-LST (figure 15 and 18). In the case of satellite pass of 05:30 GMT, the 3D-LST demonstrated a moderate deviation with SEE=1.84 K ($R^2=0.73$) as compared to the MOD-LST (figure 15). While 09:00 GMT satellite pass showed a slightly high degree of deviation (SEE=2.27 K, $R^2=0.66$) (figure 18).

Overall the 3D-LST values showed a good match with the reference LST values in the range of 270-310 K, demonstrating that the SW algorithm is working fairly well. However, for some of the daytime 3D-LST retrievals (e.g. 05:30 GMT), an unambiguous over estimation was observed as compared to MOD-LST retrievals. This overestimation in 3D-LST is apparent at all the LST values independent of low or high values in the daytime. Reasons of this overestimation in 3D LST could be: use of India-specific atmospheric profiles in present study for the RT modelling to obtain better tuning of the SW coefficients, difference in the algorithms used, difference in the spatial resolution, difference in time of data acquisition, ignorance of the reflectance term (3rd term of equation 1) in the simulation of at-sensor radiance. This reflectance term is quite small since it is multiplied with the downwelling radiance, atmospheric transmittivity and (1-emissivity) components. But probably with the presence of solar radiation it may play an important role, which has to be checked in future analysis. Moreover, there are certain issues like cloud masking remain in the present LST retrieval. At many instances in the present analysis, thresholding method for cloud masking does not perform well especially over snow regions. A robust cloud-mask algorithm has to be devised and applied to get accurate LST products.

18.7 Conclusions

This document presents results of a study to develop a method to generate LST product from the thermal infrared channels of INSAT-3D Imager sensor over India using a RT model. A modified split-window algorithm including the view angle correction was developed specifically tuned for the Imager sensor. Simulations were carried out based upon a number of model inputs to derive a set of coefficients from the atmospheric functions particularly tuned for the Imager sensor. These SW coefficients were then used to generate the LST product. The total theoretical modelling error ranged from 0.8 K (for view zenith angle equal to 0 degree) to 1.6 K (for view zenith angle equal to 55 degree) with an average error of 1.1 K. The LST derived using the proposed method was validated with the Kalpana-1 VHRR LST and MODIS LST products for day and night

datasets. This inter-comparison brought out the fact that the proposed algorithm provided encouraging results with a very good match of 3D-LST with other reference LST estimates. The comparison of satellite derived LST with other two satellite observations over India showed a fairly good agreement between satellite estimates, with a R² value up to 0.79 and RMSE of 1.37 K for 3D Vs. MODIS comparison, while a R² value up to 0.81 and RMSE of 1.1 K for 3D Vs. K1 comparison. The overestimation in the case of daytime observations in the 3D LST is to be explored in the future. A robust cloud removal algorithm has to be developed and applied on the LST images. The method developed in this report provides a theoretical base for generation of operational LST products over India from the INSAT-3D Imager data.

Acknowledgement

This study has been carried out under the INSAT-3D Utilization Project “Retrieval of land surface temperature from the INSAT-3D Imager observations”. Authors are grateful to Shri A. S. Kiran Kumar, Director, SAC, Dr. J. S. Parihar, Deputy Director, EPSA and Dr. C. M. Kishtawal, Project Director, INSAT-3D Utilization Program for their guidance and support to this project. Authors would like to acknowledge support provided by Dr. H. J. Trivedi, Head Physics Department, and Dr. Basudeb Bakshi, Principal of N. V. Patel College of Pure and Applied Sciences, Vallabh Vidyanagar for their support in carrying out this study.

18.8 References

1. Berk A., Anderson G. P., Acharya P. K., Chetwynd J. H., Bernstein L. S., Shettle E.P., Matthew M. W. and Adler-Golden S. M. (1999), MODTRAN4 User's Manual. Hanscom AFB, MA: Air Force Res. Lab.
2. Borbas E., Seemann S. W., Huang H.-L., Li J., and Menzel W. P. (2005). Global profile training database for satellite regression retrievals with estimates of skin temperature and emissivity. Proc. of the Int. ATOVS Study Conference-XIV, Beijing, China, 25-31 May 2005, pp 763-770.
3. CDR (2009). Met Payload Team. “Meteorological payloads: Critical Design Review document, Imager payload system (vol.1)”. SAC/SEDA/INSAT-3D/CDR/11/06/0901. June 2009. pp 376.
4. Dash P., Gottsche F. -M., Olesen F. -S. and Fischer H. (2002). Land surface temperature and emissivity estimation from passive sensor data: theory and practice; current trends. *Int. J. Rem. Sens.* 23: 2563-2594.
5. Jiménez-Muñoz Juan-Carlos and Sobrino J. A. (2003). A generalized single-channel method for retrieving land surface temperature from remote sensing data. *J. Geophys. Res.* 108, D22, 4688 ACL2.
6. Kerr Y. H., Lagourde J. P., Nerry F. and Ottlé C. (2004), “Land surface temperature retrieval techniques and applications: Case of the AVHRR”, in Thermal Remote Sensing in Land Surface Processes, D. A. Quattrochi and J. C. Luval, Eds. Boca Raton, FL: CRC Press, 2004, pp. 33-109.
7. Kneizys F. M. *et al* (1988), “Users guide to LOWTRAN 7,” Air Force Geophys. Lab., Bedford, MA, Rep. AFGL-TR-88-0177.
8. Lacis A. A. and Oinas V. (1991). A description of the correlated k distribution method for modeling nongray gaseous absorption, thermal emission and multiple

- scattering in vertically inhomogeneous atmospheres. *J. Geophys. Res.* 96:9027–9063.
9. Li Zhao-Liang, Bo-Hui Tang, Hua Wu, Huazhong Ren, Guangjian Ya, Zhengming Wan, Isabel F. Trigo, José A. Sobrino (2013). Satellite-derived land surface temperature: Current status and perspectives. *Remote Sens. Environ.* 131: 14-37.
 10. Liang S. (2004), Quantitative remote sensing of land surface, Wiley Interscience.
 11. McClain E. P., W. G. Pichel, and C. C. Walton (1985). Comparative performance of AVHRR-based multichannel sea surface temperatures. *J. Geophys. Res.*, vol. 90, no. C14, pp. 11 587–11 601.
 12. Pandya M. R., Shah D. B., Trivedi H. J. and Panigrahy S. (2011a). Simulation of at-sensor radiance over land for proposed thermal channels of Imager payload onboard INSAT-3D satellite using MODTRAN model. *J. Earth System Science.* 120(1):1-7.
 13. Pandya M. R., Shah D. B., Trivedi H. J., Panigrahy S. and Parihar J. S. (2011b). Evaluation of Split-Window Algorithms for Retrieving Land Surface Temperature from the INSAT-3D Imager Observations. *Vayu Mandal.* 37(1-4): 31-37.
 14. Pandya M. R., Shah D. B., Trivedi H. J., Darji N. P., Ramakrishnan R., Panigrahy S., Parihar J. S. and Kirankumar A. S. (2013). Retrieval of land surface temperature from the Kalpana-1 VHRR data using a single-channel algorithm and its validation over the Thar desert. *ISPRS Journal of Photo Engineering & Remote Sensing.* (under-review).
 15. Pandya M. R., Darji N. P., Ramakrishnan R., Panigrahy S., Parihar J. S. and Kirankumar A. S. (2010). Algorithm Theoretical Basis Definition (ATBD) of land surface temperature retrieval from the INSAT VHRR data. Scientific Report. SAC/RESA/AFEG/AMD/SSV/SR/02/June 2010.
 16. Pandya M. R. and Dadhwal V. K (1999). The simulation of top of canopy red and near infrared crop reflectances for proposed INSAT-2E CCD payload using SAIL model. *NNRMS bulletin.* Vol. NNRMS(B)-23, 17-24.
 17. Seeman S. W., Borbas E., Knuteson R. O., Stephenson G. R. and Huang H. -L. (2008), Development of a global infrared land surface emissivity data based for application to clear-sky sounding retrievals from multispectral satellite radiometers. *J. App. Climat.* 47 (1): 108-123.
 18. Sobrino J. A. and Raissouni N. (2000). Toward remote sensing methods for land cover dynamic monitoring: Application to Morocco. *Int. J. Remote Sens.* 21, 2: 353-366.
 19. Sobrino J. A., Jiménez-Muñoz Juan-Carlos, Paolin L. (2004). Land surface temperature retrieval from LANDSAT TM 5. *Remote Sens. Environ.* 90: 434-440.
 20. Sobrino J. A., Li Z. L., Stoll M. P. and Becker F. (1994), Improvements in the split window technique for land surface temperature determination. *IEEE Trans. Geosci. Remote Sens.* 32: 243-253.
 21. Sòria G. and Sobrino J. A. (2007), ENVISAT/AATSR derived land surface temperature over a heterogeneous region. *Remote Sens. Environ.* 111: 409-422.
 22. Sun D. and Pinker R. T. (2003). Estimation of land surface temperature from a Geostationary Environmental Satellite (GOES-8). *J. Geophys. Res.* 108, D11, 4326, ACL 2, doi: 10.1029/2002JD002422, 2003.

23. Sun D. and Pinker R. T. (2007). Retrieval of surface temperature from the MSG-SEVIRI observations: Part I. Methodology. *Int. J. Remote Sens.* 23-24, 28: 5255-5272.
24. Ulivieri C., Castronuovo M. M. Francioni R. and Cardillo A. (1994). A split window algorithm for estimating land surface temperature from satellites. *Advances in Space Research*, 14, 3: 59-65.
25. Wan Z. and Dozier J. (1996). A generalized split-window algorithm for retrieving land-surface temperature measurement from space. *IEEE Trans. Geosci. Remote Sens.* 34, 4: 892-905.
26. Yu Y., Tarpley D., Privette J. L., Goldberg M. D., Raja Varma M. K. R., Vinnikov K.Y. and Xu H. (2009). Developing algorithm for operational GOES-R land surface temperature product. *IEEE Trans. Geosci. Remote Sens.* 47, 3: 936-951.

Annexure (Product Specification)

Product Name	Land Surface Temperature	LST
Unit	K (Kelvin)	
Summary of Product Algorithm	<p>The LST products are derived using TIR1 and TIR2 channel data from INSAT-3D <i>Imager</i>. A physics-based algorithm considering the split-window channels and view zenith angle (θ_v) is used to define LST in terms of brightness temperatures from thermal infrared channels and land surface emissivity (ε). The generic form of the product algorithm is given as,</p> $\text{LST} = f(\text{TIR1}, \text{TIR2}, \varepsilon, \theta_v).$ <p>Source of data: TIR1/TIR2: Brightness temperatures and θ_v view zenith angle are from <i>Imager</i> and ε is monthly climatology of emissivity from MODIS</p>	
Product Resolution	4 km X 4 km	
Product Coverage	0° - 40° N and 50° - 110° E	
Spatial Interpolation Method	Not required	
Time Resolution	30-Minutes	
Product Range	250-350 K	
Product Accuracy	Absolute : 1.5-5 K	
Focal Point with Affiliation and e-mail	Dr. Mehul Pandya , EHD/BPSG/EPSA, mrpandya@sac.isro.gov.in	

19. Potential Evapotranspiration

S.No.	Product Name	Spatial Resolution	Temporal Resolution
1	TBD	TBD	TBD

19. Potential evapotranspiration (PET) from INSAT 3D insolation Product and short-range forecasts

19.1 Algorithm Configuration Information

19.1.1 Algorithm name

Potential evapo-transpiration

19.1.2 Algorithm identifier

TBD

19.1.3 Algorithm specification

Version	Date	Prepared by	Description
1.0	19 July 2012	Dr. Rahul Nigam and Dr. Bimal K. Battacharya	Potential evapo- transpiration baseline document

19.2 Introduction

The process of evapotranspiration (ET) acts as one of the main drivers of the hydrological or water cycle. One of the distinguishing factors of ET is its role as a key player between the energy and water cycles. The potential ET rate (ET_o) is influenced by several factors such as solar radiation, wind speed, air temperature and vapour pressure deficit. Among them, solar radiation is the most sensitive parameter influencing almost 60-70% variability of ET_o . The potential evapo-transpiration (PET), hereafter referred as grass reference evapo-transpiration (ET_o), is expressed in terms of amount of water transferred per unit time to atmosphere from water non-limiting surface covered with a uniformly and actively growing short grass such as Alfalfa. ET_o represents the evaporative demand of the atmosphere for a given climatic region. Deficiency in required supply of moisture leads to water stress. Reference evapo-transpiration is an agrometeorological variable widely used in hydrology and agriculture. Together with precipitation, it is a major input in soil water balance models. Several of these models require daily or hourly evapotranspiration data to provide acceptable estimate of plants' water requirements. This would provide regional water demand in different agro-climatic settings and agricultural growing season. The combination of spatial rainfall with ET_o would help in monitoring water deficit and surplus during a growing season for rainfed agriculture.

Some contours of monthly climatic ET_o have been generated by Department of Agricultural Meteorology, IMD (India Meteorological Department) from measurements of limited surface observatories in India. But interpolation from such contours will propagate large errors. No digital map of ET_o is available to scientific community, modelers, resource managers and planners in India. Moreover, real-time updated spatial ET_o product at weekly, ten-day, fortnightly and monthly scales would aid in knowing the intra and inter-seasonal climatic variability of water stress factors and their impact on deviation in biomass and yield. The climatic moisture index (ratio of rainfall and PET) is essential to know surface wetness and suitability of sowing or transplanting operations.

Therefore, it has the relevance for national agro-advisory services to farmers as well as crop forecasting.

19.2.1 Overview and background

The latent heat of vaporization, which is the energy required for evaporating water is significant in weather and climate dynamics (Priestley & Taylor, 1972; Monteith, 1973; Rowntree, 1991; Anderson et al., 2007). Although the concept of “evaporation” has been known since approximately 500 B.C. (see Brutsaert, 1982 for a chronological sketch), most of the understanding of the governing factors has been achieved in the last two centuries. Dalton (1802) was the first who proposed relationship of vapor pressure deficit ($e_{\text{sat}} - e_{\text{act}}$) of the near surface air to the evaporation rate. Later, many empirical relationships were developed based on other environmental factors (Blaney and Criddle, 1950; Hargreaves, 1975; Thornthwaite, 1948). Based on available energy considerations and turbulent flux theory, Penman (1948) developed his evaporation equation for natural surfaces for water non-limiting conditions. This is known as potential evapotranspiration (PET). Monteith (1964) developed a modified version of the Penman equation in which biophysics was introduced through a surface or canopy resistance – the now well-known Penman–Monteith (P-M) combination equation – that allowed for vegetation control on transpiration rates.

Choudhury (1997) proposed a method to assess by means of satellite data, such as remotely sensed solar radiation, air temperature (derived from infrared images and weather station measurements) and vapor pressure deficit. This method provides good evapo-transpiration estimates for low-resolution applications such as worldwide scale and monthly time step. The accuracy is limited by the high uncertainties provided by satellite-sensed vapor pressure estimation.

Later, Bois et al. (2008) used remotely sensed solar radiation from METEOSAT observations from Heliosat-2 approach (Rigollier et al. 2004) and air temperature data to estimate ET_0 using Hargreaves approach. The ET_0 can also be available as forecast bi-product from weather forecasting model. However, recent evaluation of predicted radiative fluxes and operational short-range forecasts (24 hrs average) of routine weather elements from model for a limited winter months showed that the incident shortwave radiative flux produced the highest root mean square error to the tune of 110% (Bhattacharya et al, 2012a) amongst others as compared to *in situ* measurements from INSAT-linked micrometeorological stations (popularly known as AMS). However, the errors of short-range forecast of air temperatures, relative humidity, atmospheric pressure, wind speed at 10 m height were 3%, 12%, 21% and 1.4% respectively over plain and plateau regions. The per cent RMSE for last four variables were found to increase in the hilly terrain (Bhattacharya et al, 2012a). Expectedly, the ET_0 would have substantial errors propagated mainly from incident solar radiation flux estimation. On the other hand, the operational product on daily insolation from Kalpana-1 VHRR produced around 25% RMSE (Bhattacharya et al, 2012b) with respect to same ground reference and the per cent RMSE decreased with averaging over weekly, ten-day, fortnightly and monthly scales up to 15%. After improvement in the cloud flagging and the spatial resolution of operational insolation product from INSAT 3D, it is expected to produce substantially less errors. Therefore, it seems wise to use the combination of daily insolation product from INSAT 3D and operational forecasts of air temperatures, relative

humidity, wind speed and atmospheric pressure to generate real-time digital and regional product of potential evapo-transpiration.

19.2.2 Objectives

The objectives of this document are :

- (i) To outline the algorithm for the estimation of potential evapo-transpiration (ET_o) based on Penman-Monteith (P-M) approach (FAO-56 model)
- (ii) To integrate operational product of daily insolation from INSAT 3D and 24 hrs average operational forecast of routine weather elements at finer spatial resolution to generate product of spatial ET_o at 5 km spatial resolution
- (iii) To implement the algorithm in IMDPS GPR (Geophysical Parameter Retrieval) chain for automation of ET_o product generation
- (iv) To describe validation strategy against *in-situ* measurements with initial results

19.2.3 Instrument and characteristics of input products

19.2.3.1 Indian geostationary satellite (INSAT 3D)

The Indian National Satellite (INSAT) system is a joint venture of the Department of Space (DOS), Department of Telecommunications (DOT), and India Meteorological Department (IMD). INSAT 3D is an exclusive meteorological satellite in the INSAT system, which was launched at geostationary orbit in 2013. This radiometer consists of four bands : broad VIS (0.52-0.75), SWIR (1.55-1.70), MIR(3.8-4.0), WV(6.5-7.0) and two thermal TIR1(10.2-11.2), TIR2 (11.5-12.5) with nineteen sounder channel. The spatial resolution of VIS and SWIR band is 1 km x 1 km and 4 km x 4 km for MIR, WV and two thermal IR bands. The introduction of INSAT Meteorological Data Processing System (IMDPS) provides both ‘full-globe’ and ‘sector’ data products in all the bands at half-an-hour interval at 4 km spatial resolution in an automated mode. So, there are maximum 48 acquisitions on a given day. Raw data after reception at each acquisition were corrected for servo, line-loss, radiometry, stagger and oversampling removal using the INSAT 3D data products scheduler. This results into automated generation of co-registered data in each band at Transverse Mercator (TM) projection. The dimension of each band at each acquisition is 676 rows x 721 columns for Asia Mercator sector product.

19.2.3.2 Operational insolation product

A spectrally integrated clear-sky and three-layer cloudy-sky models were developed to determine integrated atmospheric transmittances and instantaneous insolation. Half-an-hourly observations from an Indian geostationary satellite sensor, INSAT 3D, were used to provide minimum ground brightness (surrogate of surface albedo) from previous 30 days, cloud top albedo, brightness temperatures, atmospheric water vapour as inputs to these models in addition to global eight-day aerosol optical depth at 550 nm and columnar ozone. A trapezoidal scheme was implemented to obtain daily insolation (in MJm^{-2}) from half-an-hour instantaneous insolation (Wm^{-2}) throughout the day for all-sky conditions (clear + cloudy). The whole algorithm (Bhattacharya et al, 2010 & 2012b) will be operationalized and daily insolation product can available at 4 km spatial resolution with Transverse Mercator projection routinely from MOSDAC site (<http://www.mosdac.gov.in>).

19.2.3.3 Operational product of WRF short-range forecast

Weather Research and Forecasting (WRF; Skamarock et al., 2008) Model version 3.1 is used for All India Short range weather forecast. WRF is a limited area, non-hydrostatic, primitive equation model with multiple options for various physical parameterization schemes. This version employs Arakawa C-grid staggering for the horizontal grid and a fully compressible system of equations. The terrain following hydrostatic pressure coordinate with vertical grid stretching is followed in vertical. The time-split integration uses 3rd order Runge-Kutta scheme with a smaller time step for acoustic and gravity wave modes. The WRF physical options used in this proposal consists of the WRF Single Moment 6-class simple ice scheme for microphysics (WSM6); the Grell-Devenyi ensemble cumulus convection parameterization scheme; and the Yonsei University (YSU) planetary boundary layer scheme.

The WRF Model is integrated in a triple domain configuration with a horizontal resolution of 45 km, 15 km and 5 km for the All India, with grid points 260×235, 352×373 and 676×721 in x and y directions for the domains 1, 2 and 3, respectively. The model has 36 vertical levels with the top of the model atmosphere located at 10 hPa. The WRF 3D-Var is used for the assimilation of all available conventional including ISRO-AWS data and satellite observations to improve the model initial conditions. The operational WRF short-range forecasts (Kumar et al., 2011), available at MOSDAC site used climatological land surface and atmospheric parameters from global database and assimilated all available conventional including ISRO-AWS and satellite observations (Kumar et al., 2011; Singh et al., 2011) from Indian and other International agencies (e.g. EUMETCast). The operational forecast is available at finer spatial resolution (~ 5km) at three hourly interval upto 72 hours.

Examples of operational daily insolation product and 24 hrs average WRF forecast product of air temperature, relative humidity, wind speed and atmospheric pressure over Indian region are shown in Figure 1.

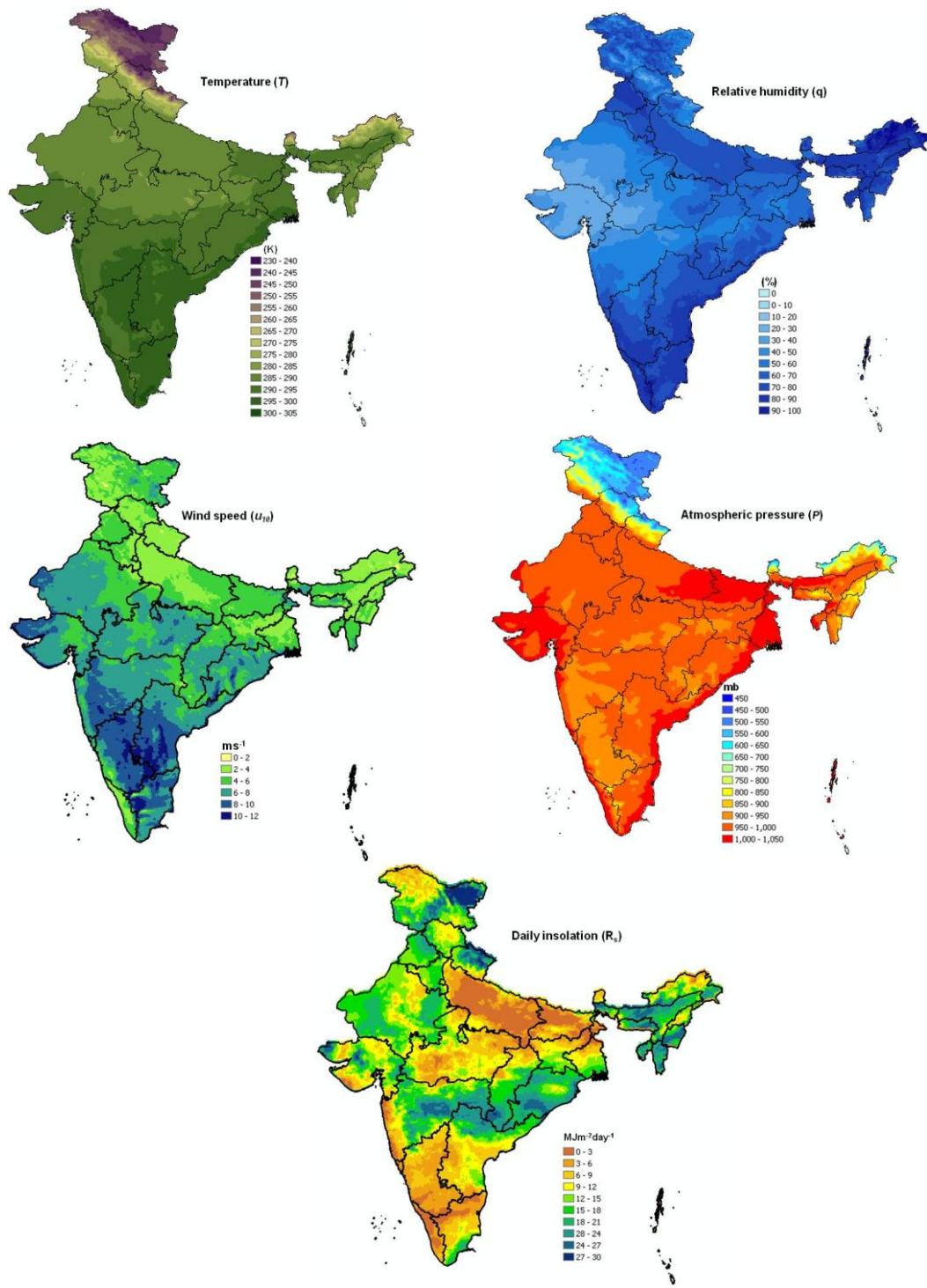


Figure 1. Example set of spatial inputs generated from WRF and K1VHRR for August 2011

19.3 Inputs

19.3.1 Static data : NIL

19.3.2 Image and pre-processing data (Dynamic)

Table 1

Parameter	Resolution	Quantization	Accepted accuracy	Source
Daily insolation product of Asia Mercator sector (e.g. h5 format)	Pixel (4 km x 4 km)	10-bit (integer) with scale factor of 0.01	10-15%	PR chain of IMDPS chain at BES
Geolocation file containing latitude and longitude corresponding to coregistered INSAT 3D data	Pixel wise	16-bit (floating point)	Less than one pixel	DP h5 product

19.3.3 Other auxiliary data and model inputs

Table 2

Parameters	Source
Operational three-hourly forecast output from WRF at $0.05^\circ \times 0.05^\circ$ spatial resolution for the following parameters in ASCII format (latitude, longitude, parameter) <ul style="list-style-type: none"> a) Air temperature (K) at 2 m height b) Relative humidity (%) at 2 m height c) Atmospheric pressure (mb) d) Wind speed (ms^{-1}) at 10 m height 	MOSDAC

19.4 Algorithm functional specifications

In 1948, Penman combined the energy balance with the mass transfer and derived an equation to compute the evaporation from an open water surface from standard meteorological records of sunshine, temperature, humidity and wind speed. This combination method was further extended to vegetated surface by introducing resistance term. The aerodynamic and surface resistances have been added to the original equation of Penman to estimate Potential evapotranspiration (ET_o) from a surface. This formulation is referred as FAO-56 Penman and Monteith (Allen et al., 1998) ET_o for a day. This is treated as standardized model worldwide. This is described as follows:

$$ET_o = \frac{0.408\Delta(R_n - G) + \gamma \frac{900}{T + 273} u_2(e_s - e_a)}{\Delta + \gamma(1 + 0.34u_2)} \quad (1)$$

ET_o = reference evapotranspiration for a day (mm day^{-1})

R_n = net radiation at the crop surface ($\text{MJ m}^{-2} \text{day}^{-1}$)

G = Soil heat flux ($\text{MJ m}^{-2} \text{day}^{-1}$)

T = mean daily air temperature at 2 meter height ($^{\circ}\text{C}$)

u_2 = wind speed at 2 meter height (ms^{-1})

e_s = saturation vapour pressure (kPa)

e_a = actual vapour pressure (kPa)

$e_s - e_a$ = saturation vapour pressure deficit (kPa)

Δ = slope of vapour pressure curve (kPa $^{\circ}\text{C}^{-1}$)

γ = Psychrometric constant (kPa $^{\circ}\text{C}^{-1}$)

T_{hr} = mean hourly air temperature ($^{\circ}\text{C}$)

The above FAO Penman and Monteith equation is a close representation of the physical and physiological factors governing the evapotranspiration process. To compute ET_o from FAO-56 Penman-Monteith approach following intermediate inputs are calculated as follows:

19.4.1 Saturation vapour pressure (e_s)

As saturation vapour pressure (SVP) is related to air temperature, it can be calculated as:

$$e^o(T) = 0.6108 \exp\left[\frac{17.27T}{T + 237.3}\right]$$

$e^o(T)$ = Saturation vapour pressure (kPa) at the air temperature T

T = air temperature ($^{\circ}\text{C}$)

19.4.2 Slope of saturation vapour pressure curve (Δ)

The relationship between saturation vapour pressure (SVP) and temperature Δ , is required. The slope of the curve at a given temperature is given by:

$$\Delta = \frac{4098[0.6108 \exp\left(\frac{17.27T}{T + 237.3}\right)]}{(T + 237.3)^2}$$

Δ = slope of saturation vapour pressure curve at air temperature T [kPa $^{\circ}\text{C}^{-1}$]

19.4.3 Actual vapour pressure (e_a)

As the dewpoint temperature is the temperature to which the air needed to be cooled to make the air saturated, the actual vapour pressure (AVP) can be computed as follows:

$$e_a = \left(\frac{RH}{100}\right) e_s$$

RH = Relative humidity (%)

e_s = Saturation vapour pressure (kPa)

19.4.4 Psychrometric constant (γ)

The psychrometric constant (γ) is given as:

$$\gamma = \frac{C_p P}{\varepsilon \lambda} = 0.000665 * P$$

P = atmospheric pressure (kPa)

λ = latent heat of vaporization (2.45 MJkg $^{-1}$)

C_p = Specific heat at constant pressure ($1.013 \times 10^{-3} \text{ MJ kg}^{-1} \text{ K}^{-1}$)

e = ratio of molecular weight of water vapour and dry weight (0.622)

19.4.5 Extraterrestrial radiation (R_a)

The radiation striking perpendicular at the top of the earth's atmosphere called the solar constant ($0.082 \text{ MJ m}^{-2} \text{ min}^{-1}$). The local intensity of radiation is dependent on angle between the direction of Sun's rays and the normal to atmosphere. This angle will change within a day and with latitude on different days of the year. Solar radiation received at the top of the earth's atmosphere on a horizontal surface is called extraterrestrial (solar) radiation, R_a . It is computed using astronomical units as listed by Iqbal (1983).

$$R_a = \frac{24(60)}{\pi} G_{SC} d_r [\omega_s \sin(\varphi) \sin(\delta) + \cos(\varphi) \cos(\delta) \sin(\omega_s)]$$

R_a = Extra-terrestrial radiation [$\text{MJ m}^{-2} \text{ day}^{-1}$]

G_{SC} = Solar constant ($0.82 \text{ MJ m}^{-2} \text{ min}^{-1}$)

d_r = inverse of relative distance between earth and sun

ω_s = Sunset hour angle (radian)

φ = Latitude (radian)

δ = Solar declination (radian)

19.4.6 Solar or shortwave radiation (R_s)

The radiation penetrates the atmosphere, some of the radiation is scattered, reflected or absorbed by the atmospheric gases, cloud and dust. The amount of solar radiation reaching horizontal plane is known as the incident solar radiation at surface R_s . The R_s should be in $\text{MJ m}^{-2} \text{ day}^{-1}$.

19.4.7 Net solar or net shortwave radiation (R_{ns})

The net shortwave radiation is net balance between incoming and reflected solar radiation in short wave range and is given by,

$$R_{ns} = (1 - \alpha) R_s$$

R_{ns} = net solar or shortwave radiation [$\text{MJ m}^{-2} \text{ day}^{-1}$]

α = albedo which is 0.23 for reference grass (e.g. Alfalfa)

R_s = incoming solar radiation [$\text{MJ m}^{-2} \text{ day}^{-1}$] received at ground surface

19.4.8 Net longwave radiation (R_{nl})

The longwave radiation emission is proportional to the absolute temperature of the surface raised to the fourth power as per Stefan-Boltzmann law. The net radiation leaving the earth's surface is however, less than emitted due to the absorption and downward radiation from the sky. The atmospheric constituents like water vapour, clouds, carbon dioxide and dust are absorbers and emitters of longwave radiation. Their concentration should be vital for assessing the net outgoing radiation. The Stefan-Boltzmann law is corrected for water vapour and cloudiness by assuming the concentration of other atmospheric constituents remain constant.

$$R_{nl} = \sigma [T_K^4] \left(0.34 - 0.14\sqrt{e_a} \right) \left(1.35 \frac{R_s}{R_{so}} - 0.35 \right)$$

R_{nl} = net outgoing longwave radiation [$\text{MJ m}^{-2} \text{day}^{-1}$]

σ = Stefan-Boltzmann constant [$4.903 \times 10^{-9} \text{ MJ K}^{-4} \text{m}^{-2} \text{day}^{-1}$]

T_K = Mean absolute temperature (K) during a day

e_a = actual vapour pressure [kPa]

$\frac{R_s}{R_{so}}$ = relative short wave radiation (≤ 1)

R_s = estimated solar radiation [$\text{MJ m}^{-2} \text{day}^{-1}$]

R_{so} = calculated clear sky radiation [$\text{MJ m}^{-2} \text{day}^{-1}$]

The term $(0.34 - 0.14\sqrt{e_a})$ expresses the correction for air humidity and becomes smaller if humidity increases. The cloudiness is expressed as $\left(1.35 \frac{R_s}{R_{so}} - 0.35 \right)$ and it becomes smaller if the cloudiness increases and hence R_s decreases.

The clear-sky radiation, R_{so} is required for computing net long wave radiation

$$R_{so} = (0.75 + 2 \times 10^{-5} Z) R_a$$

Z = station elevation above sea level (meter)

R_a = Extraterrestrial radiation [$\text{MJ m}^{-2} \text{day}^{-1}$]

The above equation is valid for station elevation less than 6000 m having low air turbidity. The equation was developed by linearizing Beer's radiation extinction law as a function of station elevation and assuming that the average angle of the sun above the horizon is about 50° . For areas of high turbidity caused by pollution or airborne dust or for regions where the sun angle is significantly less than 50° so that the path length of radiation through the atmosphere is increased, an adaption of Beer's law can be employed where P is used to represent atmospheric mass:

$$R_{so} = R_a \exp \left(\frac{-0.0018 * P}{K_t \sin \varphi} \right)$$

K_t = turbidity coefficient, $0 < K_t \leq 1.0$ where $K_t = 0.0$ for clean air and

$K_t = 1.0$ for extremely turbid, dusty or polluted air.

P = atmospheric pressure [kPa]

φ = angle of the sun above the horizon [radian]

R_a = extraterrestrial radiation [$\text{MJ m}^{-2} \text{d}^{-1}$]

19.4.9 Net radiation (R_n)

The net radiation (R_n) is difference between the incoming net shortwave radiation (R_{ns}) and the outgoing net longwave radiation R_{nl} .

$$R_n = R_{ns} - R_{nl}$$

19.4.10 Wind speed

For calculation of ET_0 , wind speed measured at 2 meter above the surface is required. To adjust wind speed data obtained from instruments placed at elevations other than the standard heights of 2 meter, a logarithmic wind speed profile may be used for such conversion.

$$u_2 = u_z \frac{4.87}{\ln(67.82z - 5.42)}$$

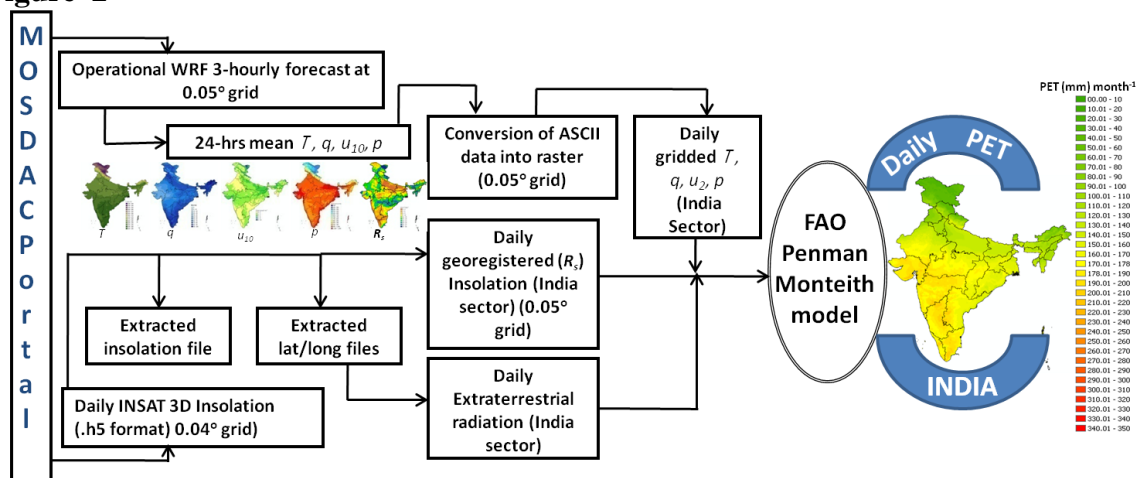
u_2 = wind speed at 2 meter above ground surface [$m s^{-1}$]

u_z = measured wind speed at z meter above ground surface [$m s^{-1}$]

z = height of measurement above ground surface [m]

19.4.11 Flow chart

Figure 2



19.4.12 Steps for operational implementation

The following steps need to be followed for operational implementation of Potential evapo-transpiration product generation :

- Daily (24 hours) average meteorological data are to be carried out by averaging 3-hourly forecast from WRF (ASCII format) at $0.05^\circ \times 0.05^\circ$ spatial grid for all the four variables
- Maximum , minimum air temperatures and relative humidity need to be generated from 3-hourly forecasts in a given day
- Conversion of all ASCII outputs of (i) and (ii) to raster of dimension approx. $0.05^\circ \times 0.05^\circ$ grid resolution
- Conversion of all INSAT 3D generated insolation output to raster of dimension approx. $0.05^\circ \times 0.05^\circ$ grid resolution
- Reprojection of operational daily insolation product present Transverse Mercator to geographic projection
- Resampling of gridded insolation to WRF grid resolution followed by subsetting for India with same dimensions as that of WRF.
- Integration of reprojected daily insolation and 2-D surface of WRF variables in to FAO P-M model to generate regional spatial output of daily ET_o is given in flow diagram (Figure 2).

19.5 Outputs

Table 3

19.5.1 Format of the output and the domain

Parameter	Unit	Min	Max	Accuracy	Temporal resolution	Spatial resolution
Daily Potential Evapo-transpiration output consist of (i) ET ₀ (ii) Latitude (iii)Longitude	mmd ⁻¹	0.5 5°N 68°E	15 40°N 100°E	80 to 90%	Daily Ten-day	~ 5 km

Table 4

Parameter	Data format	Upper left and lower right corner coordinates	Scan lines and columns	Gains and offsets for converting actual values
Daily Potential Evapo-transpiration output consist of (i) ET ₀ (ii) Latitude (iii)Longitude	In HDF5 format BYTE Floating-point	Upper left : 68°E, 40°N Lower right : 5°N, 100°E	Indian domain (approx. 676 x 721)	Gain for ET data 0.1, offset zero

19.6 Validation of INSAT 3D generated daily Potential evapo-transpiration

19.6.1 Data required

Table 5

Sensors	Parameters	Time scale	Source
Agro-Met Station (AMS)	Radiation, routine weather variables	Half-an-hourly basis	MOSDAC & EME-VS project database
MODIS	MOD16 product containing Potential evapotranspiration at 1 km	Eight-day basis	http://www.ntsg.umt.edu/project
Reanalysis field	Pot evap.	Daily, monthly basis	MEERA 2D / NCEP

19.7 Study of Potential Evapo-transpiration with K1 VHRR data

The spatio-temporal pattern of monthly cumulative ET_o for year 2011 is shown in Figure 3. The gradual increase and decrease was observed throughout the year with the seasonal

transition. Monthly ET_o linearly increased throughout India from January to June and then decreased in monsoon during July and August. After that, gradual rise in September coincident to higher insolation due to withdrawal of monsoon. The ET_o again decreases in October and November but there is rise in western part of India during December due to increase in day length in last dekad of December.

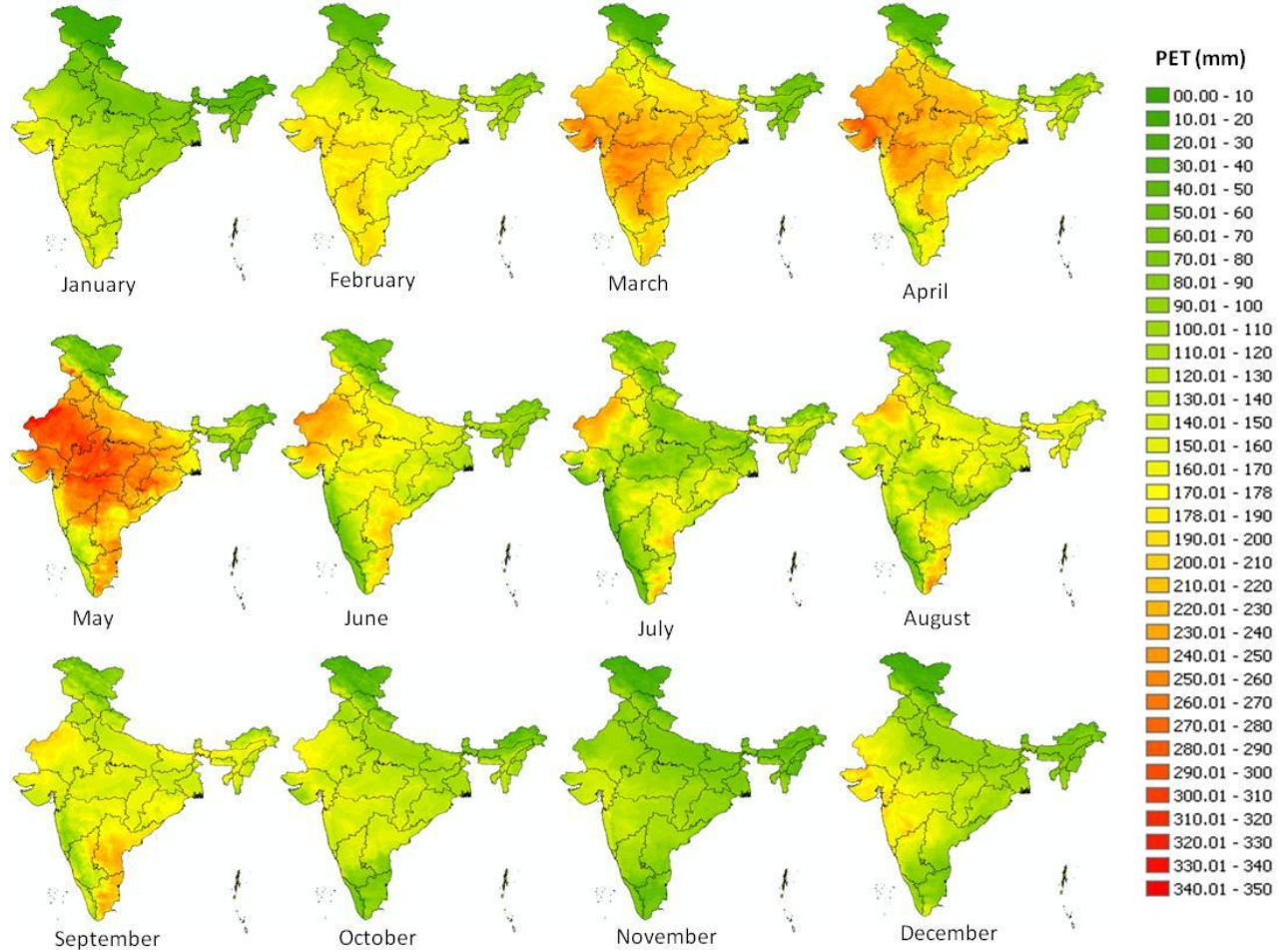


Figure 3. Example of monthly distribution of ET_o from VHRR insolation and WRF forecasts over Indian region

19.7.1 Sensitivity of P-M model to weather variables for error budgeting

The sensitivity of P-M model ET_o was carried out by Bois et al (2008) using ‘Sobol’ method. It consists of numerous simulations of the models using two independent samples of ‘N’ repetitions (rows) and ‘k’ input variables (columns), retrieved from existing data or randomly generated data from the probability distribution function (PDF) of each ‘k’ input variable. One or several variables in the first sample are substituted by the same variable (s) taken from the second sample. For each of the $(2^k - 1)$ possible combinations of variable substitutions between the two samples, ‘N’ runs of the model are computed. The sensitivity of the model to input variables was based on so-called sensitivity or Sobol’ indices, which were calculated on the principle of the decomposition of the total variance (V) of the model output, in response to individual or simultaneous variations of the ‘k’ model inputs.

In oceanic climate, the results of monthly sensitivity analyses computed using Southwest area (SW) data show clear seasonal trends (Figure 4). During the winter period (from November to February), wind speed is the main source of variation in ET_0 values calculated using P-M method (e.g. 38% of ET_0 total variance in January). Then come relative humidity and air temperature (32% and 17% of ET_0 total variance in January, respectively). Solar radiation, daily amplitude of air temperature and daily amplitude of relative humidity have little impact on evapo-transpiration process during winter. This trend changes during March and October. From April to September, ET_0 is mostly sensitive to solar radiation (up to 74% of ET_0 total variance in May, and 70% in July). From May to July, P-M formula is not very sensitive to relative humidity, air temperature and their diurnal amplitudes. Mean daily air temperature participate from 11% to 15% of ET_0 variance, from May to September. Total sensitivity indices show that, when added to other variables' variations, air temperature has a greater impact on ET_0 variability during summer, and wind speed has a greater impact during winter (Figure 4B).

In Mediterranean climate, sensitivity of ET_0 computation to climate input variables using P-M method in Southeast area (SE) is very close to the one observed. Wind speed as a major impact on ET_0 calculation during winter and solar radiation is clearly the most influent variable during summer (Figure 4C and D). The present analysis highlights the great sensitivity of this Penman–Monteith formula to solar radiation during summer period, when ET_0 reaches its highest values, and when its calculation is critical for irrigation process and ecological modelling. These results were obtained for Mediterranean and Oceanic climate, at medium latitudes. A recent work published by Gong et al. (2006) on a large range of climatic conditions in Southern China leads to similar results, except for relative humidity which had a greater impact on ET_0 during winter than it has been shown in the present study. Considering the results of Penman–Monteith sensitivity to solar radiation, it seems reasonable to evaluate the benefits of satellite-sensed solar radiation to ET_0 calculation.

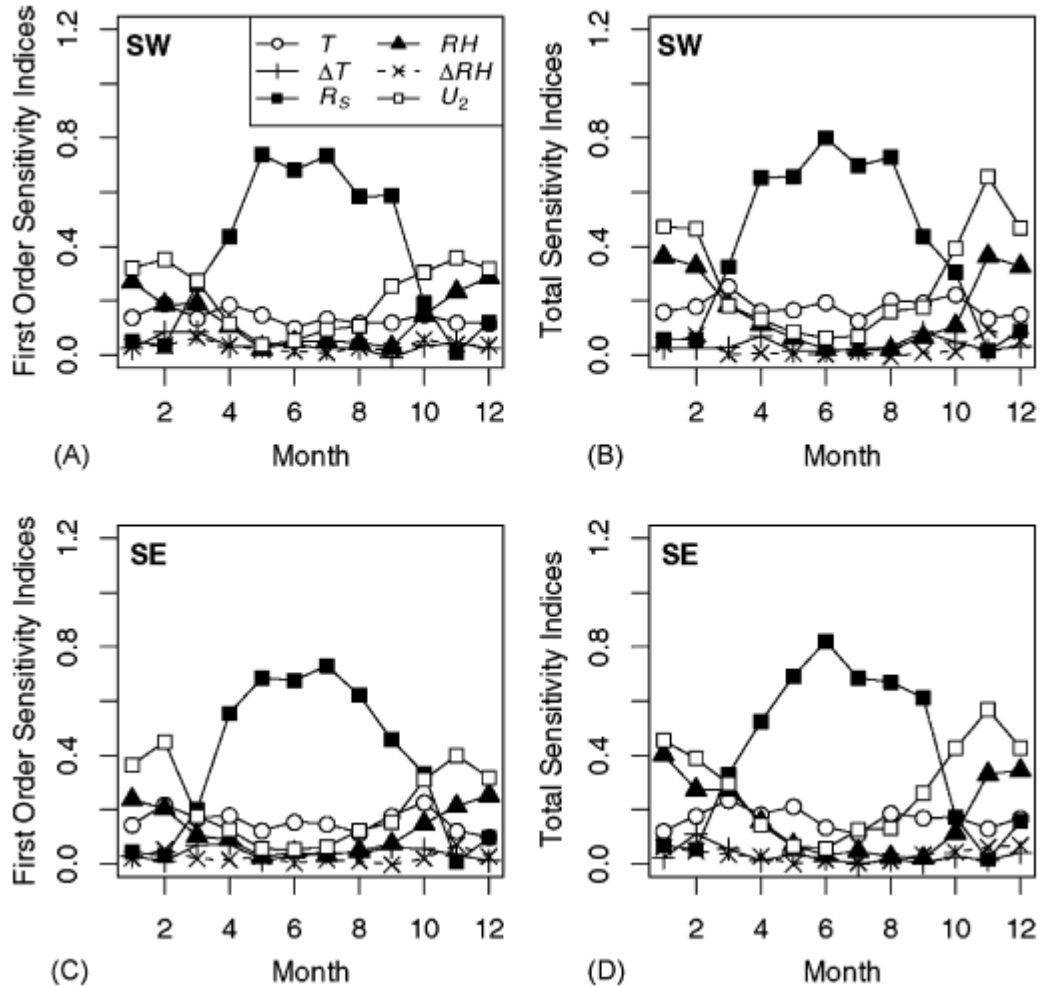


Figure 4. Plots of sensitivity indices (A–C) Southwest area (SW). and (D–F) Southeast area (SE) of ET_0 to different climatic variables

19.7.1.1 Preliminary comparison with in-situ measurements

The daily insolation product (Bhattacharya et al., 2012b) from K1VHRR available through MOSDAC (Meteorological and Oceanic Satellite Data Archival Centre) for the period January 1, 2011 to December 31, 2011 to derive radiation parameters and other routine inputs from WRF forecast were ingested into P-M model to generate daily, dekalal (ten-day) and monthly ET_0 estimates at regional scale following the steps mentioned in section 4.12. To validate satellite based regional ET_o estimates, the measurements from INSAT-linked AMS (Agro-Met-Station) data were used (Bhattacharya et al, 2009). The AMS provides all radiation and meteorological variables at 30 minutes interval and represent a fetch area of 1 km x 1 km. The AMS data from six sites over different agro-climatic zones were used to compute ET_o on daily basis for different time period as listed in Table 6. The ET_o was calculated on daily basis using AMS half-an-hour average measurements.

Table 6. Details of AMS stations and data used

Station Name	Time period	Agro-climatic region	Latitude	Longitude
Naraingarh Farm, PAU (Punjab)	1 Jan to 20 April	Trans gangetic plain region	30°36'44.92"N	76°19'17.75"E
BCKV(W. Bengal)	1 Jan to 7 June	Lower gangetic plain region	22°41'53.46"N	77°44'5.06"E
Jaisalmer (Rajasthan)	11 July to 30 Sept	Western dry region	26°50.83'N	71°18.083"E
Pawerkheda (Madhya Pradesh)	1 Jan to 8 June	Central plateau and hill region	22°41'53.46"N	77°44'5.06"E
LPSC Mahendergiri (Tamil Nadu)	1 Jan to 7 Dec	Southern plateau and hill region	8°17'53.89"N	77°33'21.77"E
Diglipur (Andaman & Nicobar)	15 Feb to 8 Dec	Island region	13°15'25"N	93°0'27"E

19.7.1.2 Validation results

A. Daily scale

Daily ET_o estimated using P-M approach was compared with daily ET_o computed from AMS measurements for different agro-climatic regions as listed in Table 6. The 1:1 plot is shown in Figure 5 and temporal comparison is shown in Figure 6. The daily ET_o computed from AMS varied from 0.7 mm to 12.0 mm while satellite derived ET_o varied from 1.1 to 11.7 mm over different seasons for selected stations. The error analysis showed the root mean square deviation (RMSD) varied from 1.13 to 3.82 $\text{mm} \text{d}^{-1}$ to the tune of 21 to 38 % of measured mean over six stations (Table 7). The overall pooled data set showed RMSD of 1.34 $\text{mm} \text{d}^{-1}$ with 29% deviation from measured mean. This was due to high fluctuation of ET_o on daily temporal scale as shown in Figure 5 for all six AMS stations. The estimated daily ET_o showed underestimation as well as overestimation for all AMS stations but extent of temporal pattern matches quite well in all the stations.

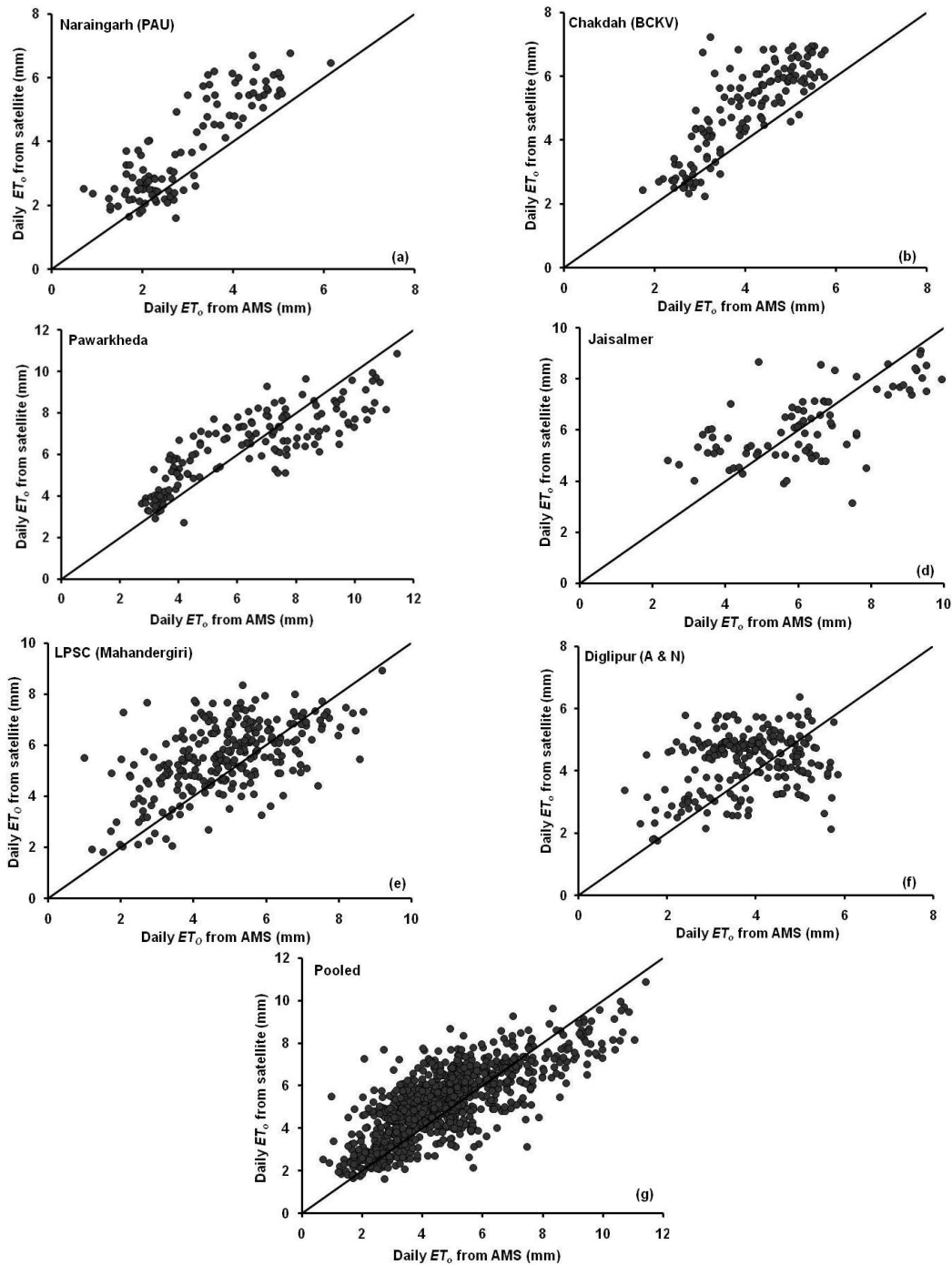


Figure 5. 1:1 scatter plot between daily ET_o from AMS and estimates from satellite and WRF

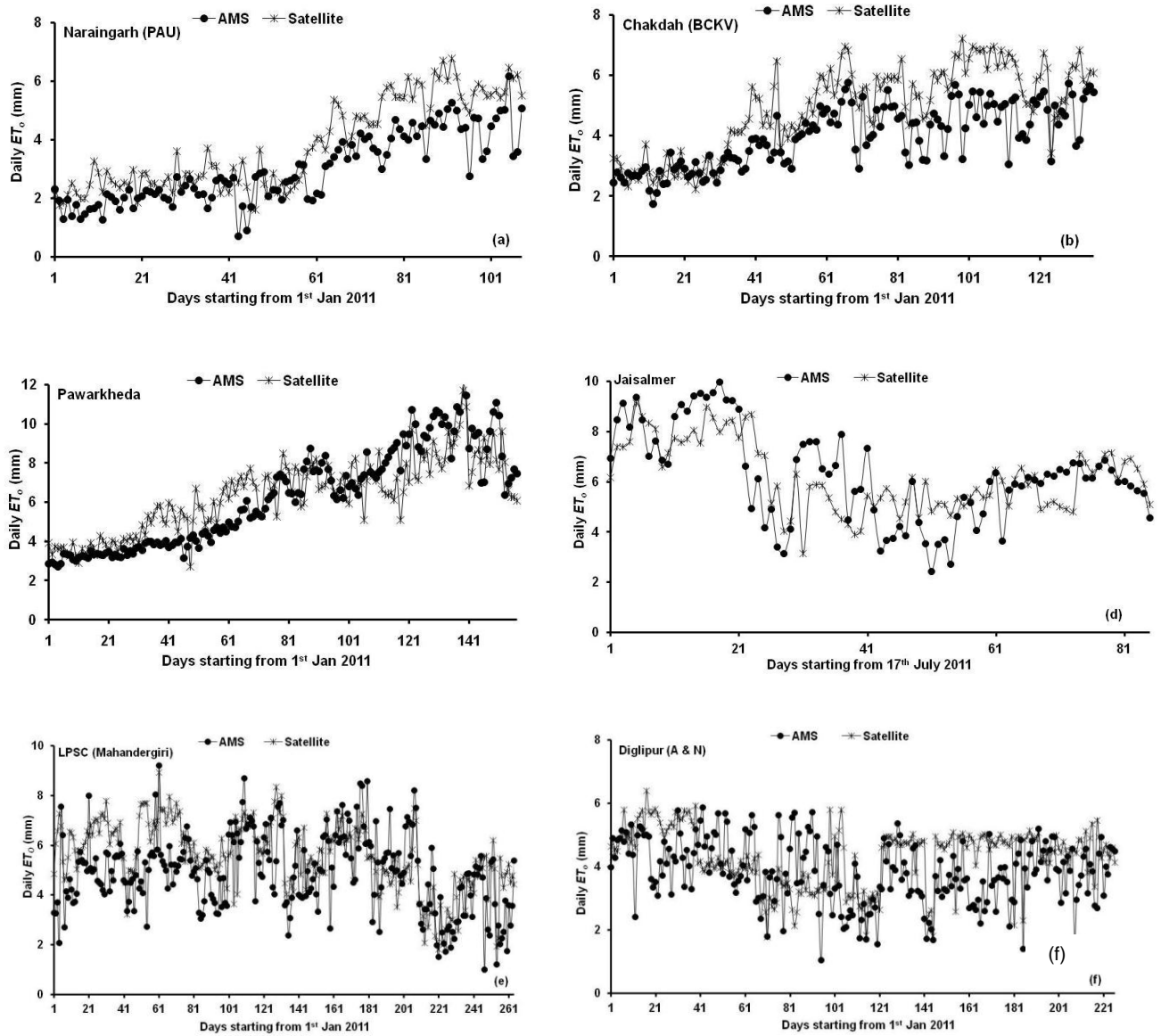


Figure 6. Comparison of temporal profile of daily ET_o from AMS and spatial estimates

Table 7. Error statistics for daily ET_o

Station name	N	RMSD	RMSD(% of AMS mean)	MAB
Naraingarh Farm (PAU)	108	1.1	38.1	0.9
Chakdah (BCKV)	136	1.2	31.1	1.0
Pawarkheda	157	1.3	21.5	1.1
Jaisalmer	85	1.4	22.8	1.1
LPSC	265	1.5	31.1	1.8
Diglipur	226	3.8	33.0	1.0
Overall	977	1.3	29.0	1.0

$$\text{RMSD (Root Mean Square Deviation)} = \sqrt{\frac{\sum_i [(P_i) - (O_i)]^2}{N}}$$

$$\text{MAB (Mean Absolute Bias)} = \frac{\sum_i ABS[(P_i) - (O_i)]}{N}$$

Where $P_i = PET_{AMS}$ at i^{th} case

$O_i = PET_{estimated}$ at i^{th} case

$N = \text{number of daily paired datasets}$

B. Dekadal scale

The daily ET_o fluctuation was high and leads to high deviation from measured AMS mean so data were summed for 10-days for further analysis. The 10-days cumulative estimated ET_o was validated with cumulative ET_o from AMS data. The temporal 10-day ET_o over different stations are shown in Figure 7 for six selected stations and error statistics are given in Table 8. The dekadal change in estimated ET_o matched well with AMS ET_o . The seasonal change was also well captured in 10-day cumulative ET_o .

In Naraingarh, Punjab, the comparison was made for the period from January to April. In January and February, ET_o remained low in the range of 16 mm to 24 mm due to low radiation and temperature. It started rising in March and reached up to 62 mm per dekad. The rise and fall of computed ET_o was well captured in estimated ET_o during January to April. The RMSD was 9.3 mm which is 28.9% of AMS mean for the stated period. The 1:1 scatter (Figure 8) showed a 91 % correlation.

Table 8. Error statistics for dekadal (10-day) ET_o

Station Name	N	RMSD	RMSD (%of AMS mean)	MAB
Naraingarh, Punjab	14	9.3	28.9	8.2
Chakdah, W.B.	14	10.5	27.4	9.1
Pawarkheda, M.P.	15	10.4	18.6	8.9
Jaisalmer, Rajasthan	8	6.3	10.2	5.8
Mahendragiri, T.N.	30	9.4	21.4	8.2
Diglipur, A.N.	22	9.3	25.0	8.4
Overall	99	9.5	21.6	8.3

$N = \text{number of dekadal paired datasets}$

The site in West Bengal represents lower gangetic plain of agro-climatic regions having moderate cold season of January and February to moderate hot season during March and April. During this period *rabi* rice is grown with available irrigation facility. The dekadal temporal profile of estimated ET_o matched well with AMS ET_o but showed small amount of deviation during April. This may be due to application of irrigation water in rice crop and was only captured in computed ET_o from AMS but not reflected in estimated ET_o . The temporal variation of dekadal ET_o was 28 to 30 mm in January with gradual rise in February. The maximum ET_o was observed in April due to rise in temperature and

radiation load. This seasonal change of ET_o was well captured in the estimates. The overall RMSD was found to be 10.5 mm (27.4 % of AMS mean) on January to April with respect to AMS.

The central plateau and hill agro-climatic region is represented here by AMS at Powarkheda site. The area falls under the catchment of Narmada where annual rainfall varies from 800 to 1200 mm. The wheat crop is dominant during *rabi* season. The estimated dekad ET_o estimates matched well throughout January to May. The dekad ET_o high and low value matched quite well and estimated ET_o always remained high as compared to AMS ET_o up to March during growth of wheat crop. After that, estimated ET_o underestimated measured ET_o . In January, both showed low values in the range of 30 to 37 mm and 35 to 46 mm but goes up to 97 to 103 mm (AMS) and 82 to 94 mm (estimated) in May. The temporal profiles matched quite well and showed RMSD of 10.4 mm over ten days (16.6% deviation from AMS mean).

The typical Indian arid region lies in western, dry agro-climatic region and represented here by Jaisalmer. The climate remains hot throughout the year except in January and February. The data over monsoon season (July, August and September) were used for computation of ET_o . In this part of India, S-W monsoon starts in July and it was well captured by dekad ET_o variation during stated months. During July, ET_o remained higher but later in the season it reduced in both the cases. The satellite estimated ET_o showed both underestimation and overestimation for selected season as compared to AMS. The temporal profile of ET_o of two followed the same pattern. The RMSD of 6.3 mm was found for monsoon season which is 10.2% with respect to AMS ET_o .

The southern part of India, AMS located in LPSC Mahandragiri represents the natural scrub vegetation. The AMS data for January to May and August to November were used for comparison with AMS ET_o value. The temporal profile of dekad ET_o matched well with AMS ET_o . The difference between two was maximum during north-east monsoon season (January to February) but later on, the difference was reduced further in May and November. The data showed a RMSD of 9.4 mm (21.4% deviation of measured AMS mean).

The island agroclimatic region of Andaman & Nicobar have different climatic conditions as compared to above stated regions. As this region is surrounded by Bay of Bengal so climatic condition remains humid throughout the year. The data from March to May and August to November were used for comparison. The AMS ET_o on an average had a range of 23 to 50 mm throughout the selected time domain. Similar order of magnitude was observed for estimated ET_o . The dekad behaviour of estimated ET_o matched well with AMS ET_o but showed little higher deviation during August and September. It showed RMSD of 9.3 mm (25.0% of AMS mean).

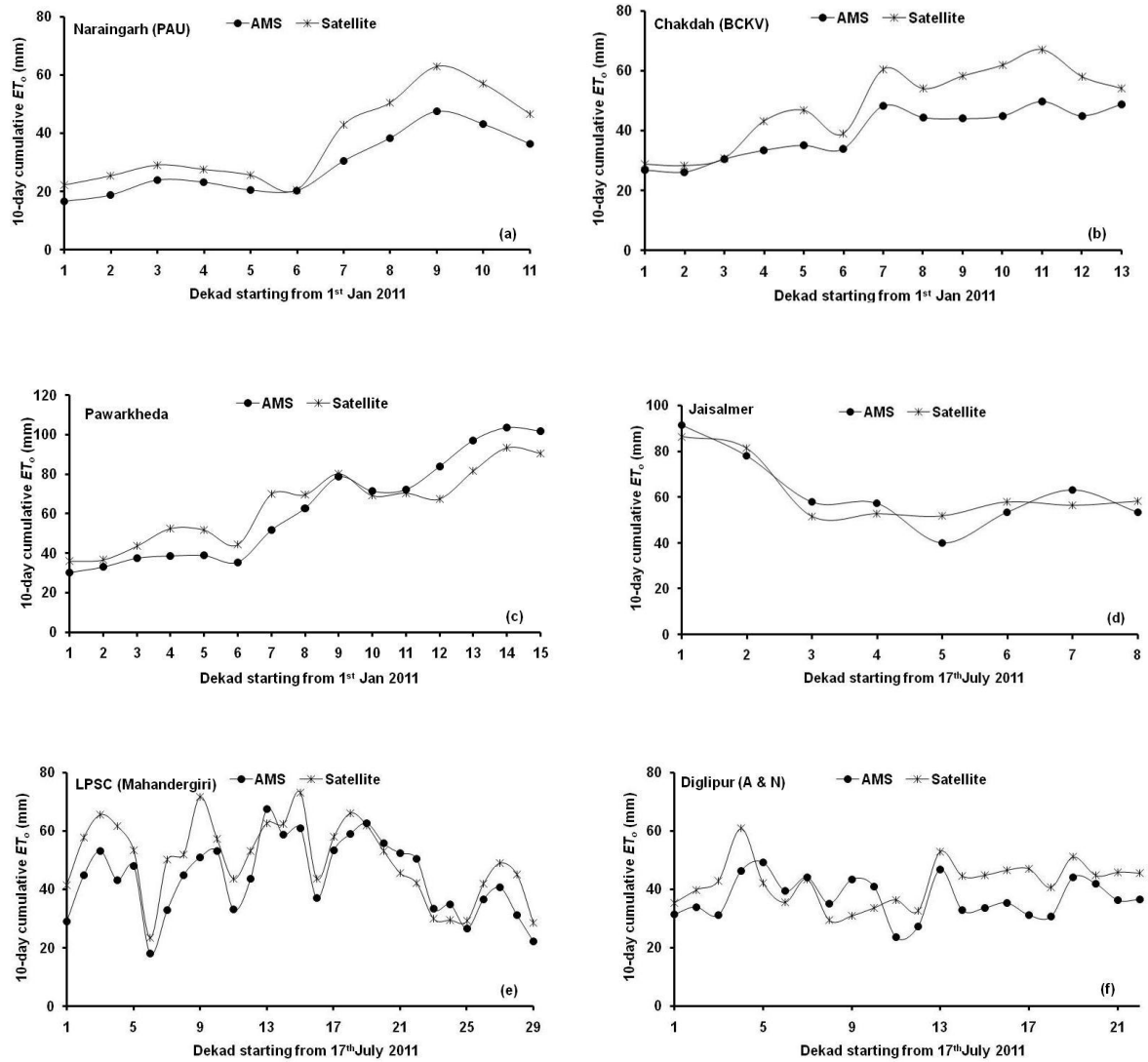


Figure 7. Temporal profiles of dekalal sum of potential evapotranspiration (ET_o) computed from AMS and fusion of satellite and WRF data.

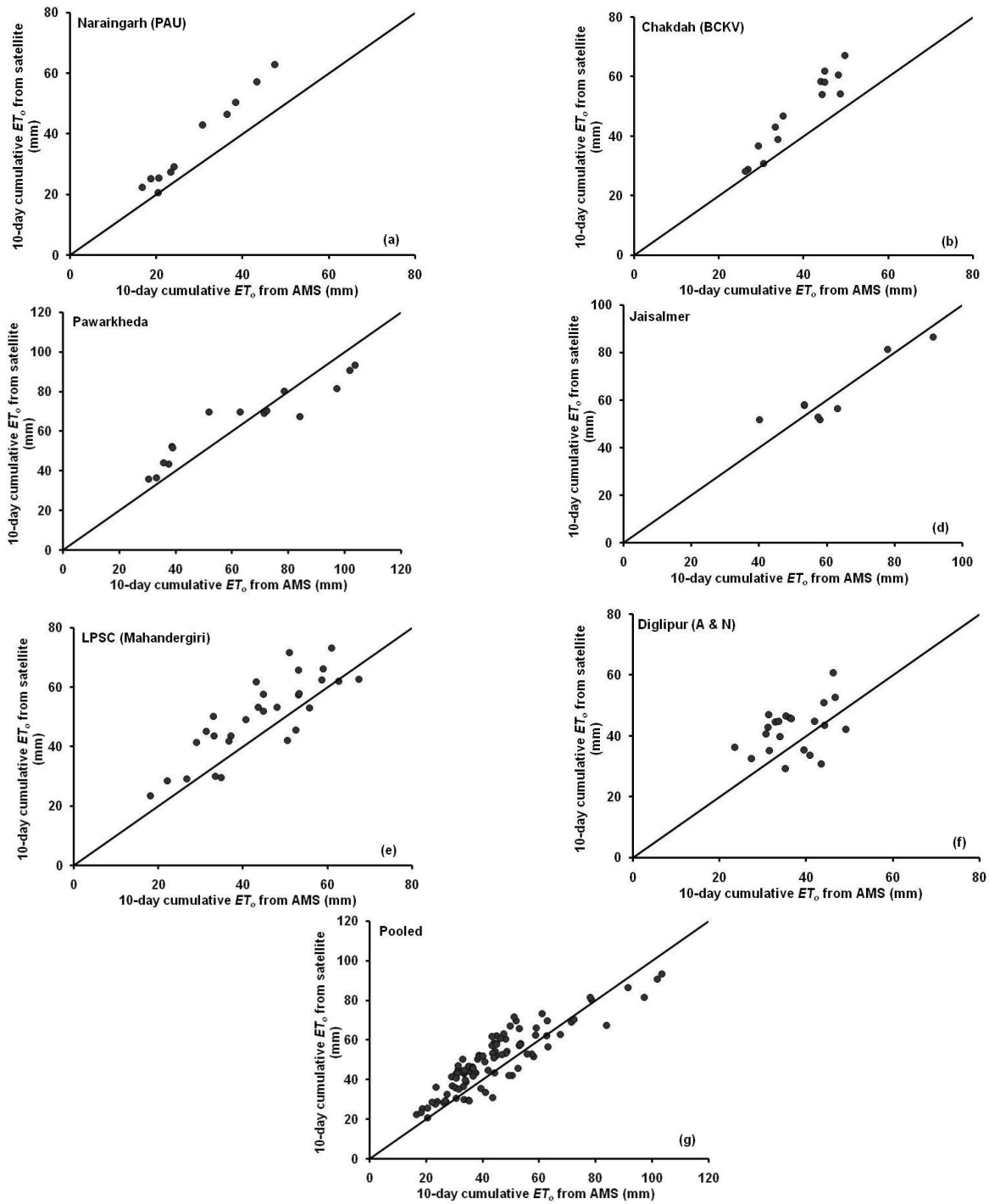


Figure 8. 1:1 Scatter plot between dekadal PET computed from AMS and with spatio-temporal estimates.

19.7.1.3 Error analysis of ET_o for variable-time accumulation

The daily estimated and AMS ET_o was compared for different time windows viz. 3-day, 5-day, 7-day and 10-day. The correlation coefficient between estimated and measured ET_o gradually increased from daily to 10-day but maximum increase was observed from daily to 7-day i.e from 8% to 23% for six AMS stations. The rise of correlation coefficient from 7-day to 10 days was nominal in Nariangarh (PAU) (0.7%), Chakdah (BCKV) (2%), Pawarkheda (2.3%) and Jaisalmer (6.3%) as compared to LPSC (Mahandergiri) (13.8%) and Diglipur (12.6%) as shown in Figure 8. Similarly per cent deviation from mean of AMS measurements also showed a similar trend as the deviation drastically came down from daily to 7-days and further nominal decrease in 10-day except than in Jaisalmer. For the latter, it decreases from 14.8% to 10.2% for 7 to 10-days as marked in Figure 9. The analysis showed that error was significantly reduced from daily to 7-days and further in 10-days over different agro-climatic zones. This will help us use this ET_o data in various applications on different time scales with known errors.

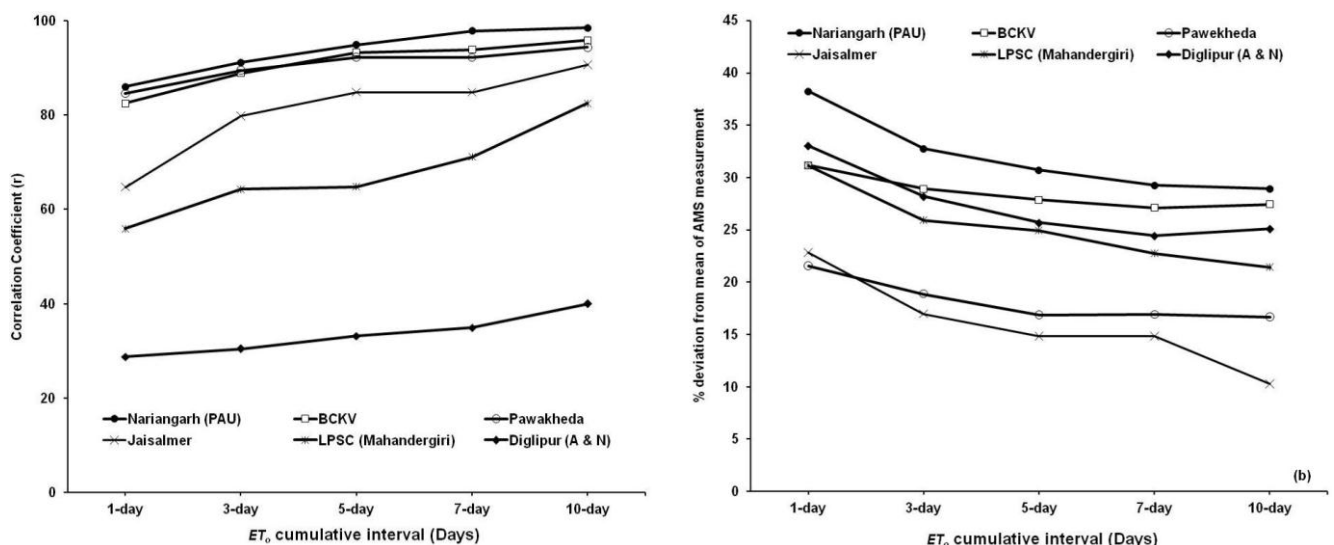


Figure 9. Error analysis of ET_o for variable-time accumulation

19.7.1.4 Comparison of errors from similar studies elsewhere

Considering the results of Penman–Monteith sensitivity to solar radiation, it seems reasonable to evaluate the benefits of satellite-sensed solar radiation to estimate spatial ET_o as no regular spatial record are available for solar radiation. Choudhury (1997) attempted monthly global ET_o at $0.25^\circ \times 0.25^\circ$ from P-M method using solar radiation from International Satellite Cloud Climatology Project (ISCCP). He derived vapour pressure and vapour pressure deficit (VPD) from TIROS operational vertical sounder TOVS data with air temperature based on interactive GCM forecast retrieval assimilation system applied to the TOVS data. He has compared the estimated ET_o with lysimeter data and on monthly scale the error was found between 15 to 40% from measured mean.

Bois et al. (2008) used remotely sensed solar radiation and weather data from AWS equipped with humidity, thermal sensors and cup anemometer to estimate ET_o using

FAO-56 P-M method. They used the solar radiation prepared from Meteosat data by following Heliosat-2 method (Rigollier et al. 2004). The study found that most of the errors occurred in partial cloudy days due to uncertainties in retrieving daily solar radiation. On daily scale, the RMSD was between 0.34 to 1.32 mm (11% to 110% from daily mean) but on annual scale the RMSD remained low (11% of ET_o mean value) at $0.05^\circ \times 0.05^\circ$ spatial resolution. This error again came down to (9.1% to 5% of ET_o mean value) during clear days in summer. Our study was unique as we used operational product of K1VHRR insolation WRF 3-hourly forecast for at 0.05° grid for estimation of ET_o at $0.08^\circ \times 0.08^\circ$. On daily scale, RMSD was 1.1 to 3.8 mm (21% to 38% from measured mean) but it came down to 10% to 28% from mean on dekalal time scale and further in monthly scale (21% from monthly mean). The overall error at different temporal domain were found in good harmony with reported errors in other part of world.

19.8 Sources of errors / uncertainties in ET_o estimates and validation issues

The following sources of uncertainties were traced out while evaluating spatial output of ET_o estimates and its comparison with ground reference

(i) Influence of vegetation in AMS

The FAO 56 P-M method is generally applied for a specific site using meteorological and radiation data from meteorological observatories or AWS weather data including direct measurement of radiation. In India, ISRO-AWS does not provide solar radiation data in terms of standard energy units. IMD AWS provide data with some lag period. The sensitivity analysis of P-M method by Gong et al. (2006) and Bois et al. (2008) highlighted that solar radiation and wind speed were clearly the most influent variables for ET_o estimation. The pyranometer and routine weather data from AMS are used. But these measurements were recorded over different vegetation cover types. Since vegetation growth influences ambient weather conditions, the ET_o computed from AMS would definitely have differential vegetation influence when compared to ET_o estimates from integration of satellite based solar radiation and WRF forecast weather variables.

(ii) Scale mismatch

Spatial ET_o was generated at approximately 8 km spatial resolution with 64 km^2 pixel area while the average footprint of AMS varies from 0.25 to 1 km^2 . This scale mismatch puts constrain in validation statistics. But this scale mismatch will reduced with INSAT 3D.

(iii) Difference in time sampling

For spatial ET_o , daily solar radiation was generated from diurnal observations at instantaneous snapshots with half-an-hour interval from satellite platform. But half-an-hourly averages from AMS measurements were used to generate validation datasets

(iv) Accuracy in cloud flagging

The product version of surface insolation algorithm has cloud detection capability of approximately 80%. It could not detect thinner clouds. Therefore, ET_o estimates have higher errors during the period more cloudy spells or for AMS sites with higher cloud dynamics such as Diglipur (A & N), LPSC, Mahendragiri etc.

(v) *Quality of WRF forecast*

An initial evaluation of WRF forecast quality showed an average error to the tune of 1-2°C, RH of 5-10% as compared to large error in wind speed and predicted radiation terms. The inherent errors in first three variables will have implications on the overall error budget.

19.9 Future scope of improvement

Recent improvement has taken place in the cloud detection of INSAT 3D insolation algorithm using additional criteria based on cloudiness index from VIS band observations. Much of the uncertainties in insolation and ET_o estimates in cloudy-skies will hopefully be improved.

Recent study on impact of updated vegetation fraction from INSAT 3A CCD showed improvement in air temperature, humidity and rainfall forecast from WRF. The use of real-time satellite based other land surface products such as albedo, LAI and soil moisture would definitely help in improving the quality of operational forecasts. Future work should address the retrieval / estimation of those variables from Indian geostationary satellites.

The INSAT 3D will provide relatively finer spatial resolution of observation of insolation. This would reduce the scale mismatch uncertainty for validation.

19.10 References

1. Allen, R., Pereira, L., Raes, D., Smith, M., 1998. Crop evapotranspiration. Guidelines for Computing Crop Water Requirements. FAO Irrigation and Drainage Series No. 56, 15-28.
2. Anderson, M. C., Norman, J. M., Mecikalski, J. R., Otkin, J. A., & Kustas, W. P. (2007). A climatological study of evapotranspiration and moisture stress across the continental United States based on thermal remote sensing: 1. Model formulation. *Journal of Geophysical Research-Atmospheres*, 112.
3. Blaney, H. F. and Criddle, W. D. (1950). Determining water requirements in irrigated areas from climatological and irrigation data (pp. 48). : US Department of Agriculture Soil Conservation Service.
4. Bhattacharya, B.K., Dutt, C.B.S. and Parihar, J.S. (2009). INSAT uplinked Agromet Station – A scientific tool with a network of automated micrometeorological measurements for soil-canopy-atmosphere feedback studies. *ISPRS Archives XXXVIII-8/W3 Workshop Proceedings: Impact of Climate Change on Agriculture*. Paper no. TS9.13
5. Bhattacharya, B. K. and Kumar, P. (2012a). AMS data Utilization for preliminary evaluation of operational forecast from WRF model. *SAC project report (no. awaited)*
6. Bhattacharya, B. K., Padmanabhan, N., Ramakrishnan, R., Panigrahy, S. and Parihar, J.S. (2012b). Algorithm Theretical Basis Document (ATBD) for surface insolation using Kalpana-1 VHRR observations. SAC/EPSA/ISRO-GBP/SR/ATBD/02/2012

7. Bhattacharya, B. K., Mallick, K., Patel, N.K. and Parihar, J.S. (2010). Regional clear sky evapotranspiration over agricultural land using remote sensing data from Indian geostationary meteorological satellite. *Journal of Hydrology*, 387, 65-80.
8. Bois, B., Pieri, P., Van Leeuwen, C., Wald, L., Huard, F., Gaudillere, J. P., Saur, E. (2008). Using remotely sensed solar radiation data for reference evapotranspiration estimation at a daily time step. *Agricultural and Forest Meteorology*. 148, 619-630.
9. Brutsaert, W. (1982). *Evaporation into the atmosphere: Theory, History and Applications* (1st ed.). Springer.
10. Choudhury, B. J. (1997). Global pattern of potential evaporation calculated from the Penman-Monteith equation using satellite and assimilated data. *Remote Sensing of Environment*. 61, 64-81.
11. Dalton, J. (1802). Experimental essays the constitution of mixed gases; on the force of steam of vapor from waters and other liquids in different temperatures, both in a torricellian vacuum and in air; on evaporation; and on the expansion of gases by heat. *Memoirs of the Manchester Lit. & Phil. Soc.*, 535–602.
12. Gong, L., Xu, C.-y., Chen, D., Halldin, S., Chen, Y.D. (2006). Sensitivity of the Penman–Monteith reference evapotranspiration to key climatic variables in the Changjiang (Yangtze River) basin. *J. Hydrol.* 329 (3/4), 620–629
13. Hargreaves, G. H. (1975). Moisture availability and crop production. *Transactions of the ASAE*, 18, 980–984.
14. Kumar, P., Singh, R., Joshi, P.C., Pal, P.K. (2011). Impact of Additional Surface Observation Network on Short Range Weather Forecast during Summer Monsoon 2008 over Indian Subcontinent. *Journal of Earth System Sciences*, 120, 2011, 1-12.
15. Monteith, J. L. (1964). Evaporation and environment. The state of movement of water in living organisms. *Symposium of the society of experimental biology*. 205–234.
16. Monteith, J. L. (1973). *Principles of environmental physics*. Edward Arnold Press. 241.
17. Penman, H. L. (1948), Natural evaporation from open water, bare soil and grass. *Proc. Roy. Sec. (London) A* 193:120- 145.
18. Priestley, C. H. B., & Taylor, R. J. (1972). On the assessment of surface heat flux and evaporation using large-scale parameters. *Monthly Weather Review*, 100,81–92.
19. Rigollier, C., Lefevre, M., Wald, L. (2004). The method Heliosat-2 for deriving shortwave solar radiation from satellite images. *Solar Energy* 77 (2), 159–169.
20. Rowntree, P. R. (1991). Atmospheric parameterization for evaporation over land: Basic concept and climate modeling aspects. In T. J. Schmugge & J. C. André (Eds.), *Land surface evaporation fluxes: Their measurements and parameterization* (pp. 5–30). New York: Springer-Verlag.
21. Singh, R., Kumar, P. and Pal, P. K. (2011). Assimilation of Oceansat-2 Scatterometer Derived Surface Winds in the Weather Research and Forecasting Model. (IEEE Transactions on Geoscience & Remote Sensing <http://dx.doi.org/10.1109/TGRS.2011.2164410>

22. Skamarock W. C., Klemp J. B., Dudhia J., Gill D.O., Barker D.M., Duda M.G., Huang X.Y., Wang Wand Powers J. G. (2008). A description of the Advanced Research WRF Version 3. NCAR/TN-475 STR; NCAR Technical Note, Mesoscale and Microscale Meteorology Division, National Center of Atmospheric Research, June 2008, 113 pp.
23. Thornthwaite, C. W. (1948). An approach towards a rational classification of climate. *Geographical Review*, 38, 55–94.

20. Surface Insolation over Land

S.No.	Product Name	Spatial Resolution	Temporal Resolution
1	3DIMG_L2C_INS	4 km approx.	30 minutes

20. Surface insolation over land from INSAT 3D

20.1 Algorithm Configuration Information

19.1.2 Algorithm name

Land surface insolation

19.1.3 Algorithm identifier

3DIMG_L2C_INS

19.1.4 Algorithm specification

Version	Date	Prepared by	Description
1.0	14 February 2013 Revised on 1 April 2014	Dr. Bimal K. Bhattacharya & Dr. Rahul Nigam	Land surface insolation baseline document

20.2 Introduction

The amount of solar radiation flux or irradiance in the shortwave ($0.3 - 3 \mu\text{m}$) reaching at ground surface is known as surface or global insolation. It is composed of direct and diffuse components. While reaching the ground from top-of-atmosphere solar radiation is attenuated by different atmospheric constituents such as water vapour, ozone, aerosol, air molecule, clouds and fogs through scattering and absorption processes. The molecular scattering by air molecules is known as Rayleigh scattering. The aerosol scattering is Mie scattering. The component of solar radiation that reaches earth surface without deviation from original direction is known as direct or beam insolation. The component of solar radiation reaching earth surface after scattering is known as diffuse insolation. Diffuse component is composed of three components such as : Rayleigh scattered, aerosol scattered and reflected multiple scattered insolation. Clouds play major role in attenuating solar radiation while reaching earth surface. It is accountable for 70% depletion of solar radiation depending on its type, distribution and ice-cloud proportioning of three-dimensional vertical structure. Moreover, aerosol acts as cloud condensation nuclei (CCN). The contribution of clouds towards diurnal variability of insolation is more than aerosol and atmospheric gases specially during monsoon season. Fog also plays an important role in attenuating solar radiation in the winter. The interaction of solar radiation with atmospheric constituents and clouds is shown in Figure 1.

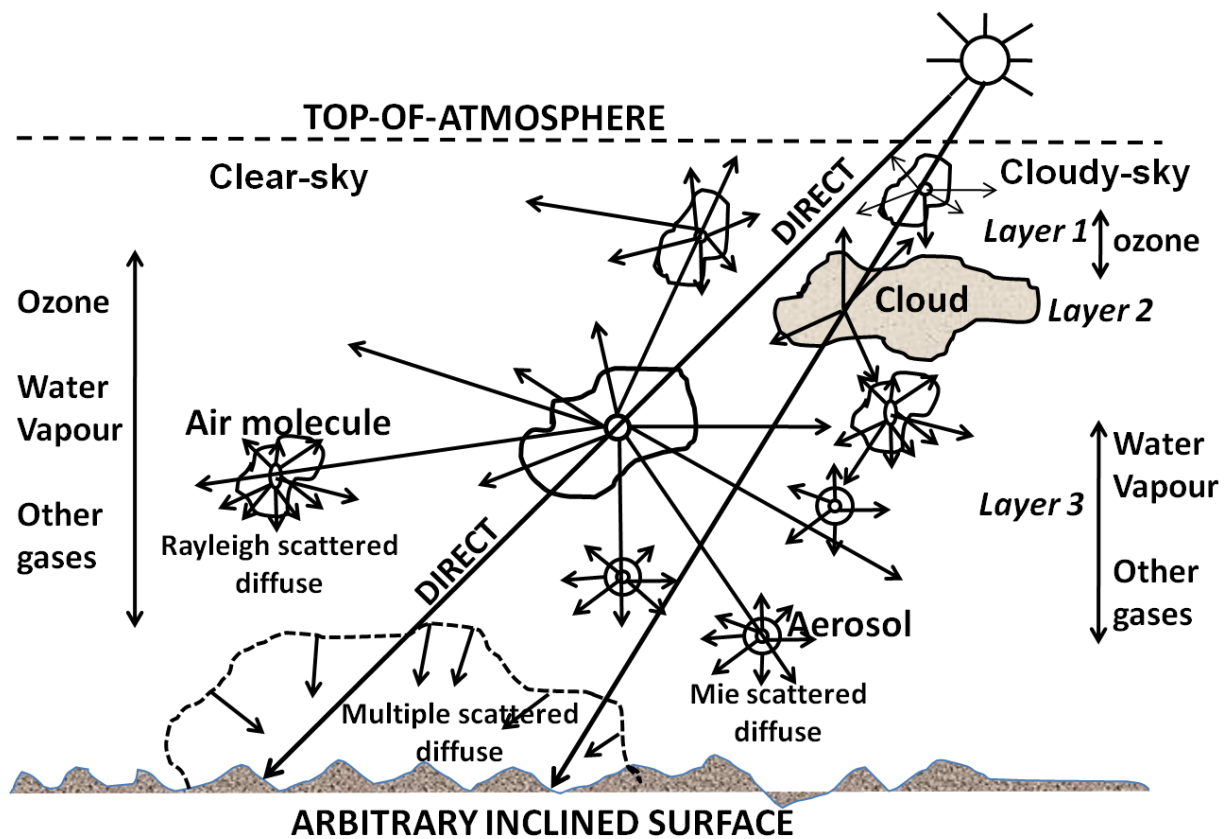


Figure 1: Interaction of incident solar radiation (irradiance) with major atmospheric agents for its depletion in clear and cloudy skies

Surface insolation is the driving input for eco-physiological processes such as evapotranspiration (Jacobs et al, 2000) and photosynthesis (Chen et al, 1999). The trapped energy through formation of ATP and NADPH in 'light reaction' is utilized in the 'dark reaction' of photosynthesis to produce carbohydrates. The photosynthetic response of plant species to different light intensity determines primary productivity, therefore, it is as critical component to assess bio-energy and bio-fuel resources. Insolation is the major contributor of earth's radiation and energy budget. It is also a crucial input to crop simulation model for yield forecasting.

In climate change adaptation and mitigation strategies, use of renewable energy resources such as solar energy plays important role to maintain a emission-free green and safe environment. Monthly solar radiation maps on spatial scale are very important to locate solar energy conversion systems such as solar PV or thermal power plants (Janjai et al, 2005). Conventionally, these maps are constructed from high density network of pyranometers. However, in India, a very sparse network of pyranometer stations is presently operating. Interpolation from such sparse network produces large errors (60-70%) due to large uncertainties of intermittent diurnal cloud cover, cloud types and atmospheric turbidity in cloudless skies. Moreover, high maintenance costs and lack of availability of real-time data are major impediments. Several estimation models have been developed based on temperature amplitude, sunshine hours or cloud cover and

combination of temperature, humidity, rainfall, but these require site and season specific calibration coefficients and thus difficult to extrapolate. Moreover, such models do not explicitly consider the role of atmospheric constituents such as air molecule, aerosol, water vapour, ozone. The use of remote sensing observations from geostationary satellite sensors that have high temporal sampling frequency (multiple passes every day) are ideal to capture spatio-temporal variability of surface insolation for those regions where regular measurements from sparse radiation network and their availability are not consistent till date.

20.2.1 Overview and background

Broadly, two approaches such as (a) statistical or empirical (Tarpley, 1979; Noia et al, 1993) and (b) physical or radiative transfer (Tanahashi et al, 2001) schemes are in use to estimate surface insolation using geostationary satellite data using broad visible band and thermal infrared bands. Empirical or statistical techniques for surface insolation include Heliosat (Dagestad, 2004), contrast ratio (Rosema et al, 2004) approaches applied to Meteosat. Heliosat model has been developed under Helioclim project of Europe and has undergone several revisions. It is based on deriving cloudiness index from maximum, minimum albedo in a time series and current albedo. This cloudiness index is converted into surface insolation through clearness index (ratio of surface insolation and insolation at-top-atmosphere) using pre-determined empirical relations. Physical modelling schemes of clear sky insolation are of two types: (i) ‘top-down’ approach that corrects incoming solar irradiance (Pinker and Lazlo, 1992; Lu et al, 2010) for atmospheric attenuation (absorption and scattering) before reaching the surface (ii) ‘bottom-up’ approach that determines surface albedo (Gautier et al, 1980) from planetary albedo by separating out atmospheric interferences and arrive at surface insolation through inversion. Several schemes are available to account for attenuation of solar radiation flux passing through clouds either using cloud top albedo or reflectivity that represents cloud backscatters or from combination of cloud-top albedo or temperature or cloud optical thickness and cloud-top pressure. Spectrally integrated irradiance model and three-layer cloudy scheme were implemented with Kalpana-1 VIS, WV and thermal IR bands to estimate instantaneous and daily insolation (Bhattacharya et al, 2012 and 2013). Statistical models are only based on visible band observations while physical model requires inputs from both visible and thermal bands in addition to determination of cloud mask. While the errors of statistical techniques varied from 12–17% for daily total insolation (Kandirmaz et al, 2004), the physical approach produces error of about $\pm 19\%$ on hourly basis and lesser for daily to monthly averaging. Moreover, the statistical models call for region-specific updates of coefficients through ground datasets which are time consuming.

20.2.2 Objectives

The objectives of this document are :

- (i) To outline a physical algorithm for surface insolation estimation
- (ii) To highlight the sensitivity of algorithm and evaluation of estimates from this algorithm applied with Kalpana-1 VHRR data
- (iii) To describe the path of integrating algorithm with Indian geostationary satellite (e.g. INSAT 3D) based on cloud properties, aerosol, water vapour and ozone products

- (iv) To implement the algorithm in a software compatible to IMDPS geophysical parameter retrieval chain for automated generation of instantaneous and daily insolation
- (v) To describe validation strategy of operational product of INSAT 3D insolation against *in-situ* measurements, reanalysis data, other satellite products
- (vi) To outline the scope of improvement in the accuracy of the estimates in future

20.2.3 Instrument characteristics

The Indian National Satellite (INSAT) system is a joint venture of the Department of Space (DOS) and India Meteorological Department (IMD). It provides half-an-hour observations from six channel ‘Imager’ and 19-channel ‘Sounder’. The Imager has one broad VIS (0.55-0.75 μm) band (1 km x 1 km), one SWIR (1.55 – 1.70 μm) band (1km x 1km), one MIR (3.8 – 4.0 μm) band (4 km x 4 km), one water vapour (6.5 - 7.1 μm) band (8 km x 8 km) and two split thermal (10.2 - 11.3 μm , 11.5 - 12.5 μm) bands (4 km x 4 km). The sounder has 19 channels to provide vertical profiles of atmospheric temperature and humidity. There are 22 geophysical products which are scheduled to be available from an operational processing known as INSAT Meteorological Data Processing System (IMDPS). This has been successfully implemented in Kalpana-1 VHRR and INSAT 3A VHRR and CCD (Anonymous, 2005). This system provides both ‘full-globe’ and ‘sector’ data products. Presently, there are 40 acquisitions against a maximum of 48 acquisitions per day. Raw data after reception at each acquisition are corrected for servo, lineloss, radiometry, stagger and oversampling removal using data products scheduler. These result into automated generation of co-registered data with fixed projection having fixed number of rows and columns. Examples of diurnal data product in VIS band from INSAT 3D over Asia Mercator are shown in Figure 2.

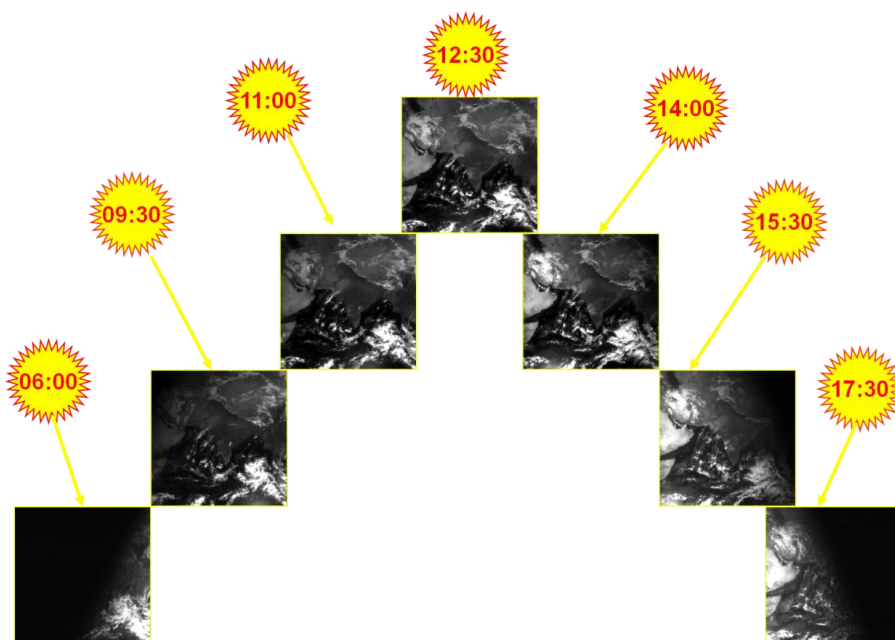


Figure 2. Diurnal VIS imageries from over Asia Mercator

20.3 Inputs

20.3.1 Static data

Table 1

Parameters	Source
1. Calibration coefficient of VIS band DN into radiance and WV, thermal IR band into radiance and brightness temperatures	DP h5 product
2. Angular geometry (solar elevation, view zenith and relative azimuth angles)	DP h5 product
3. Time of year and time in a day	Calendar day and time of image acquisition from DP file name
4. GTOPO5 elevation database at 8km at similar projection to VHRR bands	http://edc.ftp.cr.usgs.gov/pub/data/goto30/global/
5. Integrated Rayleigh optical depth in the shortwave	Pre-determined from elevation data and spectral integration

20.3.2 Image and preprocessing data (Dynamic)

Table 2

Parameter	Resolution	Quantization	Accuracy	Source
Radiometric and geometric corrected gray counts in VIS, brightness temperatures of Imager WV and thermal IR bands at each acquisition	Pixel (4 km x 4 km)	10 bit for VIS counts & 16 bit for temperatures	Co-registration accuracy less than 4000 m	DP h5 product with fixed number of rows and columns
Geophysical product on precipitable water, aerosol optical depth at 550 nm and	Pixel (4 km x 4km)	16-bit	Accuracy > 80% for precipitable water and ozone Accuracy >	GP h5 product with fixed number of rows and columns

columnar ozone at each acquisition			85% for aerosol optical depth	consistent with DP h5 product
Cloud mask and fog mask at each acquisition	4 km x 4 km	8-bit	Accuracy > 90%	GP h5 product with fixed number of rows and columns consistent with DP h5 product
Geolocation file containing latitude and longitude corresponding to coregistered Imager data	Pixel wise	-	Less than 1 pixel between acquisitions	DP h5 product

20.3.3 Other auxiliary data and model inputs

Table 3

Parameters	Source
Global climatology of 8-day ozone and aerosol optical depth at 550 nm at $1^\circ \times 1^\circ$ at least from three years average as alternative to 3D aerosol product	Eight-day global atmospheric product ($1^\circ \times 1^\circ$) from MODIS AQUA on total columnar ozone and aerosol optical depth at 550 nm (AOD_{550}) as alternative to 3D aerosol product

20.4 Algorithm functional specifications

The algorithm uses a clear-sky model with spectrally integrated radiative transfer scheme that requires solar zenith angle, elevation, slope, aspect of terrain, aerosol, water vapour and ozone as inputs. This accounts for depletion of instantaneous incoming solar radiation flux due to atmospheric perturbances or turbidity. In cloudy-sky, a separate three-layer scheme was implemented where cloud is assumed plane parallel sandwiched between upper and lower cloudless atmospheric layers.

20.4.1. Clear-sky model

20.4.1.1 Direct or beam irradiance (s_{dir}). A simple but accurate spectral irradiance model (Paulescu and Schlett 2003) was used to determine instantaneous direct or beam irradiance (in Wm^{-2}) over the entire shortwave range (0.3 to 3 μm). An integrated spectral (10 nm interval) atmospheric transmittance scheme developed by them was used in the

present study. The instantaneous direct or beam irradiance (s_{dir}) over the entire shortwave region was computed in Wm^{-2} as,

$$s_{\text{dir}} = s_0 \tau_R \tau_{\text{o}z} \tau_w \tau_g \tau_A \quad (1)$$

$$s_0 = E_0 (1 + 0.0344 \cos(360(N/365))) \quad (2)$$

Where, $\tau_{\text{o}z}$ = ozone transmittance, τ_R = Rayleigh transmittance, τ_w = water vapour transmittance, τ_A = aerosol transmittance, τ_g = transmittance of other gases, E_0 = solar constant (1367 Wm^{-2}), S_0 = Instantaneous irradiance (Wm^{-2}) at top-of-atmosphere, N = calendar day

The Rayleigh transmittance, τ_R , was computed as,

$$\tau_R = \text{EXP}[-0.008735\lambda^{-4.08} m_p] \quad (3)$$

The τ_R was computed over 10 nm interval and integrated over whole shortwave spectrum. The digital elevation model (DEM) were used to compute m_p and Rayleigh transmittance for each pixel. Here, m_p is optical airmass at a given atmospheric pressure 'p' and λ is wavelength (μm)

The relative optical airmass, m , is computed as :

$$m = 1 / [\text{Cos}\theta_s + 0.15(93.885 - \theta_s)^{-1.253}] \quad (4)$$

Here, θ_s = solar zenith angle

The generalized form of integrated spectral transmittance for a given atmospheric quantity, x , has the following functional form :

$$\bar{\tau}(x) = \text{EXP}[-x(a + bx + cx^d)] \quad (5)$$

Here, $x = ml$ for ozone (l = ozone content in atm-cm), $x = mw$ for water vapour (w = atmospheric precipitable water or columnar water vapour in gcm^{-2}), $x = m$ for other atmospheric gases (g) and $x = m\beta$ for aerosol (β = Angstrom's turbidity factor characterizing atmospheric visibility or haziness based on given aerosol type and size distribution). Here, m is relative optical airmass.

The a, b, c, d are fitted parameters for every extinction process. The values are taken from Paulescu and Schlett (2003) as given in Table 4.

Table 4. Summary of fitted parameters for different atmospheric components influencing radiative transfer through atmosphere (Paulescu and Schlett 2003)

Atmospheric variables	<i>a</i>	<i>b</i>	<i>c</i>	<i>d</i>
Ozone (I)	0.0184	0.0004	0.022	-0.66
Water vapour (W)	0.002	1.67×10^{-5}	0.094	-0.693
Other gases (G)	-5.4×10^{-5}	-3.8×10^{-6}	0.0099	-0.62
Aerosol (B)	1.053	-0.083	0.3345	-0.668

20.4.1.2 Diffuse irradiance (s_{diff}). The instantaneous diffuse irradiance (s_{diff}) is contributed from three components (i) molecular (Rayleigh) scattering (s_R) (ii) aerosol scattering (s_A) and (iii) multiple scattering (s_M) of ground reflected radiation from atmosphere.

$$s_{\text{diff}} = s_R + s_A + s_M \quad (6)$$

$$s_M = (s_{\text{dir}} + s_R + s_A)((\rho_g \rho_a)/(1 - \rho_g \rho_a)) \quad (7)$$

$$s_R = 0.79 s_0 \tau_{\text{oz}} \tau_g \tau_w (1 - (1 - w_0)(1 - m + m^{1.06})(1 - \tau_A)) 0.5 (1 - \tau_R) / (1 - m + m^{1.06}) \quad (8)$$

$$s_A = 0.79 s_0 \tau_{\text{oz}} \tau_g \tau_w (\tau_A / (1 - (1 - w_0)(1 - m + m^{1.06})(1 - \tau_A))) f_c (1 - (\tau_A / (1 - (1 - w_0)(1 - m + m^{1.06})(1 - \tau_A))) \tau_R) / (1 - m + m^{1.06}) \quad (9)$$

w_0 = single scattering albedo assumed as 1.0

The atmospheric albedo, ρ_a , was determined as,

$$\rho_a = 0.0685 + (1 - f_c) (1 - (\tau_A / (1 - (1 - w_0)(1 - m + m^{1.06})(1 - \tau_A))) \tau_R) \quad (10)$$

The ratio (f_c) of forward to backward scattering was determined as,

$$f_c = 0.9302 \cos(\theta_s)^2 \quad (11)$$

Columnar water vapour (**W**), required to compute water vapour transmittances was estimated from a semi-empirical equation developed by Bhattacharya *et al.* (2010) based on differences in brightness temperatures in thermal IR and WV channels of Kalpana-1 VHRR. The aerosol optical depth at 550 nm from MODIS product was converted to

Angstrom ‘ β ’ turbidity parameter to compute aerosol transmittance assuming Angstrom turbidity exponent parameter as 1.3 (Iqbal 1983). The ozone data from MODIS was used to compute ozone transmittance.

The monthly minimum ground brightness from previous thirty days VIS band planetary albedo (ρ_{VIS}) was dynamically determined for each acquisition and was used as surrogate for ground albedo (ρ_g). The planetary VIS band spectral albedo was corrected for Rayleigh scattering. The aerosol scattering effect and cloud interferences on planetary albedo were assumed to be removed with monthly minimum composites understanding that surface properties have not changed significantly within thirty days. The multiple scattering component contributes little to total diffuse irradiance over vegetated region (albedo between 0.1 and 0.3) but is a dominant component over snow bound areas or desert (> 0.3) with significantly higher albedo.

20.4.1.3 Global or total irradiance

Both direct and diffuse irradiance are dependent on the zenith angle of the sun that changes from sunrise to sunset and on the orientation of the surface. On an arbitrarily inclined surface with slope, α , and aspect, ϕ , at a given location on earth surface with latitude, ϕ , the angle (i) between the incident radiation and the normal to the surface is expressed as ,

$$\cos i = \sin \delta (\sin \phi \cos \alpha - \cos \phi \sin \alpha \cos \varphi) + \cos \delta \cos h (\cos \phi \cos \alpha + \sin \phi \sin \alpha \cos \varphi) + \cos \delta \sin \alpha \sin \varphi \sin h \quad (12)$$

$$\delta = 23.45 \sin(360(284 + N)/365) \quad (13)$$

δ = solar declination angle (radian)

h = sun hour angle (radian)

Depending on the terrain properties and solar geometry, the surface may be in the shadow of nearby topographic features; $\cos i$ is then assigned a value of zero that represents no direct irradiances. Diffuse radiation was assumed to be isotropic in distribution in the atmosphere, i.e. the sky is uniformly bright. Depending on the slope and nearby topography, only a fraction of hemisphere might be visible, which is referred as the sky-view factor (V_d), which is time invariant and is dependent only on terrain parameters. The total (S_{tot}) or global irradiances (Wm^{-2}) received on surface at any instance (t) is given by,

$$S_{tot(t)} = S_{dir(t)} \cos i_{(t)} + S_{diff(t)} V_d \quad (14)$$

The V_d is determined as the ratio of diffuse sky irradiance to that on an unobstructed surface. In present algorithm, this was computed using expression given by Kondratyev (1977).

$$V_d = (1 + \text{COS}\alpha)/2 \quad (15)$$

20.4.2. Cloudy-sky model

A three-layer scheme was conceptualized and implemented to compute irradiances in cloudy skies. The first layer corresponds to clear-sky atmosphere over cloud-top where direct and diffuse components were computed using algorithm mentioned in section 3.1. Molecular (above cloud) and aerosol scattering, gaseous transmission due to ozone were considered. Entire aerosol and ozone were assumed to be distributed above cloud. Both direct and diffuse components were computed and the sum of these two resulted into global irradiances without any sky-view factor. The second layer corresponds to plane parallel cloud. The vertical cloud structure and its three-dimensional effects on cloud transmission especially on diffuse component were not considered in the present model. The third layer corresponds to clear-sky atmosphere below cloud. Molecular scattering (air below cloud) was only considered in layer 3. The precipitable water was assumed entirely distributed below cloud and contributed to gaseous transmission along with other gases.

In order to compute Rayleigh scattering above cloud, the height of cloud-top was approximated from cloud-top temperature, maximum clear-sky planetary temperature within previous 30 days, ground elevation and dry-adiabatic lapse rate up to condensation level represented through cloud-top temperature. Here also, direct, diffuse and global irradiances were computed using the principles used in the section 3.1. The irradiance coming out of first and top clear-sky layer after attenuation is considered as the incoming solar radiation flux cloud layer. The energy flux that comes out after being attenuated in cloud layer was considered as influx for third layer (clear-sky layer below cloud) which again gets attenuated to reach at the ground. The global irradiance received at the ground is considered as insolation in cloudy-sky.

The transmission through cloud was computed using Kubelka-Munk theory.

$$t_c = a \text{EXP}(-b \cdot A_c) \quad (16)$$

This relates cloud-top albedo (A_c) with cloud transmittance (t_c). The coefficients (a, b) in the equation 16 vary according to different land use categories which were taken into account through typical ranges (< 0.2 for water bodies, forest; 0.21 to 0.32 for agriculture; >0.3 for desert and snow cover) of ground albedo represented by minimum ground brightness from previous thirty days.

20.4.3 Daily integration

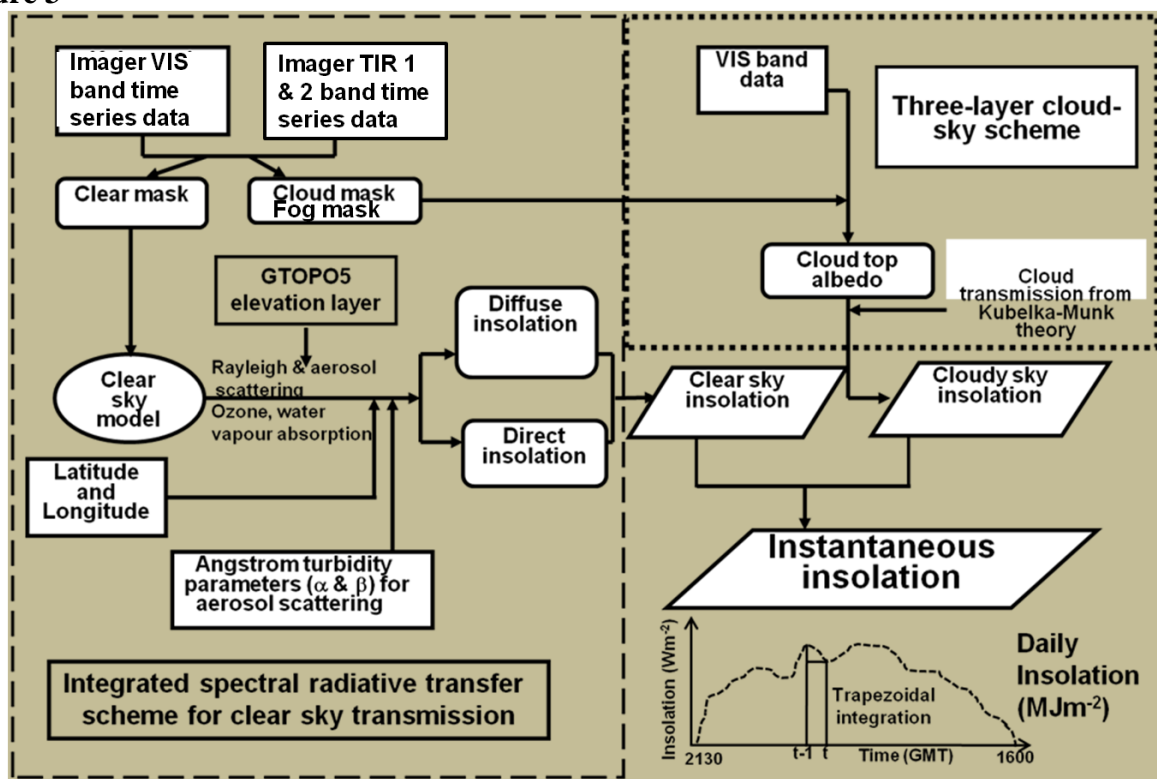
A trapezoidal integration was applied to construct daily integral from diurnal instantaneous global irradiances. The daily integral global irradiance S_d was expressed in MJm^{-2} . The mathematical expression for daily integration is:

$$S_d = 0.864 \sum_{i=0.5}^{23.5} (S_{(i-0.5)} + S_{(i)})/2 \quad (17)$$

Here i represents hours in GMT.

20.4.4 Flow chart

Figure 3



20.4.5 Operational implementation

Step 1: Unpacking and pre-processing

First sub-program should unpack h5 (Hierarchical data format) datasets from INSAT 3D Imager, reads DEM and computes date, time, year from name of file string as well as sun-sensor zenith, azimuth angles. Brightness temperatures in IR and WV bands and VIS albedo (after removing perturbation due to molecular scattering) were also computed from look-up table (LUT) and calibration coefficients provided with h5 datasets.

Step 2 : Generation of minimum ground brightness and maximum brightness temperatures for cloud-fog detection and cloud height determination

This sub-program uses INSAT 3D ‘Imager’ brightness temperatures and VIS band albedo or reflectance of a lead of previous 30 days. The maximum temperatures and minimum albedo were picked up for each pixel at a given acquisition. Both are used as bi-spectral thresholds to detect cloud. In addition, a cloudiness index is generated through normalization of VIS band TOA reflectance, its upper and lower limits. Both dynamic bispectral thresholds and threshold of cloudiness index (> 0.15) are used to for cloud and fog detection and masking during daylight hours. Temperature composites and current acquisition temperature will be used to determine cloud height from dry-adiabatic-lapse-rate (DALR)

Step 4 : Interpolation of climatic gridded AOD₅₅₀, ozone and resampling

Another sub-program should use eight-day gridded ($1^\circ \times 1^\circ$) climatological aerosol optical depth (AOD) and ozone to extract from global products for the latitude and

longitude bounds of south-east Asia corresponding to K1VHRR Asia Mercator sector coverages. These can be resampled down to 8 km spatial resolution using bilinear interpolation and reprojected to INSAT 3D Imager projection.

Step 4 : Generation of time series instantaneous insolation

The main program should compute time series instantaneous global (direct + diffuse) insolation for a given acquisition using the outputs from other sub-programs, clear-sky and cloudy-sky models.

Step 5 : Daily integration

Another program should perform trapezoidal integration of both bias-uncorrected and bias-corrected instantaneous insolation at 23:30 hrs GMT on a given day. This program should fetch instantaneous insolation from different acquisitions on a given day and make a list. This program should first check at least one acquisition within two hours and then daily integration should be performed. It means that If at least well distributed five instantaneous insolation are available in the list, the integration is performed.

The whole algorithm has been implemented with Kalpana-1 VHRR data from 2012 to generate operational products on insolation after the clearance by ATBD review committee set-up by Director, SAC and in-house T & E has also been carried out.

The same algorithm was applied with INSAT 3D ‘Imager’ data to estimate instantaneous insolation over limited datasets

20.5 Outputs

Table 5

Parameter	Unit	Min	Max	Accuracy	Resolution
A. Instantaneous outputs containing (i) Instantaneous insolation without bias correction (ii) Instantaneous insolation with bias correction (iii) Latitude (iv) Longitude	Wm ⁻² Wm ⁻² Degree Degree	0 0	1200 1200	90% 90%	4000 m 4000 m 4000 m 4000 m
B. Daily insolation (i) Insolation (ii) Latitude (iii) Longitude	MJm ⁻²	0	35	90%	8000 m

20.5.1 Format of the output and the domain

Table 6

Parameter	Data format	Upper left and lower right corner coordinates	Scan lines and columns	Gains and offsets for converting actual values
A. Daily insolation (i) Daily insolation (ii) List of files with instantaneous insolation data (iii) Latitude (iv) Longitude	HDF5 format Integer Integer		Fixed scans X columns Fixed scans X columns	Gain = 0.01
B. Coloured pictorial output of daily insolation	Jpeg with colour wedge and vector boundary overlaid	-	-	-

The example of instantaneous surface insolation is shown in Figure 4.

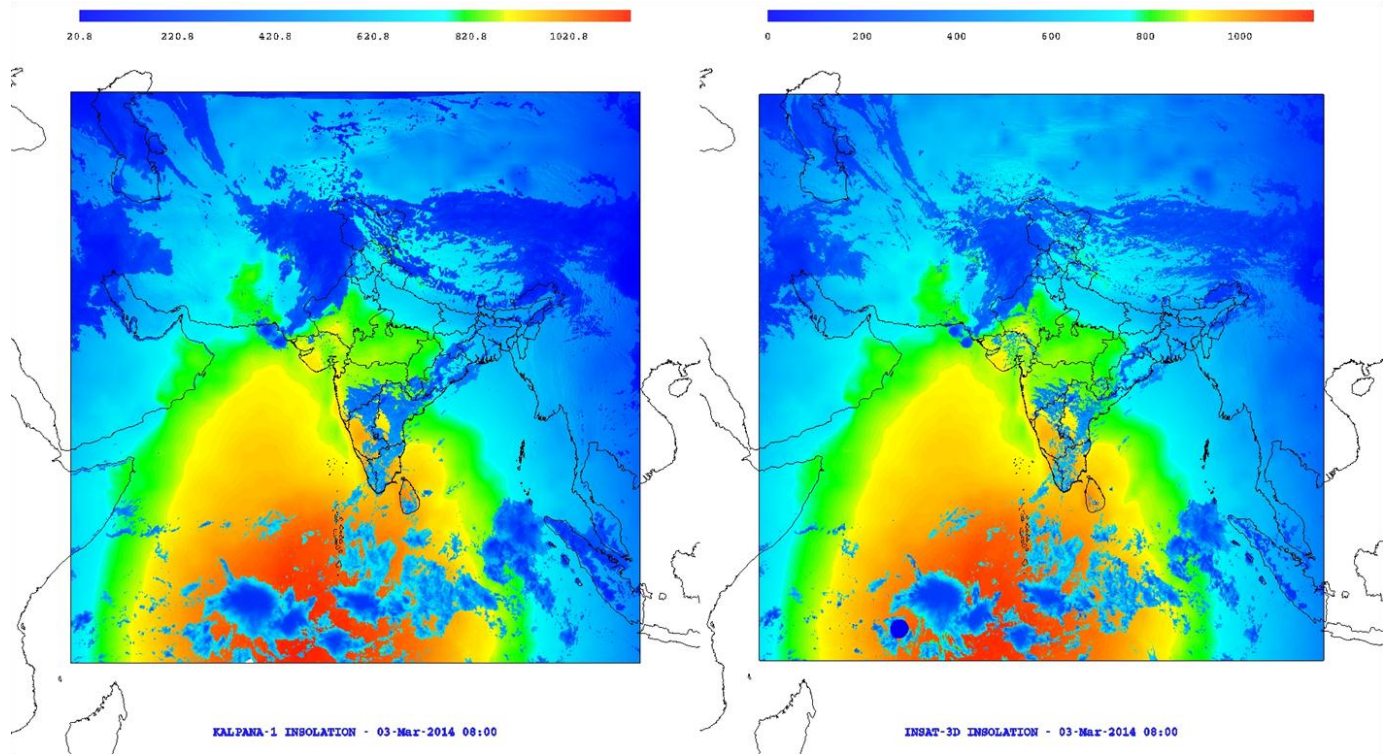


Figure 4. Example of instantaneous surface insolation (0800 UTC) from INSAT 3D ‘Imager’ on 3 March 2014

20.6 Sensitivity analysis for error budgeting

The responses of clear-sky model on global, direct and diffuse instantaneous insolation, direct/diffuse ratio, diffuse fraction to variation in solar zenith angle, atmospheric ozone, water vapour and aerosol optical depth (AOD) at 550 nm were studied. This was carried out with the observed seasonal range of AOD, water vapour and ozone over station Bijapur. The effects of change in aerosol optical depth at 550 nm (AOD_{550}) were studied at low (10-20°) and high (40-70°) levels of solar zenith angles (Figure 5a).

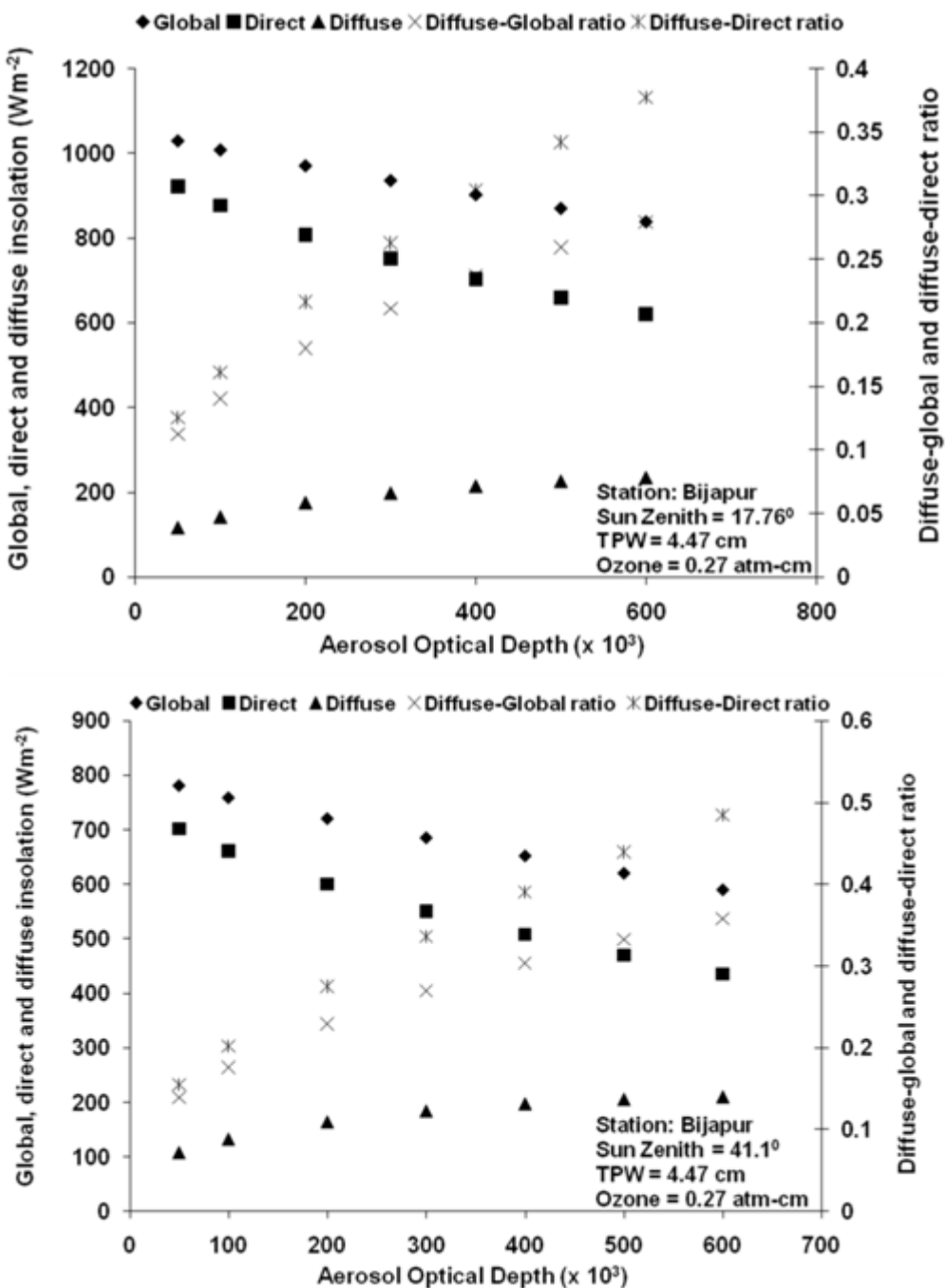


Figure 5a. Sensitivity of the clear-sky insolation model to aerosol optical depth

There was substantial and similar trend of decrease in both global (15-20%) and direct (25-30%) instantaneous insolation for a given range of AOD_{500} (0.05 to 0.6), but the gap between direct and global is reduced at higher solar zenith angle. The steepness of slopes of direct insolation was more negative (-0.67 Wm^{-2}) than global insolation (-0.35 Wm^{-2}). The slopes were less negative (-0.48 Wm^{-2} , -0.35 Wm^{-2}) at higher solar zenith angle for both the cases. Diffuse insolation, in general, showed gradual increase with increase in AOD_{500} but it reached plateau at higher solar zenith angle with AOD_{500} beyond 0.2.

Diffuse fraction was found to show sharp increase between 0.12 to 0.28 and 0.18 to 0.38 at low (17.46°) and high (41.1°) solar zenith angles with increase in AOD₅₀₀ between 0.1 to 0.6. But the higher diffuse fraction was noticed at higher solar zenith angles for similar AOD₅₀₀. It was found that there was practically little decrease (3-7%) in global, direct and diffuse insolation with increase in water vapour between 1.5 to 6.5 cm (Figure 5b). The decrease was still less for ozone (Figure 5c) varying between 240 to 290 dobson units.

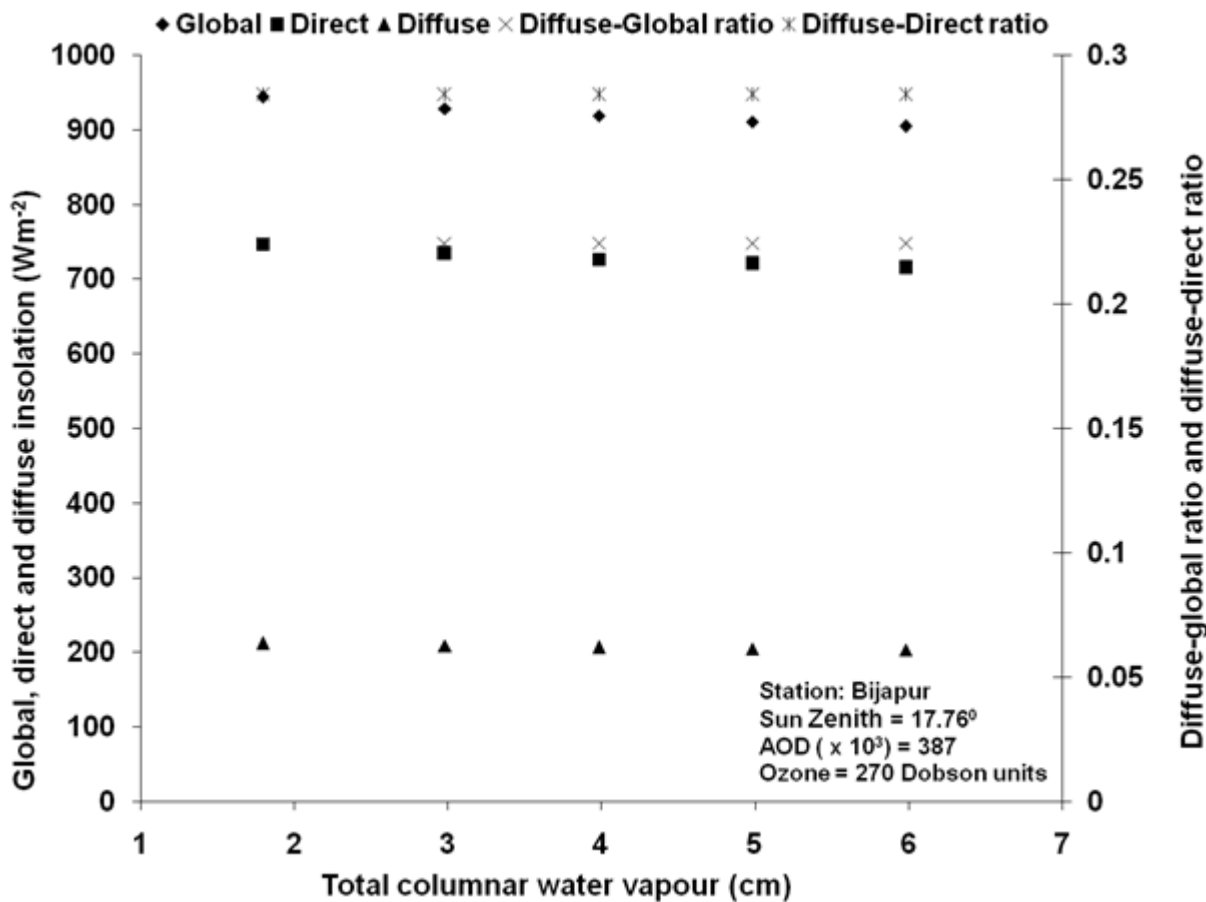


Figure 5b. Sensitivity of the clear-sky insolation model to precipitable water

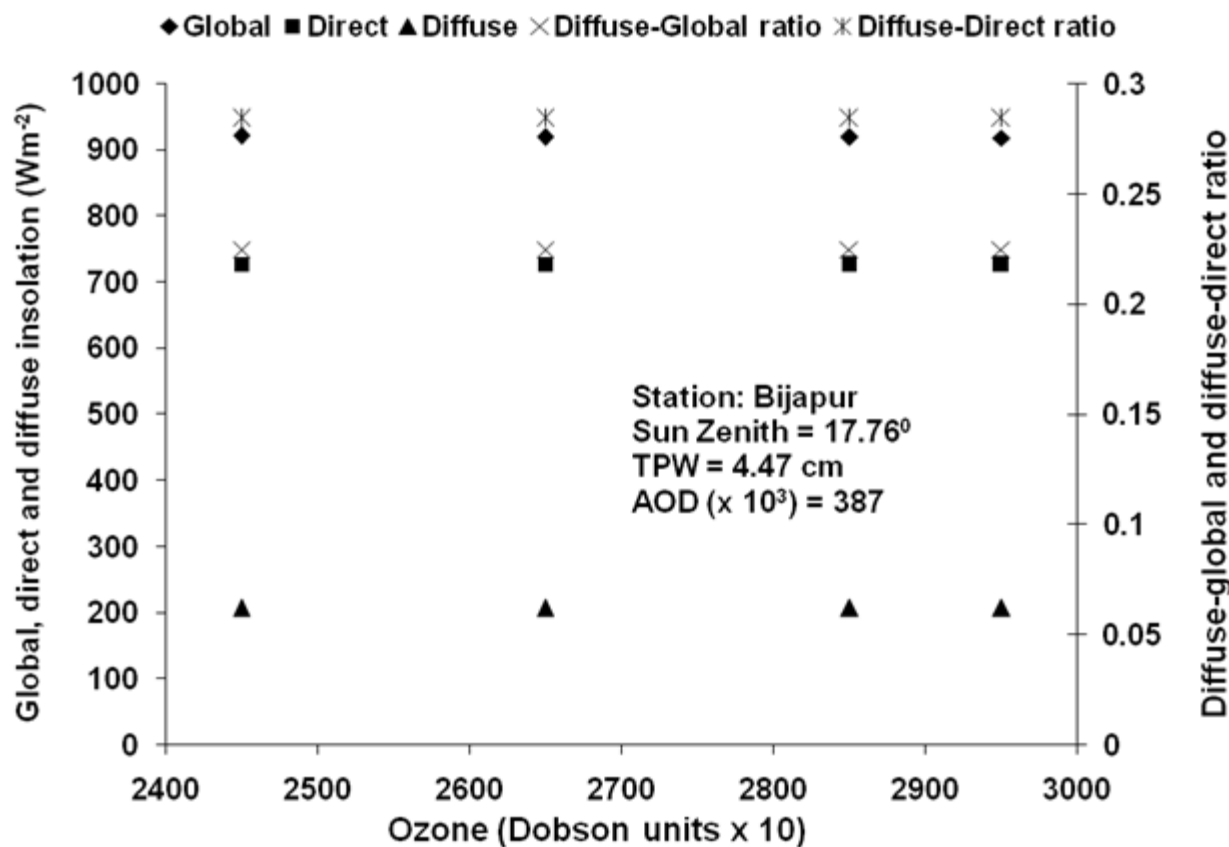


Figure 5c. Sensitivity of the clear-sky insolation model to ozone

20.7 Validation

20.7.1 Data required

Table 7

Sensors	Parameters	Time of acquisitions	Period	Source
INSAT 3D 'Imager'	surface insolation	Half-an-hourly instances, daily and monthly	Upto one year (after operationalization)	DP and PR chain of IMDPS test-bed at BES
Agro-Met Stations (AMS)	<i>In-situ</i> insolation	Half-an-hourly	One year	MOSDAC
Reanalysis field	Incoming shortwave irradiance	Monthly	One year	MEERA 2D

20.7.2 Methods of validation

20.7.2.1 Comparison with *in-situ* measurements

The INSAT 3D daily insolation estimates averaged over 3 x 3 pixels centred over ISRO-AMS (Bhattacharya et al, 2009) and eddy tower locations will be compared with *in situ* measurements from CM3 pyranometer. One year data from at least 10 locations of AMS over different climatic conditions will be used. The selection criteria for choosing quality validation datasets are described below :

- a) Days with daily insolation estimates constituted from at least one instantaneous insolation per hour between 00 GMT to 1300 GMT will only be used for validation. These maintain diurnal symmetry to produce reliable daily integral
- b) The days with *in situ* continuous half-an-hourly measurements are retained for validation. The days with any data loss due to communication failure will be rejected.
- c) Diurnality and seasonality checkings will be carried out
- d) Error statistics in the form of bias, root mean square error (RMSE) and correlation coefficient will be generated.

20.7.2.2 Comparison with other sources of spatial data

Comparison with other sources of insolation product over India or overlapping region such as insolation from MSG over Africa or insolation from GMS partly over Indian sub-continent, reanalysis product for one year and generation of error statistics, histogram matching

20.7.3 Validation results

20.7.3.1 Initial validation of instantaneous insolation estimates from limited observations of INSAT 3D ‘Imager’

In this study, INSAT 3D instantaneous surface insolation was compared with *in situ* measured incoming shortwave radiation by four-component net radiometer (model : CNR-1) placed at AMS at a height of 4 m from ground. The transmitted data through INSAT 3A were received at Bopal Earth Station (BES). The *in situ* data at half-an-hour interval for Hyatnagar (17.82°N, 78.98°E), Andhra Pradesh, Chakdah (23.06°N, 88.54°E), West Bengal, Sriharikota (13.62°N, 80.22°E), Andhra Pradesh, Hoshangabad (22.70°N, 77.75°E), Madhya Pradesh, Khazwal (23.53°N, 93.18°E), Mizoram, Chilika (19.71°N, 85.19°E), Orissa were used to validate the INSAT 3D based estimates. The data coverage was good for AMS at Hyatnagar and Hoshangabad. The AMS data coverage was less in rest of the locations. Altogether 90 (ninety) datasets could be obtained from AMS for validation for the period 1 to 15 October 2013.

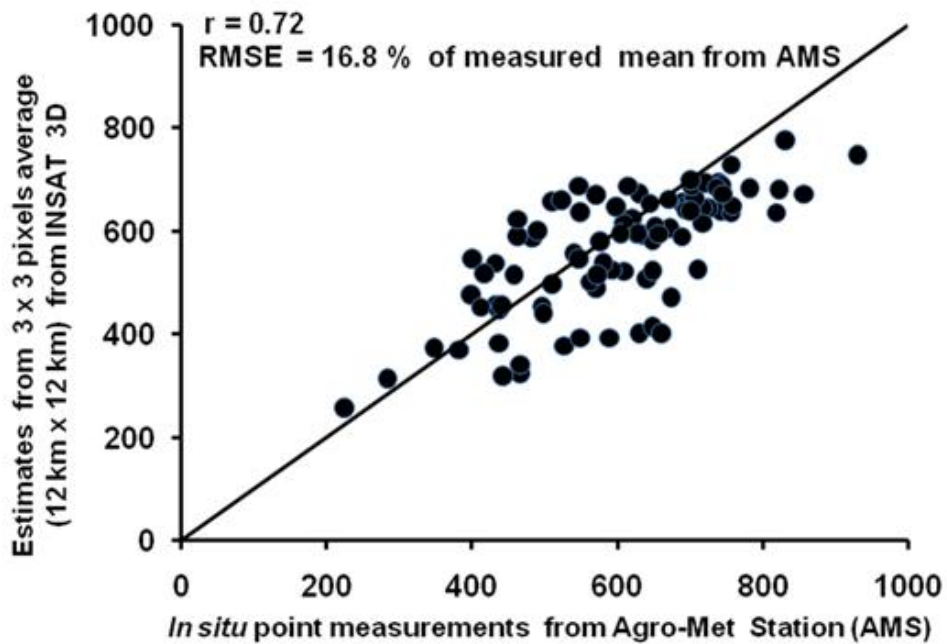
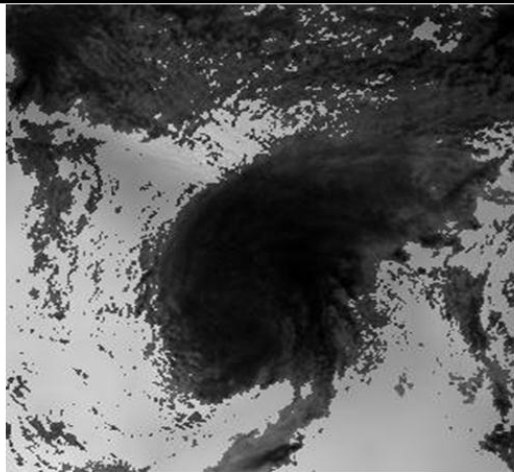
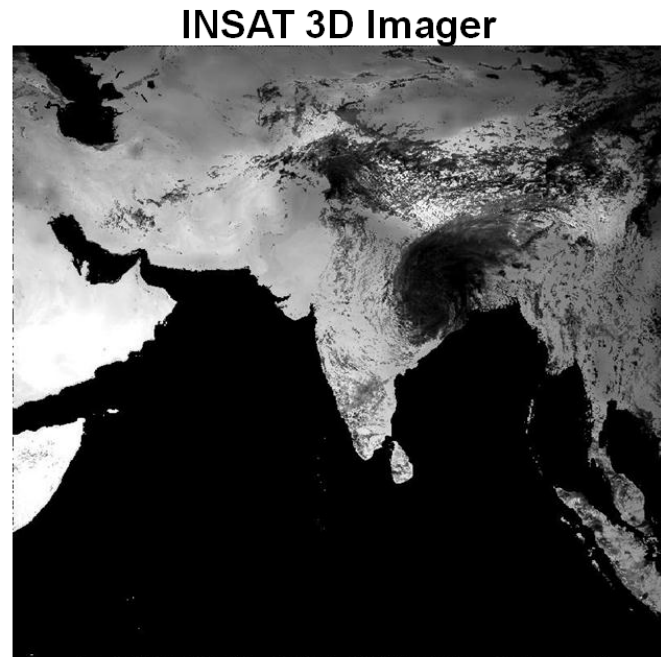
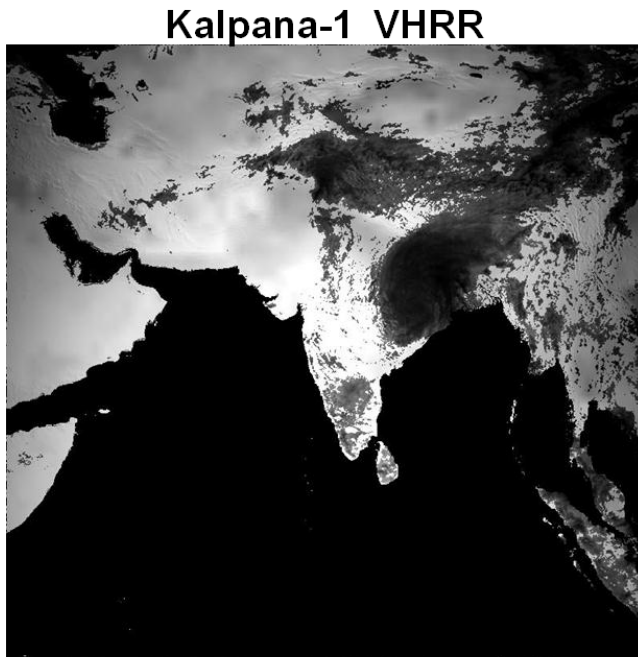


Figure 10. Validation of INSAT 3D instantaneous insolation with limited measurements from AMS

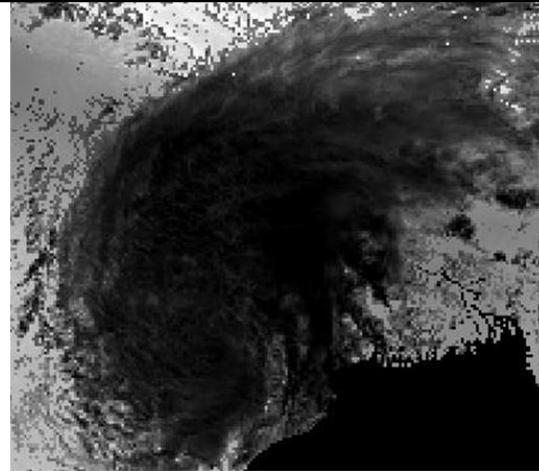
The operational product (K1-VHR-INS) of instantaneous insolation estimates at 8 km spatial resolution from Kalpana-1 VHRR were obtained for 0330, 0500, 0530, 0600, 0630, 0700, 0730, 0800, 0830, 1130 for 1 to 15 October 2013 were obtained through MOSDAC (<http://www.mosdac.gov.in>). The mean insolation from diurnal instances of Kalpana-1 VHRR was compared with mean insolation from ‘Imager’.

A comparison was made between insolation estimates averaged over 3 x 3 pixels (~ 12 km x 12 km) and *in situ* point measurements from Agro-Met Station (AMS) at coincident timings during 1 to 15 October 2013. There was significant correlation ($r = 0.72$) between these two from 90 paired datasets (Figure 6). This showed a mean bias of 37 Wm^{-2} and RMSE of the order of 16.8% of measured mean from AMS. The RMSE has been reduced substantially as compared to reported RMSE (25%) of instantaneous insolation from Kalpana-1 VHRR estimates averaged over 64 km x 64 km and with respect to AMS-based point measurements. The scatter of points around 1:1 line could be due to differences in scale mismatch between estimates and measurements leading to loss of sub-pixel cloud heterogeneity.

A qualitative comparison (Figure 7) was made between ‘Imager’ and VHRR insolation for 0730 GMT on 13 October 2013 to look into the impact of better resolution (0.04 deg) of ‘Imager’ on insolation specially in cloudy patches.



Spatial resolution ~ 8 km



Spatial resolution ~ 4 km

Figure 7. Comparison of insolation at 0730 GMT from two different sources on 13 October 2013

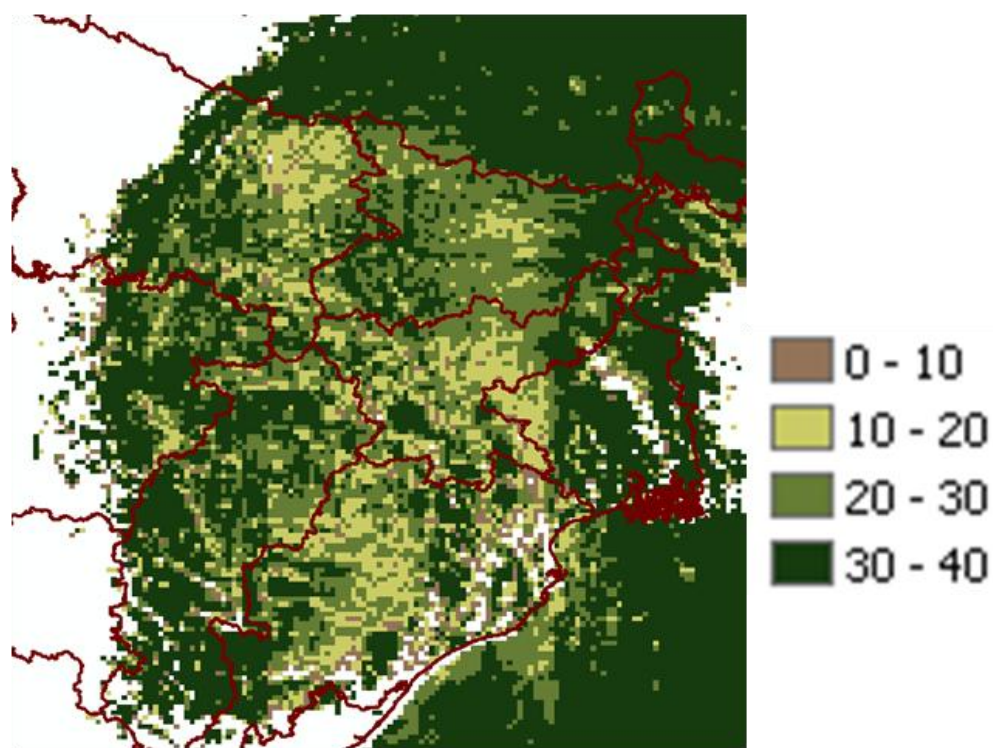


Figure 8. Difference in mean instantaneous insolation (Wm^{-2}) in cloudy patches on 13 October 2013 between INSAT 3D 'Imager' and Kalpana-1 VHRR

Finer gradation of insolation variation was seen over central India and Phailin affected eastern India in case of 'Imager' as compared to Kalpana-1 VHRR with 8 Km spatial resolution.

The difference of mean instantaneous insolation over cloudy patches (Figure 8) in eastern India on 13 October 2013 between 'Imager' and VHRR is shown in Figure 8. Majority of the difference was in the range of $10 - 30 \text{ Wm}^{-2}$.

20.7.3.3 Sources of uncertainties

The possible sources of uncertainties that contribute to errors in K1VHRR daily insolation estimates are outlined below :

Input levels

- (i) *Inherent accuracies of products of aerosol, atmospheric water vapour*
- (ii) *Inaccuracy of cloud and fog mask*
- (iii) *Uncertainty of periodic updation of calibration coefficient of VIS band*

Model structure

- (iv) *Cloud-top reflectivity is considered, no cloud absorption is considered for cloud attenuation*

- (v) Attenuation under fog is treated same as cloud over ground
- (vi) Diffuse insolation from cloud is not considered

Ground validation

- (vii) Scale mismatch between estimates and measurements

The insolation product will be generated at 4 km spatial scale which may not sometimes capture the sub-pixel variability of thin haze, clouds or early morning or late afternoon fog and their influence on insolation which can be captured through pyranometers at tower foot-print scale of few meters. The use of estimates averaged over 3 X 3 pixels for validation with measurements at tower foot-print scale may be valid for cloudless skies. But it may lead to underestimation if cloud patches are present and irregularly distributed in the surrounding pixels but not in the central pixel. It may lead to overestimation if cloudy patches are only present in the central pixel representing tower location but not in the surrounding pixels.

- (viii) Difference in temporal sampling

The ISRO-AMS observations on incident shortwave radiation were sampled at 5 minutes interval and averaged over half-an-hour. Imager will sample with instantaneous snapshots at 30 minutes interval. Therefore, it misses out intermittent cloud presence and its spatio-temporal dynamics. These differences must have introduced some uncertainties in the validation results.

Sensitivity analysis showed little influence of ozone and water vapour content on insolation at different solar zenith angles. But strong sensitivity of AOD at 550 nm was observed on insolation. Single scattering albedo (ω_0) was assumed 1.0 in the present model. In reality, it varied between 0.7603 to 0.9921 among urban-rural-ocean aerosol types (Li 1998).

20.8 Limitations of algorithm and issues in operational scenario

Present algorithm has the following limitations :

- The present algorithm does not consider scattering of incoming solar radiation with raindrops. Therefore, it will lead to inaccuracies in cloudy-sky conditions with rain occurrence.
- Cloud has different proportions of liquid water and ice. Attenuation by them individually is not considered.
- Under cloudy-sky conditions a constant precipitable water of 5.5 gcm^{-2} was assumed which may not be always true.
- All aerosols were assumed to be distributed above cloud. Perturbations by aerosols below cloud were not considered.
- Ground brightness and cloud top albedo are represented by minimum VIS TOA albedo of previous 30 days. Instead, minimum shortwave albedo needs to be used.
- Apart from the above, the sources of uncertainties enumerated in the validation section (section 1.6.3.1) are the sources of inaccuracies.

20.9 Future scope of improvement

- Megha-Tropique (MT) ScaRaB data can be utilized to know the relation between VIS spectral albedo and shortwave albedo radiance, fluxes which will help in computing shortwave albedo including surface and cloud-top. The relation can be extended to INSAT VIS band data to know the minimum ground brightness.
- Revised cloud transmission should be introduced separately for different cloud types of low, medium and high level for different background land types.
- The near-real time diurnal aerosol optical depth (AOD) at 550nm from INSAT 3D ‘Imager’ would help minimize the uncertainties introduced by aerosol climatology. The network of diurnal measurements of aerosol optical depth and its other properties from 10 IMD land stations or AERONET over India can be explored to offset bias in AOD estimates. The real-time availability of these data would help remove the residual bias.
- Bias correction model would be developed from validation results from one year datasets and will be applied later to improve the accuracy.
- Quality flag should be tagged with insolation product.

20.10 References

1. Anonymous (2005). *Task team report on reception, processing, parameter retrieval and application of INSAT-3A/Kalpana data: campaign*.
2. Bhattacharya, B. K., Dutt, C.B.S and Parihar, J.S., 2009, INSAT uplinked Agromet station — A scientific tool with a network of automated micrometeorological measurements for soil-canopy-atmosphere feedback studies. *ISPRS Archives XXXVIII-8/W3 Workshop Proceedings: Impact of Climate Change on Agriculture*, pp. 72-77.
3. Bhattacharya, B. K., Padmanabhan, N., Sazid, Md., Ramakrishna, R. and Parihar, J.S. (2013). Assessing solar energy potential over Indian landmass using diurnal remote sensing observations from Kalpana-1 satellite. *International Journal of Remote Sensing*, 34(20), 7069 - 7090
4. Chen, J.M., Liu, J., Cihlar, J. and Goulden, M.L. (1999). Daily canopy photosynthesis model through temporal and spatial scaling for remote sensing applications. *Ecol. Modelling*, 124, 99–119.
5. Dagestad, K.F. (2004). Mean bias deviation of the Heliosat algorithm for varying cloud properties and sun-ground-satellite geometry. *Theoretical and Applied Climatology*, 79, 215-224
6. Dedieu, G., Deschamps, P.Y. and Kerr, Y.H. (1987). Satellite estimation of solar irradiance at the surface of the earth and of surface albedo using a physical model applied to METEOSAT data. *J Clim. Appl. Meteorol.*, 26, 79-87.
7. Gautier, C., Diak, G. and Masse, S. (1980). A simple physical model to estimate incident solar radiation at the surface from GOES satellite data. *J.Appl. Meteorol.*, 19, 1005 –1012.

8. Hansen, V. (1984). Spectral distribution of solar radiation on clear days: a comparison between measurements and model estimates. *J. Clim. Appl. Meteorol.*, 23, 772-779.
9. Janjai, S., Lakasanaboonsong, J., Nunez, M. and Thongsathitya, A. (2005). Development of a method for generating operational solar radiation maps from satellite data for a tropical environment. *Solar energy*, 78, 739-751
10. Iqbal, M., *An introduction to solar radiation*. Canada: Academic press, 1983, 390.
11. Illera, P., Fernandez, A. and Perez, A. (1995). A simple model for the calculation of global solar radiation using geostationary satellite data. *Atmos. Res.*, 39, 79-90.
12. Jacobs, J.M., Myers, D.A., Anderson, M.C. and Diak, G.R. (2000). GOES surface insolation to estimate wetland evapotranspiration. *J. Hydrol.*, 266, 53-65.
13. Kandirmaz, H.M., Yeginil, L., Pestemalci, V. and Emrahoglu, N. (2004). Daily global solar radiation mapping of Turkey using Meteosat satellite data. *Int. J. Remote Sens.*, 25, 2159-2168.
14. Kakar, R.K. (1983). Retrieval of clear sky moisture profiles using the 183 GHz water vapour line. *J. Appl. Meteorol.*, 22, 1282-1289.
15. Kimothi, S., Bhattacharya, B.K., Semalty, P.D., Pandey, V.K. and Dadhwal, V.K. (2004). Estimation of ground insolation using METEOSAT data over India. *Current Science*, 86, 1308-1312.
16. Kondratyev, K.Y. (1977). *Radiation Regime on inclined surfaces*, World Meteorological Organization, Note Technique 152, MF 79 N11613
17. Li, Z. (1998). Influence of absorbing aerosols on the inference of solar surface radiation budget and cloud absorption. *J. Climate*, 11, 5-17.
18. Lourens, U.W., van Sandwyk, C.M., de Jager, J.M. and van den Berg, J. (1995). Accuracy of an empirical model for estimating daily irradiance in South Africa from METEOSAT imagery. *Agric. For. Meteorol.*, 74, 75-86.
19. Lu, N., Liu, Ronggao, Liu, J. and Liang, S. (2010). An algorithm for estimating downward shortwave radiation from GMS visible imagery and its evaluation over China. *Journal of Geophysical Research*, 115, 1-15
20. Noia, M., Ratto, C.F. and Festa, R. (1993). Solar irradiance estimation from geostationary data; statistical methods. *Solar Energy*, 51, 449-456.
21. Otkin, J.A., Anderson, M.C., Mecikalski, J.R. and Diak, G.R., Validation of GOES-based insolation estimates using data from the United States Climate Reference Network. *J. Hydrometeorol.*, 2005, 6, 460-475.
22. Paulescu, M. and Schlett, Z. (2003). A simplified but accurate spectral irradiance model. *Theoretical and Applied Climatology*, 75, 203-212
23. Pandithurai, G., Pinker, R. T., Devara, P. C. S., Takamura, T. and Dani, K. K. (2007), Seasonal asymmetry in diurnal variation of aerosol optical characteristics over Pune, western India, *J. Geophys. Res.*, 112, D08208, doi:10.1029/2006JD007803
24. Pinker, R.T. and Laszlo, I. (1992). Modeling surface solar irradiance for satellite applications on a global scale. *J. Appl. Meteorol.*, 31, 105-124.

25. Pinker, R.T., Frouin, R. and Li, Z. (1995). A review of satellite methods to derive surface shortwave irradiance. *Remote Sens. Environ.*, 51, 105–124.
26. Rana, S., Kant, Y. and Dadhwal, V.K. (2009). Diurnal and seasonal variation of aerosol properties over Dehradun, India. *Aerosol and Air Quality*, 9(1), 32-49.
27. Rosema, A., Verhees, L., Putten, E., Gielen, H., Lack, T., Wood, J., Lane, A., Fannon, J., Estrela, T., Dimas, M., Bruin, H., Moene, A. and Meijninger W. (2004). European energy and water balance monitoring system. *The European Community Fourth Framework Programme for Research, Technological Development and Demonstration in The Field of Environment and Climate*, Scientific Report.
28. Schadlich, S., Gottesche, F.M. and Olesen, F.S. (2001). Influence of land surface parameters and atmosphere on METEOSAT brightness temperatures and generation of land surface temperature maps by temporally and spatially interpolating atmospheric correction. *Remote Sens. Environ.*, 75, 39 – 46.
29. Smirnov, A., Holben, B.N., Eck, T.F., Slutsker, I., Chatenet, B., Pinker, R.T. (2002). Diurnal variability of aerosol optical depth observed at AERONET (Aerosol Robotic Network) sites. *Geophysical Research Letters*, 29(25), 2115-2118
30. Smith, W.L.(1983). The retrieval of atmospheric profiles from VAS geostationary radiance observations. *J. Atmos. Sci.*, 40, 2025-2035.
31. Srivastava, A.K., Devara, P.C.S., Jaya Rao, Y., Bhavanikumar, Y., Rao, D.N. (2008). Aerosol optical depth, ozone and water vapor measurements over Gadanki, a tropical station in Peninsular India. *Aerosol and Air Quality Research*, 8(4), 459-476
32. Tarpley, J.D. (1979). Estimating incident solar radiation at the surface from geostationary satellite data. *J. Appl. Meteorol.*, 18, 1172-1181.
33. Tanahashi, S., Kawamura, H., Matsuura, T., Takahashi, T. and Yusa, H. (2001). A system to distribute satellite incident solar radiation in real-time. *Remote Sens. Environ.*, 75, 412 – 422.
34. Van Laake, P. E. and S-Azofeifa, G. A. (2004). Simplified atmospheric radiative transfer modelling for estimating incident PAR using MODIS atmosphere products. *Remote Sens. Environ.*, 91, 98-113.
35. Várnai, T. and Marshak, A. (2002). Observations of three-dimensional radiative effects that influence MODIS cloud optical thickness retrievals. *J Atm. Sci.*, 59, 1607-1618.
36. Wang, J., Xia, X., Wang, P., Christopher, S.A. (2004). Diurnal variability of dust aerosol thickness and Angstrom exponent over dust sources region of China. *Geophysical Research Letters*, 31, 8107-8110

21. Application parameters from Sounder derived products

S.No.	Product Name	Spatial Resolution	Temporal Resolution
1	3DSND_L2B_SA1	10 km	1 hourly
2	3DSND_L2B_SB1	10 km	6 hourly

21. APPLICATION PRODUCTS FROM INSAT-3D SOUNDER

Under this section the algorithm for following parameters are described

1. geopotential height, 2. layer and total precipitable water, 3. lifted index from sounder, 4. dry microburst index, 5. maximum vertical theta-e differential, 6. wind index, 7. lifted index from imager

21.1. Geopotential Height

1.1 Algorithm Configuration Information

1.1.1 Algorithm Name

Geopotential Height (GPH)
(Ref : IMD RFP Section 12.3)

1.1.2 Algorithm Identifier

ISRO_INSAT_GPH_A001

1.1.2 Algorithm Specification

Version	Date	Prepared by	Description
1.0	14.02.2007	B Simon	GPH

1.2 Introduction

1.2.1 Overview and background

Geopotential height fields (GPH) at a pressure level indicate the source and sinks of air masses. Generally high pressure areas have relatively higher geopotential heights than low pressure areas. It is also a fundamental quantity that is used in atmospheric general circulation models. At mid-latitudes they also indicate the underlying large-scale waves such as Rossby waves. By looking at the geopotential heights one can infer the first guess atmospheric wind pattern (also known as geostrophic approximation) especially for mid-latitudes.

1.2.2 Objective

To derive geopotential heights at 40 pressure levels from 1000 hPa to 0.1 hPa.

1.3 Inputs

1.3.1 Static Data

Topographic data at sounder horizontal resolution.

1.3.2 Dynamic Data

Retrieved temperature and humidity profiles at 40 pressure levels

1.3.3 Other auxiliary and Model Inputs

1000 hPa analysed heights from IMD or ECMWF/NCEP or surface pressure and surface temperature.

1.4 Algorithm Functional Specifications

1.4.1 Theoretical Background

Given pressure, temperature and humidity profile from surface to 0.1 hPa, height of any pressure level or thickness of atmospheric layer from surface to a particular pressure level can be computed using the formula

$$Z = \frac{R_d \bar{T}_v}{g} \ln\left(\frac{P_s}{P}\right)$$

P_s – Surface Pressure, P – Given pressure where geopotential height is to be calculated,
 \bar{T}_v - Layer mean virtual temperature. This can be computed at all the retrieved pressure levels.

Virtual temperature T_v is given by $T_v = (1 + 0.61q)T$ where q is specific humidity expressed in Kg/Kg, T is temperature in K.

Geopotential height (GPH) is then given by

$$GPH = \frac{R_o Z}{R_o + Z}$$

Where R_o = 6356.766 km, the average radius of the earth. By using H instead of Z, one can use g = 9.8 ms⁻², a constant value in calculations. In reality, g decreases slightly with altitude. Difference between Z and H can be as much as 16m at the height of 10 km above sea level depending on pressure, temperature and humidity profile. Error in Z depends on error in retrieved temperature, specific humidity profiles as well as the surface pressure from analysis. Assuming pressure estimates are error free, a 0.5 K error in estimation of layer mean virtual temperature results in about 10 meter error in Z. Thus the error in Z is very much dependent on the uncertainties in the retrieved temperature and specific humidity profiles (Roland Stull, 2000).

1.4.2 Operational Implementation

Once temperature and humidity profiles are available from surface and all 40 standard pressure levels, Z can be estimated from the formula described in the previous section. Layer mean virtual temperature (between pressure levels p1 and p2) may be estimated by using the formula

$$\bar{T}_v = \frac{(\log_{10} p1).T_{v1} + (\log_{10} p2).T_{v2}}{\log_{10}(p1.p2)}$$

Where p1, p2 are pressure levels (p2 < p1), T_{v1}, T_{v2} are virtual temperatures at p1 and p2 respectively.

This may be carried out starting from the surface to subsequent levels in steps of one pressure level each.

1.5 Outputs

Parameter	Unit	Min	Max	Accuracy	Resolution
GPH	Meters	-	-	+/- 10 m	0.5 x 0.5 deg

1.5.1 Format of the output and the domain

Latitude, Longitude, Pressure (1000 to 0.1 hPa), GPH.

Domain: 50 S to 50 N, 30 E to 130 E.

1.6 Validation

1.6.1 Data required

Co located radiosonde measurements of temperature, humidity and geopotential heights.
Geopotential heights from NCEP/ECMWF reanalysis.

1.6.2 Methods of Validation

Difference between radiosonde/reanalysis geopotential heights, mean bias, standard deviation etc are calculated.

1.7 Technical Issues (limitation etc.)

Accuracy of the product depends on the accuracy of the retrieved temperature and humidity profiles. A simple calculation assuming a surface pressure of 1000 hPa shows that a 0.5 K error in \bar{T}_v will result in about 10 m error in 500 hPa geopotential height. To a first approximation, error in \bar{T}_v is of the same order of T. Hence achieving less than 10 m error in 500 hPa geopotential height demands that errors in retrieved temperatures be less than 0.5 K.

1.8 References

Meteorology For Scientists and Engineers, Roland Stull, 2000, Brookes/Cole (Pub.), 502 pp.

21.2. Layer and Total Precipitable Water

2.1 Algorithm Configuration Information

2.1.1 Algorithm Name

Layer and Total Precipitable water (PW)

(Ref : IMD RFP Section 12.4 and 12.5)

2.1.2 Algorithm Identifier

ISRO_INSAT_PW_A001

2.1.3 Algorithm Specification

Version	Date	Prepared by	Description
1.0	14.02.2007	B Simon D Jagadheesha	PW Baseline document

2.2 Introduction

2.2.1 Overview and background

Water vapor content in the atmosphere modifies the air mass characteristics. Presence of air mass lightens the air mass thereby increasing the potential for convective activity. As an air parcel rises, it cools dry adiabatically until saturation vapor pressure is reached. Once saturation vapor pressure is reached some of the water vapor condenses forming liquid droplets, and releasing latent heat. This latent heating reduces the amount of cooling and makes the air parcel more buoyant. This information is very essential for accurate prediction of weather and goes as an input parameter in numerical weather prediction models.

2.2.2 Objective

To compute layer precipitable water in three layers i.e. 1000hPa-900 hPa, 900-700 hPa, and 700-300 hPa and total precipitable water in the vertical column of atmosphere stretching from surface to about 100 hPa.

2.3 Inputs

2.3.1 Dynamic data

Retrieved specific humidity at standard pressure levels.

2.4 Algorithm Functional Specifications

2.4.1 Theoretical Background

Layer precipitable water may be computed using the formula

$$PW = \int_{p1}^{p2} \frac{q}{g} dp$$

where p1 and p2 are bounding pressures of each layer in Pa, q – specific humidity in Kg/Kg. Total precipitable water is also computed from the same formula with p1 as surface pressure and p2 as top of the atmosphere pressure (i.e. about 100 hPa beyond which water vapor amount is assumed to be in negligible). Unit of precipitable water is mm depth of equal amount of liquid water above a surface of one square meter (if pressure is in Pa and specific humidity is in Kg/Kg).

2.4.2 Operational Implementation

For practical purposes the above integral is evaluated numerically i.e. integral expression is replaced by summation.

$$PW = \sum_{p=p1}^{p2} \frac{q}{g} \Delta p$$

2.5 Outputs

Parameter	Unit	Min	Max	Accuracy	Resolution
PW	mm	0	100mm	25%	0.5 x 0.5 deg

2.5.1 Format of the output and the domain

lat, lon, PW (at three layers) and TPW (total precipitable water vapor).

Domain: 50 S to 50 N, 30 E to 130 E.

2.6 Validation

2.6.1 Data Required

Co located radiosonde observations, Total precipitable water from ground GPS receivers, and radiometers wherever available.

2.6.2 Methods of validation

Difference between the observational (radiosonde, GPS receiver and radiometer) and INSAT-3D derived PW and TPW are computed along with standard error statistics.

2.7 Technical Issues (Limitations etc.)

RMS error of 4-6 mm and mean bias of 1 mm (as required by IMD) will depend on the error levels of retrieved specific humidity profile.

2.8 References

Meteorology For Scientists and Engineers, Roland Stull, 2000, Brookes/Cole (Pub.), 502 pp.

21.3. Lifted Index from Sounder

3.1 Algorithm Configuration Information

3.1.1 Algorithm Name

Lifted Index from Sounder (LIS)

(Ref : IMD RFP Section 12.6)

3.1.2 Algorithm Identifier

ISRO_INSAT_LIS_A001

3.1.3 Algorithm Specification

Version	Date	Prepared by	Description
1.0	14.02.2007	B Simon D Jagadheesha	LIS Baseline document

3.2 Introduction

3.2.1 Overview and background

Lifted index is an indicator of convective activity. It is calculated in the following steps.

1. Mean boundary layer (usually lowest 100 hPa layer) temperature and humidity are calculated.
2. A parcel of air with the above calculated temperature and humidity is lifted from the middle of the boundary layer dry adiabatically up to lifting condensation level and then moist adiabatically up to 500 hPa.
3. The environmental temperature minus the parcel temperature at 500 hPa calculated in the above step is the lifted index (LI).

If the parcel temperature is warmer than the environmental temperature it indicates that the parcel can rise further on its own and LI will be negative. Based on a large number of LI calculations from radiosonde observations, it is observed that LI less than -5 implies a very strong likelihood of thunderstorm activity. Time sequence of geographical pattern of LI may be monitored to study large scale convective activity and its relation to synoptic circulation systems (Hayden *et al.*, 1996).

3.2.2 Objective

To calculate Lifted Index (LIS) from temperature and humidity profiles retrieved from the INSAT sounder.

3.3 Inputs

3.3.1 Dynamic Data

Sounder retrieved temperature and humidity profiles at standard pressure levels.

3.4 Algorithm Functional Specifications

3.4.1 Overview

3.4.1.1 Theoretical Background

Given boundary layer pressure, specific humidity and temperature, one can lift the parcel to 500 hPa dry adiabatically up to lifting condensation level (LCL) and from LCL to 500 hPa moist adiabatically and thereby compute the parcel temperature at 500 hPa. Environmental temperature at 500 hPa is the retrieved temperature at 500 hPa. Lifted

Index is then the difference between the 500 hPa parcel temperature and environmental temperature.

Moist adiabatic lapse rate (saturated adiabatic lapse rate) is given by (*Meteorology for Scientists and Engineers*, by Roland Stull, 2000)

$$\frac{\Delta T}{\Delta P} = \frac{(aT + cq)}{P(1 + (bq/T^2))}$$

Where $a=0.28571$, $b=1.35 \times 10^7 \text{ K}^2$, $c=2488.4 \text{ K}$, T – Temperature in K, P – Pressure in kPa, q – specific humidity in g/Kg.

Starting at a temperature T_1 , at pressure P_1 , temperature at pressure P_2 , can be written as

$$T_2 = T_1 + \frac{\Delta T}{\Delta P} (P_2 - P_1)$$

The difference $P_2 - P_1$ should be small enough so that the moist lapse rate does not change significantly. Thus one can estimate parcel temperature step by step at higher levels, by this method. Error in the Lifted Index calculated this way will depend on error in retrieved temperature and humidity profile.

3.4.2 Operational Implementation

Implementation of the above described algorithm is self explanatory.

3.5 Outputs

Parameter	Unit	Min	Max	Accuracy	Resolution
LIS	°C	-	-	2-3°C	0.5 x 0.5 deg

3.5.1 Format of the output and the domain

lat, lon, LIS

Domain: 50 S to 50 N, 30 E to 130 E.

3.6 Method of Validation

3.6.1 Data Required

Collocated radiosonde observations

3.6.2 Methods of Validation

Direct comparison with LI calculated from collocated radiosonde observations.

3.7 Technical Issues (Limitation etc.)

Accuracy of the product depends on the accuracy of the retrieved temperature and humidity profiles from the sounder.

3.8 References

Hayden, C. M., Wade, G. S., and T. J. Schmit, 1996: Derived Product Imagery from GOES-8. *J. Appl. Meteor.*, **35**, 153-162.

Meteorology For Scientists and Engineers, Roland Stull, 2000, Brookes/Cole (Pub.), 502 pp.

21.4 Dry Microburst Index

4.1 Algorithm Configuration Information

4.1.1 Algorithm Name

Dry Microburst Index (DMI)
(Ref : IMD RFP Section 12.8)

4.1.2 Algorithm Identifier

ISRO_INSAT_DMI_A001

4.1.3 Algorithm Specification

Version	Date	Prepared by	Description
1.0	14.02.2007	B Simon D Jagadheesha	DMI Baseline Document

4.2 Introduction

4.2.1 Overview and Background

Evaporative cooling of falling rain is often a much larger effect than the liquid water loading. In regions such as the western Great Plains of the United States (e.g. near Denver), the environmental air is often so dry that evaporative cooling causes dangerous downdraft called downbursts. Hazardous downbursts can occur even under cloud bases where precipitation evaporates before reaching the ground. The smaller-diameter but intense downbursts are called microbursts. Downbursts of 0.5 to 5 km in diameter have been observed. For extreme cases, downdraft speeds of nearly 10 m/s have been observed 100 m above ground. This is particularly hazardous to landing and departing aircraft, because this vertical velocity can sometimes exceed aircraft climb rate. Doppler radars can detect some of the downbursts and give early warning to pilots (Roland Stull, 2000). In India dry desert regions, elevated plains, mountain regions where air is very dry may be susceptible to microburst. Generally dry microburst occurs in situations characterized by high convective cloud bases and strong evaporational cooling in the sub-cloud layer, resulting in little or no precipitation at the surface.

4.2.2 Objective

To compute dry microburst index based on an empirical formula.

4.3 Inputs

4.3.1 Dynamic Data

Retrieved temperature and humidity profile at standard pressure levels.

4.4 Algorithm Functional Specifications

4.4.1 Overview

4.4.1.2 Theoretical Background

Dry microburst index is generally calculated using the formula,

$$DMI = \Gamma + (T - T_d)_{700} - (T - T_d)_{500}$$

Γ - lapse rate ($^{\circ}\text{C km}^{-1}$) of the layer from 700 hPa to melting level (i.e. layer at 0° C), T – Temperature ($^{\circ}\text{C}$), T_d – Dew point ($^{\circ}\text{C}$). Usually DMI is not calculated for any retrieval unless the following three conditions are satisfied:

- (1) $\Gamma > 6 \text{ K km}^{-1}$ (somewhat stable for convective activity)
 - (2) $(T - T_d)_{700} \geq 8 \text{ K}$ (implies a very dry atmosphere close to surface)
 - (3) $(T - T_d)_{500} \leq 8 \text{ K}$ (implies some level of saturation at this level)
- Suitability of these conditions needs to be studied for the Indian region.

4.4.2 Operational Implementation

Operational implementation simply involves evaluation of the quantities in the formula

$$DMI = \Gamma + (T - T_d)_{700} - (T - T_d)_{500}.$$

4.5 Outputs

Parameter	Unit	Min	Max	Accuracy	Resolution
DMI		-	-	2-3$^{\circ}\text{C}$	0.5 x 0.5 deg

4.5.1 Format of the output and the domain

Lat, Lon, DMI

Domain: 50 S to 50 N, 30 E to 130 E.

4.6 Validation

Doppler weather radar observations of dry micro burst index may serve as validation tool. Wind shear data from aircrafts may also give some data for validating dry microburst index.

4.6.1 Data Required

Doppler weather radar observations of dry micro burst events may be useful in validation. Wind data during aircraft landing may also give some indication of dry microburst events whenever they occur which may also be used for validation.

4.6.2 Methods of Validation

Conventional/direct comparison of computed and observed quantities.

4.7 Technical Issues (Limitation etc.)

As the index is based on observations over USA where Great Plains with a very dry air exists, applicability over Indian region may require slight modifications. For instance more emphasis may be given to study of meteorological conditions leading to dust storms, etc. and development of suitable indices. As the sounder gives vertical profiles of temperature and humidity only over cloud free regions, one may not be able to detect such events from sounder retrievals.

4.8 References

Meteorology For Scientists and Engineers, Roland Stull, 2000, Brookes/Cole, 502 pp.

Pryor, K.L., Ellrod, G.P., and A.A., Bailey, 2002: Convective downburst potential using GOES sounder derived products. *National Weather Association Electronic Journal of Operational Meteorology*, 2002-EJI.

21.5. Maximum Vertical Theta-E Differential

5.1 Algorithm Configuration Information

5.1.1 Algorithm Name

Maximum Vertical Theta-e Differential

(Ref : IMD RFP Section 12.9)

5.1.2 Algorithm Identifier

ISRO_INSAT_THETAED-A001

5.1.3 Algorithm Specification

Version	Date	Prepared by	Description
1.0	14.02.2007	B Simon D Jagadheesha	THETAED Baseline Document

5.2 Introduction

5.2.1 Overview and Background

Equivalent potential temperature (θ_e) is the potential temperature that a saturated air parcel would have if raised moist adiabatically to the top of the atmosphere. It is given by the formula

$$\theta_e = \theta \exp\left(\frac{Lq}{C_p T}\right)$$

Where θ - Potential temperature, L – Latent heat of condensation, q – Specific humidity, T – Temperature, C_p – Specific heat of dry air at constant pressure.

As the moisture decreases with height, θ_e also decreases with height and reaches a minimum in the middle troposphere, then increases again into the upper troposphere. The maximum vertical θ_e differential between the boundary layer and middle troposphere is a measure of atmospheric instability in the vertical direction. Larger the theta-e differential, more unstable is the atmosphere in the vertical direction. A quantity called dry microburst potential index (MDPI) is calculated by dividing thetaed by 30. As this formula for MDPI is empirical, its suitability over the Indian region needs to be studied.

5.2.2 Objective

To calculate thetaed from sounder retrieved temperature and humidity profile.

5.3 Inputs

5.3.1 Dynamic Data

Temperature and humidity profiles retrieved from the sounder.

5.4 Algorithm Functional Specifications

5.4.1 Overview

5.4.1.1 Theoretical Background

Equivalent potential temperature (θ_e) is defined as

$$\theta_e = \theta \exp\left(\frac{Lq}{C_p T}\right)$$

(See section 5.2.1 for details).

It is different from potential temperature in the sense that it is dependent on the moisture content (moisture content provides additional energy in the form of latent heat release). Its values will be high at lower levels due to presence of water vapor and decreases as one reaches middle troposphere. If lower troposphere is very humid and middle troposphere is very dry then there will be a large vertical difference in equivalent potential temperatures which is indicative of microburst potential if convection were to happen (Pryor *et al.*, 2002).

5.4.2 Operational Implementation

From the retrieved temperature and humidity data calculate theta-e at standard pressure levels using the equation given in the previous section. Calculate the difference between the lowest level theta-e and subsequent levels up to 500 hPa. The maximum of these differences is maximum vertical thetae difference (thetaed).

5.5 Outputs

Parameter	Unit	Min	Max	Accuracy	Resolution
THETAED	°C	-	-	2-3°C	0.5 x 0.5 deg

5.5.1 Format of the output and the domain

Lat, lon, thetaed

Domain: 50 S to 50 N, 30 E to 130 E.

5.6 Validation

5.6.1 Data Required

Collocated radiosonde measurements of temperature and humidity profiles.

5.6.2 Methods of Validation

Direct comparison between thetaed values calculated from radiosonde measurements and from the sounder.

5.7 Technical Issues (Limitations etc.)

Accuracy of thetaed calculated from the sounder depend on the accuracy of the retrieved temperature and humidity profiles.

5.8 References

Pryor, K.L., Ellrod, G.P., and A.A., Bailey, 2002: Convective downburst potential using GOES sounder derived products. *National Weather Association Electronic Journal of Operational Meteorology*, 2002-EJI.

21.6. Wind Index

6.1 Algorithm Configuration Information

6.1.1 Algorithm Name

Wind Index (WI)

(Ref : IMD RFP Section 12.7)

6.1.2 Algorithm Identifier

ISRO_INSAT_WI_A001

6.1.3 Algorithm Specification

Version	Date	Prepared by	Description
1.0	14.02.2007	B Simon D Jagadheesha	WI Baseline Document

6.2 Introduction

6.2.1 Overview and background

Wind Index (WI) is a parameter based on vertical equations of momentum and continuity with certain simplifying assumptions. It is given by the formula

$$WI = 5[H_M R_Q (T^2 - 30 + Q_L - 2Q_M)]^{1/2}$$

Where WI – Maximum wind gust (knots, at the surface)

H_M – Height above ground of melting level (in km)

R_Q – Q_L/12 but not >1, Q_L – Mean mixing ratio (g/Kg) in lowest 1 km

T – Lapse rate ($^{\circ}\text{C km}^{-1}$) from surface to melting level, Q_M – Mixing ratio at melting level. WI provides guidance on the maximum possible wind gusts that can occur with given atmospheric conditions, if convection were to occur. This is useful for generating short-range warnings and forecasts (Pryor *et al.*, 2002).

6.2.2 Objective

Calculate WI from INSAT sounder retrievals

6.3 Inputs

6.3.2 Dynamic Data

Geopotential heights of standard pressure levels, temperature and humidity retrieved from the sounder.

6.4 Algorithm Functional Specifications

6.4.1 Overview

6.4.1.1 Theoretical Background

See section 6.2.1

6.4.2 Operational Implementation

1) From the retrieved temperature profile at standard pressure level, the pressure level at which temperature reaches 0° C is estimated by means of interpolation. Height of the

melting layer is then estimated by using the standard formula based on hydrostatic approximation.

- 2) Mixing ratio at melting level is also obtained by means of interpolation of retrieved humidity.
- 3) Mean mixing ratio in the lowest one km is also estimated by using retrieved specific humidity profile at standard pressure levels.
- 4) Lapse rate between surface and melting layer is easily estimated by dividing surface temperature by height of the mixing layer (in km).

These parameters are substituted in the formula for WI given in section 6.2.1.

6.5 Outputs

Parameter	Unit	Min	Max	Accuracy	Resolution
WI	knots	0	-	-	0.5x 0.5 deg

6.5.1 Format of the output and the domain

Lat, lon, WI

Domain: 50 S to 50 N, 30 E to 130 E.

6.6 Validation

6.6.1 Data required

Collocated radiosonde measurements during convective events, measurement of wind gust at surface.

6.6.2 Methods of validation

Direct Comparison

6.7 Technical issues (Limitation etc.)

Accuracy of the product depends on the accuracy of the retrieved temperature and humidity profiles. This index may be region dependent.

6.8 References

Pryor, K.L., Ellrod, G.P., and A.A., Bailey, 2002: Convective downburst potential using GOES sounder derived products. *National Weather Association Electronic Journal of Operational Meteorology*, 2002-EJI.